The Microwave Response of Subwavelength Structures with Liquid Crystals

Submitted by

Robert John Kelly

To the University of Exeter as
a thesis for the degree of
Doctor of Philosophy

December 2007

I certify that all material in this thesis which is not my own work has been identified and that no material has previously been submitted and approved for the award of a degree by this or any other University.

_____

Abstract

The transmission of microwave frequency radiation through subwavelength structures, and the absorption of microwaves by structures of subwavelength thickness are areas of great current interest. The work presented in this thesis investigates both transmission and absorption of microwaves using subwavelength scale structure, demonstrating new modes in both transmission and absorption, and introducing the use of Liquid Crystals (LCs) to such structures in order to allow a degree of tuneability to be achieved. Finite element method mathematical modelling (Ansoft's HFSS) has been used extensively to produce model results to compare with the original data and to allow the development of a complete understanding of the nature of the various electromagnetic modes supported by each structure, and this modelling code is discussed in depth in *Chapter* 3.

The highly original experimental work in this thesis is divided into two sections. *Chapters* 5 and 6 are the first two experimental chapters, and discuss the transmission of microwaves through subwavelength structures, firstly through a modified 2-D slit structure etched into a thin metal film, and secondly through a subwavelength slit filled first with LC and subsequently with Polymer-dispersed Liquid Crystal (PDLC). The 2-D slit array allows transmission via a zeroth-order Fabry-Perot type mode, and the LC and PDLC filled slits show clearly that tuneability may be introduced.

Chapters 7 and 8 discuss the absorption of microwaves by metal-dielectric-metal structures that are of subwavelength thickness. The first set of structures are regular arrays of thin metallic "pennies" that are of subwavelength dimensions. These penny arrays allow remarkably efficient absorption of incident microwave radiation that is independent of incident angle and polarisation, and is determined by the structure dimensions and dielectric core permittivity. The second set of samples have a LC core in order to allow tuneability of the absorption resonance. Seven samples are investigated, each of which demonstrates resonant absorption that may be shifted in frequency by voltage-realignment of the LC core material.

This thesis is dedicated to my Nana, Peggy Duffy,

for all her love and support.

Contents

List of Figures

Acknowledgements

Here I would like to thank all the people who have helped and supported me in all kinds of ways in the (almost) four years since I started my PhD. First and foremost I would like to thank Professor Roy Sambles for offering me the position, and for his fantastic drive and enthusiasm throughout the project. His ability to overcome, and refusal to give in to problems of any kind was an inspiration. Secondly I would like to thank my Qinetiq supervisor, Chris Lawrence. He was always a pleasure to talk to and offered many useful suggestions for guiding the project.

My colleagues in the microwave group were also all extremely helpful. Alistair Hibbins's work was the precursor to virtually everything that has come since in the microwave group, and without him my project would never have existed. He was also a big help in dealing with any experimental or modelling problems I encountered. I would like to thank Matt Lockyear, with whom a significant portion of the work of this thesis was collaboratively achieved. His assistance as a researcher, and as a good friend has been greatly appreciated. James Suckling was also a big help on a day to day basis, both experimentally and with modelling. It was a pleasure to work in the same lab as him throughout my PhD.

Outside of the microwave group, I was privileged to receive assistance from many of the rest of the group, including those working with Professor Bill Barnes, and had good relationships with those I did not collaborate with. They include, in no particular order, Gemma, Ian, Andy, George, Sharon, John, Tim A, Tim T, Lucy, Jimmy K, Simon, Steve, Steph, Pete V and Mike Jory. More recent members of the group include James P, Ciaran, Celia and James E. Matt Biginton's work as a summer student was also a big help to me.

Next I would like to thank the support staff, who were all really approachable and helped me in various ways. In particular, Pete Cann did a huge amount of work for me, and could always come up with a solution to any problem. Thanks also to Dave Jarvis, John Meakin, Steve Tuckett, Kev, Russell, Chris and Phil V. Also thanks to the admin staff, Hilary, Yasmin, Denise, Natasha and Victoria.

Finally I would like to thank friends and family who have supported me all through my studies. Thanks in particular to Claire McPheat, who over the last 18 months especially has been so important to me. Thanks also to my parents. Without them, I would never have even been in a position to begin a PhD, so whilst I don't expect them to read this thesis from cover to cover, I would like them to take a large portion of the credit for it.

Chapter 1

Introduction

The work presented in this thesis is focused on two areas that have generated much interest within the scientific community in recent years, that is the transmission of electromagnetic radiation through subwavelength apertures, and its absorption by structures of subwavelength thickness. In addition, this thesis will demonstrate how Liquid Crystals (LCs) may be introduced into such structures to offer a degree of tuneability. The initial experimental chapters (*Chapters* 5 and 6) are concerned with the transmission of microwaves, firstly via subwavelength slits in a thin aluminium film modified by the addition of perpendicular cuts, and secondly through an LC-filled single subwavelength slit in a thick metal plate. Transmission through both structures is shown to be mediated by coupling of incident radiation to the metal surface, and the electromagnetic modes that propagate along this boundary. In the optical regime this mode is known as the surface plasmon polariton (SPP) and its presence was first found experimentally by *Wood* (1902) [1] in the spectra from ruled diffraction gratings. However, the mechanism by which transmission is achieved through a thin metal film in *Chapter* 5 is of a nature previously unreported in the literature, and is therefore a major contribution to the novelty of this thesis.

Chapters 7 and 8 are concerned with the absorption of electromagnetic radiation via structures of subwavelength thickness. These structures consist of two metal layers (one of which has some structure etched into it) separated by a dielectric core. It is shown that by suitable use of LC as the dielectric core (*Chapter* 8) it is possible to achieve a degree of tuneability of absorption resonances on such structures. The existence of these absoprtion resonances, their subsequent analysis, and the introduction of LC into the structures are all previously unreported in the literature, and are therefore considered the core achievements upon which this thesis is based.

Chapter 2 presents an historical review of the discovery of, and subsequent work undertaken to understand the physics of the SPP. A derivation of the dispersion of the SPP mode at the interface of a planar metal-dielectric boundary is presented, along with the spatial extent of the fields associated with this mode. The non-radiative nature of the mode is demonstrated, and therefore, methods of coupling to the SPP are also discussed. Particular is focus is given to grating-coupling, as this is the coupling method pertinent to this thesis.

Chapter 3 has two main sections, the first being a brief review of the theory of transmission of microwaves through perfectly conducting metal waveguides, and the second being a discussion of Liquid Crystals. In the waveguide section the characteristics of the TE (transverse electric), TM (transverse magnetic) and TEM (transverse electromagnetic) waves are discussed, and the transverse fields and cut-off wavelengths are derived for each mode from Maxwell's equations. Field profiles from a finite element method (FEM) model for propagating modes are presented where appropriate. Both rectangular and circular waveguide geometries are discussed. In the second section, the fundamental properties of LCs are discussed, with particular reference to nematic LCs. Their use at optical frequencies will be briefly described, followed by an overview of work to date involving LCs at microwave frequencies.

Chapter 4 describes Ansoft's High Frequency Structure Simulator, the Finite Element Method model used to explore the electromagnetic response of structures throughout this thesis. The physical principles of FEM modelling are explained in general, and the specific operation of this package is discussed with its advantages and limitations detailed by the use of example models. Specific models from experimental samples within this thesis are discussed in greater depth to give a clear insight into the FEM's operation.

Chapter 5 is the first experimental chapter in which the resonant transmission of microwaves through a 2-dimensional array of slits in a thin aluminium layer is discussed. Four samples are investigated, the first two of which are 2-D arrays of slits modified by the addition of electrical contacts across each slit. The third and fourth samples are further modified by the addition of "cuts" (of differing depth) perpendicular to the slits. Samples are formed from a thin aluminium layer ($\sim$40 nm) backed by a dielectric layer ($\sim$100 μm), and arrays are cut into the metal film via a wet-etch technique. Two transmission modes are shown to propagate through this structure. One of these transmission modes is a coupled surface wave, and occurs in all samples. Incident photons couple to slits that lie orthogonal to the polarisation direction, exciting a surface wave. This surface wave is then coupled to a similar wave on the back surface of the structure, which then re-radiates into free space. The second transmission mode is shown to occur due to an entirely different mechanism, and arises only on those samples that have perpendicular cuts. The cuts allow the accessing of a "zeroth-order Fabry-Perot" mode which occurs due to the role of surface currents on the metal layer, and is the first demonstration of a transmission mode mediated by this process. The resonant frequency and efficiency of this mode is shown to be highly dependent on the surface structure, and in particular the

cut dimensions. In addition, transmission is shown to occur via slits that lie parallel to the polarisation direction, contrary to all other subwavelength-slit transmission that appears in the literature.

Chapter 6 investigates the transmission of microwaves through LC- and PDLC-filled (Polymer-Dispersed Liquid Crystal) subwavelength slits, and analyses the transmission to determine microwave permittivities of these materials. Transmission through the slits is found to be mediated by Fabry-Perot like resonances, and by a simple calculation the ordinary and extraordinary indices of both LCs and PDLCs are determined. The PDLC used throughout this thesis is a mixture of LC and a UV-curing glue. Using the index determination, different wt% of LC/glue are investigated in order to determine the optimum ratio.

Chapter 7 is the third experimental chapter, and the first to examine structures in reflection. The samples investigated are arrays of metallic "pennies" separated from a metal substrate by thin dielectric layer. The samples take two forms, the first being a thick aluminium plate, 300 mm $\times$ 300 mm $\times$ 30 mm, which was covered with a 50 μm dielectric layer of Filmolux, on top of which an array of metallic pennies is assembled. Each penny has a radius of $\sim$2.875 mm and a thickness of $\sim$1 mm. Three arrays of this type are investigated, two of which are square arrays, having pitches of 6 mm and 8 mm, and the third of which is a hexagonal array, having a pitch of 8.8 mm. The second type of sample is formed from a printed circuit board (PCB), which consists of a polyester sheet of thickness 100 μm bounded by copper layers of thickness 16 μm. The array is formed by etching into one face of the copper cladding, and an array of pitch 6.25 mm with penny radii of 2.95 mm is produced. The arrays achieve remarkable resonant absorption of up to 100% from a maximum of three modes in the zero-ordered (no diffraction) region, with the resonant frequency determined by structure dimensions. Electric and magnetic field profiles from the structures on resonance provided by an FEM model reveal the absorption to be due to a previously unreported mechanism. Further to this it is shown that these fields resemble those found in waveguide theory. Using waveguide theory it is then possible to identify these modes, and calculate a cut-off frequency for each, and thereby provide a method for predicting the frequencies at which these modes will occur.

Chapter 8 is the final experimental chapter, and is focused on incorporating LC into some of the structures investigated in previous chapters. Structures are formed from two glass sheets, both of which are aluminised on one face. One sheet then has some structure incorporated into the aluminium layer via a wet-etch technique. The sheets are then coated with an aligning layer on the metalised side which is then baked and unidirectionally rubbed in order to promote homogeneous alignment of the LC. The sheets are then assembled into a cell spaced by glass microspheres, and capillary filled with LC in its isotropic phase. Seven structures are investigated, a 1-D slit array, a 2-D slit array, two "penny" arrays, and three structures that are replicas of the samples from *Chapter* 5. The absorption mechanism for each of these struc-

tures is investigated with reference to field plots provided by HFSS. The resonant frequency of each of these structures is, in part, dependent on the refractive index of the dielectric core. Therefore by applying an electric field across the LC layer the core index is changed, causing a shift in the resonant frequency of the sample. This is the first demonstration of the use of LC for providing a degree of tuneability into such structures, and is achieved in samples that already display absorption mediated by previously unreported mechanisms.

Chapter 9 is the conclusions chapter, and summarises all the work presented in the preceding chapters. In addition, possible future areas of research arising from this work are suggested, along with a list of publications and presentations.

Chapter 2

Surface Plasmon Polaritons

2.1 Introduction

Surface Plasmon Polaritons (SPPs) are a longitudinal oscillation of surface charge density at a planar interface between a metal and a dielectric that propagate without radiative loss, and have been extensively studied over the past century since their initial observation by *Wood* (1902) [1]. Whilst it is not possible to couple to the SPP on a planar surface with incident photons in free space, it is possible to couple to the mode by enhancing the momentum of the photons, for example by total attenuated reflection (ATR) with the resulting surface wave having both longitudinal and transverse characteristics and being TM (transverse magnetic) or p-polarised in nature. Therefore it may only be excited by p-polarised incident photons in this case, as there needs to be a component of the incident electric vector normal to the surface in order to generate the required surface polarisation charge. TM radiation (p-polarised) is defined as having its electric vector in the plane of incidence, whereas TE (transverse electric, s-polarised) radiation is defined as having its electric vector normal to the plane of incidence (parallel to the interface) and therefore will not couple to the SPP.

The momentum of the SPP is greater than that available to an incident photon in a dielectric at any frequency or incident angle, the SPP dispersion being outside the light line on a ω k plot. At low frequencies the SPP dispersion closely follows the light line, before curving away to an asymptotic limit as it approaches the surface plasma frequency. In the region of the dispersion plot where the SPP closely follows the light line (the microwave regime) the mode can be thought of as being analogous to a grazing photon. In the region where the mode is further from the light line (the optical regime) the mode is more plasmon like.

In this chapter, some of the properties and physics of the SPP on both planar and corrugated surfaces are described. The dispersion relation of the SPP is derived, and the extent of the fields into both media at different frequencies are investigated. Also, the methods of coupling to the SPP at both optical and microwave frequencies are explored, as it is not possible to couple to the SPP on a planar surface with incident photons in free space as discussed above. In the next section, an historical overview of the initial observations and understanding of the SPP is presented.

2.2 Historical Overview

The electromagnetic surface waves discussed in this chapter have been studied for over 100 years. Initially, *Wood* (1902) [1] studied the reflection spectra from a ruled metallic diffraction grating using an incandescent lamp as a source, and observed a series of light and dark bands in the p-polarised reflection spectra that could not be explained by the contemporary diffraction grating theory. Lord Rayleigh offered an explanation in 1907, when he published his Dynamical Theory of Gratings, suggesting that the bright bands were pseudo-critical edges which occurred at the angle of incidence at which a diffracted order became evanescent. The reduction of the available channels for the reflected power resulted in a redistribution, and consequential brightening of other propagating orders. He also predicted that the dark bands would only occur when the incident radiation had a component of its electric field perpendicular to the grooves. This was verified by the experimental work of *Wood* (1912) [2], *Ingersoll* (1920) [3] and *Strong* (1936) [4]. Strong also showed that the angular position of the dark band was dependent not only on the grating geometry, but also on the properties of the metal itself.

A full explanation of the phenomena was not provided until 1941, when *Fano* (1941) [5] published his seminal work. Fano used the diffraction grating equation proposed by Fraunhofer in 1821:

$$\lambda_g \left(\sin\vartheta_N - \sin\theta\right) = N\lambda_0$$

where θ is the angle of incidence, ϑ_N is the Nth diffracted order and λ_g is the pitch of the grating. This equation shows that the component of the in-plane momentum of the incident radiation will be modified by integer multiples of the grating momentum, $k_g = 2\pi/\lambda_g$, resulting in a series of diffracted orders. Fano proposed that when this momentum is greater than that of the incident photon, it becomes evanescent and is diffracted into a pair of surface waves that travel along the grating surface decaying exponentially perpendicular to the surface in either media. The surface waves are bound to the interface as they are constantly "reflected" by both the dielectric and the metal, and therefore no energy is dispersed outside the surface region. The extent of the fields into either media would be defined by the properties of each medium, explaining the result observed experimentally by *Strong* (1936) [4]. Fano also showed that coupling to these surface waves would require a component of the incident electric field to be polarised normal to the surface.

Further understanding of metals, and the description of free electrons as a plasma allowed *Ferrell* (1958) [6] to confirm that a beam of electrons incident on a metal layer would cause charge density oscillations in the free electrons in the metal at specific energies $h\omega_p/2\pi$, where ω_p is the plasma frequency, and therefore emission of radiation at specific frequencies. This energy unit became termed the *plasmon*, and experimental evidence for its existence was provided by *Steinmann* (1960) [7]. Further work by *Ritchie* and *Eldridge* (1961) [8] showed that the emitted radiation did indeed have the characteristic energies $h\omega_p/2\pi$ and $h\omega_p/2\pi\sqrt{2}$, where $\omega_p/\sqrt{2}$ is the surface plasma frequency for air. This work led to the modes described by Fano being termed *surface plasmon polaritons* (SPPs).

Fano, *Fano* (1941) [5] realised that the surface waves he proposed were in fact a special case of surface waves originally suggested by *Zenneck* (1907) [9] and *Sommerfeld* (1909) [10]. These Fano modes propagated along a metal-dielectric boundary, but with a momentum greater than that of the photon in the incident dielectric medium, and therefore it is not possible for them to radiate or to radiatively couple to them directly on a planar surface. However, *Teng and Stern* (1967) [11] used an optical grating to impart additional momentum to a surface plasma oscillation excited by a high energy electron beam, allowing the SPP to couple to a radiating electromagnetic field and the p-polarised emitted beam to be observed. Peaks were observed in the emission spectra, and to confirm that these were due to the SPP, they looked for reflectivity minima when electromagnetic radiation at the same frequency and incident angle as that of the peaks coupled to the SPP. This was found to be the case, and by studying the response of the grating by varying the incident angle, the existence of the Fano mode was confirmed. Additionally the dispersion curve of the SPP was plotted by calculating the momentum tangential to the interface.

Further experimental evidence for the SPP was provided by *Ritchie et al* (1968) [12] and *Beaglehole* (1969) [13]. Each of these works provided a comprehensive study of optically excited SPPs on metal gratings. *Ritchie et al* followed the experimental peaks in the p-polarised spectrum in order to plot out the dispersion curve of the SPP. Beaglehole was able to show that in addition to coupling to the SPP with p-polarised light, it was also possible to couple to the SPP with s-polarised light by rotating the grating grooves by 90° with respect to the plain of incidence.

2.3 The Surface Plasmon Polariton

2.3.1 The Dispersion relation

In order to derive the dispersion relation for the SPP, the planar interface between two semi-infinite isotropic media must be considered. Each of the two media are characterised by frequency dependent, complex dielectric constants, $\varepsilon_d = \varepsilon\varepsilon_0$, where ε is the relative permittivity of the medium being considered, and ε_0 is the permittivity of free space. The relative permittivity may be considered a complex quantity, such that $\varepsilon = \varepsilon_r + i\varepsilon_i$ where the subscripts r and i denote the real and imaginary parts of the permittivity respectively. Both materials are considered to be non-magnetic, having a relative permeability $\mu = 1$, (where the permeability of the media is characterised by $\mu_d = \mu\mu_0$ and μ_0 is the permeability of free space) which is true in the visible regime, but may not always be true in the microwave regime.

From Maxwell's equations it can be shown that the normal component of the electric displacement $\mathbf{D}$, must be continuous across the interface. The electric field, $\mathbf{E}$ is linked to the electric displacement by the following relation:

$$\mathbf{D} = \varepsilon\varepsilon_0\mathbf{E} \tag{2.1}$$

where ε is the relative dielectric constant of the medium being considered, and ε_0 is the

permittivity of free space. If the two media being considered have values of ε_r that are opposite in sign, i.e. a metal (negative ε_r) and a dielectric (positive ε_r), then the normal component of $\mathbf{E}$ will invert as the interface boundary is crossed. A surface charge density may propagate along the interface as a longitudinal charge oscillation that is bound to the surface with associated fields that decay exponentially into either medium. It should be noted here that a common assumption at microwave frequencies is to consider metals as a perfect conductor, if this were the case the fields are entirely excluded from the metal and the SPP is not formed. However it will be shown later in this chapter that fields are indeed able to penetrate into metals at microwave frequencies, and therefore the SPP is supported at microwave frequencies.

Consider a p-polarised (TM) electromagnetic wave incident at the interface between two semi-infinite, non-magnetic media, as shown in *Figure* 2.1. The upper medium is a dielectric with a dielectric constant ε_1, and the lower is a metal with a dielectric constant ε_2. The incident, reflected and transmitted waves all propagate in the xy-plane. In order to couple to the surface mode, any incident photon must have a component of its electric vector perpendicular to the interface, therefore an s-polarised (TM) incident beam is incapable of coupling to a surface mode in this geometry.

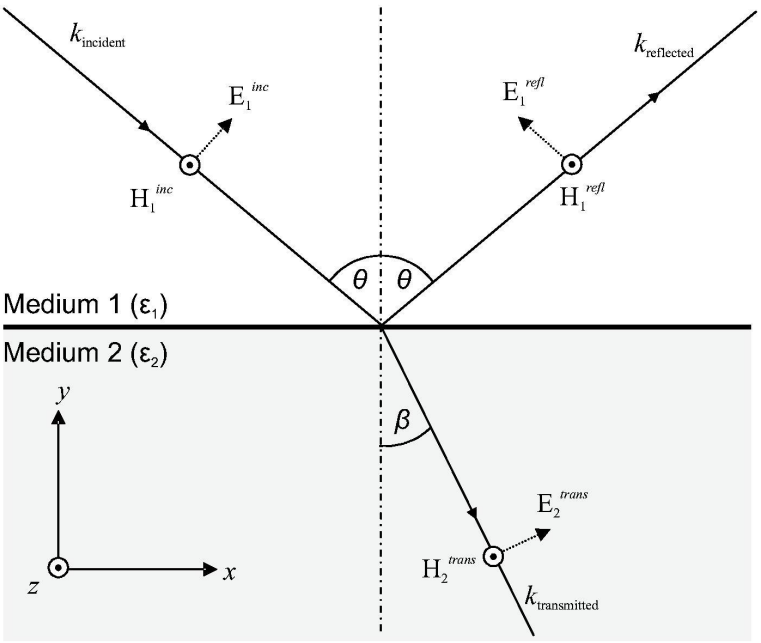

Figure 2.1: Incident, reflected and transmitted radiation at the interface between metal and dielectric layers. Incident radiation is p-polarised, with the z-axis being directed out of the page.

For an incident TM electromagnetic wave propagating with a wavevector $\mathbf{k} = (k_x, k_y, 0)$, the electric and magnetic field components can be written as:

$$\mathbf{E} = [E_x, E_y, 0] \exp i\,(k_x x + k_y y - \omega t) \tag{2.2}$$

$$\mathbf{H} = [0, 0, H_z] \exp i\,(k_x x + k_y y - \omega t) \tag{2.3}$$

Using Maxwell's equation in the absence of free charges:

$$\bigtriangledown \times \mathbf{H} = \varepsilon_d \frac{\delta \mathbf{E}}{\delta t} \tag{2.4}$$

leads to:

$$H_z = \frac{\varepsilon_d \omega}{k_y} E_x = -\frac{\varepsilon_d \omega}{k_x} E_y \tag{2.5}$$

Substituting *Equation* 2.5 back into *Equations* 2.2 and 2.3 allows the expressions for the incident, reflected and transmitted waves to be obtained:

$$\mathbf{E}_1^{inc} = E_{x1}^{inc} \left[1, -\frac{k_x}{k_{y1}}, 0\right] \exp i\,(k_x x + k_{y1} y - \omega t) \tag{2.6}$$

$$\mathbf{E}_1^{refl} = E_{x1}^{refl} \left[1, \frac{k_x}{k_{y1}}, 0\right] \exp i\,(k_x x + k_{y1} y - \omega t) \tag{2.7}$$

$$\mathbf{E}_2^{trans} = E_{x2}^{trans} \left[1, -\frac{k_x}{k_{y2}}, 0\right] \exp i\,(k_x x + k_{y2} y - \omega t) \tag{2.8}$$

$$\mathbf{H}_1^{inc} = E_{x1}^{inc} \left[0, 0, \frac{\omega \varepsilon_1}{k_{y1}}\right] \exp i\,(k_x x + k_{y1} y - \omega t) \tag{2.9}$$

$$\mathbf{H}_1^{refl} = E_{x1}^{refl} \left[0, 0, -\frac{\omega \varepsilon_1}{k_{y1}}\right] \exp i\,(k_x x + k_{y1} y - \omega t) \tag{2.10}$$

$$\mathbf{H}_2^{trans} = E_{x1}^{trans} \left[0, 0, \frac{\omega \varepsilon_2}{k_{y2}}\right] \exp i\,(k_x x + k_{y2} y - \omega t) \tag{2.11}$$

The SPP is non-radiative, therefore either the incident or reflected fields may be set to zero. (Here, the incident field will be set to zero.) At the boundary of a metal-dielectric interface, the tangential components of the electric and magnetic fields must be continuous, leading to:

$$E_{x1}^{refl} = E_{x2}^{trans} \tag{2.12}$$

and

$$H_{z1} = H_{z2}, \tag{2.13}$$

which gives:

$$H_z = -E_{x1}^{refl} \frac{\varepsilon_1 \omega}{k_{y1}} = E_{x2}^{trans} \frac{\varepsilon_2 \omega}{k_{y2}}. \tag{2.14}$$

Combining *Equations* 2.12 and 2.5 gives:

$$-\frac{\varepsilon_1}{k_{y1}} = \frac{\varepsilon_2}{k_{y2}} \tag{2.15}$$

A wavevector may be described by individual orthogonal components along the x and y axes using the properties of the media in which the wave propagates:

$$\mu_1\varepsilon_1\omega_0^2 = k_x^2 + k_{y1}^2 \tag{2.16}$$

$$\mu_2\varepsilon_2\omega = k_x^2 + k_{y2}^2 \tag{2.17}$$

For simplicity, both media are considered to be non-magnetic, having $\mu = 1$ therefore $\mu_1 = \mu_2 = \mu_0$. This leads to *Equations* 2.16 and 2.17 reducing to:

$$k_{y1} = \left(\varepsilon_1 k_0^2 - k_x^2\right)^{1/2} \tag{2.18}$$

$$k_{y2} = \left(\varepsilon_2 k_0^2 - k_x^2\right)^{1/2} \tag{2.19}$$

Substituting *Equations* 2.18 and 2.19 back into *Equation* 2.15 gives the SPP dispersion relation:

$$k_x = k_0\left(\frac{\varepsilon_1\varepsilon_2}{\varepsilon_1 + \varepsilon_2}\right)^{1/2} = k_{SPP} \tag{2.20}$$

The above equation is the general form for the SPP dispersion for any frequency regime, as the permittivity values are complex qualities. However, approximations to the above equation may be made when dealing with particular frequency regimes, such as the optical, where often only the real parts of the permittivities are used. In order to examine further the SPP dispersion at microwave frequencies a further derivation follows that takes into account the complex forms of the permittivities and wavevectors. These are substituted into *Equation* 2.19 to obtain:

$$\frac{k_{xr}^2 - k_{xi}^2 + 2ik_{xr}k_{xi}}{k_0^2} = \frac{\varepsilon_1(\varepsilon_{2r} + i\varepsilon_{2i})}{\varepsilon_1 + \varepsilon_{2r} + i\varepsilon_{2i}} \tag{2.21}$$

The right hand side of the equation can be separated out into real and imaginary parts by multiplying by the complex conjugate of the denominator to give:

$$\frac{k_{xr}^2 - k_{xi}^2 + 2ik_{xr}k_{xi}}{k_0^2} = \frac{\varepsilon_1\varepsilon_{2r}(\varepsilon_1 + \varepsilon_{2r}) + \varepsilon_1\varepsilon_{2i}^2}{(\varepsilon_1 + \varepsilon_{2r})^2 + \varepsilon_{2i}^2} + i\frac{\varepsilon_1^2\varepsilon_{2i}}{(\varepsilon_1 + \varepsilon_{2r})^2 + \varepsilon_{2i}^2} \tag{2.22}$$

Which can be separated into a real part:

$$\frac{k_{xr}^2 - k_{xi}^2}{k_0^2} = \frac{\varepsilon_1\varepsilon_{2r}(\varepsilon_1 + \varepsilon_{2r}) + \varepsilon_1\varepsilon_{2i}^2}{(\varepsilon_1 + \varepsilon_{2r})^2 + \varepsilon_{2i}^2} \tag{2.23}$$

and an imaginary part:

$$\frac{2ik_{xr}k_{xi}}{k_0^2} = \frac{\varepsilon_1^2\varepsilon_{2i}}{(\varepsilon_1+\varepsilon_{2r})^2+\varepsilon_{2i}^2} \tag{2.24}$$

These two equations can be solved simultaneously to give two quadratics in $\frac{k_{xr}^2}{k_0^2}$ and $\frac{k_{xi}^2}{k_0^2}$ respectively:

$$\frac{k_{xr}^4}{k_0^4} - \frac{k_{xr}^2}{k_0^2}\left(\frac{\varepsilon_1\varepsilon_{2r}(\varepsilon_1+\varepsilon_{2r})+\varepsilon_1\varepsilon_{2i}^2}{(\varepsilon_1+\varepsilon_{2r})^2+\varepsilon_{2i}^2}\right) - \frac{1}{4}\left[\frac{\varepsilon_1^2\varepsilon_{2i}}{(\varepsilon_1+\varepsilon_{2r})^2+\varepsilon_{2i}^2}\right]^2 \tag{2.25}$$

$$-\frac{k_{xi}^4}{k_0^4} - \frac{k_{xi}^2}{k_0^2}\left(\frac{\varepsilon_1\varepsilon_{2r}(\varepsilon_1+\varepsilon_{2r})+\varepsilon_1\varepsilon_{2i}^2}{(\varepsilon_1+\varepsilon_{2r})^2+\varepsilon_{2i}^2}\right) + \frac{1}{4}\left[\frac{\varepsilon_1^2\varepsilon_{2i}}{(\varepsilon_1+\varepsilon_{2r})^2+\varepsilon_{2i}^2}\right]^2 \tag{2.26}$$

Solving and simplifying these equations leads to:

$$\frac{k_{xr}}{k_0} = \sqrt{\frac{\varepsilon_1(\varepsilon_e^2+\sqrt{\varepsilon_e^4+\varepsilon_1^2\varepsilon_{2i}^2})}{2[(\varepsilon_1+\varepsilon_{2r})^2+\varepsilon_{2i}^2]}} \tag{2.27}$$

$$\frac{k_{xi}}{k_0} = \sqrt{\frac{\varepsilon_1(\sqrt{\varepsilon_e^4+\varepsilon_1^2\varepsilon_{2i}^2}-\varepsilon_e^2)}{2[(\varepsilon_1+\varepsilon_{2r})^2+\varepsilon_{2i}^2]}} \tag{2.28}$$

where $\varepsilon_e^2 = \varepsilon_{2r}^2 + \varepsilon_{2i}^2 + \varepsilon_1\varepsilon_{2r}$. *Equations* 2.27 and 2.28 provide an exact relation for the wavevector of the non-radiative SPP at any frequency. In the microwave regime the imaginary part of the permittivity is generally much larger than the real part $\varepsilon_i \gg \varepsilon_r$, therefore the position of the real part of the surface plasmon wavevector relative to the light line is given by *Equation* 2.27 and reduces to:

$$k_{SPP} = k_0 \tag{2.29}$$

This means that the SPP at microwave frequencies resembles a grazing photon, and is often referred to as a surface wave by microwave engineers. The imaginary part of the surface plasmon wavevector is described by *Equation* 2.28, and describes the non-radiative damping of the mode due to each medium. The extent of the damping in either medium will be discussed in later sections.

2.3.2 Brewster modes

The derivation in the previous section deals with the case where the two media have permittivities of opposite signs. A reflectivity minimum also occurs at the interface between two lossless dielectrics $(\varepsilon_1, \varepsilon_2, 0)$ and is termed the Brewster mode. The Brewster mode is not bound to the interface, but nonetheless can be put in the same class as the Fano mode as it has no reflected beam in the upper half space. The dispersion relation for the Brewster

mode can be determined from Snell's law, and will be shown to be identical to that found in *Equation* 2.20.

$$n_1 \sin\theta_1 = n_2 \sin\theta_2 \tag{2.30}$$

is Snell's law, where n_1 and n_2 are the refractive indices of the two media and θ_1 and θ_2 are the angles to the normal of the reflected and transmitted beams respectively. The Brewster mode occurs when the transmitted beam is at 90° to the reflected beam, and this angle is given by:

$$\tan\theta_B = \frac{n_1}{n_2} = \sqrt{\frac{\varepsilon_1}{\varepsilon_2}} \tag{2.31}$$

where θ_B is the Brewster angle. Using Snell's law at the Brewster angle we have:

$$\sin\theta_B = \frac{n_2}{(n_1^2 + n_2^2)^{1/2}} = \left(\frac{\varepsilon_2}{\varepsilon_1 + \varepsilon_2}\right)^{1/2} \tag{2.32}$$

If *Equation* 2.32 is substituted into the x-component of the incident wavevector, $k_x = k_0 n_1 \sin\theta$, the following relation results:

$$k_x = k_0 \frac{n_1 n_2}{(n_1^2 + n_2^2)^{1/2}} = k_0 \left(\frac{\varepsilon_1 \varepsilon_2}{\varepsilon_1 + \varepsilon_2}\right)^{1/2} \tag{2.33}$$

As each medium is considered to be lossless, the above equation is identical to that derived in *Equation* 2.20.

2.3.3 Spatial extent of the surface plasmon fields

As mentioned above, the imaginary part of the surface plasmon wavevector given by *Equation* 2.28 describes the non-radiative damping of the mode in each medium. From *Equation* 2.2 the fields associated with the SPP fall off as exp-($k_{xi}x$) and therefore the intensity reduces as exp-($2k_{xi}x$). The propagation length, L_x is defined as the distance over which the field magnitude is reduced to by $1/e$ of its initial value along the interface. The propagation length can be written as:

$$L_x = \frac{1}{2k_{xi}} = \frac{1}{2k_0} \sqrt{\frac{2\left(\left(\varepsilon_1 + \varepsilon_{2r}\right)^2 + \varepsilon_{2i}^2\right)}{\varepsilon_1\left(\sqrt{\varepsilon_e^4 + \varepsilon_1 \varepsilon_{2i}^2} - \varepsilon_e^2\right)}} \tag{2.34}$$

In order to assign a numerical value to the propagation length along the metal-dielectric interface, the dielectric function of the materials constituting the interface must be known. Here the dielectric may be considered as air, which has a negligible dispersion of its dielectric constant due to an absence of any strong resonances. Therefore the permittivity of medium 1 may be considered as frequency independent. This is certainly not the case for the metal being considered as medium 2, and ε_2 will be highly dependent on frequency. Using the

simple approximation of a Drude free electron model yields the real and imaginary parts of the dielectric constant as a function of wavelength. The Drude model assumes the electrons within the metal are entirely free and are not subject to any restoring force when an oscillating electric field is applied:

$$\varepsilon_r = 1 - \frac{\omega_p^2 \tau^2}{1 + \omega^2 \tau^2} \tag{2.35}$$

$$\varepsilon_i = \frac{\omega_p^2 \tau}{\omega\left(1 + \omega^2 \tau^2\right)} \tag{2.36}$$

where τ is the mean time between collisions and ω_p is the plasma frequency, which is defined as the frequency at which a metal becomes dielectric in nature, and is given by:

$$\omega_p = \sqrt{\frac{Ne^2}{\varepsilon_0 m}} \tag{2.37}$$

where N is the free electron density, e is the charge on the electron and m is the electron mass. *Figures* 2.2 and 2.3 display the real and imaginary dielectric constants plotted against wavelength, with values of $\omega_p = 1.93 \times 10^{16}\text{s}^{-1}$ and $\tau = 5.07 \times 10^{-15}\text{s}$ which are empirically derived from fitting to reflectance data at an aluminium-air boundary. The Drude model assumption is generally a good one for metals in the low frequency regime, however features such as the inter-band transition that occurs in the near infrared have been omitted for clarity.

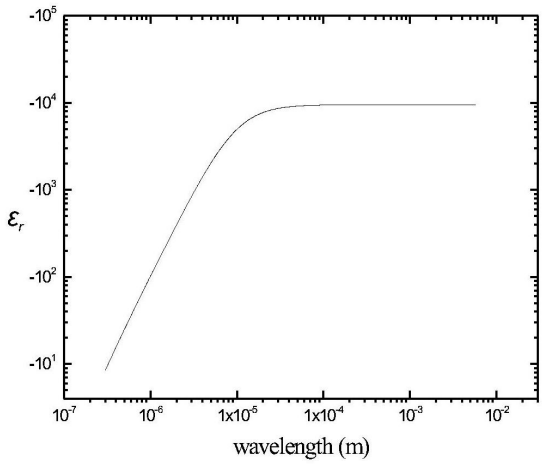

Figure 2.2: ε_r as a function of wavelength derived from the Drude free electron model. Here, $\omega_p = 1.93 \times 10^{16}\text{s}^{-1}$ and $\tau = 5.07 \times 10^{-15}\text{s}$.

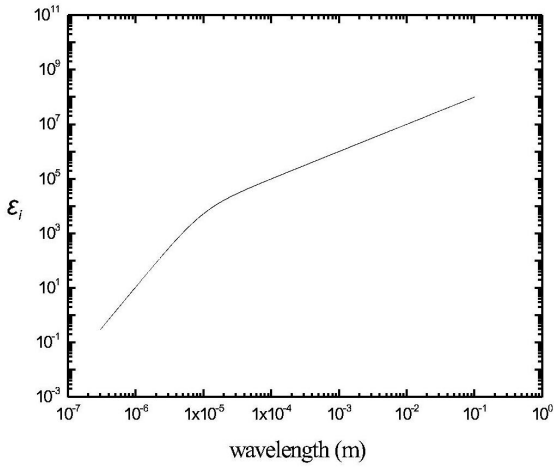

Figure 2.3: ε_i as a function of wavelength derived from the Drude free electron model. Here, $\omega_p = 1.93 \times 10^{16}\text{s}^{-1}$ and $\tau = 5.07 \times 10^{-15}\text{s}$.

By combining *Equation* 2.34 with the values of the dielectric constant obtained from the Drude model it is possible to obtain the propagation length for a planar aluminium-air interface over a range of wavelengths, as displayed in *Figure* 2.4. It is clearly shown that at microwave frequencies the propagation length extends over 1 km, which illustrates why the SPP is often considered to be a surface current as opposed to a bound surface wave in the microwave regime.

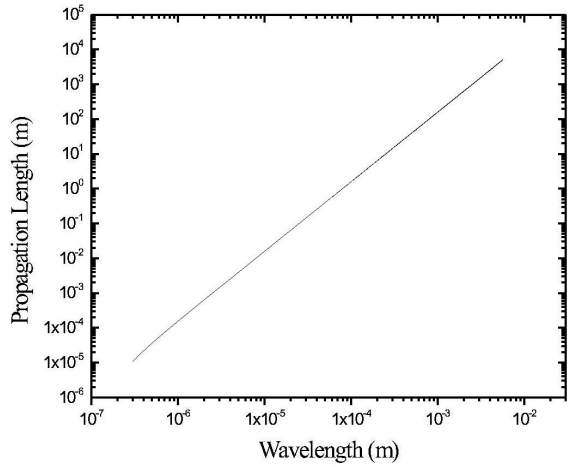

Figure 2.4: The propagation length of the SPP mode along the interface plotted as a function of wavelength.

The skin depth, or penetration length, L_y is a measure of the extent to which the fields decay into either of the two media, and is determined by the imaginary part of the wavevector, k_y. The penetration length is defined as the the distance from the interface over which the field strength falls to $1/e$ of its initial value. As this distance is determined by the non-radiative damping of the wavevector, an expression must be obtained for the imaginary part of k_y in order to determine L_y. Taking $k_y^2 = k_0^2\varepsilon_j - k_x^2$,

$$\frac{k_{yj}}{k_0} = \sqrt{(\varepsilon_{rj} + \varepsilon_{ij}) - \left(\frac{k_x^2}{k_0^2}\right)} \tag{2.38}$$

where the subscript j denotes the medium being described, with medium $j = 1$ being air, and medium $j = 2$ being aluminium. This expression can then be split into real and imaginary parts, yielding:

$$\frac{k_{yj}}{k_0} = \sqrt{\left(\varepsilon_{rj} - \frac{\varepsilon_1\varepsilon_e^2}{(\varepsilon_1 + \varepsilon_{r2})^2 + \varepsilon_{i2}^2}\right) + i\left(\varepsilon_{ij} - \frac{\varepsilon_1^2\varepsilon_{i2}}{(\varepsilon_1 + \varepsilon_{r2})^2 + \varepsilon_{i2}^2}\right)} \tag{2.39}$$

which leads to

$$\frac{k_{yrj}^2 - k_{yij}^2 + 2ik_{yrj}k_{yri}}{k_0^2} = \left(\varepsilon_{rj} - \frac{\varepsilon_1\varepsilon_e^2}{(\varepsilon_1 + \varepsilon_{r2})^2 + \varepsilon_{i2}^2}\right) + i\left(\varepsilon_{ij} - \frac{\varepsilon_1^2\varepsilon_{i2}}{(\varepsilon_1 + \varepsilon_{r2})^2 + \varepsilon_{i2}^2}\right) \tag{2.40}$$

and then solving simultaneously gives :

$$\frac{k_{yij}}{k_0} = \sqrt{\frac{\varepsilon_{rj} - \frac{\varepsilon_1\varepsilon_e^2}{(\varepsilon_1+\varepsilon_{r2})^2+\varepsilon_{i2}^2} - \sqrt{\left(\varepsilon_{rj} - \frac{\varepsilon_1\varepsilon_e^2}{(\varepsilon_1+\varepsilon_{r2})^2+\varepsilon_{i2}^2}\right)^2 + \left(\varepsilon_{ij} - \frac{\varepsilon_1^2\varepsilon_{i2}}{(\varepsilon_1+\varepsilon_{r2})^2+\varepsilon_{i2}^2}\right)^2}}{-2}} \tag{2.41}$$

The penetration depth is $L_{yj} = 1/k_{yj}$ therefore the final expression for the penetration depth is:

$$L_{yj} = \frac{\lambda_0}{2\pi}\sqrt{\frac{-2}{\varepsilon_{rj} - \frac{\varepsilon_1\varepsilon_e^2}{(\varepsilon_1+\varepsilon_{r2})^2+\varepsilon_{i2}^2} - \sqrt{\left(\varepsilon_{rj} - \frac{\varepsilon_1\varepsilon_e^2}{(\varepsilon_1+\varepsilon_{r2})^2+\varepsilon_{i2}^2}\right)^2 + \left(\varepsilon_{ij} - \frac{\varepsilon_1^2\varepsilon_{i2}}{(\varepsilon_1+\varepsilon_{r2})^2+\varepsilon_{i2}^2}\right)^2}}} \tag{2.42}$$

Figures 2.5 and 2.6 show the penetration depth for both air and aluminium respectively. At a wavelength of 0.1 mm (30 GHz) penetration into the metal is shown to be 0.75 μm, as compared with a penetration of ∼10 m into the air at the same frequency. The large decay length in the dielectric explains why the mode is often considered to be analogous to a grazing photon, however the SPP is still bound to the surface, albeit much more weakly than in the optical regime.

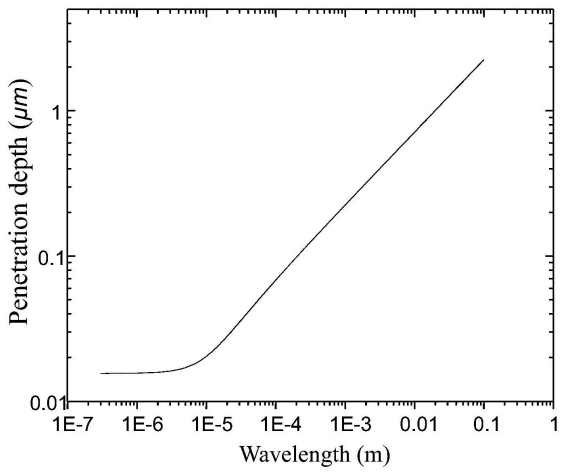

Figure 2.5: The penetration depth of the SPP fields into an aluminium layer as a function of wavelength.

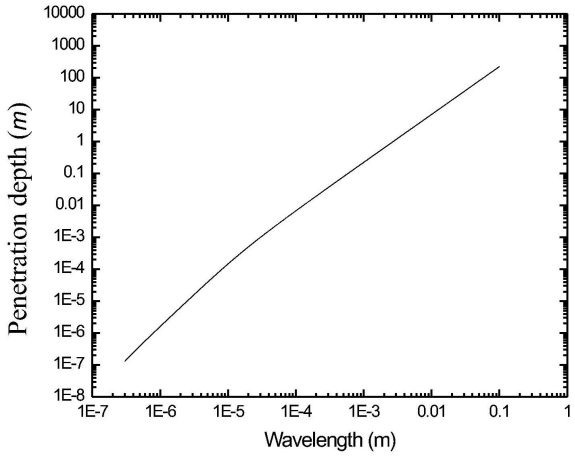

Figure 2.6: The penetration depth of the SPP fields into air as a function of wavelength.

The dispersion of the SPP mode is plotted in *Figure* 2.7 along with the Brewster mode and the light line. The light line indicates the maximum in-plane momentum available to an incident photon at a particular frequency, i.e., a grazing photon. The Brewster mode arises inside the light line, and can be coupled to with incident radiation. However the SPP mode always has greater momentum than that available to an incident photon, even at low frequencies, although in the microwave region the momentum mismatch is so small that it is clear that the SPP bears a close resemblance to a photon at grazing incidence. At low frequencies the metal more closely resembles a perfect conductor, and making this simplification allows a

reduction of the SPP dispersion equation. The response of a perfect conductor to an applied field is instantaneous and acts to cancel it, also a perfect conductor is lossless, having a permittivity that has a infinitely negative real part, and zero imaginary part. At this limit the SPP dispersion reduces to $k_x = \sqrt{\varepsilon_1}(\omega/c)$, which is identical to that of a grazing photon.

At the high frequency limit the SPP dispersion asymptotically approaches the surface plasma frequency at $\omega_{sp} = \omega_p/(1+\varepsilon_1)^{1/2}$ which is the frequency at which the real parts of the dielectric functions of the metal and air are equal in magnitude and opposite in sign. This limit exists because above ω_{sp}, k_x is purely imaginary and no solutions exist. At higher frequencies above ω_p, k_y is real, indicating that the mode is no longer bound to the surface, and the Brewster mode propagates.

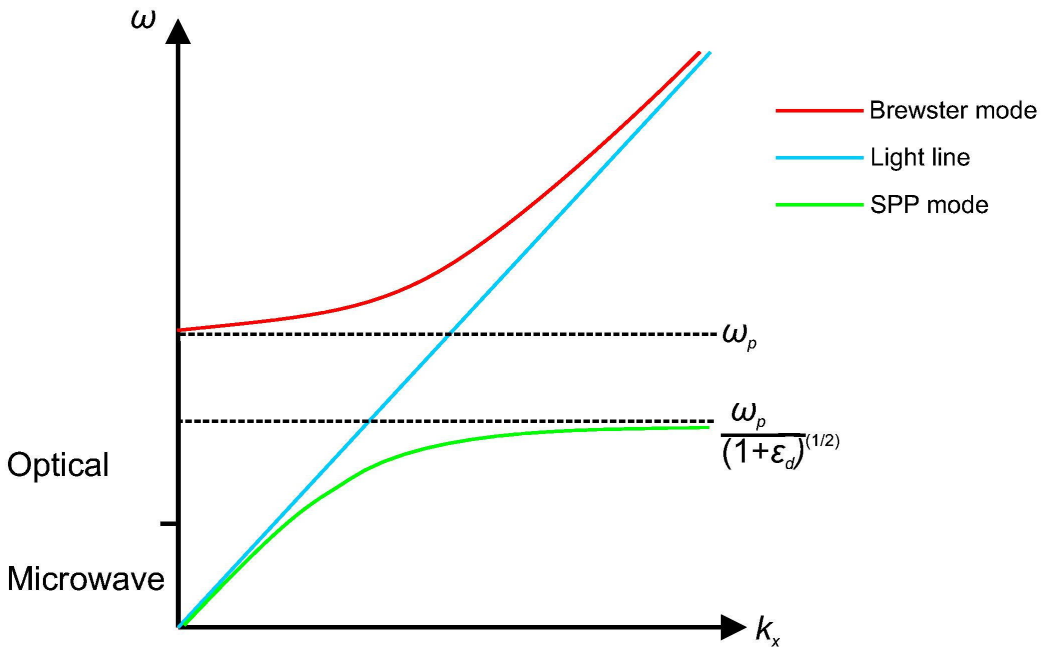

Figure 2.7: An approximate plot of the dispersion of the Fano mode and Brewster mode shown as frequency against in-plane momentum.

2.3.4 Coupling to the SPP

In the above sections it is clearly stated that it is not possible to couple directly to the SPP on a planar interface with incident photons, as the mode is non-radiative and therefore any incident photon will always have less momentum than is required for excitation of the mode. However, it has also been shown that in the microwave regime the SPP dispersion lies very close to the light line, and so the momentum mismatch is far less than in the optical regime. Nonetheless a method for enhancing the momentum is required for coupling to occur. There are two main methods by which this is achieved, the first of these, commonly employed at optical frequencies is prism coupling, or total attenuated reflection (ATR) [*Kretschmann* and *Raether* (1968) [14] and *Otto* (1968) [15]]. Prism coupling can be achieved at microwave frequencies with large wax prisms, however the size of the prisms can make experimentation difficult, and is not used in the work presented in this thesis so will not be discussed further.

The other commonly used method of coupling to the SPP mode is grating coupling. Any surface roughness or corrugation at the interface between the two media destroys the translational symmetry of the surface, and the tangential momentum of any photon incident in the plane of the interface need no longer be conserved. The introduction of a periodicity to the surface profile allows scattering of the incident photons by an integer number of grating vectors $\boldsymbol{k_g}$ ($k_g = 2\pi/\lambda_g$ where λ_g is the grating pitch) with the grating vector being normal to the direction of the corrugations.

Grating coupling is associated with the disappearance of a propagating diffracted order. The grating imparts additional momentum to the reflected photon, and once this momentum becomes greater than that permissible in medium 1 the diffracted order ceases to propagate and becomes evanescent. This photon then may couple to the SPP that exists beyond the light line. For this to occur, the incident photon must have a component of its electric vector parallel to the grating vector. The condition for the SPP matching to the grating vector in the plane of incidence is as follows:

$$k_{SPP} = n_1 k_0 \sin\theta \pm N k_g \tag{2.43}$$

where θ is the polar incident angle, $n_1 k_0 \sin\theta$ is the in-plane wavevector of the incident photon, and N is an integer representing the scattering order number. *Figure* 2.8 displays the surface plasmon dispersion curve for radiation incident on a metal-air interface with a periodic corrugation perpendicular to the plane of incidence. The grating introduces multiple scattering centres at integer multiples of the grating vector, and each centre has a light line and SPP dispersion associated with it. Some of the newly introduced SPP modes are folded back within the light cone, which allows some parts of the SPP dispersion from these additional scatterings to be coupled to with p-polarised incident radiation when the grating vector is in the plane of incidence.

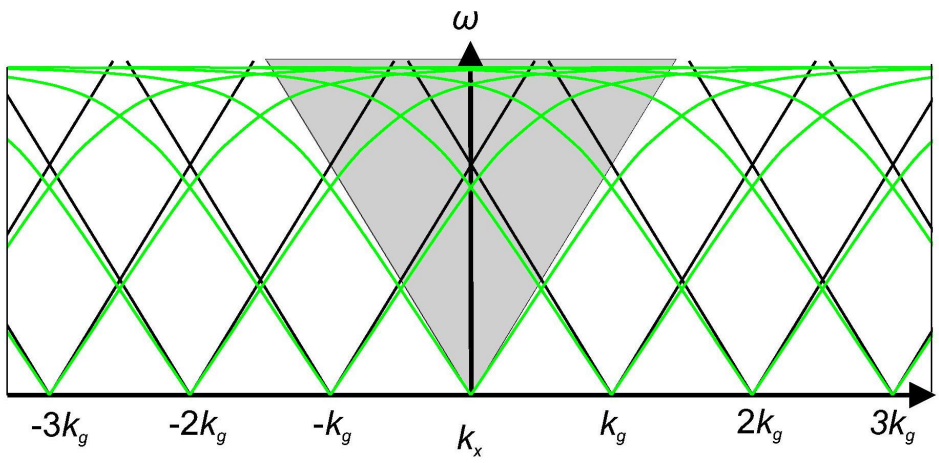

Figure 2.8: The multiple SPP dispersion curves (green lines) resulting from the introduction of a periodic surface profile. The shaded region indicates the area accessible to incident photons.

It is also possible to excite the SPP with *s*-polarised radiation by rotating the grating through 90°. Indeed, *p*-polarised radiation incident on the grating at normal incidence is indistinguishable from *s*-polarised incident radiation at normal incidence when the grating is rotated by 90°. Off normal incidence, the SPP may still be excited by *s*-polarised radiation as long as there is a component of the electric vector perpendicular to the groove direction.

The co-ordinate system used throughout this thesis is displayed in *Figure* 2.9, indicating that such a rotation of the plane of incidence is through the azimuthal angle, ϕ. The polar angle, θ is defined as the angle of incidence as measured from the normal to the average surface plane of the profile, also indicated in *Figure* 2.9.

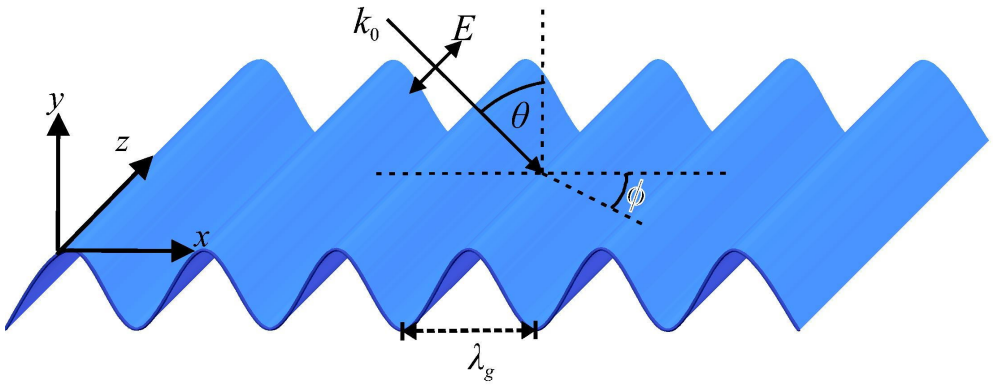

Figure 2.9: *p*-polarised radiation incident on a sinusoidal grating. The co-ordinate system used throughout this thesis is indicated, with polar angle, θ and azimuthal angle, ϕ defined.

If the azimuthal angle, ϕ is non-zero, k_{spp}, k_0 and k_g are collinear, and conservation of in-plane momentum gives:

$$k_{spp}^2 = n_1^2 k_0^2 \sin^2\theta + N^2 k_g^2 \pm 2 n_1 N k_g k_0 \sin\theta\cos\phi \tag{2.44}$$

The possible solutions from the above condition are illustrated in *Figure* 2.10, where the light cones seen in *Figure* 2.8 are viewed from above showing a cross section through the xy-plane at an arbitrary point on the z-axis. The dashed circle centered on the origin is the light cone, indicating the maximum momentum available to an incident photon, therefore coupling is only possible to modes lying within this circle. The solid line just outside it, centered on the origin, also represents the zero-order SPP dispersion. Additional SPP modes occur around each additional scattering centre provided by integer multiples of the grating vector, represent by dashed lines when lying outside the light cone, and solid lines when they fall inside it. These regions of the SPP dispersion may be coupled to by incident photons at the appropriate azimuthal and polar angles.

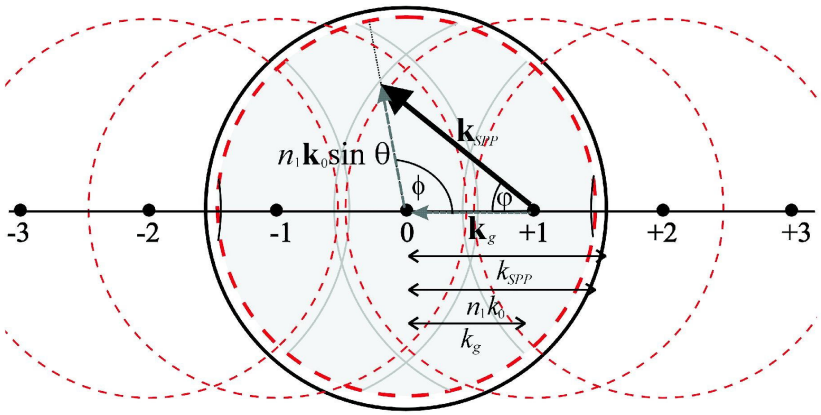

Figure 2.10: View of *Figure* 2.8 down the frequency axis. The solid radius circle represents the SPP mode, and the dashed circle centered on the origin represents the maximum momentum available to an incident photon. Arcs of scattered SPP modes falling within the shaded circle may be coupled to with incident radiation. The arrow indicates one such instance of this with a photon with angles θ and ϕ coupling to an SPP via a grating vector k_g which propagates at an angle φ with respect to the grating grooves.

2.4 Summary

In this chapter the surface plasmon has been introduced as an oscillation in surface charge density occurring at the interface between a metal and a dielectric. The SPP on a planar surface has been shown to be non-radiative, but may be coupled to by the introduction of an appropriate surface corrugation. It has been shown that the properties of both the metal and the dielectric result in the existence of the mode and determine the propagation length and decay length of the fields associated with it. Further to this, the frequency dependent nature of both these characteristic lengths has been discussed, and the comparative penetration of fields into either medium has revealed the reasoning for the common interpretation of the SPP as a surface current at microwave frequencies. Also, an exact form for the dispersion of the surface mode has been derived.

Chapter 3

Waveguides modes and Liquid Crystals

3.1 Introduction

In *Chapters* 7 and 8 the reflectivity of a series of samples consisting of a metal-clad dielectric structure will be explored, where the top layer of metal has had some structure etched into it in order to achieve absorption. In the analysis of some these structures, analogies with waveguide modes will be drawn. Therefore this chapter will contain an introduction to waveguiding in general as an aid to understanding the analysis in later chapters. In order to simplify matters, the metal walls of waveguides will be assumed to be perfect conductors. This assumption was introduced in the previous chapter, and in simple terms may be considered valid here. (Later chapters will illustrate situations where the failings of this assumption are important.) Waveguides will be considered to have propagation along the z-axis and be infinite in length and uniform along that axis. The derivations found in this chapter are adapted from *Microwave Engineering* by D.M. Polzar, Wiley, New York (1998).

The metal-clad dielectric structures presented in *Chapter* 8 have Liquid Crystal (LC) as their dielectric core material, and therefore this chapter will also include a discussion of the LCs and their applications. In recent years there has been been extensive use of LCs in optical devices. Over the last few decades the Liquid Crystal Display (LCD) has almost entirely replaced the cathode ray tube as the display device of choice, especially for use in compact, portable devices, so much so that it is said there are more LCDs in the world than there are people. Whilst the use of LCs in optical devices continues to increase and expand, they are also now being employed in other frequency regimes, where their birefringent properties can be advantageous. In order for the potential of LCs to be maximised in frequency regimes other than the optical, it is important to fully understand the underlying physics associated with them.

This chapter will discuss the fundamental properties of LCs, their various phases, and in particular the nematic phase. Following this there will be a brief discussion of the use of LCs in devices that operate at microwave frequencies.

3.2 Waveguides

3.2.1 Boundary conditions - Fields at a perfectly conducting wall

It has already been stated that the following discussion of waveguides will consider them to have perfectly conducting walls, therefore it is necessary to begin by discussing the boundary conditions at such a wall. A perfect conductor or perfect metal has an infinite conductivity ($\sigma = \infty$), and therefore a zero skin depth, such that all fields are entirely excluded from the metal. Using Maxwell's equations and Gauss' Law the boundary conditions may be obtained by constructing a simple rectangle or pillbox across the interface and assuming uniform fields across it. As the metal is a perfect conductor, we assume that the side of the pillbox lying within the metal has $E = B = 0$, and therefore the fields just outside the metal may be defined as:

$$\hat{n} \cdot \mathbf{D} = \rho_s \tag{3.1}$$

$$\hat{n} \cdot \mathbf{B} = 0 \tag{3.2}$$

$$\hat{n} \times \mathbf{E} = 0 \tag{3.3}$$

$$\hat{n} \times \mathbf{B} = \mathbf{J}_s \tag{3.4}$$

where ρ_s is the surface charge density, $\mathbf{J}_s$ is the surface current density and $\hat{n}$ is the normal unit vector to the perfectly conducting surface. As the surface is a perfect conductor tangential components of $\mathbf{E}$ drop to zero at the interface, such a surface is known as an *electric wall*.

3.2.2 General solutions for TE, TM and TEM waves

In the interior of the waveguide, propagating modes can be categorised by the direction of their magnetic and electric vector components relative to the direction of propagation. For one set of modes the magnetic field has no longitudinal or axial component, the magnetic field is entirely transverse to the direction of propagation, hence these modes are termed transverse magnetic (TM). Transverse electric (TE) modes are those that propagate with the electric field entirely transverse to the direction of propagation. The TEM (transverse electromagnetic) mode is actually the fundamental TM solution, and is characterised by having a complete lack of any axial component of either electric or magnetic fields.

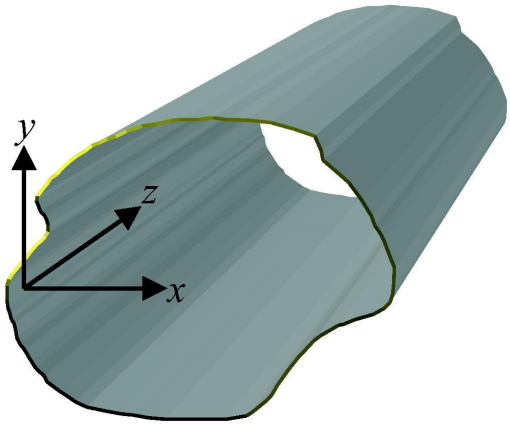

Figure 3.1: A hollow waveguide of arbitrary cross-section. The waveguide is constructed from an infinitely conducting wall and is considered to be uniform and infinite in the z-direction.

To begin the analysis of waveguides we will consider a hollow waveguide of an arbitrary cross-section, as shown in *Figure* 3.1 and find general solutions for both TM and TE modes. Waves propagating in the waveguide in the $+z$-direction have electric and magnetic components defined by:

$$\mathbf{E} = \left[\overline{E}(x,y) + \hat{z}E_z(x,y)\right] e^{-ikz} \tag{3.5}$$

$$\mathbf{H} = \left[\overline{H}(x,y) + \hat{z}H_z(x,y)\right] e^{-ikz} \tag{3.6}$$

where $\overline{E}(x,y)$ and $\overline{H}(x,y)$ represent the transverse electric and magnetic field components, E_z and H_z are the axial field components and $k_z = 2\pi/\lambda_z$ where λ_z is the wavelength of the guided wave. If the waveguide is free of sources, then Maxwell's curl equations become:

$$\bigtriangledown \times \mathbf{E} = -i\omega\mu_d\mathbf{H} \tag{3.7}$$

$$\bigtriangledown \times \mathbf{H} = -i\omega\varepsilon_d\mathbf{E} \tag{3.8}$$

Introducing axial invariance into these equations and separating into their three components yields:

$$\frac{\delta E_z}{\delta y} = ik_z E_y = -i\omega\mu H_x \tag{3.9}$$

$$-ik_z E_x - \frac{\delta E_z}{\delta x} = -i\omega\mu H_y \tag{3.10}$$

$$\frac{\delta E_y}{\delta x} - \frac{\delta E_x}{\delta y} = -i\omega\mu H_z \tag{3.11}$$

$$\frac{\delta H_z}{\delta y} = ik_z H_y = -i\omega\varepsilon E_x \tag{3.12}$$

$$-ik_z H_x - \frac{\delta H_z}{\delta x} = -i\omega\varepsilon E_y \tag{3.13}$$

$$\frac{\delta H_y}{\delta x} - \frac{\delta H_x}{\delta y} = -i\omega\varepsilon E_z \tag{3.14}$$

The above equations can now be solved in terms of E_z and $H_z$to present the four transverse components:

$$H_x = \frac{i}{k_c^2}\left(\omega\varepsilon\frac{\delta E_z}{\delta y} - k_z\frac{\delta H_z}{\delta x}\right) \tag{3.15}$$

$$H_y = -\frac{i}{k_c^2}\left(\omega\varepsilon\frac{\delta E_z}{\delta x} + k_z\frac{\delta H_z}{\delta y}\right) \tag{3.16}$$

$$E_x = -\frac{i}{k_c^2}\left(k_z\frac{\delta E_z}{\delta x} - \omega\mu\frac{\delta H_z}{\delta y}\right) \tag{3.17}$$

$$E_y = \frac{i}{k_c^2}\left(-k_z\frac{\delta E_z}{\delta y} + \omega\mu\frac{\delta H_z}{\delta x}\right) \tag{3.18}$$

where $k_c^2 = k_0^2 - k_z^2$ and $\frac{ck_c}{2\pi} = f_c$ where f_c is the waveguide cut-off frequency. The above equations are general results that apply to any waveguide geometry, and which will now be specified for TM, TE and TEM cases.

3.2.2.1 TE modes

TE modes are characterised by having electric fields that are entirely transverse to the direction of propagation; $E_z = 0$ and $H_z \neq 0$. Under these conditions, *Equations* 3.15 to 3.18 reduce to:

$$H_x = -\frac{ik_z}{k_c^2}\frac{\delta H_z}{\delta x} \tag{3.19}$$

$$H_y = -\frac{ik_z}{k_c^2}\frac{\delta H_z}{\delta y} \tag{3.20}$$

$$E_x = -\frac{i\omega\mu}{k_c^2}\frac{\delta H_z}{\delta y} \tag{3.21}$$

$$E_y = \frac{i\omega\mu}{k_c^2}\frac{\delta H_z}{\delta x} \tag{3.22}$$

The propagation constant for the TE case is a function of both the geometry of the guide and the frequency of the wave within the guide. To apply *Equations* 3.19 to 3.22 to a specific geometry, H_z must first be found. This is done by using the Helmholtz wave equation:

$$\bigtriangledown^2\mathbf{H} + \omega^2\mu\varepsilon\mathrm{H} = 0 \tag{3.23}$$

which reduces to the following 2-D equation for H_z since $H_z(x, y, z) = H_z(x, y)e^{-ik_z z}$:

$$\left(\frac{\delta^2}{\delta x^2} + \frac{\delta^2}{\delta y^2} + k_c^2\right) H_z = 0 \tag{3.24}$$

This equation may then be solved by consideration of the specific boundary conditions of the particular waveguide geometry.

3.2.2.2 TM modes

TM modes are defined by $E_z \neq 0$ and $H_z = 0$, under these conditions *Equations* 3.19 to 3.22 reduce to:

$$H_x = \frac{i\omega\varepsilon}{k_c^2}\frac{\delta E_z}{\delta y} \tag{3.25}$$

$$H_y = -\frac{i\omega\varepsilon}{k_c^2}\frac{\delta E_z}{\delta x} \tag{3.26}$$

$$E_x = -\frac{ik_z}{k_c^2}\frac{\delta E_z}{\delta x} \tag{3.27}$$

$$E_y = -\frac{ik_z}{k_c^2}\frac{\delta E_z}{\delta y} \tag{3.28}$$

In the same way as for the TE mode the propagation constant is a function of both the geometry of the guide and the frequency of the wave within the guide. Again, the wave equation reduces to a 2-D wave equation for E_z.

$$\left(\frac{\delta^2}{\delta x^2} + \frac{\delta^2}{\delta y^2} + k_c^2\right) E_z = 0 \tag{3.29}$$

Once more this equation may then be solved by consideration of the specific boundary conditions of the particular waveguide geometry.

3.2.2.3 TEM modes

The TEM mode is characterised by having $E_z = H_z = 0$. It can be seen from *Equations* 3.19 to 3.22 that all the transverse components will become zero unless $k_0 = 0$, for which a singularity is produced in the first term. By using *Equations* 3.9 and 3.12 to eliminate H_z and remembering $E_z = H_z = 0$ gives:

$$k_z^2 E_y = \omega^2 \mu\varepsilon E_y \tag{3.30}$$

Given that $\omega\sqrt{\mu\varepsilon} = k_0$ *Equation* 3.30 reduces simply to $k_0 = k_z$. The cut-off wavenumber has been given as $k_c = \sqrt{(k_0^2 - k_z^2)}$ therefore the TEM mode propagates without cut-off, and the phase velocity of the wave in vacuum or air is c regardless of the frequency or waveguide geometry. Once more the wave equation reduces to a 2-D wave equation for E_x:

$$\left(\frac{\delta^2}{\delta x^2} + \frac{\delta^2}{\delta y^2}\right) E_x = 0 \tag{3.31}$$

with a similar result being obtained for E_y. This leads to the expression:

$$\nabla_t^2 \overline{E}(x, y) = 0 \tag{3.32}$$

where $\nabla_t^2 = \frac{\delta^2}{\delta x^2} + \frac{\delta^2}{\delta y^2} + \frac{\delta^2}{\delta z^2}$ is the Laplacian operator in the transverse dimension and $\overline{E}(x, y)$ are the transverse electric field components. Therefore the fields of the TEM mode satisfy Laplace's equation, and are the same as the static fields that can exist between a pair of conductors.

3.2.3 The Rectangular Waveguide

In order to apply the general results obtained in the preceding section, the waveguide geometry must be considered so that the 2-D wave equation may be solved. Transverse fields can then be calculated from E_z and H_z, and then the unknown constants k_c and k_z can be found by applying boundary conditions to the appropriate field components. The first geometry to be considered will be rectangular, with the longest side being chosen to be parallel to the x-axis, and side lengths a and b, where $a < b$. The waveguide is considered uniform and infinite in length in the z-direction. The waveguide geometry is shown in *Figure* 3.2.

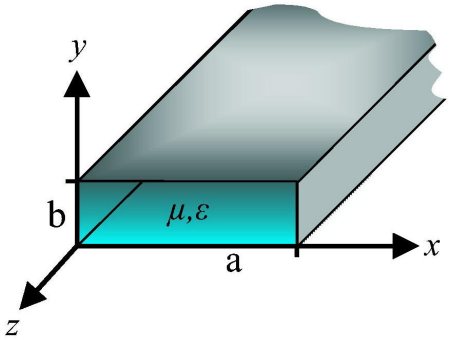

Figure 3.2: The rectangular waveguide geometry with co-ordinates marked.

Recall that all waveguides being considered in this chapter are considered to be hollow tubes constructed from a perfectly conducting wall surrounding a lossless dielectric defined by parameters ε and μ. The first set of modes to be considered in this geometry will be TE modes.

3.2.3.1 TE modes

TE modes have no electric component in the propagation direction, hence, $E_z = 0$. H_z must now satisfy the wave equation, *Equation* 3.24. This partial differential equation can be solved by the separation of variables method to give:

$$\frac{1}{X}\frac{d^2X}{dx^2} + \frac{1}{Y}\frac{d^2Y}{dy^2} + k_c^2 = 0 \tag{3.33}$$

where $H_z(x, y) = X(x)Y(y)$. This equation can then be separated out into two equations with the inclusion of separation constants, k_x and k_y:

$$\frac{1}{X}\frac{d^2X}{dx^2} + k_x^2 = 0 \tag{3.34}$$

$$\frac{1}{Y}\frac{d^2Y}{dy^2} + k_y^2 = 0 \tag{3.35}$$

where

$$k_x^2 + k_y^2 = k_c^2 \tag{3.36}$$

Therefore the general solution for H_z is given as:

$$H_z(x, y) = (A\cos k_x x + B\sin k_x x)(C\cos k_y y + D\sin k_y y) \tag{3.37}$$

In order to evaluate the constants A, B, C and D the boundary conditions at the walls of the waveguide must be applied to define the tangential components of E as:

$$E_x(x, y) = 0 \qquad \text{at} \qquad y = 0, b \tag{3.38}$$

$$E_y(x, y) = 0 \qquad \text{at} \qquad x = 0, a \tag{3.39}$$

We can then find expressions for E_x and E_y from H_z using *Equations* 3.21 and 3.22:

$$E_x = -\frac{i\omega\mu}{k_c^2} k_y (A\cos k_x x + B\sin k_x x)(-C\sin k_y y + D\cos k_y y) \tag{3.40}$$

$$E_y = -\frac{i\omega\mu}{k_c^2} k_x (-A\sin k_x x + B\cos k_x x)(C\cos k_y y + D\sin k_y y) \tag{3.41}$$

By combining *Equations* 3.38 and 3.40 it can be shown that $D = 0$ and $k_y = n\pi/b$ for $n = 1, 2, 3, ...$ In the same way, *Equations* 3.39 and 3.41 that $B = 0$ and $k_x = m\pi/a$ for $m = 1, 2, 3, ...$ which yields a final solution for H_z of:

$$H_z = (x, y, z) = A_{m,n}\cos\frac{m\pi x}{a}\cos\frac{n\pi y}{b}e^{-ik_z z} \tag{3.42}$$

where $A_{m,n}$ is an arbitrary amplitude constant comprised of the remaining constants A and C. The transverse field components can now be found by substituting the above equation into *Equations* 3.19, 3.20, 3.21 and 3.22:

$$E_x = \frac{i\omega\mu n\pi}{k_c^2 b}A_{m,n}\cos\frac{m\pi x}{a}\sin\frac{n\pi y}{b}e^{-ik_z z} \tag{3.43}$$

$$E_y = -\frac{i\omega\mu m\pi}{k_c^2 a}A_{m,n}\sin\frac{m\pi x}{a}\cos\frac{n\pi y}{b}e^{-ik_z z} \tag{3.44}$$

$$H_x = \frac{ik_z m\pi}{k_c^2 a}A_{m,n}\sin\frac{m\pi x}{a}\cos\frac{n\pi y}{b}e^{-ik_z z} \tag{3.45}$$

$$H_y = \frac{ik_z n\pi}{k_c^2 b}A_{m,n}\cos\frac{m\pi x}{a}\sin\frac{n\pi y}{b}e^{-ik_z z} \tag{3.46}$$

With the propagation constant being:

$$k_z = \sqrt{k_0^2 - k_c^2} = \sqrt{k_0^2 - \left(\frac{m\pi}{a}\right)^2 - \left(\frac{n\pi}{b}\right)^2} \tag{3.47}$$

From *Equation* 3.47 it is clear that the propagation constant is real when k_0 is greater than the cut-off wavevector. Each of the TE modes supported by the waveguide (any combination of m and n where m and n refer to the periodicity in the direction with which they are associated) has a cut-off frequency $f_{c_{m,n}}$ given by:

$$f_{c_{m,n}} = \frac{k_c}{2\pi\sqrt{\mu\varepsilon}} = \frac{1}{2\pi\sqrt{\mu\varepsilon}}\sqrt{\left(\frac{m\pi}{a}\right)^2 + \left(\frac{n\pi}{b}\right)^2} \tag{3.48}$$

The mode with the lowest cut-off frequency is termed the dominant mode, and since the mode $m = n = 0$ cannot exist (as from *Equations* 3.43, 3.44, 3.45 and 3.46 **E** and **H** are reduced to zero) and as for this geometry $a > b$ the dominant mode is the TE_{10}, which gives a fundamental cut-off frequency of the waveguide as:

$$f_{c_{1,0}} = \frac{1}{2a\sqrt{\mu\varepsilon}} \tag{3.49}$$

For any modes to propagate they must satisfy the condition $f \geq f_c$, whereas modes with a frequency $f < f_c$ will not propagate, but instead will decay evanescently from the waveguide entrance.

Figures 3.3 and 3.4 display field profiles corresponding to the four lowest frequency TE propagating modes in a rectangular waveguide. The field plots are provided by an FEM modeling package, HFSS (described in detail in *Chapter* 4). The waveguide is modeled as consisting of a perfect conductor surrounding a vacuum, and being infinite in the z-direction, with a thin cross section in the xy-plane being shown. The field magnitude is colour-coded, with red corresponding to a field magnitude of 1, and blue corresponding to a field magnitude of zero. Each figure illustrates (i) the time-averaged electric field magnitude plotted across the xy-plane, and the E (i) and H (ii) vector plotted at a phase corresponding to maximum field enhancement, also across the xy-plane.

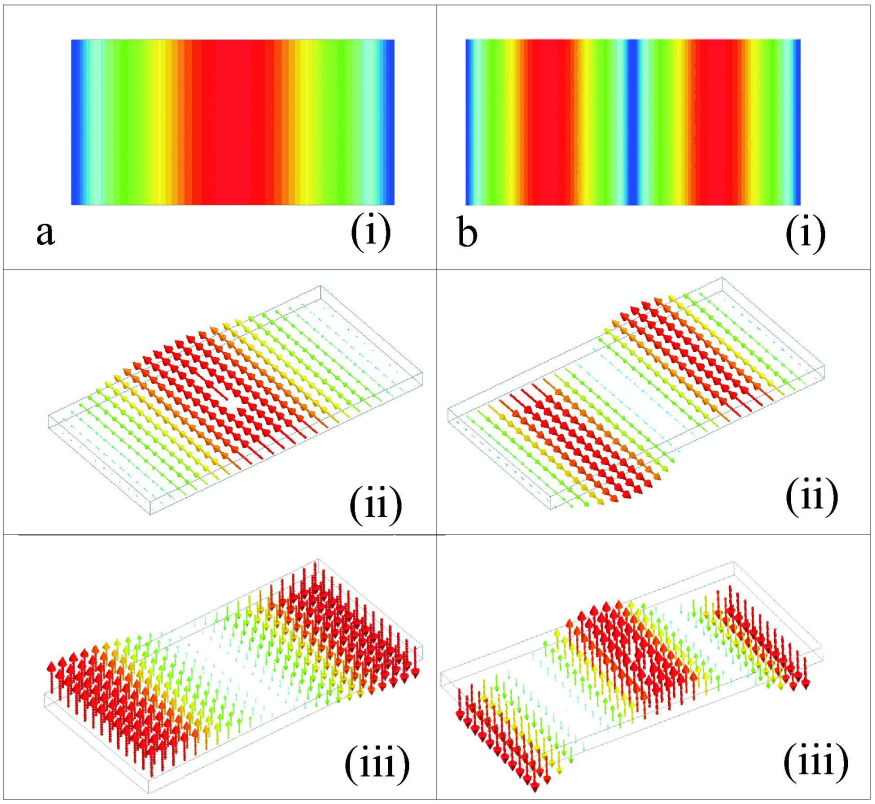

Figure 3.3: The field profiles corresponding to a) the TE_{10} and b) TE_{20} modes propagating within a vacuum filled perfectly conducting rectangular waveguide. For each mode, the i) time-averaged electric field magnitude and the ii) electric field and iii) magnetic field vectors plotted at a phase corresponding to maximum enhancement are displayed. Each field plot is across the xy-plane, with red corresponding to maximum field, and blue corresponding to zero field.

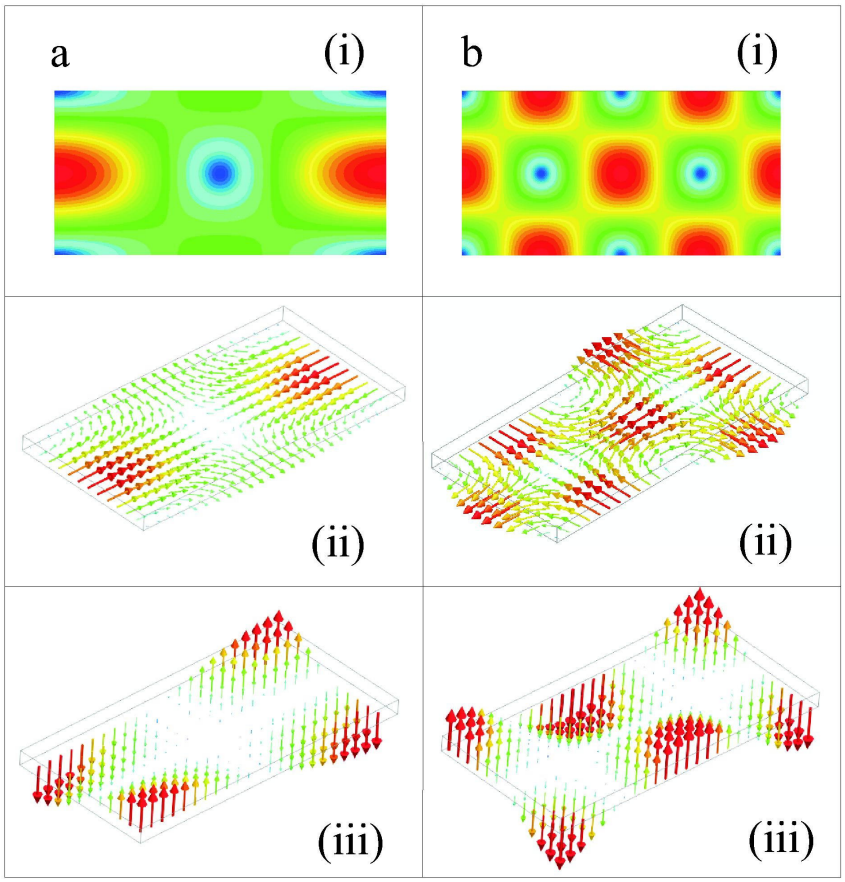

Figure 3.4: The field profiles corresponding to a) the TE_{01} and b) TE_{11} modes propagating within a vacuum filled perfectly conducting rectangular waveguide. For each mode, the i) time-averaged electric field magnitude and the ii) electric field and iii) magnetic field vectors plotted at a phase corresponding to maximum enhancement are displayed. Each field plot is across the xy-plane, with red corresponding to maximum field, and blue corresponding to zero field.

3.2.3.2 TM modes

The TM mode is characterised by $H_z = 0$ and $E_z \neq 0$. *Section* 3.2.2.2 discusses the fields satisfying the wave equation to give $E_z(x, y, z) = E_z(x, y)e^{-ik_z z}$ and $k_c^2 = k_0^2 - k_z^2$. Again, separation of variables can be used to give a general result for TM modes of:

$$E_z(x, y) = (A\cos k_x x + B\sin k_x x)(C\cos k_y y + D\sin k_y y) \tag{3.50}$$

The boundary conditions for E_z can then be applied directly:

$$E_z(x,y) = 0 \qquad \text{at} \qquad x = 0, a \tag{3.51}$$

$$E_z(x,y) = 0 \qquad \text{at} \qquad y = 0, b \tag{3.52}$$

By applying *Equation* 3.51 to *Equation* 3.50 we achieve the result $A = 0$ and $k_x = m\pi/a$ for $m = 1, 2, 3, 4...$. In a similar way, applying *Equation* 3.52 to *Equation* 3.50 yields $C = 0$ and $k_y = n\pi/a$ for $n = 1, 2, 3, 4...$. The solution for E_z then becomes:

$$E_z(x,y,z) = B_{m,n}\sin\frac{m\pi x}{a}\sin\frac{n\pi x}{a}e^{-ik_z z} \tag{3.53}$$

where $B_{m,n}$ is an arbitrary amplitude constant. By combining *Equations* 3.53 and 3.25, 3.26, 3.27 and 3.28 the transverse fields can be obtained:

$$E_x = \frac{ik_z m\pi}{k_c^2 a}B_{m,n}\cos\frac{m\pi x}{a}\sin\frac{n\pi y}{b}e^{-ik_z z} \tag{3.54}$$

$$E_y = \frac{ik_z n\pi}{k_c^2 b}B_{m,n}\sin\frac{m\pi x}{a}\cos\frac{n\pi y}{b}e^{-ik_z z} \tag{3.55}$$

$$H_x = \frac{i\omega\varepsilon n\pi}{k_c^2 a}B_{m,n}\sin\frac{m\pi x}{a}\cos\frac{n\pi y}{b}e^{-ik_z z} \tag{3.56}$$

$$H_y = \frac{i\omega\varepsilon m\pi}{k_c^2 a}B_{m,n}\cos\frac{m\pi x}{a}\sin\frac{n\pi y}{b}e^{-ik_z z} \tag{3.57}$$

The propagation constant is then found to be:

$$k_z = \sqrt{k_0^2 - k_c^2} = \sqrt{k_0^2 - \left(\frac{m\pi}{a}\right)^2 - \left(\frac{n\pi}{b}\right)^2} \tag{3.58}$$

which, as in the case for TE modes, is real for propagating modes and imaginary for evanescent modes. The cut-off frequency for each TM_{mn} modes is identical to the corresponding TE_{mn} mode frequency, as is the phase velocity. However, it is clear from *Equations* 3.54 to 3.57 that if either m or n are zero then the transverse components themselves reduce to zero, meaning that the TM_{00}, TM_{10} and TM_{01} modes are not supported by the rectangular waveguide. The lowest frequency propagating TM mode is therefore the TM_{11}, with a cut off frequency of:

$$f_{c_{1,1}} = \frac{1}{2\pi\sqrt{\mu\varepsilon}}\sqrt{\left(\frac{\pi}{a}\right)^2 + \left(\frac{\pi}{b}\right)^2} \tag{3.59}$$

which is higher in frequency than the TE cut-off mode. Therefore the lowest seven modes to propagate in the rectangular waveguide in frequency order are the TE_{10}, TE_{20}, TE_{01}, then the TE_{11} and TM_{11}, and finally the TE_{21} and TM_{21}. Field profiles for the lowest four propagating TM modes (TM_{11}, TM_{21}, TM_{12} and TM_{31}) are shown in *Figures* 3.5 and 3.6.

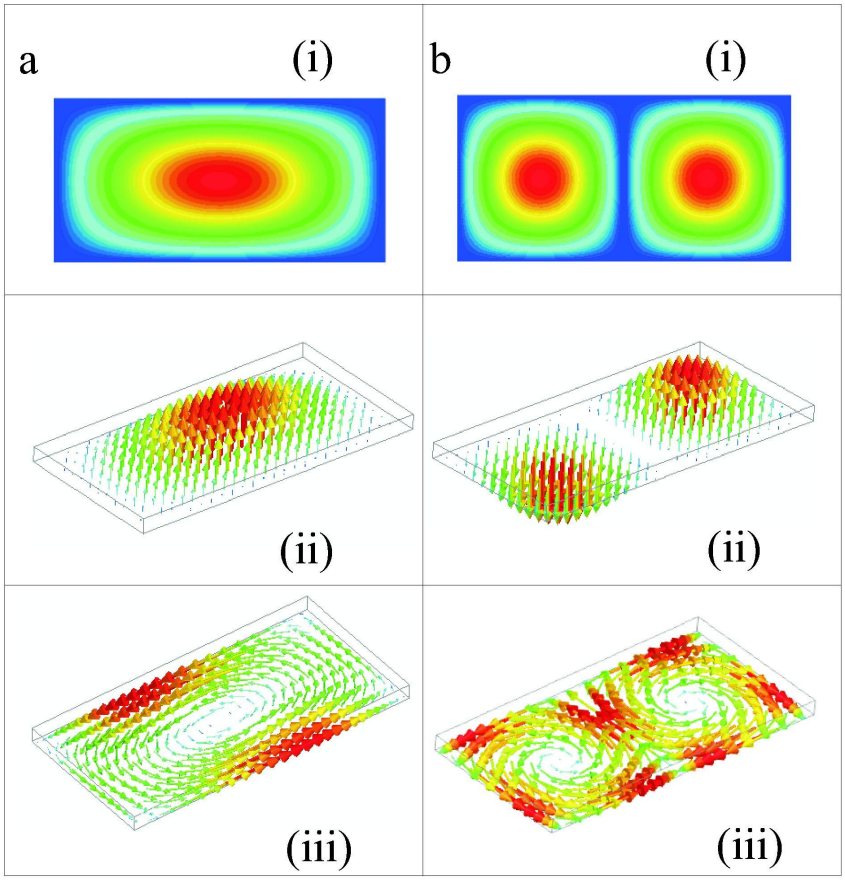

Figure 3.5: The field profiles corresponding to a) the TM_{11} and b) TM_{21} modes propagating within a vacuum filled perfectly conducting rectangular waveguide. For each mode, the i) time-averaged electric field magnitude and the ii) electric field and iii) magnetic field vectors plotted at a phase corresponding to maximum enhancement are displayed. Each field plot is across the xy-plane, with red corresponding to maximum field, and blue corresponding to zero field.

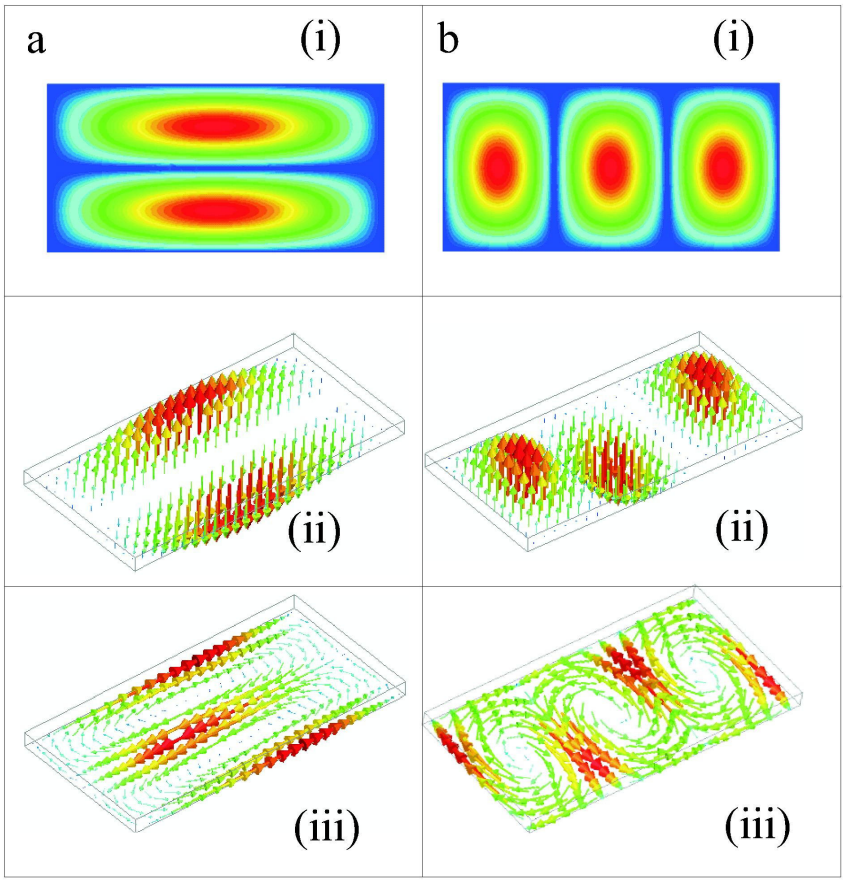

Figure 3.6: The field profiles corresponding to a) the TM_{12} and b) TM_{13} modes propagating within a vacuum filled perfectly conducting rectangular waveguide. For each mode, the i) time-averaged electric field magnitude and the ii) electric field and iii) magnetic field vectors plotted at a phase corresponding to maximum enhancement are displayed. Each field plot is across the xy-plane, with red corresponding to maximum field, and blue corresponding to zero field.

3.2.4 The Circular Waveguide

Like the rectangular waveguide, the circular waveguide also supports both TE and TM modes, and the transverse field components, and cut-off frequencies can be found in a similar way to those of the rectangular waveguide derived above. However, the TEM mode is not supported due to the boundary condition that the tangential E field must fall to zero at the boundary wall. The circular waveguide is displayed in *Figure* 3.7. Similarly to the rectangular waveguide it is considered to consist of a perfectly conducting wall surrounding a vacuum, and is infinite and uniform in the z-direction. Due to the circular symmetry the waveguide will be treated with cylindrical co-ordinates.

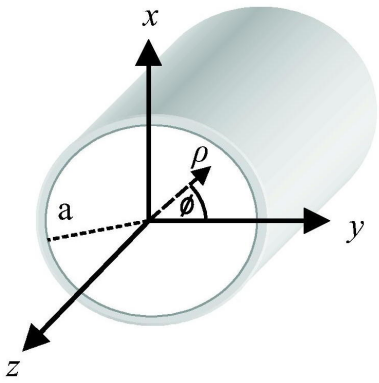

Figure 3.7: The circular waveguide geometry with co-ordinates marked.

The transverse field components may be derived from the longitudinal components E_z and H_z, and are expressed in cylindrical co-ordinates:

$$E_\rho = -\frac{i}{k_c^2}\left(k_z\frac{\delta E_z}{\delta\rho} + \frac{\omega\mu}{\rho}\frac{\delta H_z}{\delta\phi}\right) \tag{3.60}$$

$$E_\phi = \frac{i}{k_c^2}\left(\frac{k_z}{\rho}\frac{\delta E_z}{\delta\phi} - \omega\mu\frac{\delta H_z}{\delta\rho}\right) \tag{3.61}$$

$$H_\rho = \frac{i}{k_c^2}\left(\frac{\omega\varepsilon}{\rho}\frac{\delta E_z}{\delta\phi} - k_z\frac{\delta H_z}{\delta\rho}\right) \tag{3.62}$$

$$H_\phi = -\frac{i}{k_c^2}\left(\omega\varepsilon\frac{\delta E_z}{\delta\rho} - \frac{k_z}{\rho}\frac{\delta H_z}{\delta\phi}\right) \tag{3.63}$$

3.2.4.1 TE modes

Recall that for TE modes $E_z = 0$, and H_z is a solution of the wave equation, which must now be expressed in cylindrical co-ordinates as the following:

$$\left(\frac{\delta^2}{\delta\rho^2} + \frac{1}{\rho}\frac{\delta}{\delta\rho} + \frac{1}{\rho^2}\frac{\delta^2}{\delta\phi^2} + k_c^2\right) H_z(\rho,\phi) = 0 \tag{3.64}$$

where $H_z(\rho,\phi) = H_z(\rho,\phi)e^{-ik_z z}$. Once more, this equation can be solved using the separation of variables method. If we let $H_z(\rho,\phi) = R(\rho)P(\phi)$ and substitute into *Equation* 3.64 we obtain:

$$\frac{\rho^2}{R}\frac{d^2R}{d\rho^2} + \frac{\rho}{R}\frac{dR}{d\rho} + \rho^2 k_c^2 = \frac{-1}{P}\frac{d^2P}{d\rho^2} \tag{3.65}$$

Now both sides of the above equation may be set equal to a constant, which we will denote k_ϕ^2. Therefore:

$$\frac{d^2P}{d\phi^2} + k_\phi^2 P = 0 \tag{3.66}$$

$$\rho^2\frac{d^2R}{d\rho^2} + \rho\frac{dR}{d\rho} + (\rho^2 k_c^2 - k_\phi^2) = 0 \tag{3.67}$$

Here k_c has dimensions of $1/e$ whereas k_ϕ is dimensionless. *Equation* 3.66 has the general solution of:

$$P(\phi) = A\sin k_\phi\phi + B\cos k_\phi\phi \tag{3.68}$$

The solution to H_z must be periodic, therefore k_ϕ must be an integer, n. This leads to:

$$P(\phi) = A\sin n\phi + B\cos n\phi \tag{3.69}$$

If we make the same $k_\phi = n$ substitution into *Equation* 3.67 shows it to be a Bessel differential equation, which has a solution of the following form:

$$R(\rho) = CJ_n(k_c\rho) + DY_n(k_c\rho) \tag{3.70}$$

where $J_n(x)$ and $Y_n(x)$ are Bessel functions of the first and second kinds respectively, and C is a constant. As $\rho \to \infty$, $Y_n(k_c\rho)$ becomes infinite therefore being invalid for circular symmetry, and $D = 0$. Therefore the solution for H_z now becomes:

$$H_z(\rho,\phi) = (A\sin n\phi + B\cos n\phi)J_n(k_c\rho) \tag{3.71}$$

Remembering that tangential E is zero at the boundary wall, and that $E_z = 0$ for TE modes, we have:

$$E_\phi(\rho,\phi) = 0, \qquad \text{at} \qquad \rho = a \tag{3.72}$$

This allows us to find the transverse fields from *Equations* 3.60 to 3.63:

$$E_\rho(\rho,\phi,z) = -\frac{i\omega\mu n}{k_c^2\rho}\left(A\cos n\phi + B\sin n\phi\right) J_n(k_c\rho)e^{-ik_z} \tag{3.73}$$

$$E_\phi(\rho,\phi,z) = \frac{i\omega\mu}{k_c}\left(A\sin n\phi + B\cos n\phi\right) J_n(k_c\rho)e^{-ik_z} \tag{3.74}$$

$$H_\rho(\rho,\phi,z) = -\frac{ik_z}{k_c}\left(A\sin n\phi + B\cos n\phi\right) J'_n(k_c\rho)e^{-ik_z} \tag{3.75}$$

$$H_\rho(\rho,\phi,z) = -\frac{ik_z n}{k_c^2}\left(A\cos n\phi + B\sin n\phi\right) J_n(k_c\rho)e^{-ik_z} \tag{3.76}$$

where $J'_n(k_c\rho)$ is the first derivative of J_n with respect to its argument. If E_ϕ is to vanish at the point $\rho = a$ as the boundary conditions require, this derivative must equal zero. If we take the roots of the function to be defined as $p'_{m,n}$, the m^{th} root of $J'_n(k_c\rho)$, then k_c has to take the value:

$$k_{c(m,n)} = \frac{p'_{m,n}}{a} \tag{3.77}$$

which is the cut-off wavenumber for the TE_{mn}. In this case, m refers to the number of radial nodes, and n refers to the number of circumferential nodes. The propagation constant, k_z for the TE_{mn} mode in a circular waveguide is given as:

$$k_z = \sqrt{k_0^2 - k_c^2} = \sqrt{k_0^2 - \left(\frac{p'_{m,n}}{a}\right)^2} \tag{3.78}$$

having a cut-off wavelength of:

$$\lambda_{c(m,n)} = \frac{2\pi a}{p'_{m,n}} \tag{3.79}$$

Therefore the lowest frequency mode to propagate is that with the lowest value of $p'_{m,n}$. Values of $p'_{m,n}$ are shown in *Table* 3.1 below, and the TE_{11} is shown to be the dominant circular waveguide mode. *Figures* 3.8 and 3.9 display the electric and magnetic field profiles for the lowest four frequency TE modes.

n	p'_{n1}	p'_{n2}	p'_{n3}
0	3.832	7.016	10.174
1	1.841	5.331	8.536
2	3.054	6.706	9.970

Table 3.1: Values of p'_{nm} for the TE mode in a circular waveguide.

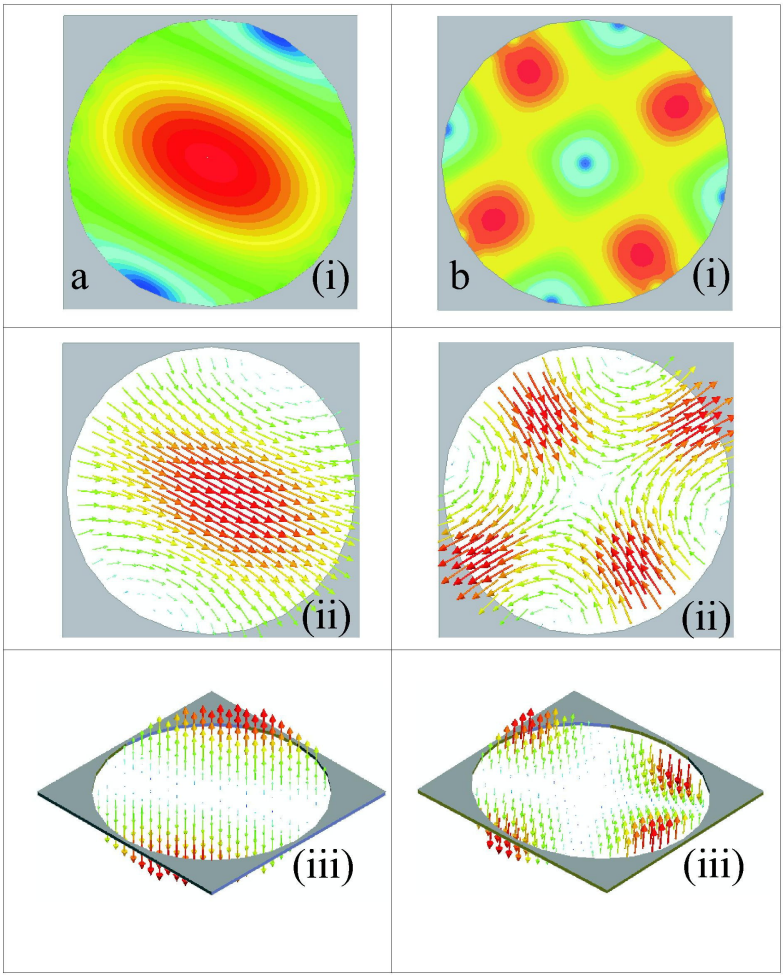

Figure 3.8: The field profiles corresponding to a) the TE_{11} and b) TE_{21} modes propagating within a vacuum filled perfectly conducting circular waveguide. For each mode, the i) time-averaged electric field magnitude and the ii) electric field and iii) magnetic field vectors plotted at a phase corresponding to maximum enhancement are displayed. Each field plot is across the xy-plane, with red corresponding to maximum field, and blue corresponding to zero field.

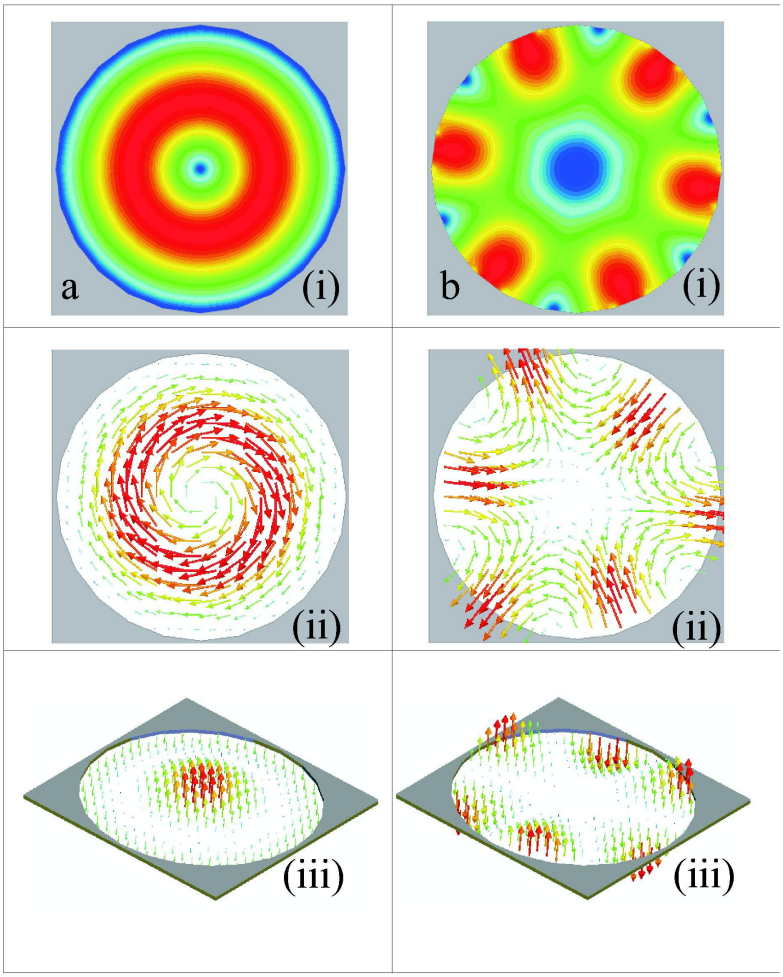

Figure 3.9: The field profiles corresponding to a) the TE_{01} and b) TE_{31} modes propagating within a vacuum filled perfectly conducting circular waveguide. For each mode, the i) time-averaged electric field magnitude and the ii) electric field and iii) magnetic field vectors plotted at a phase corresponding to maximum enhancement are displayed. Each field plot is across the xy-plane, with red corresponding to maximum field, and blue corresponding to zero field.

3.2.4.2 TM modes

For TM modes $H_z = 0$ and $E_z \neq 0$. Therefore we may solve the Helmholtz wave equation for E_z in cylindrical polar co-ordinates where $E_z(\rho, \phi,) = E_z(\rho, \phi)e^{-ikz}$.

$$\left(\frac{\delta^2}{\delta\rho^2} + \frac{1}{\rho}\frac{\delta}{\delta\rho} + \frac{1}{\rho^2}\frac{\delta}{\delta\phi^2} + k_c^2\right) e_z = 0 \tag{3.80}$$

the general solution to the above equation has the form:

$$e_z(\rho,\phi) = (A\text{sin}n\phi + B\text{cos}n\phi)J_n k_c\rho \tag{3.81}$$

and recalling that for TM modes:

$$E_z(\rho,\phi) = 0, \qquad \text{at} \qquad \rho = a \tag{3.82}$$

therefore we may apply boundary conditions directly to E_z:

$$J_n k_c a = 0 \tag{3.83}$$

and

$$k_{c(n,m)} = \frac{p_{m,n}}{a} \tag{3.84}$$

where $p_{m,n}$ is the the m^{th} root of the Bessel function $J_n(p_{n,m}) = 0$. *Table* 3.2 lists the lowest few values of $p_{m,n}$.

n	p'_{n1}	p'_{n2}	p'_{n3}
0	2.405	5.520	8.654
1	3.832	7.016	10.174
2	5.135	8.417	11.620

Table 3.2: Values of p'_{nm} for the TM mode in a circular waveguide.

Therefore we can define the propagation constant and the cut-off wavelength of the TM_{mn} mode as the following:

$$k_z = \sqrt{k_0^2 - k_c^2} = \sqrt{k_0^2 - \left(\frac{p_{m,n}}{a}\right)^2} \tag{3.85}$$

$$\lambda_{c(n,m)} = \frac{2\pi a}{p_{m,n}} \tag{3.86}$$

It can be seen from *Table* 3.2 and the above equation that the lowest frequency mode to propagate is the TM_{01}. Like the TE modes, $m \geq 1$ therefore the TM_{10} is not supported. Finally, the transverse fields of the TM modes may be derived as the following from *Equations* 3.60, 3.61, 3.62 and 3.63.

$$E_\rho(\rho,\phi,z) = -\frac{ik_z}{k_c}\left(A\text{sin}n\phi + B\text{cos}n\phi\right) J'_n(k_c\rho)e^{-ik_z} \tag{3.87}$$

$$E_\phi(\rho,\phi,z) = -\frac{ik_z n}{k_c^2\rho}\left(A\text{cos}n\phi - B\text{sin}n\phi\right) J_n(k_c\rho)e^{-ik_z} \tag{3.88}$$

$$H_\rho(\rho,\phi,z) = -\frac{i\omega\varepsilon n}{k_c^2\rho}\left(A\cos n\phi - B\sin n\phi\right) J_n(k_c\rho)e^{-ik_z} \tag{3.89}$$

$$H_\phi(\rho,\phi,z) = \frac{i\omega\varepsilon}{k_c}\left(A\sin n\phi + B\cos n\phi\right) J'_n(k_c\rho)e^{-ik_z} \tag{3.90}$$

Figures 3.10 and 3.11 below display the electric and magnetic field profiles of the four lowest frequency propagating TM modes, with field plots provided from HFSS.

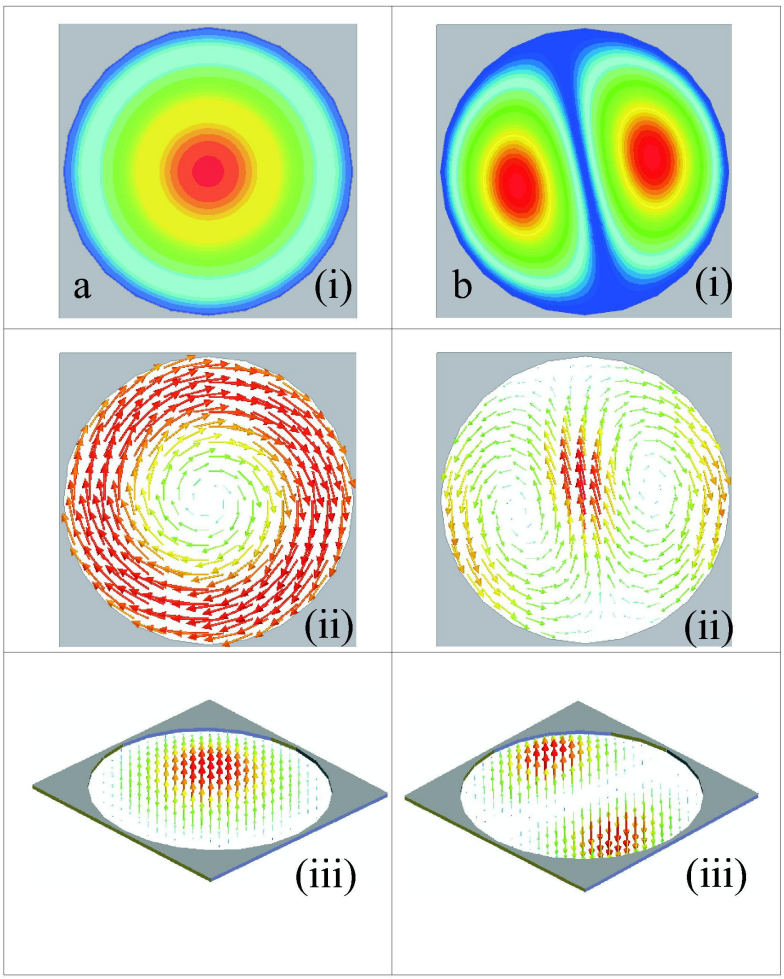

Figure 3.10: The field profiles corresponding to a) the TM_{01} and b) TM_{11} modes propagating within a vacuum filled perfectly conducting circular waveguide. For each mode, the i) time-averaged electric field magnitude and the ii) magnetic field and iii) electric field vectors plotted at a phase corresponding to maximum enhancement are displayed. Each field plot is across the xy-plane, with red corresponding to maximum field, and blue corresponding to zero field.

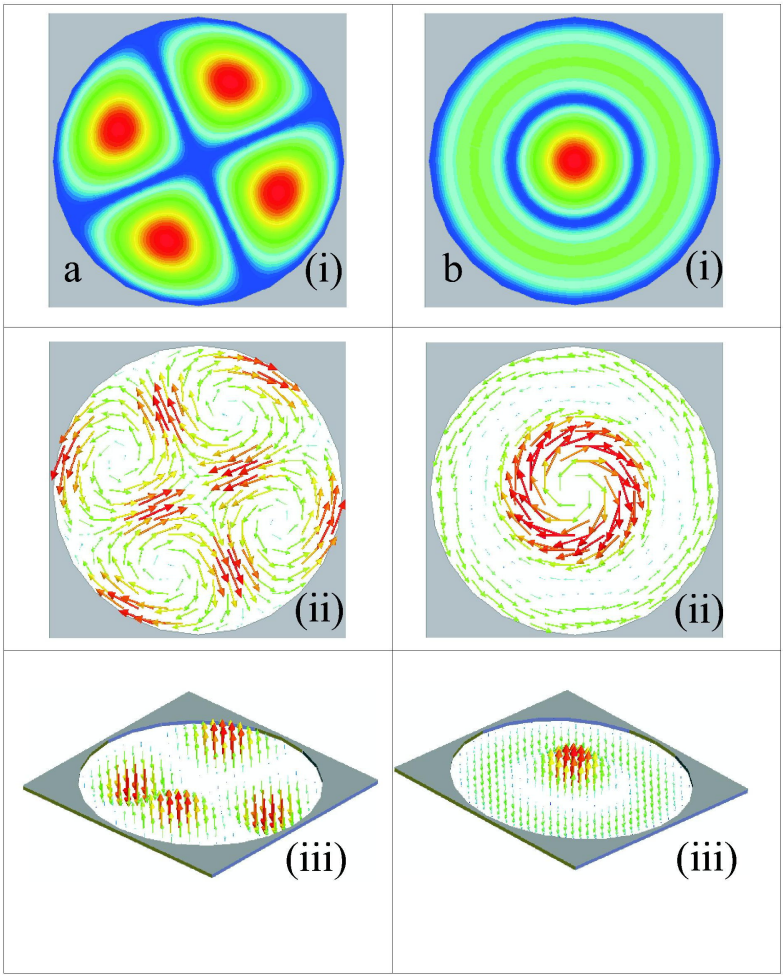

Figure 3.11: The field profiles corresponding to a) the TM_{21} and b) TM_{02} modes propagating within a vacuum filled perfectly conducting circular waveguide. For each mode, the i) time-averaged electric field magnitude and the ii) magnetic field and iii) electric field vectors plotted at a phase corresponding to maximum enhancement are displayed. Each field plot is across the xy-plane, with red corresponding to maximum field, and blue corresponding to zero field.

3.2.5 Summary

In the first half of this chapter using perfectly conducting walls the general solutions for the TEM, TE and TM waves have been derived using the Helmholtz wave equation, before using the boundary conditions for both rectangular and circular waveguides to generate solutions for the propagation of modes within the guides. The cut-off frequency for each waveguide has been calculated, and field profiles for the lowest four propagating modes in each waveguide have been displayed with plots from an FEM model.

3.3 Liquid Crystals

3.3.1 Liquid Crystal Phases

The term "Liquid Crystal" refers to a collection of phases of matter which all share common properties. An LC phase is one where a material is comprised of organic anisotropic molecules, and has a degree of fluidity that would normally be associated with a liquid, but the molecules retain a degree of ordering such that they will align with each other on a macroscopic scale. The Liquid Crystal phase occurs in one of two ways.

- Lyotropic liquid crystals occur when a material is dissolved in a particular solvent over a given concentration range.
- Thermotropic liquid crystals occur as a stable state in a material's solid-liquid phase change, and are highly temperature dependent.

Lyotropic LCs tend to occur in biological systems, and will not be discussed further in this thesis. Instead, the remainder of this chapter will be concentrated on thermotropic LCs.

3.3.1.1 Thermotropic LCs

Thermotropic LCs are categorised into three groups dependent on the shape of the molecules making up the LC.

- Calamitic liquid crystals are composed of rod-like molecules, having one long axis and two shorter ones of comparable size. These molecules tend to align with their long axes parallel.
- Discotic liquid crystals are disc-shaped, having one axis shorter than the other two (of comparable size). These molecules tend to align by stacking up in columns.
- Polymeric liquid crystals are composed of long chain molecules.

Of these groups, most devices to date have employed calamitic LCs, so this group will remain the focus of this chapter. *Friedel* (1922) [16] classified the calamitic group into three further subgroups determined by the degree of order within the LC.

- Nematics have the least degree of order. The molecules tend to align in the same direction, i.e. with their long axes parallel, but the centres of mass of the molecules are randomly distributed throughout the material.
- Smectics have an increased degree of order than nematics, and have layers of molecules, with each layer containing molecules aligned with their long axes parallel. Smectics are further classified by the angle of alignment within individual layers.
- Cholesterics have a similar degree of order as nematics, but are arranged into a helical structure with its axis normal to the alignment direction.

The LC phase most commonly used in devices designed to operate in the microwave regime is the nematic phase, so this is the LC phase that will be focused on in the remainder of this chapter.

3.3.1.2 The nematic phase

In the nematic phase the liquid crystal has orientational order, but no positional order. The molecules are are approximately rod-shaped, and have typical dimensions of 50 nm $\times$ 200 nm. Within each macroscopic region the LC molecules will not be perfectly aligned, and thermal fluctuations will cause fluctuations of orientation with time. Therefore the average orientation of all molecules is defined by a unit vector called the director, and denoted by $\underline{\mathbf{n}}$. The director defines the average orientation over a macroscopic volume of liquid crystal, rather than to specific LC molecules, and corresponds to the average direction of the long axis of the molecules. The LC molecules have their long axis denoted as the extraordinary axis, with the remaining two axes being called the ordinary axes. Positive and negative values of the director are indistinguishable.

3.3.2 Optical and dielectric anisotropy

Liquid crystals have been extensively employed at optical frequencies due to their optical anisotropy. Light polarised with its electric vector parallel to the director will sense a different refractive index to that sensed by light polarised with its electric vector perpendicular to the director. The indices are termed the extraordinary index and the ordinary index respectively. The optical anisotropy of any LC is defined as the difference between these two indices, and is dependent on frequency and temperature. The temperature dependence is due to the order parameter decreasing as temperature increases, and above the liquid crystal-isotropic fluid transition the refractive index becomes single valued.

$\triangle n = n_{\|} - n_{\perp}$,

where $\triangle n$ is the optical anisotropy, $n_{\|}$ is the extraordinary refractive index and $n_{\perp}$ is the ordinary refractive index. The refractive index of a material is linked directly to its permit-

tivity, and therefore a birefringence in refractive index leads to a birefringence in permittivity. This dielectric anisotropy is defined as follows:

$\triangle\varepsilon = \varepsilon_{\parallel} - \varepsilon_{\perp}$,

where subscripts refer to extraordinary and ordinary axes as above. This dielectric anisotropy governs the response of the director to an applied electric field. If a material has a positive dielectric anisotropy then its director will tend to align with an applied electric field, whereas if it has a negative dielectric anisotropy its director will align perpendicular to the applied field. The LC used within this thesis has a positive dielectric anisotropy, and therefore alignment is always parallel to an applied electric field.

3.3.3 Liquid Crystal cells

The most basic device into which LCs are incorporated is the LC cell. This is an optical device that allows the optical and dielectric anisotropies of LCs to be exploited. The typical LC cell in the homogeneous state is shown in *Figure* 3.12 and consists of two glass plates, each of which has one side coated with an electrode layer (typically a pre-deposited optically thin indium tin oxide layer with a thickness of ∼50 nm), followed by an aligning layer. These two plates are then assembled into a cell with the electrode and aligning layers facing each other. The cell is spaced by glass microspheres of ∼50 μm, and fixed together with a UV curing glue. Once the glue is set, the cell is LC filled by capillary action on a heat-stage in order to keep the LC in its isotropic stage. This encourages the LC molecules to align well as the cell cools. Once the LC has cooled the cell is sealed with an epoxy resin and wires are attached to the electrodes so that a field may be applied across the cell. The LC alignment under application of a voltage is shown in *Figure* 3.13 For the purposes of optical experiments cells tend to be a few tens of millimetres in size. However, for microwave experiments described later in this thesis cell sizes will be much larger, approximately 150 mm × 150 mm.

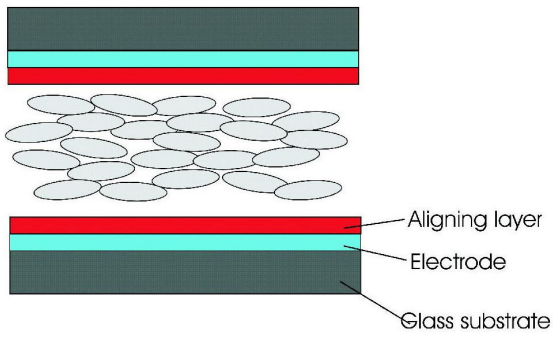

Figure 3.12: A typical LC cell with the LC in the homogeneous state.

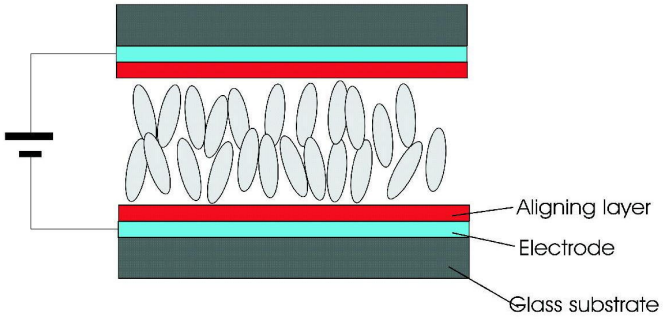

Figure 3.13: A typical LC cell with the LC in the homeotropic state.

3.3.3.1 Alignment techniques

The alignment of LC within a cell depends upon the aligning layer that is used in the cell construction. Alignment of the director parallel to the substrate is called homogeneous alignment, and this is promoted by the aligning layers within the cell. It is possible to induce alignments other than parallel to the substrate with the correct choice of aligner, but this is not pertinent to this thesis so will not be discussed any further. The aligning layer used throughout this thesis is a rubber polyimide, as this provides a relatively easy way of promoting homogeneous alignment over a large surface area, for relatively low cost. The polyimide is a compound composed of long chain molecules which is applied to the cell substrate in liquid form. The substrate is then spun at approximately 4000 rpm, producing a layer of $\sim$100 μm. The substrate can then be baked, which hardens the polyimide to a solid layer. Once the substrate has cooled the polyimide layer can be hand-rubbed with a velvet cloth, which aligns the polymer and produces microgrooves in the aligning layer. A combination of these effects promotes homogeneous alignment of the LC when the cell is capillary filled, and the alignment then propagates into the bulk via elastic interactions.

3.3.4 LC devices

The following section will give a review the work undertaken in recent years involving LCs at microwave frequencies. Initial studies focused on determining the birefringence of LCs at microwave frequencies, with further studies developing devices such as phase shifters, wavelength selectors, deflectors and lenses.

Lim et al (1992) [17] determined the birefringent properties of two LCs at microwave frequencies, and proposed a microwave phase shifter. The birefringence of the LC was determined by containing it within a section of rectangular waveguide and placing it in one arm of an interferometer. The LC produced a phase shift in the guide which was compensated for by a 360° phase shifter in the other arm of the interferometer. The initial alignment of the LC molecules was random, achieved by mechanical stirring of the material. Next, a pair of

large 5 kG magnets were mounted externally to the guide to achieve parallel alignment of the LC molecules with the field, due to the positive magnetic anisotropy of the LC. The magnets were placed such that the magnetic field was applied parallel to the electric vector of the wave propagating within the guide.

The microwave phase shifts caused by the LC in both the random alignment, and parallel alignment with the magnetic field, were measured as a function of the length of the LC column within the guide. The relative phase shift was found to be directly proportional to the path length, and is given by:

$$\delta\theta = 360d\left(\sqrt{\frac{n^2}{\lambda_0^2} - \frac{1}{4a^2}} - \sqrt{\frac{1}{\lambda_0^2} - \frac{1}{4a^2}}\right)$$

where $\delta\theta$ is the relative phase shift, a is the waveguide broad dimension and λ_0 is the microwave wavelength in free space. Clearly, the above equation shows that the phase shift, $\delta\theta$ is directly proportional to the microwave path length, d for a given refractive index n. Using this equation the birefringence $\triangle n$ at 30 GHz of LCs BL001 and BL006 were calculated to be:

$\triangle n(BL001) = 0.192$

$\triangle n(BL006) = 0.223$

These values are roughly 85% and 78% of the optical birefringence of each material respectively.

Lim et al (1992) [17] also realised a microwave phase shifter constructed using a similar arrangement to that used in the birefringence determination experiment. The phase shifter consisted of a rectangular waveguide placed between a pair of permanent magnets to produce a constant aligning field. A centre plane electrode was placed within the waveguide and used to apply a modulating electric field to the LC. Thus the magnetic field was perpendicular to the electric vector of the wave propagating within the guide, whereas the electric field between the centre plane electrode and the sidewalls was nominally parallel to the electric vector. The induced electric field could then be increased so as to oppose the alignment of the LC due to the magnets, and above a threshold voltage of 60 V there was a clear increase in phase shift with increasing voltage, until saturation at around 200 V where the LC was completely aligned with the applied electric field. The response time of the LC was found to be $\sim$0.1 s, with a relaxation time under the magnetic field of $\sim$2 s.

The above work demonstrated the birefringent properties of LCs at microwave frequencies, and their potential for use in phase shifting devices. Further work on the birefringent properties of LCs was conducted by *Lim et al* (1993) [18]. In this work it was found that the most favorable LC structures for high birefringence in the microwave regime are the rod-like *calamitics* described above. A phase shifter was also studied by *Guerin et al* (1997) [19], where the phase shifting was extended into the 30-40 GHz range, allowing large phase shifts of around 40-50°cm^{-1} with low insertion losses.

Tanaka et al (2000) [20] investigated the transmission properties of a grating-patterned electrode structure LC cell, using grating patterned ITO electrodes. The transmittance of the cell was found to be 70-80% for radiation polarised with its electric vector parallel to the grating vector, and 7-8% for radiation polarised perpendicular to the grating vector. It was found that changing the orientation of the LC molecules via an applied electric field also had an effect on the transmissive properties of the cell, even though the field was inhomogeneous due to the grating pattern of the electrode structure. This study also investigated the effect of the thickness of the LC layer within the cell, finding that in thicknesses greater than around 100 μm it is difficult to achieve reliable alignment of the LC.

Fujikake et al (2001) [21] demonstrated the possibility of using a fine polymer network to stabilize the molecules within a thick LC cell, by applying a photopolymerisation-induced phase separation technique, also allowing a reduction in the relaxation time of the LC cell. Again, the device being constructed was a phase shifting device with a LC layer thickness of 100 μm. The polymer network was formed by mixing a UV light-curing monomer with the LC at room temperature. The solution was then sandwiched between two substrates that had been coated with aligning layers. The cell was then subjected to intense UV radiation from a Hg-Xe discharge lamp to cause polymerisation of the monomer component. This polymer network had a concentration of 7wt %, and was found to greatly reduce the relaxation time of the LC alignment from around 40 s down to $\sim$100 ms. However, although increasing the polymer concentration reduced the relaxation times of the cell, it was also found that the LC alignment became increasingly disordered for increasing concentration of polymer. The device that used this polymer-doped LC was a phase shifter that realised similar results to previous devices, with a faster relaxation time due to a polymer network.

Some optical devices that incorporate LCs may be adapted for use in the microwave regime. *Tanaka et al* (2001) [22] investigated the effects of an LC prism consisting of a wedge-shaped layered stack structure of metal substrates and nematic LC. The metal substrates acted as electrodes to change the alignment of the LC director. Incident microwaves were polarised with their electric vector parallel to the grating vector of the stack to achieve high levels of transmission. By applying an electric field across the LC layers the angle of deflection of the transmitted beam could be controlled. The device structure is shown in *Figure* 3.14. One of the drawbacks of this structure was that reflections at both entrance and exit faces caused it to have a high insertion loss.

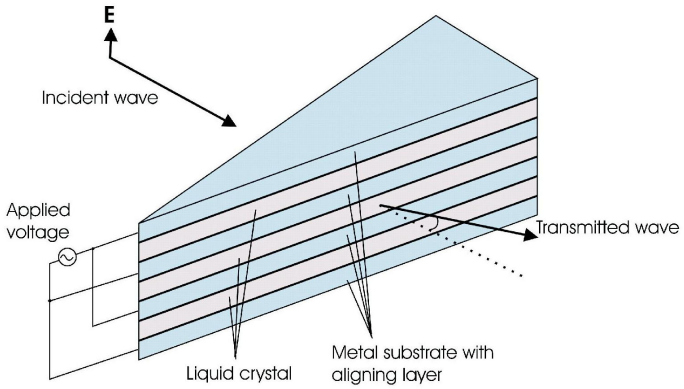

Figure 3.14: The wedge-shaped prism investigated by *Tanaka et al* (2001) [22].

Another stack-layered structure was investigated by *Yang and Sambles* (2001) [23] in the form of a microwave wavelength selector. The device consisted of a stack of 1 mm thick aluminium slats separated by 75 μm gaps filled with nematic LC. The slats were individually coated with a polyimide (AL1254) aligning layer on both sides, then baked and unidirectionally rubbed along the short axis of the slats to promote homogeneous alignment of the LC. Resonant transmission was observed for incident microwave radiation that had its electric vector oriented perpendicular to the slats, which was due to coupling into cavity modes in the LC layers. A voltage was applied across adjacent pairs of slats in order to realign the LC, changing the sensed refractive index within the LC layers. This in turn caused a change in the resonant transmission frequency of the device, allowing voltage control of the transmission wavelength. The structure of this sample is shown in *Figure* 3.15.

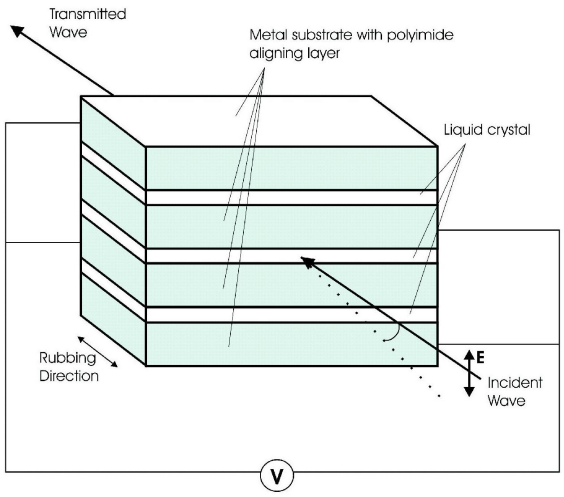

Figure 3.15: The stack layered wavelength selector investigated by *Yang and Sambles* (2001) [23].

Tanaka and Sato (2002) [24] devised an LC lens based on the same principles as the LC prism discussed above. A stack-layered LC lens was prepared using nematic LC and planoconvex-shaped metal plates as electrode substrates. The LC layers and metal substrates were stacked alternately having thicknesses of 0.3 mm and 0.8 mm respectively, with the LC layers having glass microspheres within them to give the metal plate spacing. The metal substrates were coated with a layer of polyvinyl alcohol which was unidirectionally rubbed. The polarisation of the incident microwaves was parallel to that of the grating vector of the stack, as shown in *Figure* 3.16. The LC director was aligned parallel to each substrate due to the aligning layer, and a change in focal length was achieved by applying a voltage to realign the LC. A focal point of $\sim$78 mm was found with no voltage applied, and this changed to $\sim$ 62 mm on application of 10 V.

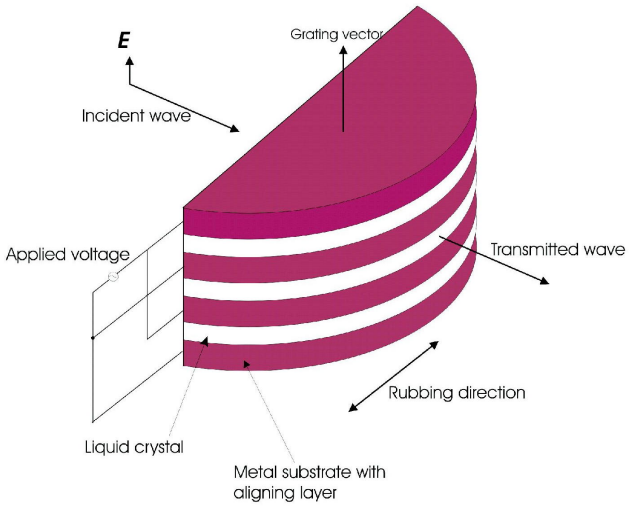

Figure 3.16: The LC lens devised by *Tanaka and Sato* (2002) [24].

Whilst *Lim et al* (1992) [17] had determined the birefringence of LCs at microwave frequencies, *Yang and Sambles* (2002) [25] went further, determining the separate ordinary and extraordinary indices of LC at microwave frequencies. This was achieved using a single metallic subwavelength slit which showed enhanced transmission due to the excitation of Fabry-Perot type modes within the slit cavity. By filling this simple slit geometry with a nematic LC a straightforward procedure for determining microwave permittivities was demonstrated. The Fabry-Perot like nature of the transmission means that the resonant transmission frequencies are dependent on the refractive index of the material within the slit cavity, and therefore by applying a voltage across the LC layer a shift in the resonant frequency peaks was achieved. The transmission maxima are at wavelengths that closely satisfy the naive Fabry-Perot condition, and therefore a simple calculation allowed the ordinary and extraordinary indices of the LC to be determined in the chosen frequency range. The structure and experimental set-up are displayed in *Figure* 3.17.

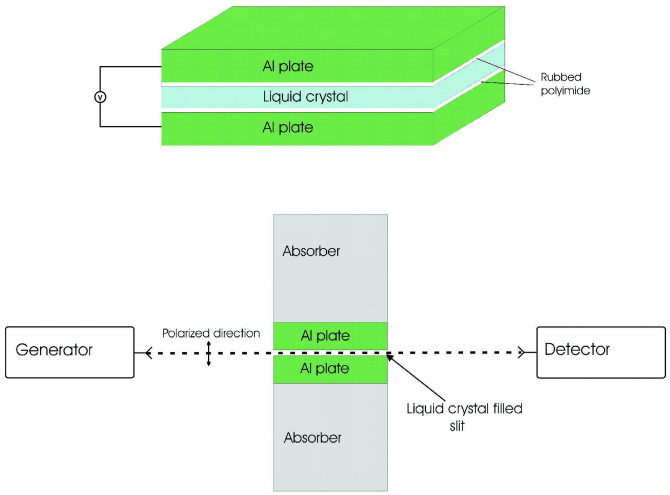

Figure 3.17: The sample (top) and experimental set-up of *Yang and Sambles* (2002) [25] used to determine microwave permittivities of LCs.

Two of the limiting factors found in some of the devices discussed above are slow response times and high insertion loss. These issues were addressed by *Kuki et al* (2002) [26] in the construction of a variable delay line. A dual frequency switching mode LC (DFSM LC) was used, as it was known to have a fast response time from use in other devices. The advantage of DFSM LC is that the alignment of the LC due to the application of an electric field is dependent on the frequency of the control voltage. The DFSM LC used here aligned parallel to the field when the control voltage was in the low frequency region, near d.c., whereas in the higher frequency region of several hundred kilohertz the DFSM LC aligned perpendicular to the applied field. This meant the LC could be driven into either parallel or perpendicular alignment, rather than having to relax from one to the other, reducing response time. The insertion loss was dominated by the conductor loss of the strip conductor due to its narrow width. Using a thicker LC layer allowed a thicker strip to be used, reducing insertion loss. The use of a DFSM LC allowed a 50 μm layer to have a decay time of 1.5 s, less than half that of previous devices. Also, a 9 dB reduction in insertion loss was achieved with a 200 μm LC layer as compared with that of a 50 μm layer.

Yang and Sambles (2004) [27] realised a variable microwave phase grating allowing low voltage control of output beam profile and intensity. This was achieved by constructing a stack of 71 aluminium strips of 1 mm thickness separated by 75 μm spacers, with the gaps filled with nematic LC. The 70 gaps within the structure were divided into 7 groups of 10 gaps, and an a.c. source was used to apply different voltages independently to each gap within one group, with the corresponding gaps in each group having the same voltage across them. The aluminium slats were coated with a polyimide, as in previous devices of this nature, and baked and rubbed to facilitate alignment of the LC layer. By applying different

voltages across the gaps within each group it was possible to tune the transmitted frequencies to destructively interfere, resulting in almost zero transmission at selected frequencies. Thus a voltage controlled variable phase grating at microwave frequencies was demonstrated. The device is shown in *Figure* 3.18.

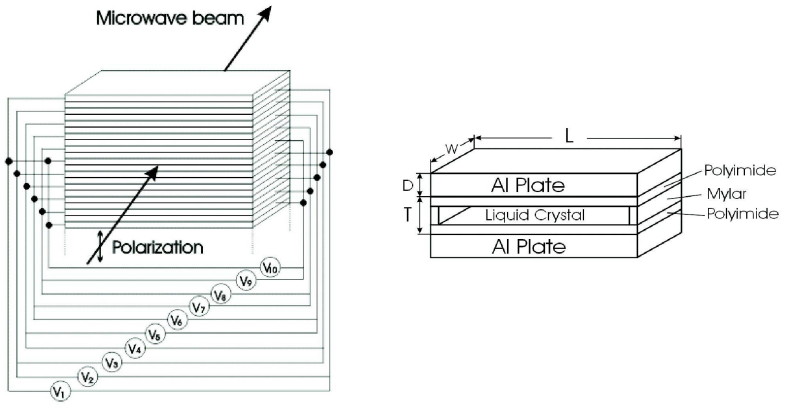

Figure 3.18: The sample constructed by *Yang and Sambles* (2004) [27] (left), and a close-up view of the individual slit configuration (right).

Applying a voltage of 3.0 V_{rms} across the top six gaps in each group of ten, and a voltage of 1.6 V_{rms} across the remaining four gaps in each group of ten resulted in two signals of almost equal intensity and opposite phase. These two components destructively interfered resulting in almost zero transmission at a frequency of 59.20 GHz. The voltages were then changed to 2.5 V_{rms} across the top four gaps, and 1.5 V_{rms} across the remaining six, resulting in the transmission zero point occurring at 56.70 GHz. The transmission zero-point was shown to move, thereby proving a voltage controlled variable phase grating at microwave frequencies.

3.4 Summary

In the first half of this chapter there has been a summary of waveguide theory. The general solutions for the TEM, TE and TM waves have been derived, and the general solutions for the propagation of modes within both rectangular and circular waveguides has been discussed. In the second half of this chapter, some of the fundamental properties of Liquid Crystals have been explored. The basic construction of an LC cell has been shown, including reference to alignment techniques. Finally, some of the devices incorporating LCs that have been constructed to operate in the microwave regime have been discussed.

Chapter 4

Modelling

4.1 Introduction

This chapter is concerned with the computer modelling package that is used exclusively throughout this thesis for generating theoretical predictions to compare with data. Ansoft's High Frequency Structure Simulator (HFSS) v 10.1 is the modelling package used to predict the electromagnetic responses of the structures presented in the experimental chapters. The Finite Element Method (FEM) is utilised by HFSS, which involves fragmenting the model space into many thousands of tetrahedra, and then solving Maxwell's equations numerically across each of these small volumes, which allows the response of the entire structure to be predicted. HFSS was initially designed to model industrial systems such as waveguides where radiation may be injected via a port, however the package has been developed considerably in order to now make predictions for infinite periodic arrays in free space, in both transmission and reflection. Also, HFSS can model finite structures in infinite planes, such as a single slit or hole in a metal plate. HFSS is designed to predict the response of a structure at a designated frequency, but also has coding that allow it to perform frequency sweeps in user-defined frequency steps, or automate variations in structural dimensions to give a parametric analysis of a sample.

This chapter will give a brief overview of Ansoft's HFSS. Firstly, a description of the FEM is presented with reference to the importance of the correct "mesh" resolution and the balance between modelling accuracy and processing speed, and computational memory requirements. The computer-aided-design (CAD) package within HFSS will also be discussed, and how symmetry considerations may be used to reduce model size. The various boundaries that are employed to provide electromagnetic terminations or symmetries will be detailed, along with the post-processing package that allows the frequency response of models to be examined.

4.2 The Finite Element Method

The FEM involves breaking up the complete model space into a series of small elements, or tetrahedra to create a large mesh filling the entire model area. Different materials within the

model space are each filled with a mesh the outer boundary of which is shared with that of the mesh of the adjacent material. Each tetrahedron has a value of the vector field quantity stored within it, such as the electric or magnetic field. Tangential field components to the edges of an element are stored explicitly at the vertices, with tangential fields at the faces of each element stored at the edges. The field within each element can then be calculated with reference to these values by transforming Maxwell's equations into matrix equations and solving numerically. The calculations are simplified somewhat by making the properties of each material, (metal, dielectric or vacuum) constant within the interior of each element, therefore clearly making the spatial resolution of the mesh the defining factor in determining the accuracy of the predictions of the model. However, increasing the spatial resolution of the model results in a significant increase in the number of calculations to be performed, and so the processing time and computational memory requirements are increased in turn. It is therefore important to generate a mesh that is sufficient to provide reliable predictions for the sample being reproduced, but that has an acceptable solving time. This means that the way in which the mesh is generated is very important to achieve the optimum solving parameters. The methods used to generate the mesh are described in *Section* 4.3.4.

4.3 Creating a model

4.3.1 Drawing the model

HFSS has an integrated CAD package that can be used to recreate experimental samples to scale in 3-D. Simple tools allow the construction of 3-D objects such as spheres or cubes either by cursor control, or by defining starting points and vectors in Cartesian, spherical or polar coordinates. Alternatively 2-D objects may be created and then manipulated into 3-D by sweeping along a plane or vector, or rotating about an axis. A higher degree of complexity can be achieved by the use of subtracting and uniting tools, that allow simple objects to be built up into a larger more complicated structure. Duplication tools and mirror planes allow replication of objects within the model (along vectors or about axes) to allow easy creation of an element that may be repeated several times within the structure. A history tree of each action within the model creation is automatically generated so that changes can be readily made or mistakes edited. Drawing a model correctly can take some time, so to allow for parameter variations to be easily implemented HFSS allows the numerical value of each parameter to be replaced with a variable name. This variable may then be assigned a value, or made a dependent on other parameters in the model. This means the whole sample geometry can be changed by the reassignment of a variable value, without the need to draw the structure again. Of course, care must be taken to ensure the change in variable does not render the structure invalid, however HFSS provides a simple checking procedure to confirm that the model dimensions remain viable. In addition it is possible to draw objects that will not be considered by the solver, but may later be assigned as boundary planes, or evaluation planes over which numerical answers may be extracted.

4.3.2 Assigning materials

Once constructed, objects in the model space must be assigned material properties. HFSS contains a database with a variety of standard materials, and allows for the creation of new materials. Each material within the the database (and created materials) are defined by several fundamental properties. These are as follows:

- Relative permittivity, ε
- Relative permeability, μ
- bulk conductivity, σ
- dielectric loss tangent, $\frac{\varepsilon_i}{\varepsilon_r}$
- magnetic loss tangent, $\frac{\mu_i}{\mu_r}$

The above properties may be defined by numerical values, or a user-defined function may be entered. The real parts of the relative permittivity and permeability are entered by the user, as are the dielectric and magnetic loss tangents, therefore the user is required to calculate each loss tangent by dividing the imaginary part (of the permittivity or permeability) by the real part (of the permittivity or permeability), with the imaginary part not being entered explicitly. If the defined property is frequency-dependent, HFSS allows a number of values to be designated over the desired frequency range from which it interpolates values to the corresponding frequencies run by the solver by using a fitting procedure on the defined values.

A material may be defined by either permittivity or conductivity, depending on the value of the conductivity. For any materials with a conductivity greater than $1 \times 10^5 \mathrm{Sm}^{-1}$ HFSS no longer uses ε and μ , and instead solely uses σ and a surface impedance approximation (SIA). The SIA simplifies the model by calculating the impedance of the metal at the surface, and uses this value to calculate conductive losses within the metal. This reduces the model size considerably, because at very high conductivities the penetration of electromagnetic fields into the material surface is so small it would otherwise require an extremely large number of small tetrahedra within this region. For perfect metals, (infinite conductivity) electromagnetic fields are completely excluded from the metal and the electric field is forced to be perpendicular to the metal surface. For metals with finite conductivity the fields may deviate from normal. The tangential field is given by:

$$E_{tan} = Z\left(\hat{n} \times H_{tan}\right)$$

Where E_{tan} and H_{tan} are the tangential electric and magnetic fields at the surface, $\hat{n}$ is the normal to the surface of the metal and Z is the surface impedance, which for a good conductor is given by:

$$Z = \frac{E}{H} = (1 + j)\left(\frac{\omega\mu}{2\sigma}\right)^{\frac{1}{2}}$$

where σ is the bulk conductivity, μ is the permeability of the metal and ω is the frequency of the incident radiation. As the E-field has a tangential component at the surface of an imperfect conductor, this implies a lossy surface. The surface approximation approach that allows HFSS to greatly reduce the required mesh size when dealing with metallic objects. It may be noted that it is possible to override this approximation and insert tetrahedra into metals within HFSS models, but due to the high levels of processing power required this is only viable for extremely small volumes of metal, and this method is not employed in the models within this thesis.

4.3.3 Assigning boundaries and excitations

HFSS allows electromagnetic excitations to be applied to models in a variety of ways. Driven solutions in HFSS have radiation incident on the sample, either injected through a port, such as a waveguide, or injected in the incident medium, replicating an electromagnetic wave propagating in free space. The injected wave is simulated simultaneously at all points in the model, and can take the form of a planar, Gaussian or spherical wave. The excitation is defined in terms of incident angle and polarisation in either Cartesian or polar coordinates. It is therefore possible to replicate the experimental set-up described in later chapters and examine the fields in the model in three modalities: the incident field, the scattered field (resulting from an interaction with model structures) and the total fields (combined incident and scattered fields).

All outermost faces of the model space must be assigned a boundary condition within which the incident and scattered electromagnetic fields must be contained. The choice of boundary is crucial to correctly replicating the experimental sample being modelled. Many experimental samples consist of a periodic array which may be considered infinite as compared with the incident beamspot, and HFSS allows for easy modelling of such periodic samples. Pairs of boundaries called master-slave boundaries replicate all electromagnetic fields on the master and transfer them to the slave. The incident angle of the excitation must also be defined with respect to the master-slave assignment so that no secondary sources occur as a result of phase discontinuities. An example of the master-slave boundaries is shown in *Figure* 4.1.

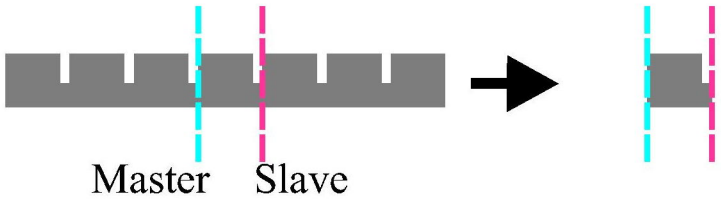

Figure 4.1: An example of the use of master-slave boundaries. A reflection grating may be simplified to a single unit cell, thus vastly reducing the problem space.

As an alternative to master-slave boundaries, Perfect E and Perfect H boundaries can sometimes be employed. Perfect E boundaries force the tangential E field to zero at the boundary surface, thereby representing a perfect conductor. Perfect H boundaries force the tangential H field to be identical on either side of the boundary, resulting in a natural boundary through which the field propagates. These boundaries may be used as symmetry planes in order to reduce model size when the polarisation of either component is perpendicular to the boundary, as illustrated in *Figure* 4.2.

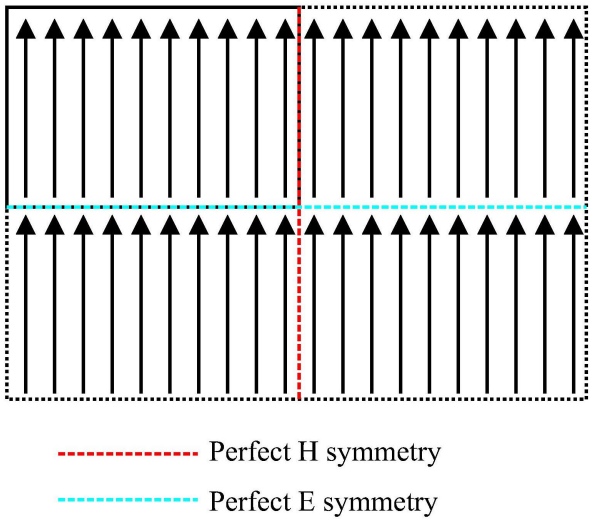

Figure 4.2: An illustration of the nature of Perfect E and Perfect H symmetry boundaries. The arrows indicate the direction of the electric vector.

The main boundary types used for exit and entrance surfaces are radiation, impedance and perfectly matched layers (PMLs). Radiation boundaries are used to simulate open problems where radiation is allowed to propagate freely as if passing into free space. Impedance boundaries allow radiation to propagate away in a medium that has user-defined values of

resistance and reactance, set to default values for free space of 377 Ω for resistance and 0 Ω for reactance. It is also possible to define a surface roughness through the use of a layered impedance boundary, which enables the user to define a depth to which there is an alteration in the surface conductivity of a bulk material. PMLs are similar to radiation boundaries in that they do not allow any reflections from the boundary back into the model space, with the advantage of being able to absorb radiation from much higher angles of incidence. However the PML boundary must have a thickness comparable to one half wavelength of the operating frequency (as opposed to other boundary types that have zero thickness), this layer also requires a mesh to be injected, increasing the overall model size.

4.3.4 Mesh generation

Once the structure has been drawn, an excitation inserted and the correct boundaries assigned, a mesh must be generated in order to solve the model. An initial mesh may be generated at a set frequency, either to user defined specifications, or automatically by HFSS. For either case, the mesh is then refined by an adaptive pass method. HFSS uses the FEM to identify the areas in which the model contains large field gradients, and refines the mesh in these areas by the generation of a second, higher resolution mesh. This process continues iteratively until a user-defined number of passes has been made, or a value of "convergence" has been achieved, again specified by the user. The convergence is a measure of difference in the field gradients calculated from one mesh to the next (typically deemed satisfactory at a level of ≤ 0.01). The rate of convergence of the mesh can also be controlled by entering a percentage value of the current number of tetrahedra to be injected on the next pass. Once the adaptive pass process is finished, it is still possible to further refine the mesh by increasing the number of tetrahedra in any object by specifying the number of elements, or the maximum element size. This is particularly useful when performing frequency sweeps, as the mesh is generated at a single frequency, and the regions of high field gradient may change across the entire frequency range. Another advantage of generating a high resolution manual mesh at a given frequency is that it allows higher resolution field plots to be generated, which can be useful for analysing the electromagnetic response of the structure. A simple method of checking whether or not a mesh is of suitable resolution is to run the post-processing software and extracting a value (such as transmission or absorption from the structure), running again to a higher resolution mesh and then extracting the same value. If they agree to a reasonable degree, then the mesh can be considered acceptable. Generating a mesh of the correct resolution is crucial to running a model that solves in a reasonable amount of time, whilst still producing reliable solutions. *Figure* 4.3 display a typical mesh generation.

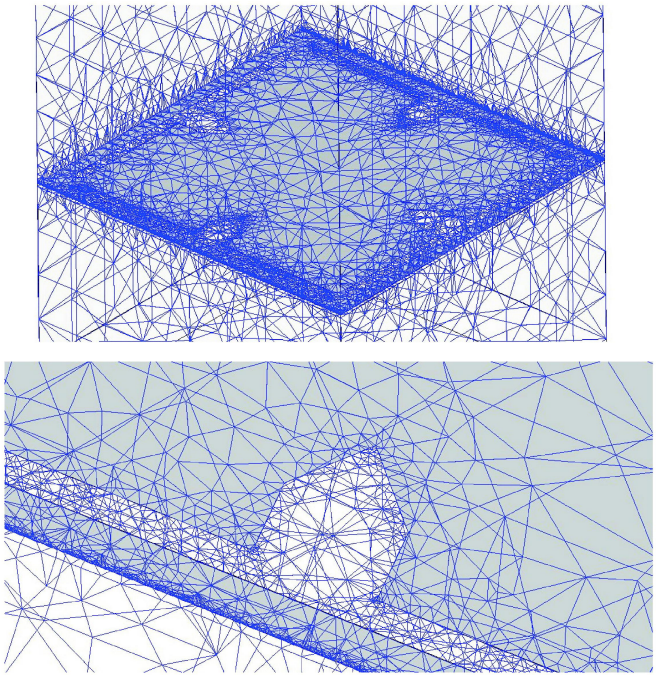

Figure 4.3: An example of a mesh within HFSS. The structure shown is sample C from *Chapter* 5. (top) A view of the majority of the sample space and (bottom) a zoomed-in view of one of the cuts.

4.3.5 Solutions and post-processing

Once the FEM model has generated the electromagnetic response of the structure an integrated calculator is used to extract the required results. Plots of the electric or magnetic field magnitudes or vectors are available, as are quantities such as Poynting vector and current density. These may be plotted across the face of any object in the model, or a new plane can be drawn over which the fields can be plotted. In addition, the user may define two 2-D planes over which power flow can be computed, allowing evaluation of the incident, scattered and total fields across that surface. Incident fields represent the injected field as if there was no interaction with the sample, total fields represent the fields that exist in the presence of the sample, and scattered fields are calculated by subtracting the incident field from the total field. For a reflection model the solution plane is placed away from the structure in the upper half-space and is determined from scattered fields divided by incident fields. For a transmission model the structure is surrounded by an air box in both upper and lower half-spaces, transmission is evaluated from the scattered fields in the lower (transmission) half-space divided by the incident fields in the upper (incident) half-space. These calculations may be automated by use of a post processing macro, allowing solutions for a frequency sweep to be output to a MS Excel file. This file contains data for frequency, transmission, reflection and absorption (1- [transmission + reflection]). Once the response of the structure has been determined, electromagnetic field plots can be produced at the relevant frequency to give insight into the

resonant behaviour. These field plots have a colour scale indicating the magnitude of the field relative to the incident field. The incident field has an electric magnitude of 1 Vm^{-1}, and a magnetic magnitude of 0.0026 Am^{-1}.

4.4 Models from this thesis

The following section explores selected models from this thesis in more depth, in order to demonstrate the general process described above in specific examples. The dimensions and boundaries used in each model will be detailed, as will the process of producing models that provide accurate answers whilst running in the quickest possible time. A model from each chapter will be selected and discussed in the order they appear in this thesis.

4.4.1 Patterned metal film

In *Chapter* 5 the transmission of microwaves through a thin metal film patterned with a subwavelength structure is examined. Four structures are investigated, each of which consists of a 2-D slit array, and two or which are modified by the addition of "cuts" perpendicular to the slits. The model investigated in this section replicates sample D from *Chapter* 5, and is shown in *Figure* 4.4. It has a unit cell of 5.9 mm × 5.9 mm with the slit located 0.24 mm from the edge of the unit cell. Each slit is terminated where the slits would otherwise cross by a connecting wire of thickness 0.18 mm at 45° to the slit direction. The cut for structure D has a width of 0.57 mm and extends 0.99 mm towards the centre of the unit cell, tapering to a point over a further 0.40 mm. The array is formed from an aluminium film of thickness ∼40 nm backed by a dielectric layer of thickness 100 μm, with the final sample having some 450 unit cells formed into arrays measuring approximately 105 mm × 150 mm, surrounded with a border of continuous metal of ∼20 mm on each side. Samples are placed in an experimental set-up such that microwaves are incident on the metalised side, and transmission data is recorded.

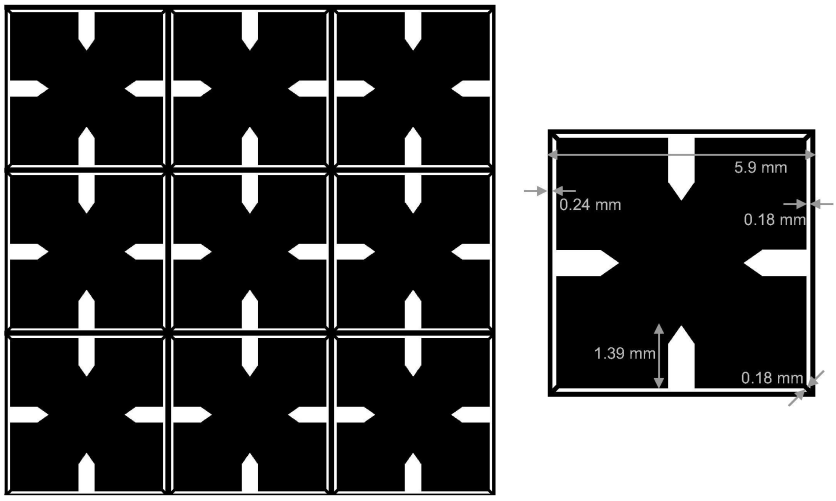

Figure 4.4: The structure investigated in *Chapter* 5. (left) The arrangement when unit cells are arranged into an array. (right) The dimensions of an individual unit cell.

The computer model is drawn for a single unit cell so as to reduce the model space. This unit cell will be replicated into an infinite array by appropriate selection of boundary conditions. The model is replicating experimental conditions whereby an electromagnetic wave propagating in air is incident on the sample, and then transmission from the sample is collected, therefore the basic structure of the model will be drawn within an "airbox". The airbox has dimensions relating to the pitch of the unit cell in the x- and y-dimensions, in this case 5.9 mm $\times$ 5.9 mm, and has a length of 11 mm in the z-dimension, and is centered at $z = 0$ mm for ease of construction of the sample structure which must be placed at the centre of the airbox. Despite being termed an "airbox", this part of model space remains vacuum filled. The values for vacuum within HFSS are $\varepsilon = 1$, $\mu = 1$, $\sigma = 0\,\mathrm{Sm}^{-1}$, and is lossless, having $\varepsilon_i/\varepsilon_r = \mu_i/\mu_r = 0$.

The sample is then drawn by creating a box that has dimensions relating to that of the aluminium, 5.9 mm $\times$ 5.9 mm $\times$ 40 nm. The default material assignment for any 3-D object that is created is vacuum, so once the box has been drawn the material library must be entered and aluminium selected. The aluminium has a conductivity, $\sigma = 3.8 \times 10^7 \mathrm{Sm}^{-1}$, relative permeability, $\mu = 1.000021$. Due to the high conductivity of the metal the SIA is used and the relative permittivity of the metal is not considered, so $\varepsilon_i/\varepsilon_r = \mu_i/\mu_r = 0$. Next the structure that is etched into the aluminum must be drawn. This is achieved by first drawing a box that is assigned as aluminium, from which a large central section is removed, leaving an aluminium frame. Within this frame a smaller aluminium box is drawn, therefore creating an aluminium layer with a slit close to each edge of the layer. At this point the slit is continuous around the aluminium, so further boxes are drawn to act as connecting wires, and these are then united to the existing structure. Next the "cuts" must be included in the structure. This process is simplified by the use of some drawing tools, which give several options for drawing

complex structures. A polyline allows an initial point to be specified, then vectors are drawn to subsequent user-defined points, allowing any shape to be drawn. When the point entered is the same as the initial point, the vectors are joined to produce a 2-D object. The "sweep" tool can then be used to extend this object into a 3-D form along a specified vector. This is the method used for drawing a single "cut" along one edge of the metal layer. Once the single cut has been drawn, it may be duplicated around the origin at the centre of the structure. In this way, the slit and cut can be duplicated around this this axis by specifying a 90° rotation with a total of four objects remaining (see *Figure* 4.5).

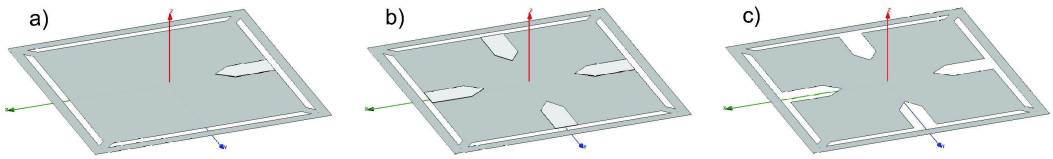

Figure 4.5: The process of making cuts in the structure in the model. a) A single cut shape is drawn using a polyline tool. b) The cut shape is duplicated around a central axis. c) The cut shapes are subtracted from the existing aluminium layer.

Once the metal structure is complete a dielectric layer is also assigned. This is placed on the back face of the metal replicating the experimental arrangement and has a relative permittivity $\varepsilon = 2.96$ and a dielectric loss tangent $\delta = 0.02$. At this stage the metal and dielectric layers have a dual material assignment, with the vacuum filling the entire model space including the volume where structures have been introduced. Therefore when metal is removed in order to form the structure, vacuum remains in its place. Once the structure has been completely formed the subtract tool may be used again, but this time using an additional clone tool. This results in an area identical to the metal structure being removed from the airbox, while the metal layer itself remains unaffected. (This means that if the metal layer were now to be removed from the model space, the airbox would now display an area of non-model space of the metal layer dimensions). The model space layout is displayed in *Figure* 4.6 with dimensions and axes indicated.

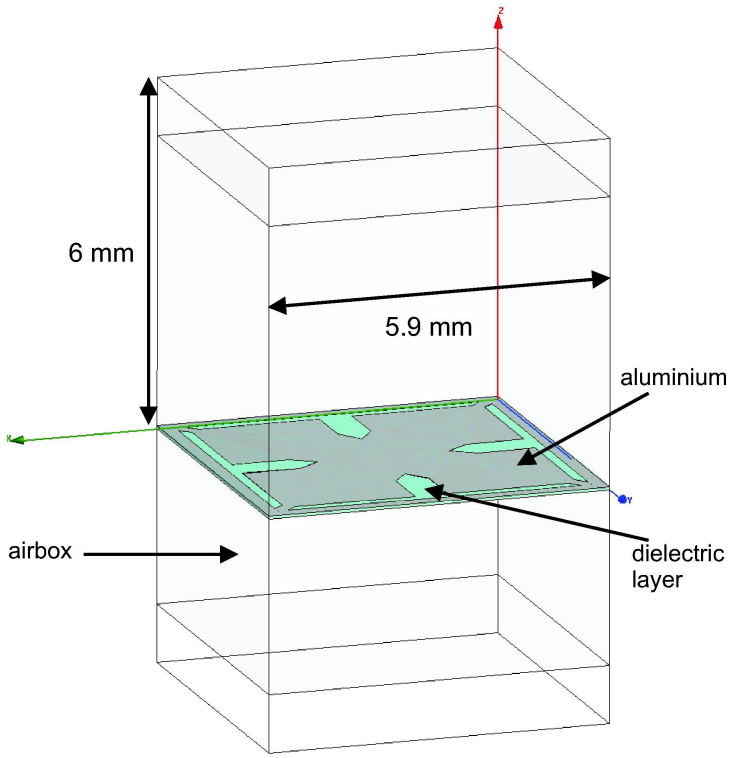

Figure 4.6: A schematic of the model space for the structure investigated in *Chapter* 5.

Once the model structure has been created, an incident beam is assigned. This is defined as propagating down the z-axis, with the electric vector polarised parallel to the x-axis. Next, the model boundaries must be applied. The entrance and exit faces at the top and bottom of the model in the xy-plane are assigned as radiation boundaries. If the model needed to consider non-normal incident radiation then PMLs would have to be considered, but this is not the case here. The vertical sides of the model are assigned as master-slave boundaries, with one pair in opposing sides in the xz-plane, and the other pair in opposing sides in the yz-plane. The airbox is drawn so that the top and bottom 1 mm exist as separate objects (see *Figure* 4.6). This ensures that when a mesh is generated no tetrahedra cross this boundary. It is at these boundaries that the evaluation planes are assigned over which the response of the structure will be determined.

The mesh is created at a frequency of 26 GHz (as initial scans reveal a transmission feature close to this frequency) and the range studied is $18 < f < 45$ GHz in 0.5 GHz steps, mimicking the range which is investigated experimentally and over which features are observed. The adaptive pass method alone is used to refine the mesh, with the final mesh of around 30,000 tetrahedra found to be satisfactory, with additional tetrahedra not significantly changing the model output. Further meshes are generated at specific frequencies 27.5 GHz and 42.5 GHz of higher resolution, having ∼120,000 and ∼125,000 tetrahedra respectively. This is done at frequencies corresponding to transmission peaks in both the data and the model, and is for

the purpose of achieving higher resolution field plots in order to understand the nature of the transmission.

Figure 4.7 displays a comparison of data with the model described above. It is clear that the prediction provided by HFSS is a good fit to the data, with significant features occurring in both plots at 27.5 GHz and 42.5 GHz.

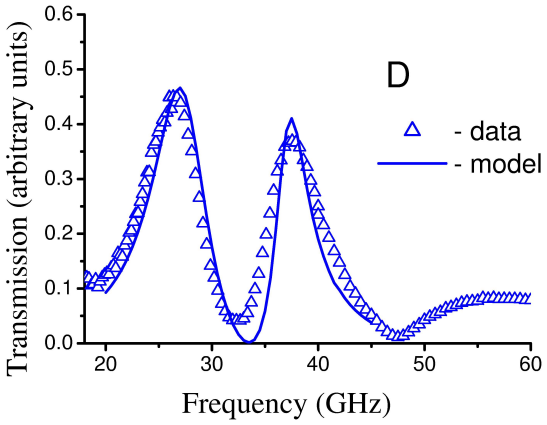

Figure 4.7: An example of the prediction provided by HFSS compared with the data taken for sample D in *Chapter* 5.

Figure 4.8 displays an example of a field plot generated by HFSS. The plot is generated by drawing a plane through the centre of the unit cell in the yz-plane, and then selecting to plot the magnetic vector across this plane at a chosen frequency at a phase corresponding to maximum field enhancement. This plot is made at a frequency of 42.5 GHz, corresponding to a peak in transmission. Once an initial plot is generated, it is possible to vary the maximum and minimum field strengths indicated by the key, in order to produce a colour-contrast that allows field maxima and minima to be easily identified. It is also possible to change the way the arrows are displayed, by varying arrowhead size or density, or by adding arrow tails in order to improve the clarity of the plot. Using plots such as this it is possible to gain insight into the interaction of fields with the structure, and thereby determine the nature of the resonant transmission.

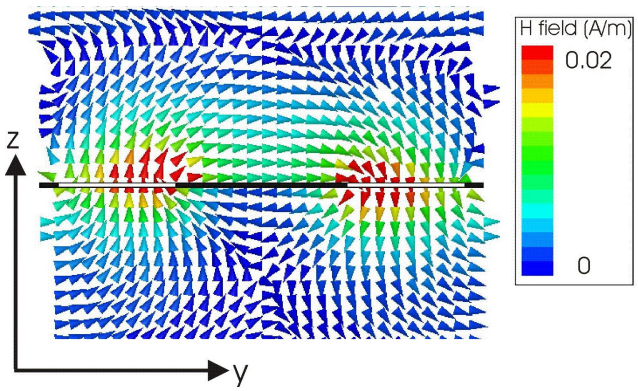

Figure 4.8: An example of a field plot generated by HFSS. The magnetic field vector is plotted through the centre of the unit cell in the yz-plane.

4.4.2 LC filled single slit

In *Chapter* 6 the microwave permittivities of LCs and PDLCs are determined by confining them within a single subwavelength slit, and analysing the transmission through the slit. The slit is formed from two glass blocks, measuring 60 mm × 60 mm ×20 mm, each of which has had ∼200 nm of aluminium evaporated onto each face. This is done in order to achieve a much smoother surface on the inside of the slit than would be possible with a solid metal block, the metal layer on the glass being thick enough to ensure no radiation penetrates through it. One of the large faces of each of the blocks is then coated with a polyimide aligning layer, which is then baked and unidirectionally rubbed. The blocks are then assembled together spaced by 50 μm Mylar spacers at each end to form a slit with the aligning layers on the inside, and fixed with a strong glue. The slit is then capillary filled with LC in its nematic phase, and allowed to cool so that the LC aligns homogeneously. Wires are then attached to each block in order to apply a voltage across the slit, which causes the LC to realign homeotropically with the applied field. Transmission through the slit is observed in both off- (0 V) and on-states (15 V), and is mediated by Fabry-Perot type resonances.

The model for this structure is constructed by first drawing an airbox of dimensions 10 mm × 0.1 mm ×28 mm. Within this airbox the sample is drawn, consisting of two aluminium blocks located centrally in the z-dimension. Each block measures 4.975 mm× 0.1 mm ×20 mm, and they are located on the x-axis such that a 50 μm slit is positioned centrally in that dimension. Both the x- and y-dimensions of the blocks are reduced by the appropriate choice of boundary conditions, however the z-dimension clearly cannot be reduced, as this length determines the frequency of transmission of the slit. The aluminium has identical parameters as that described in the previous section. Boundaries are assigned such that the xz-plane faces are assigned as Perfect H boundaries, meaning that the slit is considered as infinitely long in the y-direction. All other boundaries are assigned as radiation boundaries in the

incident half space, and impedance boundaries in the transmission half space. Evaluation planes are assigned in the same way as in the above section, and an excitation is assigned to be normally incident, propagating in the -z-direction, and polarised parallel to the x-axis (perpendicular to the slit). As the frequency range investigated experimentally is relatively large, three separate meshes are generated at 20, 40, and 60 GHz. Each of these is refined by the adaptive pass method, up to a total of approximately 25,000 tetrahedra. Each mesh generation has a frequency sweep associated with it, these are $20 < f < 40$ GHz, $40 < f < 60$ GHz and $60 < f < 80$ GHz respectively, each in 0.5 GHz steps. The model is displayed in *Figure* 4.9.

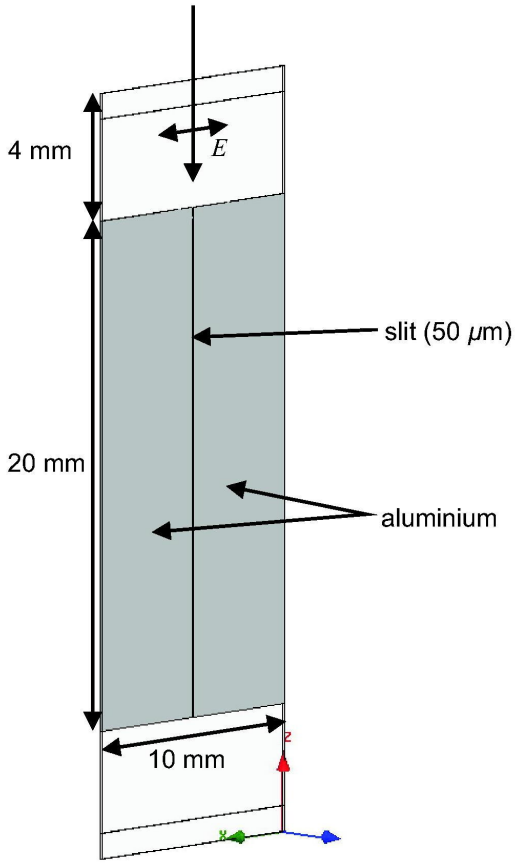

Figure 4.9: The model used to replicate the single slit filled with LC in *Chapter* 6.

Figure 4.10 displays a comparison of data with the model described above. The HFSS prediction provides a good fit to the three observed peaks in transmission occurring at approximately 41.5 GHz, 46 GHz and 51 GHz.

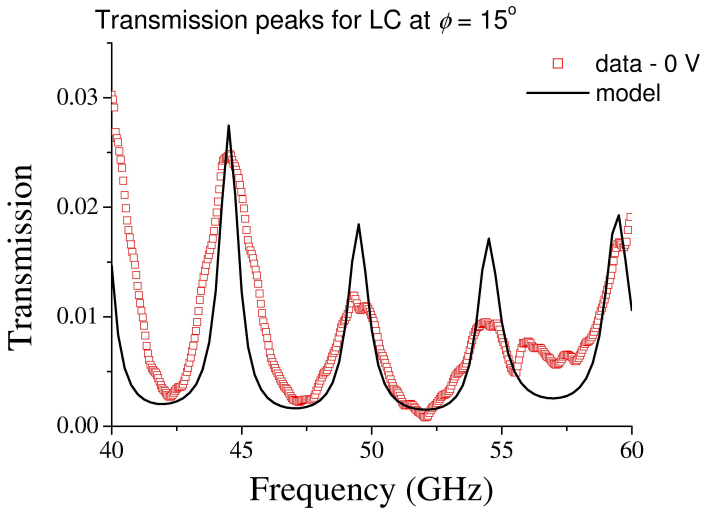

Figure 4.10: An example of the comparison of data with the prediction provided by HFSS for the LC-filled single slit discussed in *Chapter* 6.

Figure 4.11 shows an example of a field plot generated by HFSS. It is generated by plotting the magnitude of the electric vector across the yz-plane through the centre of the unit cell at a phase corresponding to maximum field enhancement. The plot is made a at frequency corresponding to one of the transmission peaks observed in the data. Again, it is possible to change the appearance of the plot by varying the maximum and minimum of the field strengths indicated by the key, and by changing the arrow size and density. In this plot, arrows with tails have been used for the sake of clarity. This plot then allows insight into the mediating transmission mechanism of the structure.

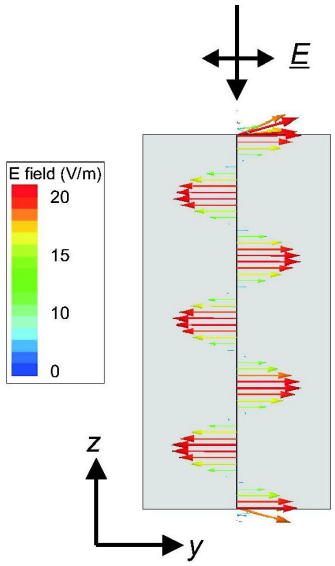

Figure 4.11: An example of a field plot generated by HFSS. The electric field vector is plotted through the centre of the unit cell in the yz-plane.

4.4.3 Penny array

Chapter 7 discusses the absorption of microwave radiation by arrays of metallic discs or "pennies" separated from a metal substrate by a thin dielectric layer. Two sample types are investigated, the first consists of a thick aluminium substrate 300 mm × 300 mm × 30 mm, covered with a 50 μm dielectric layer. On top of this layer an array of pennies is assembled, with each penny having a diameter of ∼5.75 mm and thickness of 1 mm. Three array arrangements are investigated for this sample. The second sample consists of a copper-clad dielectric circuitboard (CRB) that has copper removed from one of the layers to produce an array of pennies. The CRB dimensions are 100 μm of polyester sheet clad by 18 μm of copper above and below. The penny array etched into the top layer has a pitch of 6.25 mm, with each penny having a radius of ∼2.95 mm. A schematic of the CRB penny array structure is shown in *Figure* 4.12.

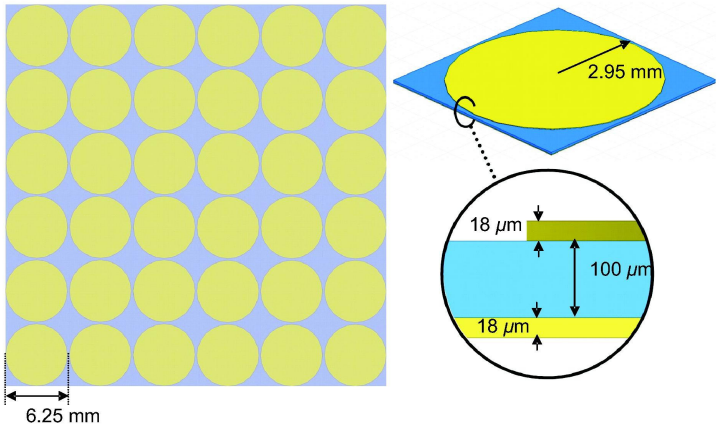

Figure 4.12: The structure investigated in *Chapter* 7. (left) A top-down view of a section of the array. (right) A single penny and the copper-clad dielectric structure.

The model is constructed in a similar way to those previously described. Objects are drawn of the appropriate dimensions in order to replicate the unit cell of the structure, and materials are assigned. The copper has a conductivity, $\sigma = 5.8 \times 10^7 \mathrm{Sm}^{-1}$, relative permeability, $\mu = 0.999991$, $\mu_i/\mu_r = 0$, and the polyester sheet has a relative permittivity $\varepsilon = 3.2$ and a dielectric loss tangent $\delta = 0.003$. The boundary assignment is that of master-slave boundaries on each xz- and yz-plane face, with the top xy-plane face being assigned a PML. A major difference between this model and those previously described is that in this case the model is being solved for absorption rather than transmission. This does not greatly change the model set-up, boundary assignment remains almost the same, with the only difference being that no boundary assignment is required on the bottom xy-plane face of the airbox, as no radiation should penetrate the continuous metal layer above it. This also means that the sample structure is drawn such that it lies at the base of the airbox, as opposed to being placed

centrally within it in the z dimension. In previous transmission models, the evaluation planes have been drawn both above and below the structure in order to evaluate the transmission. For this model however, two evaluation planes are drawn *at the same position* above the structure, and in this way one can be used to evaluate the incident field, and the other to determine the reflected field, and from this the absorption due to the structure can be determined. The experimental study was undertaken at a polar angle of $\theta \approx 15°$, and therefore the excitation is assigned to have the same angle (hence the use of a PML as opposed to a radiation boundary on the top xy-plane face). The mesh is generated at a frequency of 25 GHz, with ~70,000 tetrahedra used at the end of the adaptive pass method, and a frequency sweep is taken over the range $20 < f < 28$ GHz in 0.2 GHz steps, agreeing well with data. The model for the thin penny array in *Chapter* 7 is shown in *Figure* 4.13.

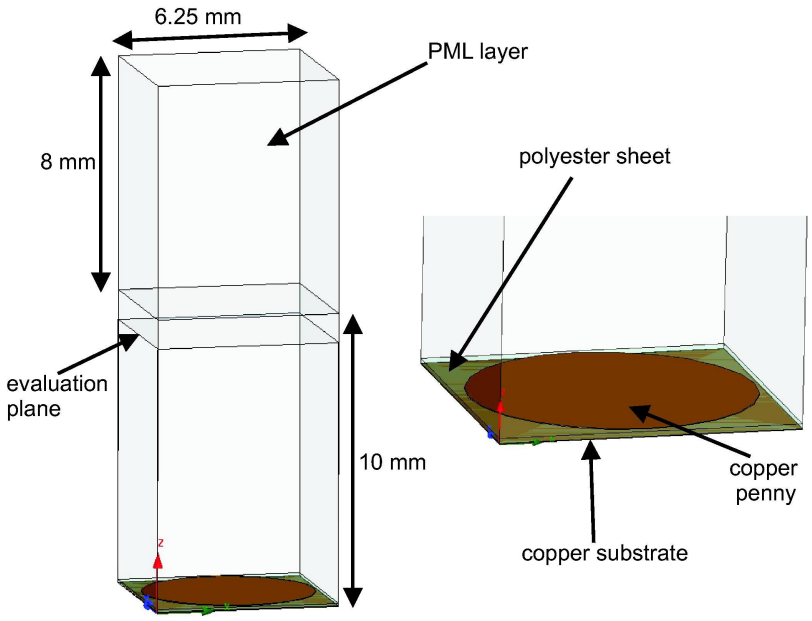

Figure 4.13: A schematic of the model used to replicate the thin penny array sample from *Chapter* 7.

Figure 4.14 shows a comparison of data with the prediction provided by the HFSS model described above. The model displays good agreement with the data, and therefore the field plots generated at the resonant frequency may be assumed to be a good representation of the fields occurring due to the structure.

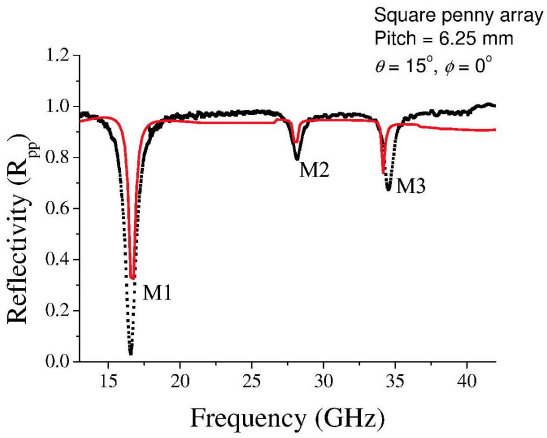

Figure 4.14: An example of the comparison of data with the prediction provided by HFSS for the CRB penny array from *Chapter* 7.

Figure 4.15 shows an example of field plots provided by HFSS. The time-averaged electric (left) and magnetic (right) field magnitudes are plotted across the xy-plane in the dielectric layer at a frequency of ∼16.5 GHz. Each plot has the field maximum and minimum indicated in the key selected so as to highlight peaks in the field magnitudes. These plots then allow insight into the nature of the resonant absorption observed in the data.

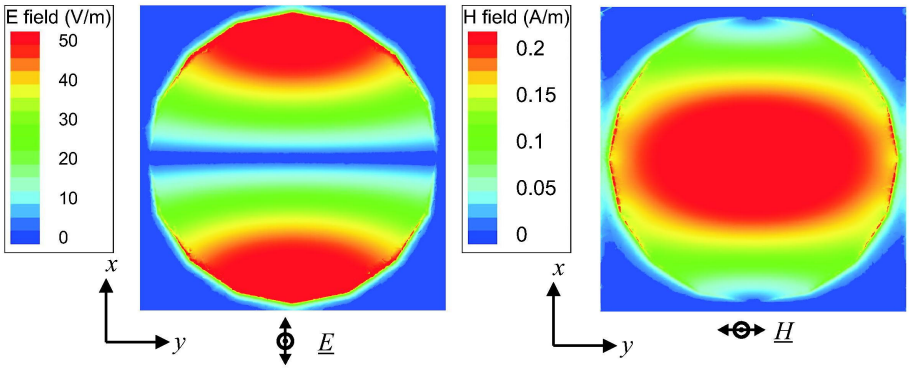

Figure 4.15: An example of the field plots generated by HFSS. (left) The time-averaged electric field magnitude plotted across the xy-plane in the dielectric layer. (right) The time-averaged magnetic field plotted at the same point.

4.4.4 A large LC cell

In *Chapter* 8 the absorption response of a series of samples is investigated. These samples are based on a similar metal-dielectric-metal structure to that of the penny array in the previous section, however these samples have LC as their dielectric layer in order to introduce a degree of tuneability to them. The model investigated in this section replicates sample T, a slit array. The sample consists of two 300 mm × 300 mm × 1 mm glass sheets, each of which has ∼200

nm of aluminium evaporated onto one side. A slit array is wet-etched into the metalised side of one of these sheets, and they are then arranged into an LC cell. This involves the metalised side of each sheet being coated with an aligning layer, which is then baked and uni-directionally rubbed. The sheets are then assembled into a cell, spaced by glass microspheres and capillary filled with LC in its isotropic phase. Once the cell is filled, wires are attached to the metalised side of the sheets so that a voltage may be applied across the LC layer. The LC molecules align homogeneously with the aligning layer with no voltage applied, and realign homeotropically on the application of a voltage.

The model replicates the structure described above, and gives a prediction for the absorption due to the structure. However, it is found that the model absorption response is largely unchanged by the presence of the glass layer, so this is excluded from the model construction. Therefore the model consists of a 200 nm thick continuous metal layer at the base of the airbox, followed by a 25 μm polyimide layer, a 100 μm LC layer, a second polyimide layer, and the top metal layer. The polyimide layer is assigned from HFSS's material library and has dielectric properties $\varepsilon = 3.5$ and $\delta = 0.008$, however the LC assignment cannot be made in this way as there is no LC in the library, and therefore a new material must be added. This is achieved simply by entering the LC permittivity and absorption (dielectric loss tangent), which are taken as $\varepsilon = 2.70$ and $\delta = 0.05$ for the homogeneous state, and $\varepsilon = 2.98$ and $\delta = 0.05$ for the homeotropic state. In order to model both off- and on-states, two separate models are run to replicate the properties of the LC in either alignment.

Once again, the model space is reduced to the minimum necessary to replicate the structure, and therefore the x-dimension is the pitch of the array, 5.85 mm, and the yz-plane faces are assigned as master-slave boundaries in order to produce an infinite slit array in the x-direction. The y-dimension of the model space is 0.1 mm, as there is no periodicity along the slit length. This also means that Perfect H boundaries may be used as opposed to master-slave boundaries, reducing the required model resolution. The choice of a 0.1 mm y-dimension is somewhat arbitrary, but is small enough to greatly reduce the required model resolution and running time so that reliable results may be achieved relatively swiftly.

The evaluation planes and excitation are assigned in the normal way, with the incident radiation having a polar angle, $\theta = 10°$. At this angle it is sufficient to assign the top xy-plane face as a radiation boundary (a PML assignment does not improve the model accuracy). The mesh is generated at a frequency of 16 GHz, and using the adaptive pass method a total of $\sim$30,000 tetrahedra is used to give sufficient accuracy. A frequency sweep of $12 < f < 18$ GHz in 0.1 GHz steps is set, and correctly predicts the structure response for both homogeneous and homeotropic LC alignments. A schematic of the model structure is displayed in *Figure* 4.16.

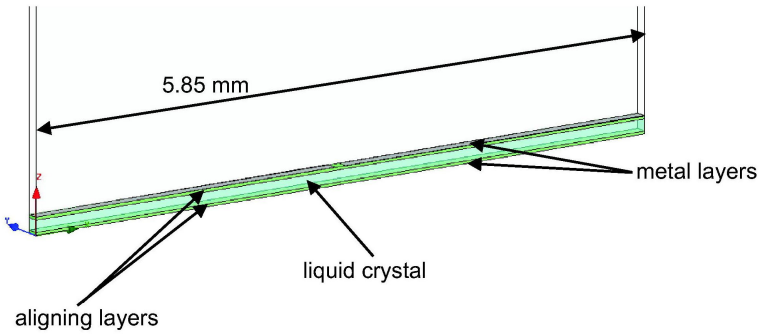

Figure 4.16: A schematic of the model used to replicate the slit array sample from *Chapter* 8.

Figure 4.17 shows a comparison of data with the model described above. Data are compared with a prediction from HFSS for both homogeneous (off-state) and homeotropic (on-state) LC alignments, and good agreement is shown for the frequency of resonant absorption and breadth of resonance. The discrepancy in the depth of the modes is due to sample size and variability.

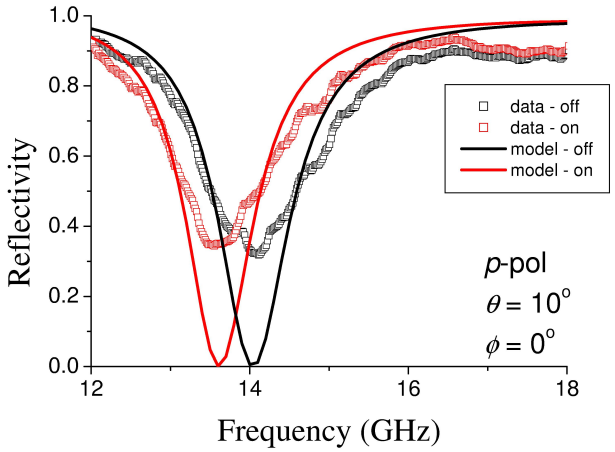

Figure 4.17: An example of the comparison of data with the prediction provided by HFSS for the slit array from *Chapter* 8.

Figure 4.18 shows an example of a field plot provided by HFSS. The plot shown is the time-averaged electric field magnitude, plotted through the centre if the unit cell in the xz-plane at a frequency of 14 GHz, corresponding to the reflectivity minima in the homogeneous (off-state) alignment. *Figure* 4.18a shows the unit cell, and *Figure* 4.18b is a close-up view of the same plot. As in previous cases, the field maximum and minimum shown on the key are chosen so as to illustrate the peaks in field magnitude. The red regions indicating the highest

field magnitude are located on opposing sides of the slit opening, allowing the absorption mechanism to be determined.

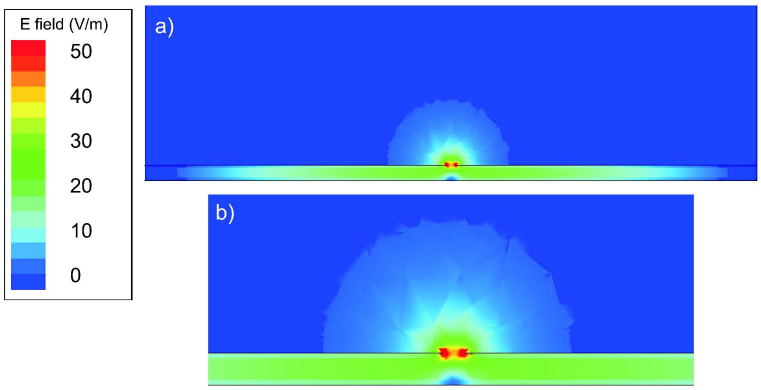

Figure 4.18: An example of a field plot generated by HFSS. The time-averaged electric field magnitude is plotted across the centre of the xz-plane.

In order to demonstrate the importance of the correct convergence, *Figure* 4.19 displays three HFSS predictions given with different resolution meshes taken from the model described above. The resonance being modelled is that of the homeotropically (on-state) aligned LC-filled slit array. The three predictions displayed are produced from meshes of approximately 60,000, 28,000 and 6,000 tetrahedra; denoted models A, B and C respectively. Model B was the one used in *Figure* 4.17 above. It is clear that the predictions generated by model A and B are virtually identical, however model A takes considerably longer to solve, more than double the time taken by model B. Model C solves in a much shorter time than model B, but does not give an identical prediction, and therefore the resolution is deemed to be insufficient. The correct mesh resolution should solve in the shortest time possible, whilst giving a virtually indistinguishable prediction to that of a higher resolution mesh.

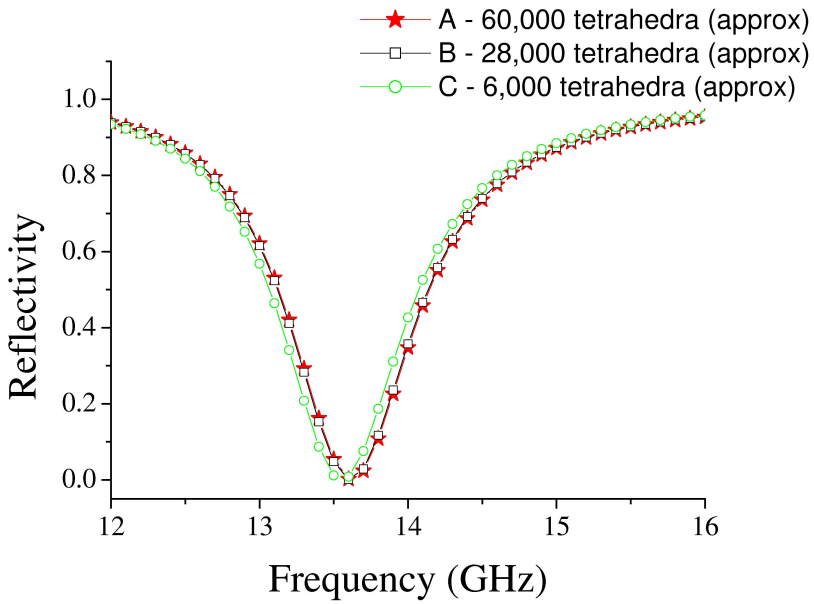

Figure 4.19: Three HFSS predictions for the same resonance generated using different mesh resolutions.

4.5 Summary

In this chapter an overview of Ansoft's High Frequency Structure Simulator (HFSS) has been presented. The FEM has been explained, and the method by which models within HFSS are constructed has been introduced, with reference to drawing of models, assignment of boundaries and excitations, and mesh generation. Solutions are also discussed in terms of frequency dependent reflection and transmission response, and electromagnetic field plots at given frequencies over user-defined planes. Finally, a selection of models from the later chapters in this thesis are discussed in greater depth.

Chapter 5

Microwave transmission via a patterned metal film

5.1 Introduction

In *Chapter* 2 the transmission of electromagnetic radiation by an array of subwavelength slits in metal was introduced. The transmission of radiation through both deep and shallow slit arrays has been extensively studied by others, initally in the optical regime, and later in longer wavelength regimes such as the infared and microwave. Transmission through such slit arrays has been shown to occur when the incident radiation has a component of its electric vector polarised perpendicular to the slit direction [28]. Transmission can occur due to both coupled SPPs, primarily in shallow slit arrays, and cavity modes, primarily in deep slit arrays. The frequency at which resonant transmission occurs depends on structure dimensions, such as pitch, slit depth and slit width.

In this chapter a novel form of slit array will be investigated where slits within the array are modified by the addition of a perpendicular cut, resulting in the following distinctions from arrays previously studied. Firstly, transmission occurs via slits that lie *parallel* to the incident electric vector polarisation, and secondly, the frequency of resonant transmission is shown to depend primarily on the dimensions of the cut. All the arrays presented in this chapter are fabricated from a metal film which is considerably thinner than the skin depth of the metal at the operating frequency. A metal layer that is less than the skin depth might erroneously be imagined to readily transmit even if it were continuous, however it will also be shown that the metal is indeed thick enough to screen all microwave transmission other than that which occurs due to the structure cut into the metal.

5.2 Background

Initial studies on subwavelength slit arrays were undertaken to gain an insight into the extraordinary transmission of subwavelength hole arrays demonstrated by *Ebbesen et al* (1998) [29], however, the transmission of slits and holes was later discovered to be mediated by differ-

ent mechanisms. The intention was that the investigation of a simplified 1-D slit array might give insight in the phenomenon of the 2-D hole array transmission. *Schroter et al* (1998) [30] modelled a 1-D slit array in silver at optical frequencies in order to gain an insight into the hole transmission mechanism, demonstrating that surface plasmons aided the coupling of radiation from incident to exit surfaces, therefore enhancing transmission, at least for slits. *Porto et al* (1999) [28] investigated transmission through slit arrays in more depth, recognising that they are somewhat different to hole arrays. They investigated slit arrays in gold, and discovered two different classes of mode. The lowest frequency mode was shown to be due to surface plasmons coupled between the top and bottom surfaces of the metal. Higher frequency modes were found to be cavity resonances of the slit. These cavity resonances resembled the eigenmodes of a Fabry-Perot interferometer, although with different boundary conditions. Further investigation of resonant fields within the slit was carried out by *Astilean et al* (2000) [31] in the optical and infared regime, and also the effect of altering slit width on the resonant frequency of the grating was noted. It was observed that a decrease in slit width caused an increase in the effective index of the slit cavity. *Collin et al* (2002) [32] further studied the resonant fields both within the slit, and on the surface of the grating.

Transmission through slit arrays in the microwave regime was investigated by *Went et al* (2000) [33], using an array of aluminium slats 3 mm $\times$ 64.7 mm $\times$ 600 mm separated by 500 μm dielectric spacers. A series of resonant peaks were shown, the same in nature as the cavity modes observed by *Porto et al* (1999) [28]. This geometry was extended into a 2-D array by *Hibbins et al* (2000) [34], where strong transmission was observed for both polarisations at normal incidence. In many of these structures, cavity modes within deep slits are discussed as Fabry-Perot type modes. Indeed, modes investigated later in this chapter will be shown to be analogous to Fabry-Perot type modes, despite occurring in a thin metal of only $\sim$40 nm thickness.

5.2.1 The Fabry-Perot interferometer

The Fabry-Perot interferometer can be a good analogy to a deep single slit or slit array, and the Fabry-Perot equation can give good predictions of the resonant frequencies of such structures.

A Fabry-Perot interferometer may be considered in an idealised form as consisting of two parallel aligned perfectly reflecting mirrors with a dielectric core, here a vacuum, inbetween. As the mirrors are perfectly reflecting, it is not possible to couple into the system, however, it is possible to predict the eigenmodes of the system, and therefore its resonant frequencies, which are dependent on the separation of the mirrors, d. As the boundary conditions of the system require the tangential component of the electric field to reduce to zero at the mirror surface as it is a perfect metal mirror, and the photon direction of motion must be perpendicular to the mirror surface, only a tangential magnetic field is present at the mirror surface. This means that there must be a null in the electric field at the boundary walls, and therefore the fundamental mode of the system has an electric field null at each wall, and one field maximum at the central point between boundary walls (*Figure* 5.1). The resonant wavelength of the system is therefore simply twice the separation between the walls. Higher order modes can

exist, with the mode number equalling the number of field maxima between boundary walls. Therefore the wavelength of the modes of the system are given by:

$$\lambda_N = \frac{2d}{N}$$

where N is the resonant mode number. From this the resonant frequency and wavevector of the Fabry-Perot interferometer is simply:

Frequency: $f_N = \frac{cN}{2D}$

Wavevector: $k_N = \frac{\pi N}{d}$

where c is the speed of light.

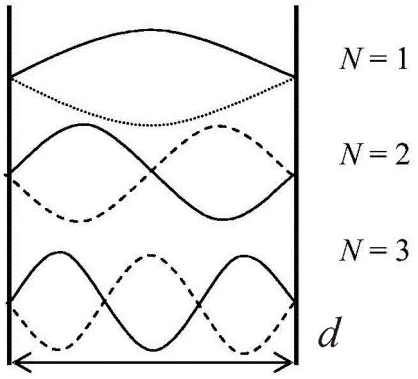

Figure 5.1: The first three resonant Fabry-Perot modes that exist between two ideal metal mirrors separated by a distance d.

A single slit in metal or a slit array is a good approximation to the Fabry-Perot resonator, however, the boundary conditions of the system are quite different. In a single slit the entrance and exit of the slit behave as the mirrors due to the impedance mismatch between the slit cavity and free space. In this case as the "walls" of the cavity are now the slit exit, the boundary conditions are altered substantially, with the electric field being maximum at the slit entrance and exit. The fundamental resonance now has one node in electric field, with higher order modes having additional nodes. It may be noted that in principal a “zeroth-order” mode is also available, being a mode that has no nodes in electric field through the depth of the slit. This mode would be analogous to the slit behaving as a parallel plate capacitor, *Figure* 5.2.

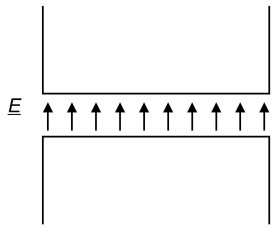

Figure 5.2: The zeroth-order mode in the "single slit in metal" analogy to the Fabry-Perot interferometer.

5.2.2 The single slit geometry

Takakura et al (2001) [35] modelled the response of a single slit in a perfect metal in the infared regime when the slit has a depth greater than $\frac{\lambda}{2}$. The single slit was shown to be analogous to a Fabry-Perot interferometer, and that photons polarised with their electric vector perpendicular to the subwavelength slit may resonate between the open ends of the slit. Photons polarised with their electric vector parallel to the slit direction are reflected. Slit width was found to play an important part in the resonant frequency, as when the slit was widened end effects become more important and the resonant frequency would drop. *Takakura* gives the shift in resonant wavelength of the following form:

$$\frac{\lambda_{shift}}{\lambda_{FP}} = \frac{2(\frac{w_s}{d})[\ln(\frac{\pi w}{\lambda_{FP}}) - \frac{3}{2}]}{2(\frac{w_s}{d})[\ln(\frac{\pi w}{\lambda_{FP}}) - \frac{1}{2}] - \pi}$$

where λ_{shift} is the shift in the resonant wavelength, λ_{FP} is the resonant wavelength, determined by the slit depth, $w_s$is the slit width and d is the slit depth.

Takakura assumed the metal to be a perfect conductor, which may be an oversimplification in the infared, and is certainly not the case at optical frequencies, but is often assumed at microwave frequencies meaning that the predictions made should be applicable to microwaves. However, *Suckling et al* (2004) [36] showed that even at microwave frequencies the finite conductance of metal influences the transmission through a single slit. In the *Takakura* model, the resonant frequency of the single slit continues to rise as slit width is reduced. However, *Suckling* investigated the single slit experimentally, and found that below a slit width of ~70 μm the resonant frequency began to reduce dramatically. Additionally, at slit widths above ~100 μm the *Takakura* model predicts a reduction in resonant frequency greater than that observed experimentally. HFSS model data agreed well with experimental data, *Figure* 5.3. This unequivocally proves the *Takakura* model to be incorrect.

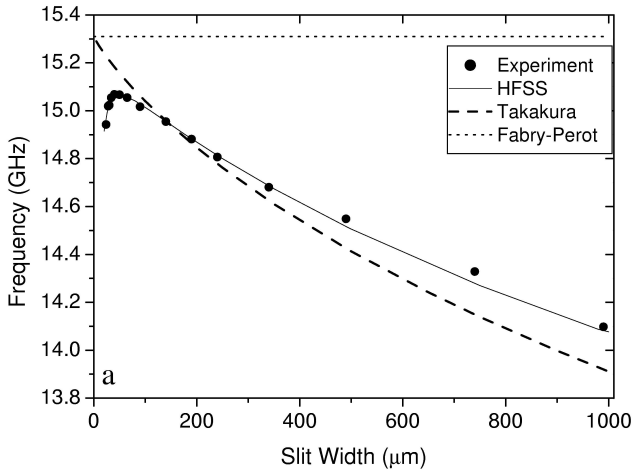

Figure 5.3: Graph displaying frequency plotted against slit width for an $N = 2$ Fabry-Perot mode. Predictions from the Fabry-Perot equation, Takakura's equation and HFSS are shown along with experimental data.

Here the down turn at low slit widths is due to the field matching conditions at the walls leading to a small but significant imaginary k-vector perpendicular to the slits. This in turn leads to a reduced k_{total} and hence a reduced frequency. Therefore the reduction in resonant frequency at low slit widths is entirely due to the finite conductivity of the metal. This is perhaps surprising as metals at microwave frequencies are often assumed to be perfect conductors. This assumption is made due to the relative lengths of skin depth and wavelength. In the optical regime, the ratio of skin depth to wavelength may be 20:1, whereas in the microwave regime the skin depth is of the order of ∼400 nm, with a wavelength of 5 mm, a ratio of 12500:1. This large ratio allows the approximation of perfect conductivity as such a small portion of the wavelength penetrates the metal. However, it is clear from the above result that in certain cases the finite conductivity of metal at microwave frequencies can play an important role.

5.2.3 A zeroth-order Fabry-Perot mode

It has been shown that deep slit arrays or single slits in metal display transmission mediated by Fabry-Perot type modes when the incident radiation is polarised with its electric vector perpendicular to the slit direction, whereas radiation polarised with its electric vector parallel to the slit direction is reflected. However, *Suckling et al* (2004) [36] demonstrated transmission of radiation polarised with its electric vector parallel to a single slit in a thick metal plate by making a series of cuts perpendicular to the slit. The samples consisted of two thick metal plates (∼20 mm) which had a series of perpendicular cuts made into them. These plates were then brought together, and spaced by a dielectric spacer (∼50 μm). The three samples investigated are shown in *Figure* 5.4.

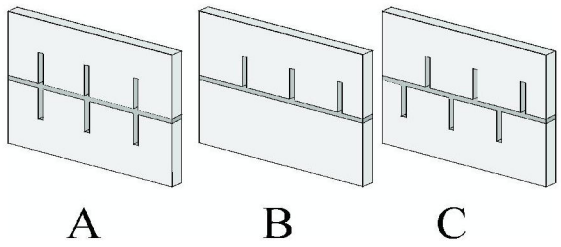

Figure 5.4: Samples investigated by *Suckling et al* [36] to excite a zeroth-order Fabry-Perot mode.

The addition of these perpendicular cuts allowed the excitation of a mode termed a "zeroth-order" Fabry-Perot mode. It was termed as such because there were no nodes observed through the depth of the slit, and it was shown that the resonant frequency of the zeroth order mode is almost entirely independent of slit depth. *Figure* 5.5 shows how the $N = 0$, 1, 2, 3, 4, 5 and 6 Fabry-Perot modes depend on slit depth. The frequency of the zeroth-order mode remains largely unchanged above a depth of $\sim$1 mm.

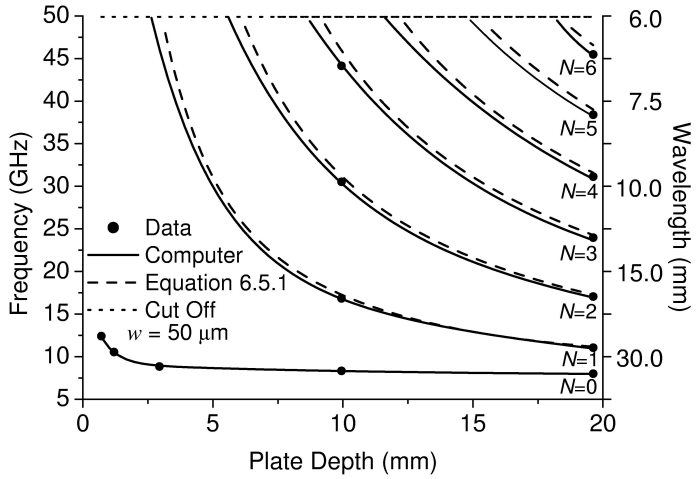

Figure 5.5: Graph showing that the zeroth-order Fabry-Perot mode is largely independent of plate depth as compared to higher order modes.

The existence of the zeroth-order Fabry-Perot mode was shown to be due to the behaviour of surface currents. Partial current loops are created around the cuts causing an inductive region, whilst an induced electric vector across the slit creates a capacitive region. These

capacitive and inductive parts were then described by an equivalent circuit theory to give an analytical form for the zeroth order mode, which is as follows:

$$f = \left[\frac{w_s \left(p - w_c\right)}{2\pi^2 D d w_c \varepsilon_0 \left(p^2 - l_c^2 + w_c^2 - 2pw_c\right)} \right]$$

where w_s is slit width, w_c is cut width, d is cut depth, p is the separation between cuts, l_c is the offset between cuts on either side of the slit and D is a constant of proportionality.

This equation contains no term for the slit depth. As the zeroth-order mode is largely independent of slit depth, it may therefore be possible to excite a similar mode on a slit array in thin metal film. Higher order Fabry-Perot modes shift to increasingly higher frequencies as slit depth is reduced, for example the $N = 1$ mode is constrained to having one half wavelength across the slit depth. The zeroth order mode does not have this constraint, and therefore may be accessible with very thin metal.

5.2.4 Skin depth

It was stated above that the skin depth of metals at microwave frequencies may be ~400 nm. The skin depth of electric fields into a metal is evaluated only from the metal properties, and in the microwave regime frequencies are sufficiently low for the Drude model to be a good approximation. The skin depth of a metal, δ at microwave frequencies is given by:

$$\delta = \frac{c}{\omega}\sqrt{\frac{2}{\varepsilon_i}}$$

The imaginary part of the permittivity, ε_i can be expressed in terms of the conductivity, σ from the Drude model, $\varepsilon_i = \frac{\sigma}{\varepsilon_o \omega}$. Substituting for ε_i and c gives:

$$\delta = \sqrt{\frac{2}{\mu_o \sigma \omega}}$$

This equation only holds when $\omega \ll \gamma$, where γ is the damping constant with $\gamma = \frac{1}{\tau}$ where τ is the mean scattering time for electrons. Given that for a metal at room temperature $\gamma \approx 1.97 \times 10^{14}\,\mathrm{s}^{-1}$, and taking the conductivity of aluminium as $\sigma = 3.8 \times 10^7\,\mathrm{Sm}^{-1}$ gives a skin depth of approximately 400 nm at a wavelength of ~7.5 mm. It is clear from the above equation that as the wavelength changes linearly with frequency and the skin depth changes as the square root of frequency, the ratio of skin depth to wavelength is much larger at low frequencies. However it will also be clear from the data displayed later in this chapter that a metal layer of thickness ~40 nm, which is much less than δ, is thick enough to screen all microwave transmission to below our noise level of detection. This is due to the very large impedance mismatch between air, which has a relative permittivity of $\varepsilon \approx 1$, and the metal which has a relative permittivity of $\varepsilon \approx 10^7$ at these frequencies.

5.3 The samples

The samples consist of four slit arrays in a thin aluminium film (∼40 nm) backed by a dielectric layer (100 μm). The arrays are all cut into the metal film using a wet-etch technique. Initially the array design is drawn out as an A1 (841 mm × 594 mm) pattern in CorelDraw 12. This pattern is then printed and used to produce a mask that is reduced in size by a factor of 6. This is to ensure a high degree of accuracy in the mask dimensions. The aluminium film is coated with a positive photoresist layer, and this is then exposed through the mask in a UV light box. The photoresist is then developed, and the film is then placed in an aluminium etchant. The dielectric layer prevents the aluminium being etched from the back. The four samples will henceforth be termed A, B, C and D. *Figure* 5.6 shows the unit cells of the structures. Structure A is a simple 2-D slit array. It has a pitch of 6.62 mm, with a slit width of 0.26 mm. The slits are terminated by a connecting "wire" located centrally between the points where the two orthogonal slit directions cross. These "wires" are 0.26 mm in width. The purpose of these wires are to provide electrical contacts as will become clear in *Chapter* 8, where similar structures are investigated in reflection. The unit cell of structure B consists of a square patch of metal perforated by four slits close to the edge of the patch, and is also shown in *Figure* 5.6. The unit cell has dimensions 5.9 mm × 5.9 mm with the slit located 0.24 mm from the edge of the unit cell. Each slit is terminated in the where the slits would otherwise cross by a connecting wire of thickness 0.18 mm at 45° to the slit direction. Structures C and D have the same unit cell but with an additional cut directed centrally from each slit and of differing lengths between the two structures, illustrated by the dashed lines in *Figure* 5.6. The cut for structure C has a width of 0.57 mm and extends 0.43 mm towards the centre of the unit cell, tapering to a point over a further 0.40 mm. For structure D, the cut again has the same cut width, but extends 0.99 mm towards the centre of the unit cell, again tapering to a point over a further 0.40 mm. The cuts have a tapered shape so that they may extend as close to the centre of the unit cell as possible without needing to have their shape modified. For the purpose of the work presented here, the cuts extend no further that 0.99 mm towards the centre of the unit cell.

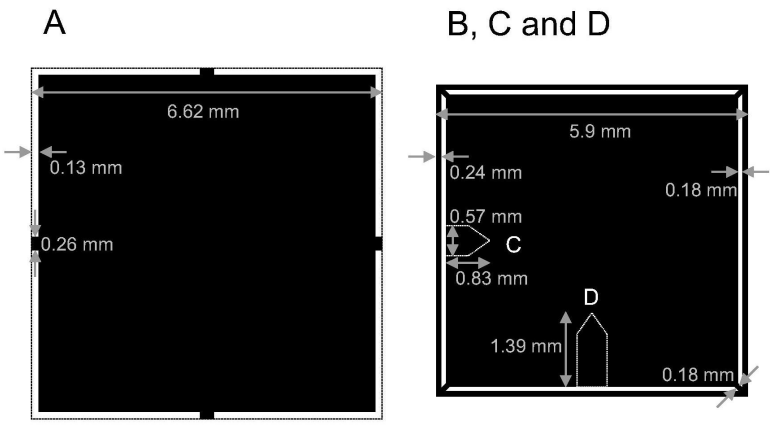

Figure 5.6: The unit cells of the structures. A is shown on the left, and B on the right, with the dashed lines illustrating the additional cuts to be made in structures C and D.

Figure 5.7 shows each of the four structures with 9 unit cells formed into an array. The final samples have some 450 unit cells formed into arrays measuring approximately 105 mm × 150 mm, and each array is surrounded with a border of continuous metal of ∼20 mm on each side.

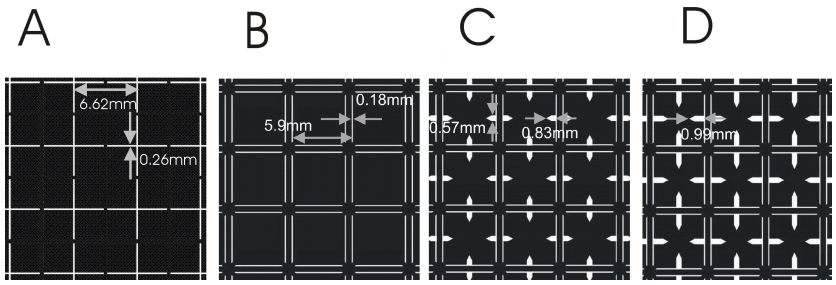

Figure 5.7: The four structures under investigation each with 9 unit cells being formed into an array.

5.4 Transmission experiments

Transmission spectra are obtained over the range 18 GHz $< f_o <$ 60 GHz by placing samples between matched microwave source and detector horns, with each horn 500 mm away from the sample. *Figure* 5.8 displays the experimental apparatus in a similar set up, but using spherical mirrors in order to give planar wavefronts. Incident radiation may otherwise be reduced to a well-collimated central part by an aperture formed from microwave absorbing material with dimensions 100 mm × 120 mm. Data is normalised to transmission through the same aperture

with the sample removed. The experimental set-up is not identical to the model in that the model assumes a totally planar wave front, whereas experimentally the wave fronts will be somewhat curved. However, it will be shown that the model still gives excellent agreement with the transmission data from these structures. The mounts for the source and detector horns are wooden to reduce the possibility of stray reflections interfering with the experiment.

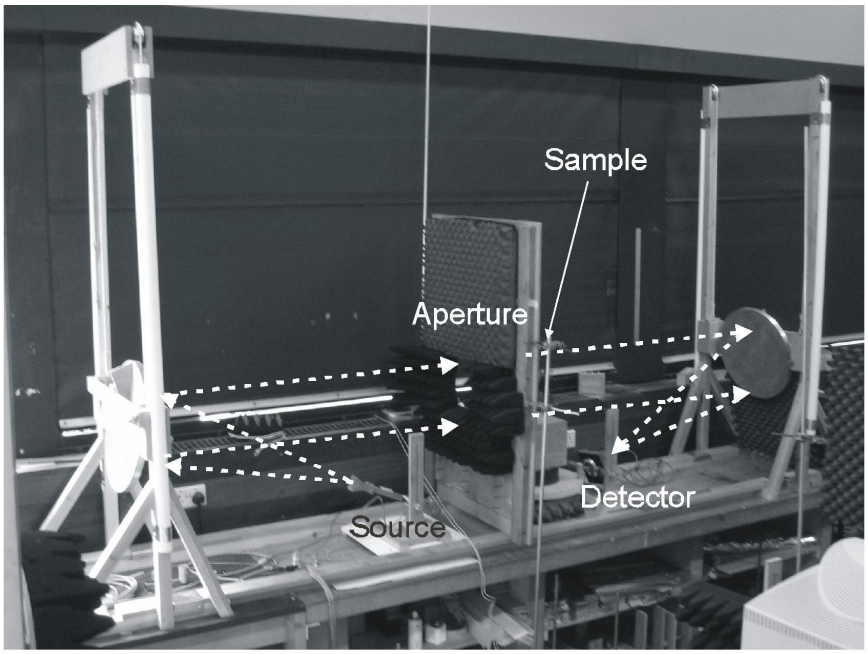

Figure 5.8: The experimental apparatus used for the investigation.

The microwave source is a Hewlett-Packard 8350B sweep oscillator together with an 83550A plug-in which generates a microwave signal between 8 and 20 GHz (15.00 and 37.48 mm). Three separate Agilent millimetre wave source modules are used as frequency multipliers, each of which has an associated high gain microwave horn attached. The three source modules and horns cover the ranges 18 to 26.5 GHz, 26.5 to 40 GHz and 40 to 60 GHz. A matched horn is used for each range as the detector. Two Agilent 82505C detector adapters are used to amplify both the main transmitted signal and a reference signal, with the reference being taken as a direct feed from the source. These signals are sent to a Hewlett Packard 8757D scalar network analyzer. The transmitted and reference signal together allow the evaluation of a normalised signal. Each frequency range is split into 401 frequency steps, and can then be output as a .dat file to be read in any standard spreadsheet software. The .dat file contains information on frequency, azimuthal angle, ϕ, and intensity.

5.5 Modelling

The computer modelling package used to give predictions to compare with the experimental data has already been discussed in depth in *Chapter* 4. However, the specific models used to match data for the four samples studied will now be briefly discussed. The unit cell of each model is based on the dimensions described above, with the metal and dielectric layers lying in the xy-plane. Models consist of an aluminium layer of 40 nm thickness, backed by a dielectric layer of thickness 100 μm, and for each model the metal layer has sections removed from it equivalent to the structure under investigation. The material parameters are taken from the model library such that the aluminium has a conductivity, $\sigma = 3.8 \times 10^7 \mathrm{Sm}^{-1}$, and relative permeability $\mu = 1.000021$. A surface impedance approximation is used (discussed further in *Chapter* 4) as the conductivity is so high, and therefore the relative permittivity is ignored. The dielectric layer has a permittivity of $\varepsilon = 2.96 + 0.003i$. A vacuum-filled volume extends above and below the metal-dielectric layer, extending 10 mm in the z-direction in total. The model space has a mesh injected into it consisting of approximately 40,000 tetrahedra, and a plane wave is injected from the upper half space of the model, i.e. propagating in the -z direction. Once the mesh has been inserted, a frequency sweep is run from 18 GHz to 50 GHz in 0.5 GHz steps. Transmission, reflection and absorption predictions can then be exported to provide the expected electromagnetic response of each structure.

5.6 Results and discussion

To investigate the transmissive properties of the structures described above, the transmission spectra from each structure will be discussed and compared to theory provided from the FEM model. Field plots from HFSS will then provide insight into the transmission mechanism of each structure. Figures 5.9-5.12 show transmission spectra from the four structures, A, B, C and D. Figure 5.9 shows transmission from sample A, the 2-D slit array. (The pitch of the array is 6.62 mm, and the slit width is 0.26 mm, there is also a connecting wire across each slit that has a width of 0.26 mm.) The sample is illuminated with radiation at normal incidence and has its electric field orthogonal to one of the slit directions. Data are shown as open circles, and the prediction from the FEM model as a solid line.

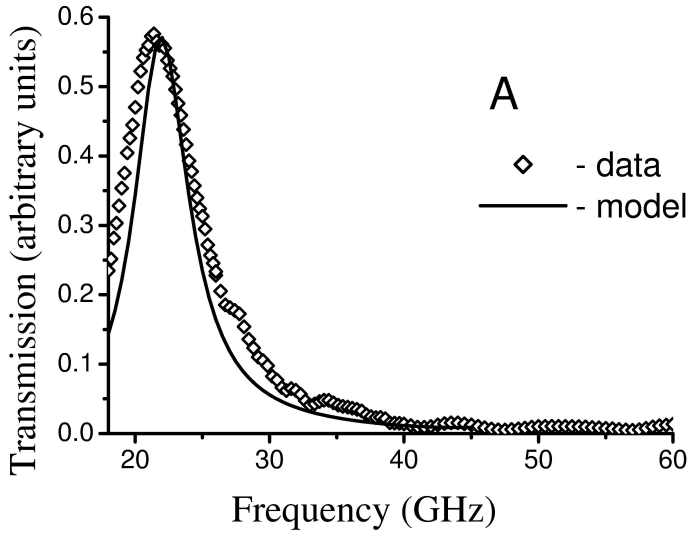

Figure 5.9: Experimental data plotted against HFSS prediction for transmission from structure A, the 2-D slit array. Incident radiation is normally incident and polarised with its electric field orthogonal to one of the slit directions.

Resonant transmission is observed as a single peak in the transmission at ∼21.5 GHz, and good agreement is shown with model predictions. The resonant wavelength of the structure, ∼13.95 mm, is close to twice the pitch of the structure, 13.24 mm, and therefore is clearly associated with the structure dimensions. There are no further peaks in transmission over the scanned frequency range.

Transmission spectra from structure B is shown in *Figure* 5.10. (Here the pitch is 5.9 mm with the slits of thickness 0.18 mm, and located 0.24 mm from the edge of the unit cell, see *Figure* 5.6.) The connecting wire is located at the point where slits cross, as opposed to being located centrally between crossing points, as in sample A.

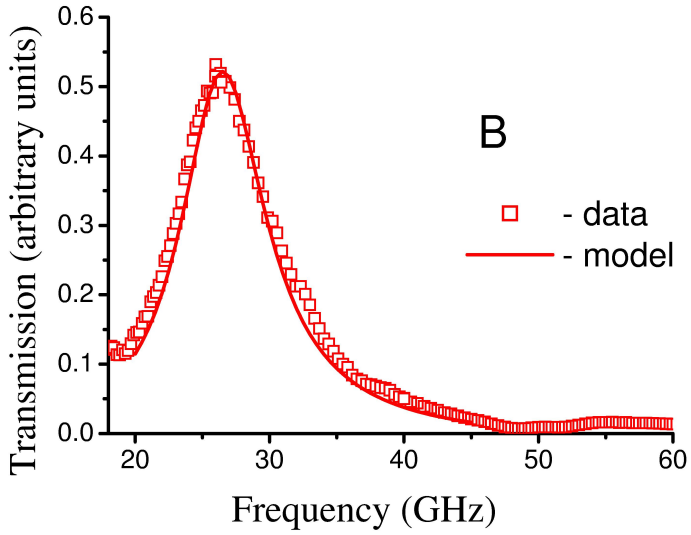

Figure 5.10: Experimental data plotted against HFSS prediction for transmission from structure B. Incident radiation is normally incident and polarised perpendicular to one set of slits.

Resonant transmission is observed as a single peak in transmission at ∼26.5 GHz. This sample is not simply a 2-D slit array, as slits are not located at the edge of the unit cell (see *Figure* 5.6). This means that while this structure has a single repeat period of 5.9 mm, within the unit cell slits are separated by 5.24 mm. This is illustrated in *Figure* 5.7 where the unit cells of each structure are shown in an array. The separation between adjacent slits is alternately 0.66 mm and 5.24 mm. The wavelength at which this structure transmits is ∼11.30 mm, so half the resonant wavelength, 5.65 mm, is almost midway between the two slit separations $\left(\frac{5.9+5.24}{2} = 5.57\text{mm}\right)$.

Figure 5.11 displays transmission from structure C. This structure has the same dimensions as the previous sample, with the addition of perpendicular cuts at the centre of each slit directed towards the centre of the unit cell. The cuts have a width of 0.57 mm, and extend 0.40 mm towards the centre of the unit cell, tapering to a point over a further 0.43 mm.

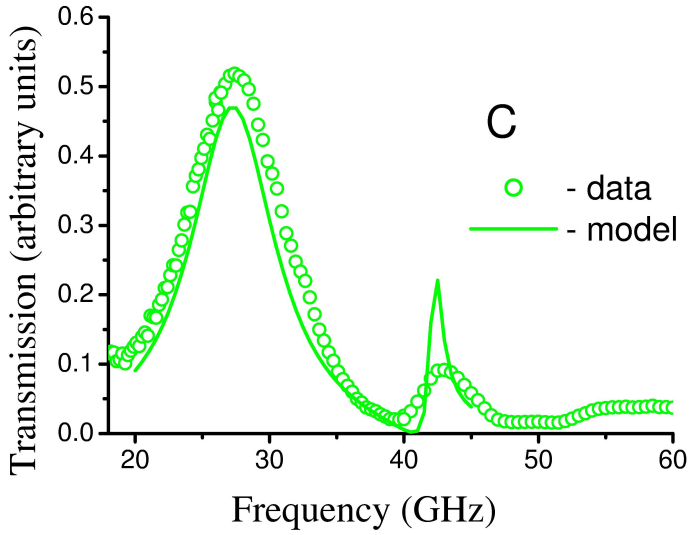

Figure 5.11: Experimental data plotted against HFSS prediction for transmission from structure C. Incident radiation is normally incident and polarised perpendicular to one set of slits.

As in sample B, we see resonant transmission at ∼26.5 GHz. In addition, a secondary mode is observed at 43 GHz, which corresponds to a wavelength of 6.97 mm. It is not immediately apparent that this wavelength is associated with any structural dimensions. Additionally, transmission due to the secondary mode is only ∼1/5 of the peak intensity of the primary mode, and as this mode did not exist for the previous sample and the only difference between the two structures is the presence of the cuts, the cuts are therefore indicated as being involved in the transmission mechanism for the secondary mode.

Transmission spectra from the final structure, D, is displayed in *Figure* 5.12. This structure is similar to that of C, but with the cuts having been elongated so that they now extend 0.99 mm from the slit towards the centre of the unit cell, tapering to a point over a further 0.40 mm. The cuts in structure D also have a width of 0.57 mm.

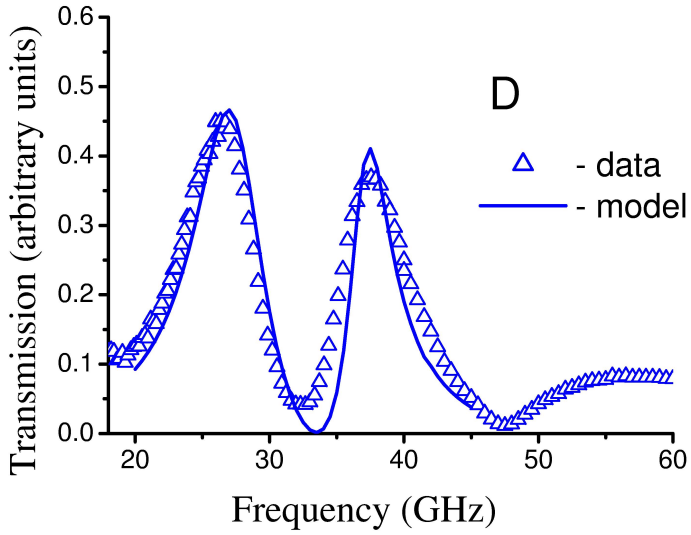

Figure 5.12: Experimental data plotted against HFSS prediction for transmission from structure D. Incident radiation is normally incident and polarised perpendicular to one set of slits.

As in structure C, two transmission modes are observed. One of these is the now familiar ~ 26.5 GHz mode, which was observed for structures B and C. The secondary mode observed here appears quite different to that seen in structure C. The resonant frequency of this mode is 37.5 GHz, and the mode has a transmission efficiency approaching that of the mode at 26.5 GHz. The wavelength associated with the resonant transmission of the secondary mode is 7.59 mm, which again does not correspond to any obvious structure dimensions. Once more the likely suspect for the cause of the second mode is the cuts. If the secondary modes in structures C and D both occur due to the cuts, then it would seem that changing the cut dimensions has a dramatic effect on both the coupling efficiency, and the resonant frequency of the secondary mode.

In order to gain further insight into the nature of these modes, field plots from the FEM model will be examined. For clarity, the primary modes observed in all structures will be termed Mode 1, and the secondary modes observed in structures C and D will be termed Mode 2. The field plots will clearly display that the secondary modes observed in structures C and D occur due to a similar transmission mechanism, therefore terming both modes as the same is justified. Firstly, the field plots for sample A will be investigated.

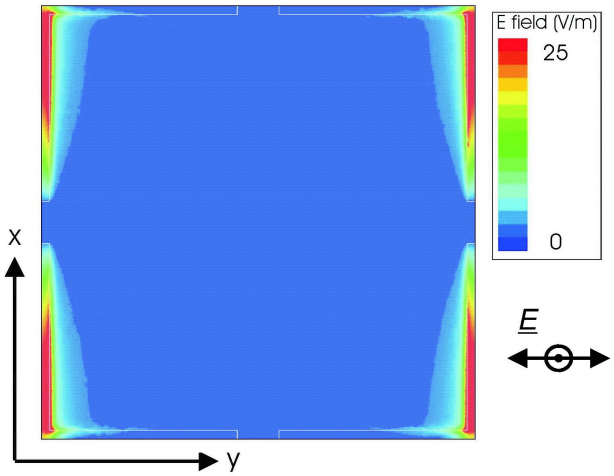

Figure 5.13: FEM field profile showing the time-averaged electric field magnitude in the xy-plane for Mode 1 in structure A. Incident radiation is polarised perpendicular to the x-axis.

Figure 5.13 shows the time-averaged magnitude of the electric field provided by the FEM model for Mode 1 in structure A. Field enhancement is indicated by shading as illustrated by the key. Fields are plotted in the xy-plane at a position 0.025 mm behind the back face of the structure. Fields located in the region of the slits that are perpendicular to the incident polarisation direction are enhanced by a factor of 25 as compared with the incident field. This field enhancement drops dramatically over the region of the metal links.

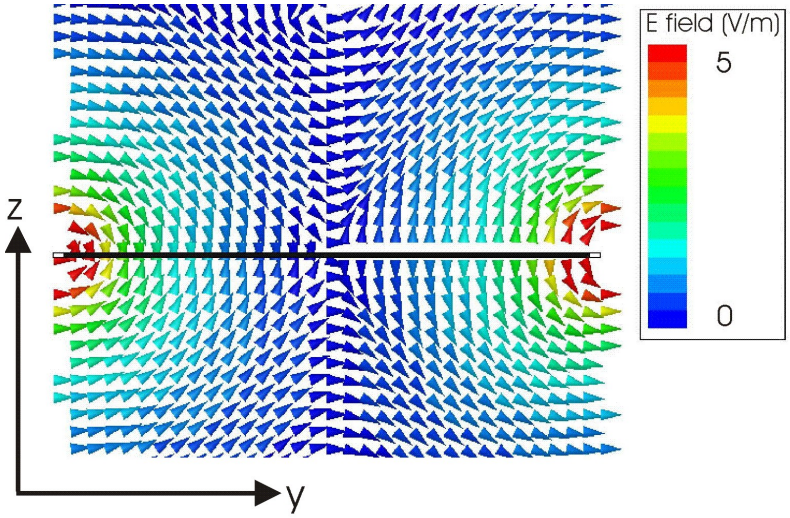

Figure 5.14: FEM field profile showing the electric vector in the yz-plane for Mode 1 in structure A at $x = 1.655$ mm.

Figure 5.14 shows the electric vector for Mode 1 in structure A plotted at a phase corresponding to maximum field enhancement. Fields are plotted in the yz-plane at a position $x = 1.655$ mm which is 1/4 of the pitch of the sample. Fields are at peak intensity over this plane as they drop to zero in the locality of the electrical contacts and are reduced at the point where slits cross (see *Figure* 5.13) Arrowheads indicate the direction of the electric vector and shading indicates field enhancement. The electric vector direction in the upper half-space indicates that the incident radiation has diffractively coupled to a surface wave, which has a wavelength corresponding to twice that of the slit array pitch. The surface wave is quantised along the distance between the slits, with a node at the centre, having maximum field located around each slit. A similar field profile is displayed in the lower half space. Electric fields are unable to penetrate the metal due to its high conductivity at these frequencies, and therefore couples through the gaps, increasing the field in the vicinity of the slit and exciting a surface wave on the back face of the metal. The surface wave on the back face is then diffracted by the slit array and matches to an outgoing propagating plane wave which has a wavelength equal to that of the surface wave. The presence of the dielectric layer on the back face causes the coupling efficiency of the front and back surfaces to be reduced, as it introduces a slight mismatch in the in-plane momentum of the respective surface waves. However, the effect is minimal as the dielectric layer is very thin compared to the extent of the fields away from the structure, which is several millimeters at these frequencies.

Next the fields for Mode 1 in structure B will be examined.

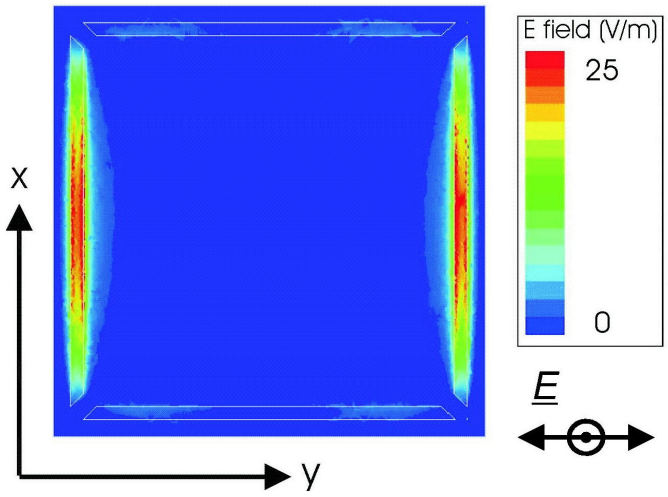

Figure 5.15: FEM field profile showing the time-averaged electric field magnitude in the xy-plane for Mode 1 in structure B. Incident radiation is polarised perpendicular to the x-axis.

Figure 5.15 shows the time-averaged electric field magnitude for Mode 1 in sample B. As for sample A, radiation is normally incident and is polarised perpendicular to the x-axis. The field strength and distribution is similar to that of structure A, however in this case the

reduction in field is located near the point of the crossing of slits (corners), as this is where the metallic link is located. Again the enhancement factor of the electric field is 25.

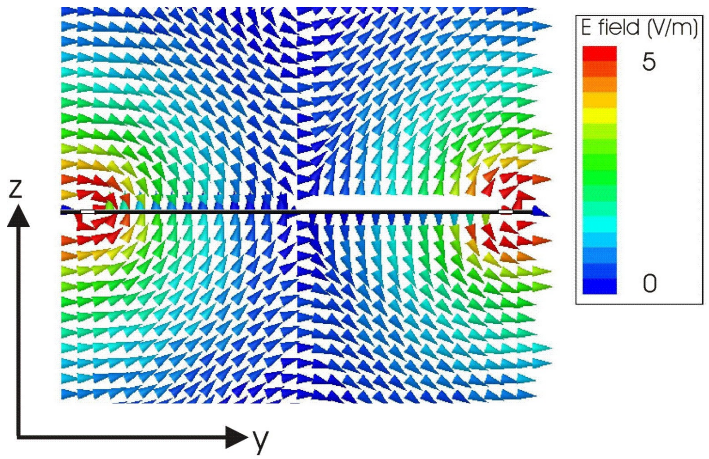

Figure 5.16: FEM field profile showing the electric vector in the yz-plane for Mode 1 in structure B at $x = 2.95$mm.

The electric vector for Mode 1 in structure B is plotted in *Figure* 5.16. Fields are enhanced by a factor of 5 times at maximum, and are plotted at a phase corresponding to this field enhancement. Fields are plotted in the yz-plane at a position $x = 2.95$ mm, i.e. through the centre of the model unit cell. The behaviour of the electric vector is very similar to that of mode 1 in structure A, indicating that incident radiation has diffractively coupled to a surface wave on the front face of the structure, and is then matched to a similar surface wave on the back surface. In *Figure* 5.15 the field enhancement appears to be largely confined to the vicinity of the slit, whereas in *Figure* 5.16 it can be seen that as the fields extend away from the slit an enhancement to the field is maintained over a wider area than just the slit vicinity. It was stated above that the resonant wavelength of this structure falls almost midway between the two slit separations that occur on the structure, and it is shown here the peak intensity occurs in this region, thereby confirming this mode is associated with structure dimensions.

It is reasonable to assume that the Mode 1 occurring in structures C and D is similar in nature to that occurring in structures A and B. In order to confirm this, the fields for Mode 1 in structures C and D will be briefly examined.

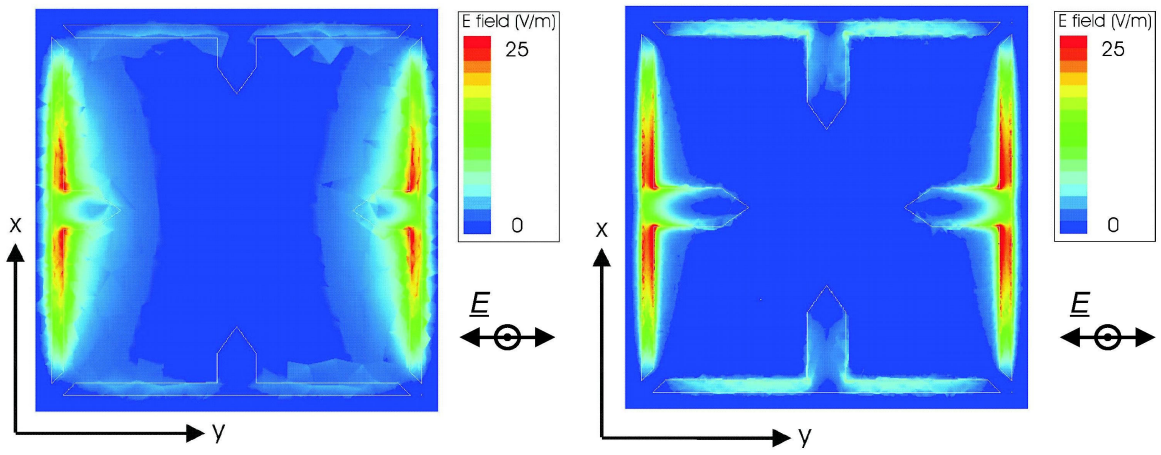

Figure 5.17: FEM field profile showing the time-averaged electric field magnitude in the xy-plane for Mode 1 in structures (a) C and (b) D. Incident radiation is polarised perpendicular to the x-axis.

Figure 5.17 shows the time-averaged electric field for Mode 1 in structures C and D at a phase corresponding to maximum field enhancement. Fields are plotted in the same way as for structure B. Once again, the field distribution is similar to that of the two previous samples A and B, however there is an additional perturbation to the field caused by the presence of the cuts. *Figure* 5.18 shows the electric vector at a position $x = 2.95$ mm, again revealing Mode 1 for these structure to be the same in nature as Mode 1 in samples A and B.

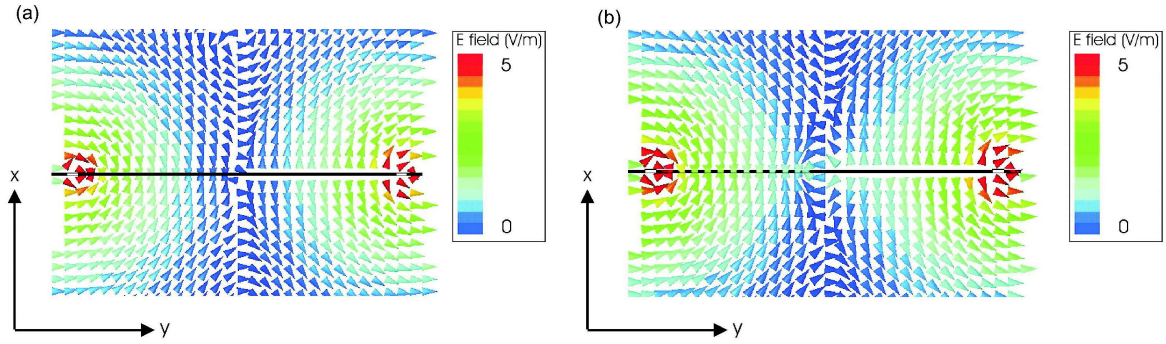

Figure 5.18: FEM field profile showing the electric vector in the yz-plane for Mode 1 in structures (a) C and (b) D at a position $x = 2.95$ mm.

Now the field plots arising from the FEM model for Mode 2 in structure C will be investigated, beginning with the time-averaged electric field. As with previous plots, radiation is normally incident with its electric vector polarised perpendicular to the x-axis.

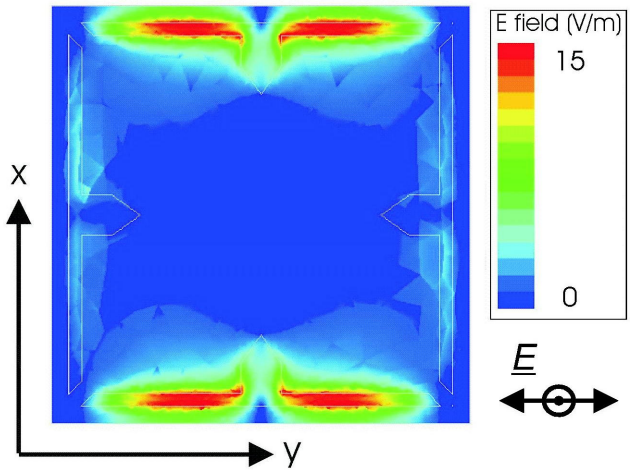

Figure 5.19: FEM field profile showing the time-averaged electric field magnitude in the xy-plane for Mode 2 in structure C. Incident radiation is polarised perpendicular to the x-axis, note that high fields are located in the slits lying parallel to the incident electric vector polarisation, rather than perpendicular as seen in Mode 1.

Figure 5.19 shows the time-averaged electric field magnitude for Mode 2 in sample C. Fields are plotted on the xy-plane at a distance 0.025 mm behind the back face of the metal. Resonant fields are enhanced by a factor of 15 as compared with the incident field, however, fields are enhanced in the slits that lie *parallel* to the polarisation direction, whereas the slits that lie perpendicular to the polarisation direction display negligible field enhancement. This is unexpected as transmission via a 2-D slit array is usually due to diffractive coupling to slits orthogonal to the polarisation direction, as has been already seen in this, and previous samples. In a 1-D slit array when there is no component of the electric vector orthogonal to the slit direction there is no coupling, and therefore no transmission. This structure is modified from a 2-D slit array by the addition of the centrally directed perpendicular cuts. This therefore implies that coupling to Mode 2 is facilitated by the presence of the cuts. In order to further understand how this occurs, we must examine other aspects of the field profile.

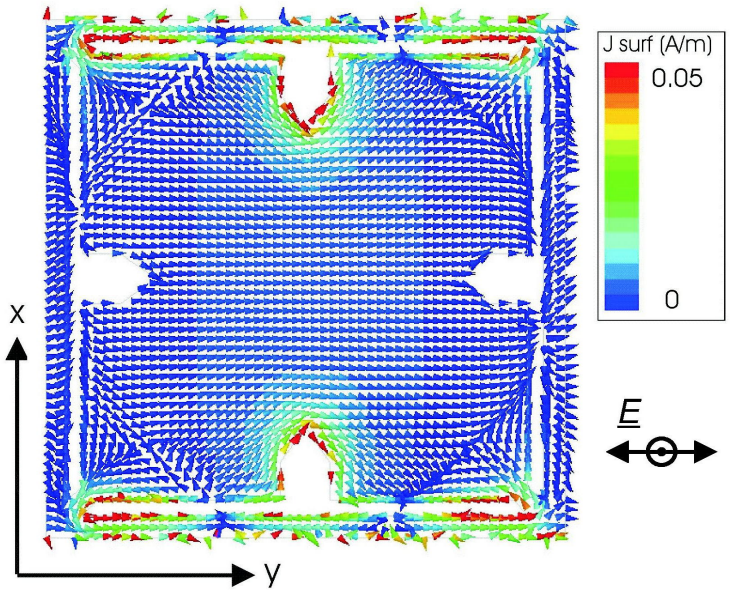

Figure 5.20: FEM field profile for surface currents on the metal layer, plotted at a phase corresponding to maximum enhancement for Mode 2 in structure C.

Figure 5.20 shows the surface current vector on the metal layer at a phase corresponding to maximum field enhancement for Mode 2 on structure C. Over most of the structure the surface currents are aligned with the polarisation direction of the electric vector, as expected. However, in the locality of the cuts, there is a perturbation in the surface current field. The width of the cut is such that the current flows around the cut, causing an enhancement in the current strength around the cut, producing partial current loops. This only occurs around those cuts that are made on the slits that lie parallel to the incident electric vector polarisation.

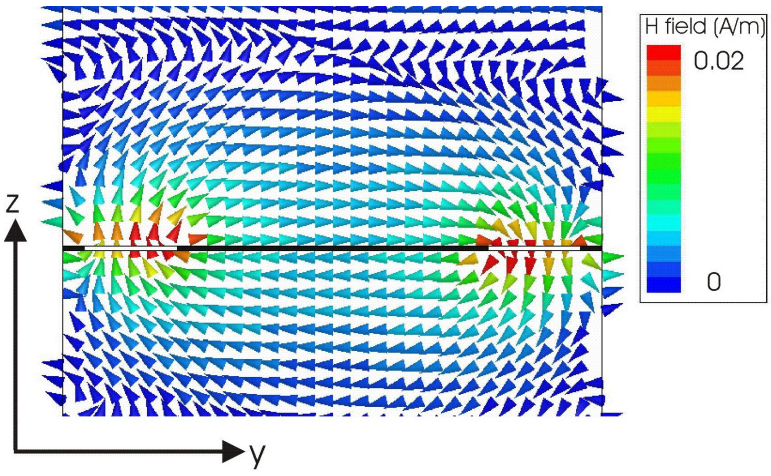

Figure 5.21: FEM field profile showing the magnetic vector direction in the yz-plane for Mode 2 in structure C.

Figure 5.21 shows the magnetic vector in the yz-plane through the centre of the unit cell, and at a phase corresponding to maximum field enhancement for mode 3 in structure C. The partial current loops produced by the surface current behaviour around the cuts effects an inductance, shown here by the magnetic field looping through adjacent cuts.

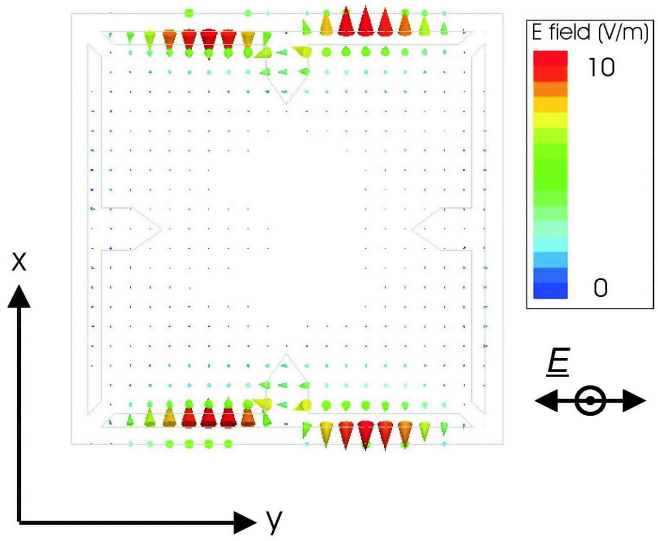

Figure 5.22: The electric vector in the xy-plane provided by the FEM model for Mode 2 in structure C. Fields are plotted at a phase corresponding to maximum enhancement.

Additionally, the behaviour of the surface currents causes the incident electric vector to undergo a 90° rotation in order to satisfy the boundary conditions across the slit. The perturbation of the surface currents by the cut causes the density of charge on opposite sides of the slit to be of opposite sign, inducing an electric vector orthogonal to the slit, resembling capacitive behaviour.

Therefore Mode 2 observed in structure C exists as a result of surface current behaviour, with the cuts behaving as inductive elements, and the slit behaving as a capacitive element, confirming this mode to be analogous to a zeroth-order Fabry-Perot mode. This is the first observation of such a mode in an array of slits in a thin metal film. The field enhancement is greatest in the slits lying parallel to the polarisation direction as the cuts extending from these slits cause a much greater perturbation to the surface current flow than those cuts extending from slits perpendicular to the polarisation. *Figures* 5.11 and 5.12 show that the secondary modes from structures C and D have different resonant frequencies and different transmissivities. Therefore the field plots for Mode 2 in structure D will be examined to confirm that it is indeed the same in nature as Mode 2 in structure C.

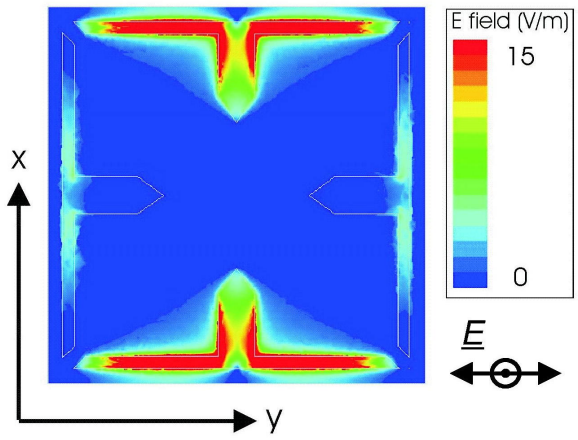

Figure 5.23: FEM field profile showing the time-averaged electric field magnitude in the xy-plane for Mode 2 in structure D. Incident radiation is polarised perpendicular to the x-axis.

The time-averaged electric field for Mode 2 in structure D is shown in *Figure* 5.23. Fields are plotted on the same scale as that of structure C, indicating that the field enhancement within the slit is much greater for structure D than for structure C. As in structure C the field enhancement occurs in those slits lying *parallel* to the polarisation direction.

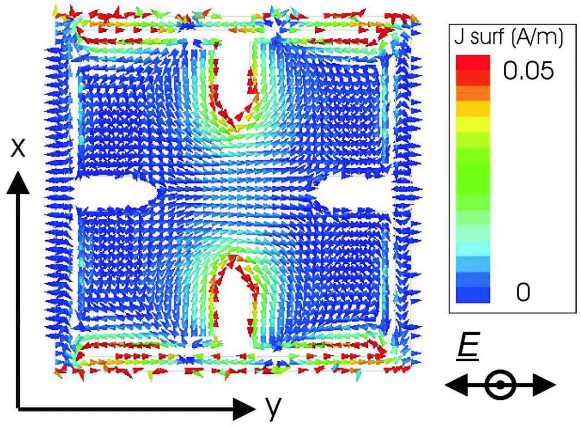

Figure 5.24: FEM field profile for surface currents on the metal layer, plotted at a phase corresponding to maximum enhancement for Mode 2 in structure D.

Figure 5.24 shows the surface currents on the metal layer for sample D. As in sample C the surface currents loop around the cuts that protrude from the slits that lie parallel to the polarisation direction. However, as the cuts are larger for sample D, the perturbation to the

surface currents is greater, causing the magnetic field loops induced by the partial current loops to be further enhanced than for sample C, leading to an increase in the inductive character of the structure, as shown in *Figure* 5.25.

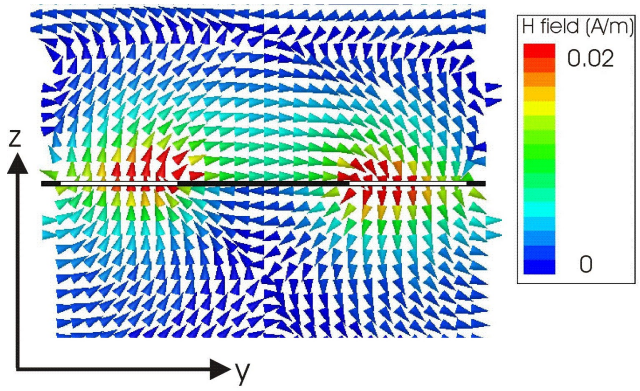

Figure 5.25: FEM field profile showing the magnetic vector direction in the yz-plane for Mode 2 in structure D.

The increased perturbation in the surface current field also leads to the electric field magnitude perpendicular to the slit to be increased. Therefore there is an additional increase in the capacitive part of the structure, as displayed in *Figure* 5.26.

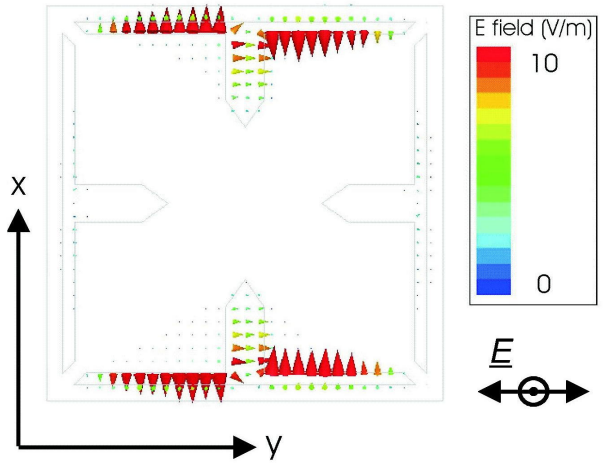

Figure 5.26: The electric vector in the xy-plane provided by the FEM model for Mode 2 in structure D. Fields are plotted at a phase corresponding to maximum enhancement.

Therefore Mode 2 observed in structure D is indeed the same in nature as that observed in structure C, and both are in effect zeroth-order Fabry-Perot modes. It is also clear that

changing the cut dimensions has a dramatic effect on the resonant frequency and the coupling efficiency of this mode. It is the combination of the inductive and capacitive parts of the structure that determine the resonant frequency, therefore a change in these quantities will lead to a change in the resonant frequency. *Suckling et al* (2004) [36] found, for cuts in a single slit in a thick metal plate, that the transmission via the zeroth-order Fabry-Perot mode was largely independent of plate thickness, and the frequency of transmission was estimated using equivalent circuit theory. However this analytical model assumed the capacitance of the slit resembled a parallel plate capacitor. As the plate size is simply the thickness of the metal, and in the structures present above the metal thickness is ~40 nm, the parallel plate capacitor assumption is not valid here, as edge effects dominate.

5.7 Summary

Selective transmission of microwaves via a very thin slit array of subwavelength slits has been achieved. Two transmission modes have been observed with their transmission mediated by different mechanisms. The primary mode on all structures has been shown to be due to incident radiation diffractively coupling to a surface wave. Diffractive coupling occurs when the incident radiation has a component of its electric vector perpendicular to the slit direction, so fields are enhanced in those slits that lie perpendicular to the polarisation direction. The secondary mode has been shown to be analogous to a zeroth-order Fabry-Perot mode, and is observed only on those structures with the addition of perpendicular cuts. The zeroth-order Fabry-Perot mode has been shown to be due to the behaviour of surface currents, and has not been previously observed in such structures. The surface currents are perturbed by the presence of the cuts, and induce inductive and capacitive regions on the metal structure. This allows the electric field to be enhanced in those slits that lie parallel to the polarisation direction. The resonant frequency and coupling efficiency of this mode has been shown to be highly dependent on slit dimensions. The slit array is 2-D, therefore both modes are accessible to any input polarisation.

Chapter 6

Transmission through a single subwavelength slit

6.1 Introduction

In *Chapter* 2 the transmission of microwaves through subwavelength apertures was introduced. Additionally, in *Chapter* 3 the birefringence of LCs at microwave frequencies was discussed, as was the process of characterising LCs at microwave frequencies, as well as some LC devices. *Yang et al* (2002) [25] investigated the transmission of microwaves through a subwavelength single slit filled with LC. In this chapter, this work will be replicated and a Polymer Dispersed Liquid Crystal (PDLC) will be investigated in the same way, extending to a larger frequency range.

6.2 Background

The discovery of enhanced transmission of radiation through subwavelength holes by *Ebbesen et al* (1998)[29] sparked a wealth of research into the ability of subwavelength apertures to transmit more radiation than that impinging upon merely that of the aperture area, by focusing that radiation impinging on the surrounding metal also. Subsequently it was found that the transmission via slits and holes was mediated by different mechanisms. *Schroter et al* [30] showed that surface plasmons aided the coupling of radiation from incident to exit surfaces. *Porto et al* [28] went further, and classified two different kinds of mode in deep and shallow gratings. One type of mode was found to be a cavity resonance, resembling the eigenmodes of a Fabry-Perot interferometer, albeit with different boundary conditions. Further studies on the resonant fields within slits were carried out by *Astilean et al* [31] and *Collin et al* [32]. Studies on slit arrays were carried out by *Went et al* [33] and *Hibbins et al* [34] in 1-D and 2-D respectively.

6.2.1 The single slit

The Fabry-Perot interferometer can provide a good analogy to the resonant transmission of a single slit in metal, with the equation for a Fabry-Perot interferometer providing good predictions of the resonant frequencies of such structures.

A Fabry-Perot interferometer may be considered as consisting of two parallel aligned perfectly reflecting mirrors with a dielectric core. It is not possible to couple into the system as the mirrors are perfectly reflecting, however there exist a series of eigenmodes at set frequencies dependent on the mirror spacing and dielectric permittivity. The boundary conditions of the system determine the field profile between the mirrors, and the wavelength of the modes given by the system are:

$$\lambda_N = \frac{2d}{N}$$

Where N is the resonant mode number. Consequently the resonant frequencies of the Fabry-Perot interferometer can be easily calculated.

A single slit in metal is a good approximation to a Fabry-Perot interferometer, with a reversal of boundary conditions. The slit entrance and exits behave as the boundary mirrors, with the reflection being due to the impedance mismatch between fields contained within the slit, and free space.

6.2.2 Liquid Crystals (LCs)

A full discussion of LCs and their properties is given in *Chapter* 3, but it is felt necessary to include a brief review of them here also. There are several types of LC phase, all of which are discussed in *Chapter* 3, however this chapter will be concerned only with the LC phase pertinent to this chapter and thesis. The liquid crystalline phase is an umbrella term for several phases of matter that occur in certain materials due to their molecular arrangement. *Thermotropic* LCs are temperature dependent, with the LC phase occurring as a stable phase between the transition between a solid and liquid. Of the types of thermotropic LC, *calamitic* LCs are composed of rod-like molecules, having one axis longer than the other two. The degree of order present in an LC determines its phase. A *nematic* LC is one in which the molecules tend to align in the same way (with their long axes pointing in the same direction), but their centres of mass are randomly distributed throughout the sample. The average orientation of the LC molecules in a nematic LC is defined by a unit vector $\underline{\mathbf{n}}$ called the director. LCs have an optical anisotropy due to their rod-like shape. Radiation polarised with its electric vector parallel to the average molecular long axis will sense a different refractive index to that sensed by radiation with its electric vector polarised parallel to the average molecular short axis. The average long axis is called the extraordinary axis, while the average short axis is called the ordinary axis. This birefringence is the property that is exploited in all LC devices, and crucially, has been shown to extend into the microwave regime [23]. In addition to optical anisotropy LCs also display dielectric anisotropy. This allows the director to respond to an applied electric field; if the molecules have a positive dielectric anisotropy they will tend to align

parallel to the applied field. This then leads to the possibility of confining a small amount of LC between two metallic substrates coated with some aligning layer to promote parallel (homogeneous) alignment to the substrate surface (see *Figure* 6.1) and then on application of a voltage across the LC layer the molecules will realign with the field (homeotropic alignment) thereby changing the sensed permittivity of the LC layer for radiation confined within that layer (see *Figure* 6.2).

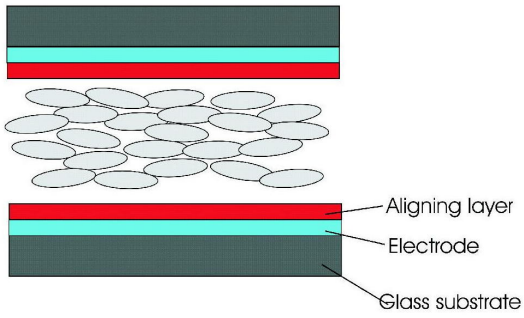

Figure 6.1: A typical LC cell with the LC in the homogeneous state.

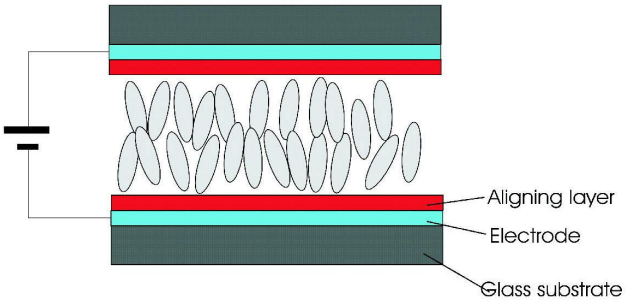

Figure 6.2: A typical LC cell with the LC in the homeotropic state.

The LC used throughout this chapter and thesis is Merck BL001, and at room temperature is in the nematic phase.

6.2.3 Polymer dispersed Liquid Crystals (PDLCs)

Polymer dispersed Liquid Crystals (PDLCs) are a mixture of LC and some polymer. The introduction of a polymer to an LC allows a higher degree of mechanical robustness to the LC layer, as the LC droplets are held in a polymer matrix, thus allowing the PDLC layer to retain the LCs birefringence. The degree of stability and the size of the LC droplets within the network depends on the proportion of LC to polymer, and offers different options to the nature of the PDLC layer. Droplet size is primarily determined by the rate of polymerisation, and due the polymerisation technique employed here, droplets are likely to be of a variable size (due to

different regions of the layer polymerising at different rates). For high proportions of polymer ($>$ 50 %wt) LC droplets are held within a polymer matrix, and it is not possible to align the director with that of a surface aligner on the substrates. If this is the case, the birefringence of the layer is reduced significantly, with $>$ 50 %wt of the PDLC having no birefringence at all (the polymer part) and the remaining part (LC) having a limited birefringence as the LC molecules may only switch between a random alignment (off-state) and homeotropic alignment (on-state) as opposed to switching between homogeneous and homeotropic alignments, as displayed in *Figure* 6.3. This high concentration of polymer in a PDLC allows for thick, stable layers to be produced, but the birefringence of the layer is much reduced.

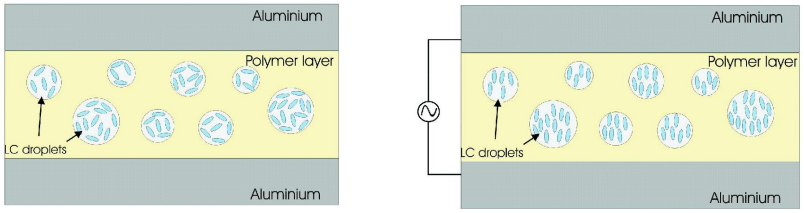

Figure 6.3: An example of a PDLC-filled single slit in (left) off- and (right) on-states.

Lowering the %wt of polymer within the PDLC may allow a greater birefringence to be achieved, however the %wt of polymer must remain high enough for the mechanical robustness of the PDLC layer to be maintained. This effect of varying the polymer %wt will be investigated later in this chapter.

6.2.4 Liquid crystal devices

Several devices designed to operate in the microwave regime and incorporating LCs have already been reported. These works focused on determining microwave birefringence and permittivities (*Lim et al* (1992) [17], *Lim et al* (1993) [18], *Yang and Sambles* (2002) [25]), phase shifters (*Lim et al* (1992) [17], *Guerin et al* (1997) [19], *Fujikake et al* (2001) [21]) and microwave prisms and wavelength selectors (*Tanaka et al* (2001) [22], *Tanaka and Sato* (2002) [24], *Yang and Sambles* (2001) [23]) amongst others. These structures are described in *Chapter* 3.

6.3 The samples

A single slit in metal is constructed from two glass blocks that have had 200 nm layer of aluminium evaporated onto each face. The block dimensions are 50 mm $\times$ 6 mm $\times$ 19 mm (*Figure* 6.4). Each block is then coated with a polyimide aligning layer on one 50 mm $\times$ 19 mm face. The polyimide is then baked and unidirectionally rubbed in order to promote

homogeneous alignment of the LC. The plates are then separated by 50 μm dielectric spacers, and the blocks are fixed together with a UV curing glue. Once the glue has set the slit is then capillary filled with LC in the isotropic phase, then allowed to cool to the nematic phase such that the director aligns homogeneously with the rubbed polyimide layer. Wires are attached to each plate so that a voltage may be applied across the gap in order to realign the LC homeotropically.

In addition to investigating the LC permittivities, PDLCs were also investigated. The PDLC was made from Merck BL001 LC and a UV curing glue. The LC and glue are combined and then mixed by magnetic stirrers with the LC in its isotropic phase. The material is mixed thoroughly for several minutes, and is then poured onto one of the metal substrates. A glass sheet is placed on top of the substrate separated from it by dielectric spacers of 50 μm thickness. The PDLC layer is then subject to UV radiation in order to polymerise the UV curing glue. Once this has occurred the glass sheet is removed and the top substrate is then placed on top of the LC layer and fixed at the sides. Wires are then attached to each substrate in order to apply a voltage across the PDLC layer. Different LC/polymer ratios are investigated in order to find the optimum balance between the stability introduced by the polymer, and the birefringence of the LC.

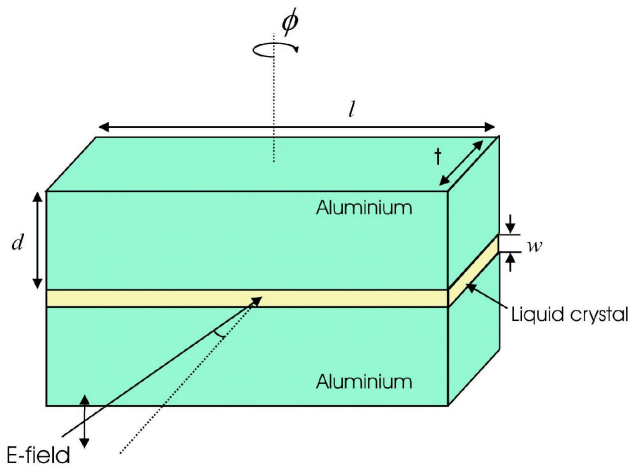

Figure 6.4: An example of an LC filled slit. $l = 50$ mm, $d = 6$ mm, $t = 19$ mm and $w = 50\,\mu$m.

6.4 Transmission experiments

Transmission spectra are obtained over the range 18 GHz $< f_o <$ 60 GHz by placing samples between matched microwave source and detector horns, with each horn 500 mm away from the sample as shown in *Figure* 6.5, in the same way as the previous chapter. Each sample is tightly fitted into an aperture cut into microwave absorbing material. Data is normalised to

transmission through the same aperture with the sample removed. The experimental set-up is not identical to the model in that the model assumes a totally planar wave front, whereas experimentally the wave fronts will be somewhat curved. However, it will be shown that the model still gives good agreement with the transmission data from these structures. The mounts for the source and detector horns are wooden to reduce the possibility of stray reflections interfering with the experiment.

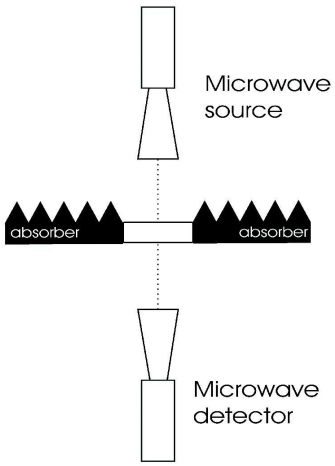

Figure 6.5: A top-down view of the basic experimental set-up.

The microwave source is a Hewlett-Packard 8350B sweep oscillator together with an 83550A plug-in which generates a microwave signal between 8 and 20 GHz (15.00 and 37.48 mm). Three separate Agilent millimetre wave source modules are used as frequency multipliers, each of which has an associated high gain microwave horn attached. The three source modules and horns cover the ranges 18 to 26.5 GHz, 26.5 to 40 GHz and 40 to 60 GHz and 50 to 75 GHz. A matched horn is used for each range as the detector. Two Agilent 82505C detector adapters are used to amplify both the main transmitted signal and a reference signal, with the reference being taken as a direct feed from the source. These signals are sent to a Hewlett Packard 8757D scalar network analyzer. The transmitted and reference signal together allow the evaluation of a normalised signal. Each frequency range is split into 401 frequency steps, and can then be output as a .dat file to be read in any standard spreadsheet software. The .dat file contains information on frequency, azimuthal angle, ϕ, and intensity.

6.5 Modelling

The FEM model used to provide predictions for comparison with data has already been discussed in *Chapter* 4. The specific model used to fit to data in this chapter is created by first drawing an airbox of dimensions 10 mm $\times$ 0.1 mm $\times$28 mm. Within this airbox the sample is

drawn, consisting of two aluminium blocks located centrally in the z-dimension. Each block measures 4.975 mm$\times$ 0.1 mm $\times$19 mm, and they are located on the x-axis such that a 50 μm slit is positioned centrally in that dimension. Both the x- and y-dimensions of the blocks are reduced by the appropriate choice of boundary conditions, however the z-dimension clearly cannot be reduced, as this length determines the frequency of transmission of the slit. The aluminium has identical parameters to that described in the previous section. Boundaries are assigned such that the xz-plane faces are assigned as Perfect H boundaries, meaning that the slit is considered as infinitely long in the y-direction. All other boundaries are assigned as radiation boundaries in the incident half space, and impedance boundaries in the transmission half space. Evaluation planes are assigned in the same way as in the above section, and an excitation is assigned to be normally incident, propagating in the -z-direction, and polarised parallel to the x-axis (perpendicular to the slit). The mesh is generated at a frequency of 40 GHz, and additional meshes are generated at frequencies corresponding to transmission peaks. Each of these is refined by the adaptive pass method, up to a total of approximately 120,000 tetrahedra. The mesh has a frequency sweep associated with it, from 40 to 60 GHz in 0.2 GHz steps.

6.6 Results and discussion

The transmissive properties of the structures described above will now be discussed with reference to predictions provided by the FEM model, HFSS. Field plots from HFSS will then give insight into the transmission mechanism of the structure. *Figures* 6.6 and 6.7 display transmission through an LC-filled single subwavelength slit over the frequency range 40 to 75 GHz, with a range of voltages applied as indicated in the legend. Data is taken at an azimuthal angle $\phi = 15°$, as at normal incidence the transmission suffers interference from stray reflections.

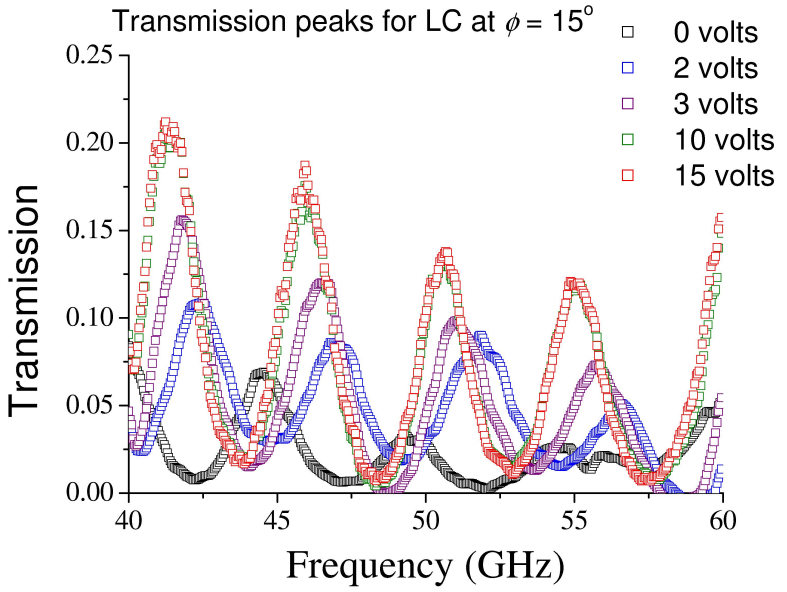

Figure 6.6: Transmission data from an LC-filled single subwavelength slit with different applied AC voltages of 1 kHz.

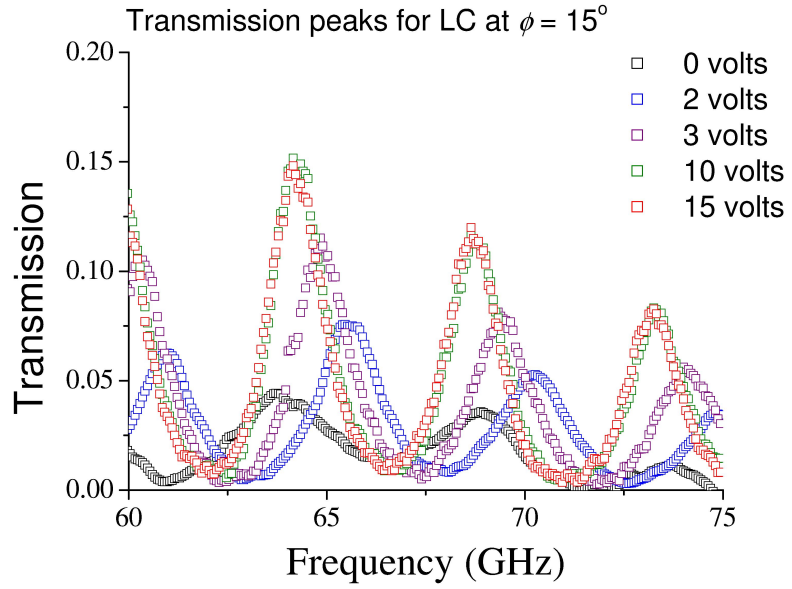

Figure 6.7: Transmission data from an LC-filled single subwavelength slit with different applied AC voltages of 1 kHz.

It is clear that a series of peaks in the transmission occur, and that the frequency at which these transmission peaks appear shifts on application of a voltage. This is consistent with

the LC being intially aligned homogeneously with the aligning layer, and on application of a voltage the LC molecules realign homeotropically with the applied field. It should be noted that the applied electric field is significantly greater than any electric field occurring due to structural effects. The applied field is in the region of 300,000 Vm^{-1}, much greater than any field enhancement due to structural effects. This realignment of the LC causes a shift in the sensed index of the slit cavity, and it is this index change that in turn produces a shift in the frequency of the transmission peaks. We can use the FEM model to ascertain the transmission mechanism, and therefore establish the relationship between a change in index and a change in the frequency of transmission peaks.

Figure 6.8 shows both of the previous plots shown on the same graph, indicating that despite the data being taken using different source horns and detectors to cover the two ranges, the data sets match up well when plotted on the same axes.

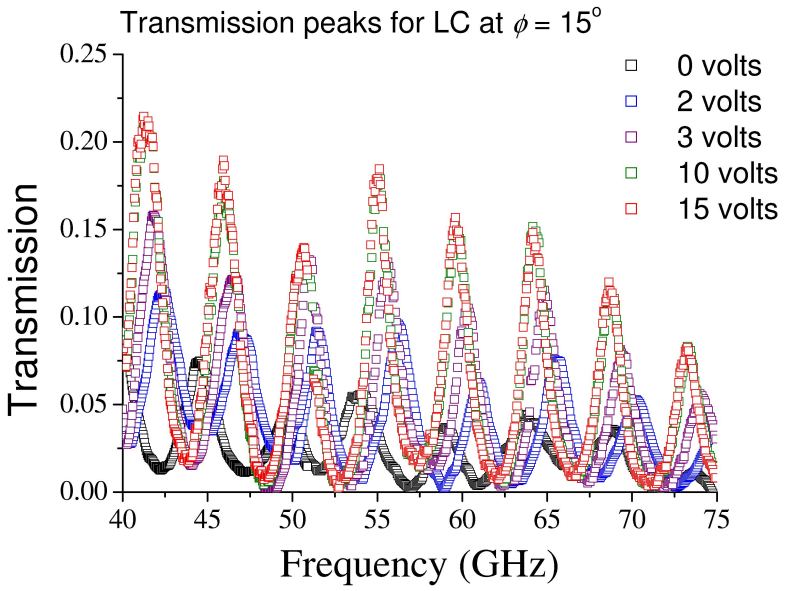

Figure 6.8: Transmission data from an LC-filled single subwavelength slit with different applied AC voltages of 1 kHz.

Figure 6.9 displays a comparison between the data in the off-state (0 V applied, homogeneous alignment) and a prediction from the FEM model for the transmission of the LC-filled slit over a frequency range of 40-60 GHz at an azimuthal angle $\phi = 15°$. The model provides a good fit by adjusting the permittivity of the LC filling the slit. The relative permittivity required to achieve this fit is 2.70, which gives a refractive index of 1.64, closely corresponding to previous work undertaken to determine the microwave indices of this LC. [23]

Figure 6.10 displays a comparison between the data in the on-state (15 V applied, homeotropic alignment) and a prediction from the FEM model for the transmission of the LC-filled slit over the same frequency range, 40-60 GHz at an azimuthal angle $\phi = 15°$. The model is identical

to that used to fit the off-state data, with the exception of the relative permittivity now being 2.98. This gives a refractive index of 1.73, again, agreeing well with the previously determined value.

In both of the above figures the model fits very well to the mode in terms of frequency position, but not so well to the height of the peaks and the breadth of the modes. This is due to the mode breadth and height being due to a combination of factors, including the sample quality, and absorption due to the LC. It is not possible to determine the relative contributions to the breadth and height of the modes, and therefore there is no value in trying to achieve a perfect fit to those aspects of the modes.

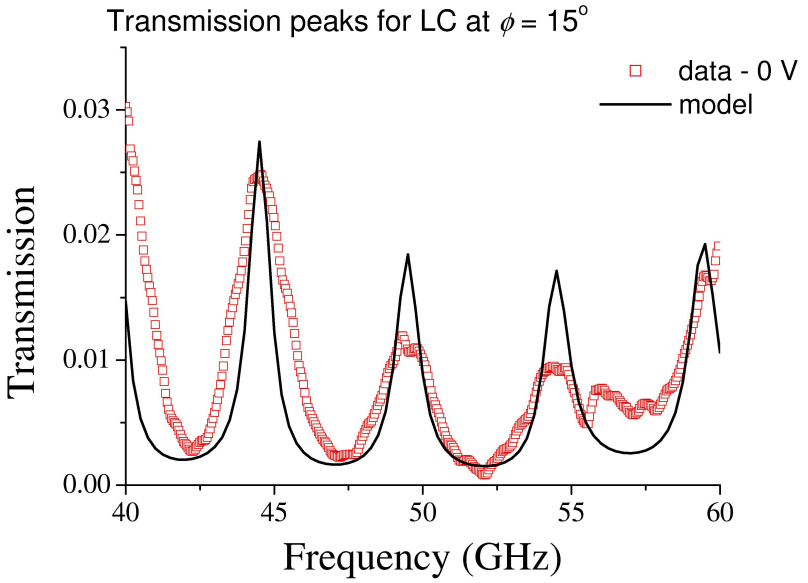

Figure 6.9: A comparison between data and a prediction provided by the FEM model for the LC-filled slit with no voltage applied.

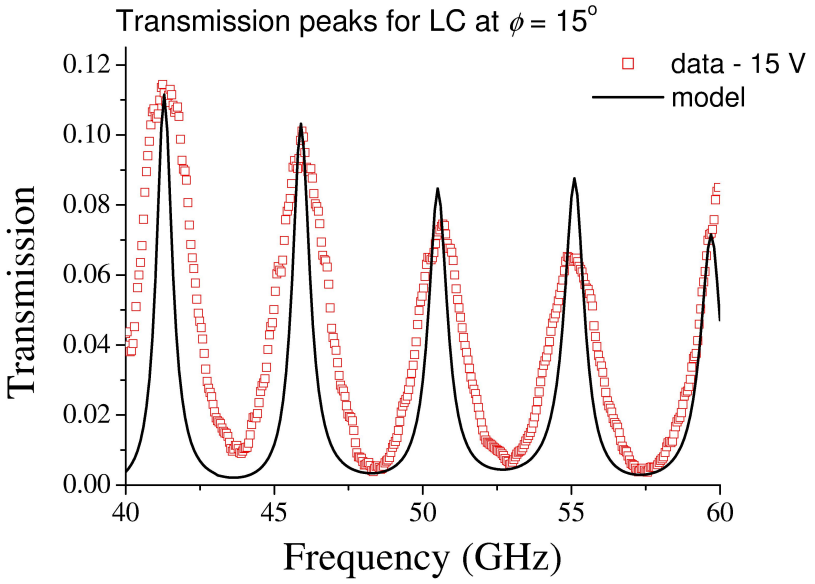

Figure 6.10: A comparison between data and a prediction provided by the FEM model for the LC-filled slit with 15 V applied.

Examination of field plots provided by HFSS allow insight into the transmission mechanism of the slit structure. *Figures* 6.11 and 6.12 display the time-averaged electric field magnitude taken from each model at a frequency corresponding to one of the transmission peaks.

Figure 6.11 (left) displays the time-averaged electric field magnitude (from the off-state model) across the yz-plane through the LC layer confined within the slit at a frequency of 44.5 GHz, corresponding to one of the transmission peaks. A schematic of the model (right) indicates the plane over which the field is plotted (dotted line). It is clear that the electric field is high at the slit entrance and exit, with 9 field minima through the slit length. This field profile is consistent with the Fabry-Perot analogy described above, and corresponds to the $N = 9$ Fabry-Perot mode. The Fabry-Perot equation can give an approximation prediction of the frequency at which this transmission mode will occur:

$$f = \left(\frac{cN}{2t\left(n^2 - \sin^2\phi\right)^{\frac{1}{2}}} \right)$$

where f is the resonant frequency, t is the slit depth, ϕ is the azimuthal angle and n is the refractive index of the core. This gives a frequency of 44.8 GHz, a good approximation to the frequency at which the mode occurs, 44.5 GHz.

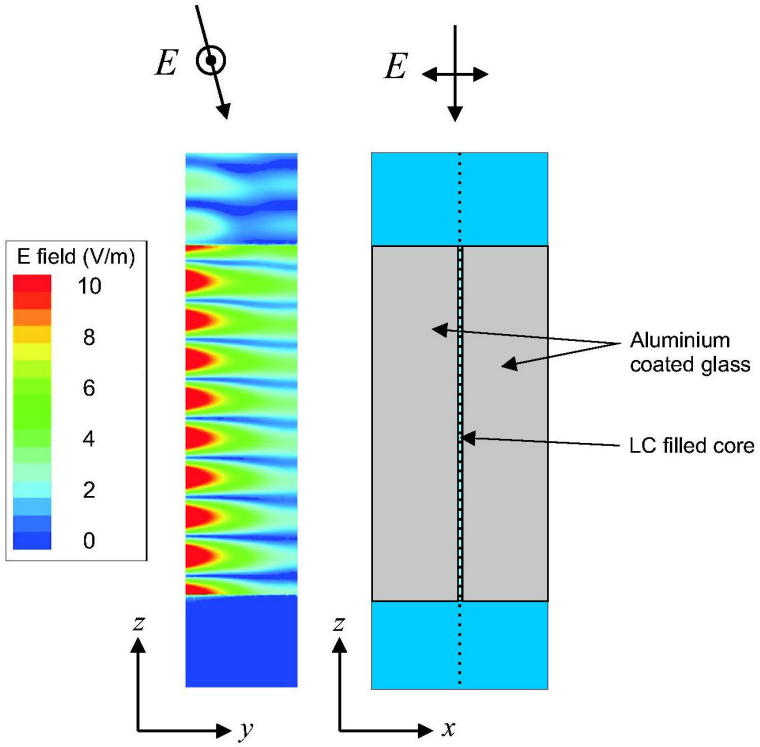

Figure 6.11: (left) Time-averaged electric field magnitude taken from the LC-filled single slit in the off-state (0 V) at a frequency of 44.5 GHz. (right) A schematic of the model, the dotted line indicates the plane over which the electric field magnitude is plotted.

In the same way we can calculate the frequency to which the mode should shift when a voltage is applied and the LC realigns with the field in the homeotropic state. *Figure* 6.12 shows the time-averaged electric field magnitude (taken from the on-state model) across the yz-plane through the LC layer confined within the slit at a frequency of 41.3 GHz, corresponding to one of the transmission peaks. A schematic of the model (right) indicates the plane over which the field is plotted (dotted line). It is clear that although this transmission mode occurs at a lower frequency, it is the same $N = 9$ Fabry-Perot mode as in the off-state model, confirming that simply changing the index of the LC core the modes may be shifted in frequency. By again using the Fabry-Perot equation with the on-state refractive index we can approximate the transmission of the $N = 9$ Fabry-Perot mode, which yields a frequency of 41.6 GHz, as compared with the observed transmission frequency of 41.3 GHz.

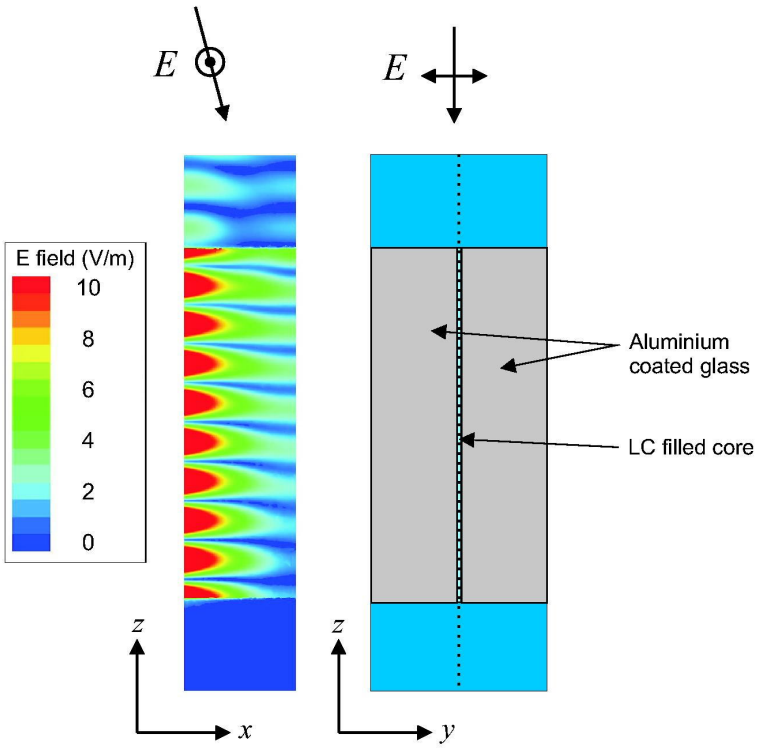

Figure 6.12: (left) Time-averaged electric field magnitude taken from the LC-filled single slit in the on-state (15 V) at a frequency of 41.3 GHz. (right) A schematic of the model, the dotted line indicates the plane over which the electric field magnitude is plotted.

Figure 6.13 displays the electric vector direction plotted at a phase corresponding to maximum enhancement for the off-state model at a frequency of 44.5 GHz. The electric vector direction is consistent with that which may be expected from the Fabry-Perot analogy.

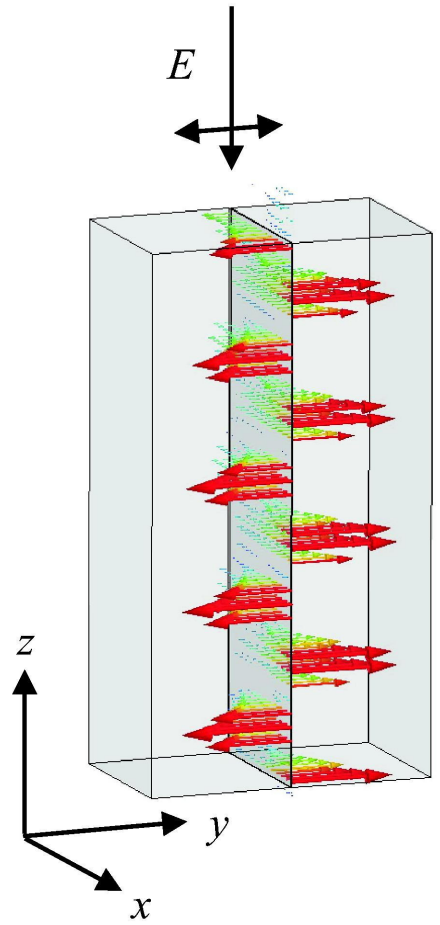

Figure 6.13: The electric field vector plotted at a phase corresponding to maximum enhancement and taken from the LC-filled single slit in the off-state (0 V) at a frequency of 44.5 GHz.

In addition to investigating the transmission of microwaves through an LC-filled single subwavelength slit, an investigation into the transmission properties of a PDLC confined in the same geometry was also undertaken. The PDLC consists of an LC/polymer mix, in order to introduce a degree of stability to the dielectric layer. However, the optimum ratio of LC to polymer requires some investigation. *Figure* 6.14 displays transmission data from a PDLC-filled single subwavelength slit, where the PDLC consists of 50 %wt polymer. Transmission data are obtained for a range of applied voltages, and the slit dimensions are identical to that of the LC-filled sample described above.

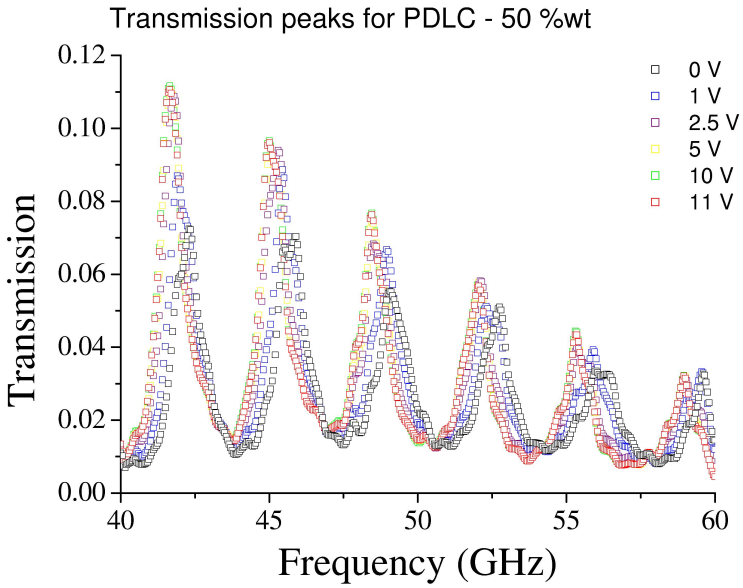

Figure 6.14: Transmission data taken from a PDLC-filled single slit with the PDLC having 50 %wt polymer. Applied voltage is AC at a frequency of 1 kHz.

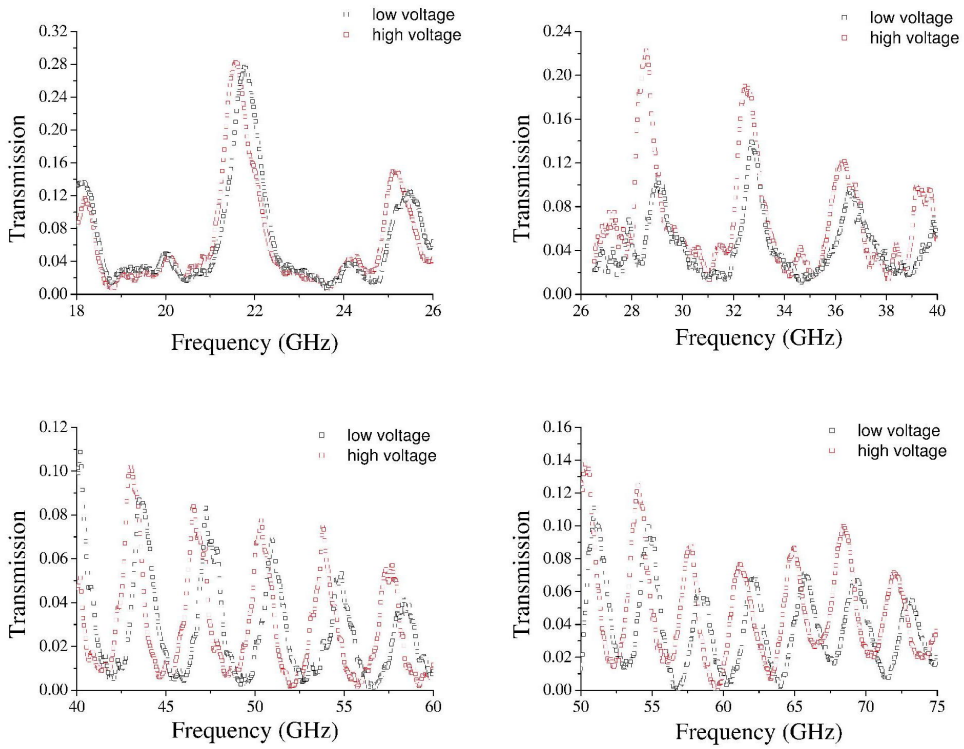

Figure 6.15: Transmission data over an extended frequency range taken from a PDLC-filled single slit with the PDLC having of 50 %wt polymer.

Transmission data for another PDLC filled sample were taken over a wide range of frequencies using the four source and detector horn sets described in *Section* 6.4 and shown in *Figure* 6.15. The four ranges shown are taken at different azimuthal angles, and therefore the data do not match up perfectly between ranges. The different azimuthal angles chosen are those at which there were low levels of interference for that particular set of source and detector horns.

Figure 6.16 displays transmission data from a PDLC-filled single subwavelength slit, where the PDLC consists of 10 %wt polymer. Transmission data are obtained for a range of applied voltages, and the slit dimensions are identical to that of the LC-filled sample described above. The voltage is increased up to 15 V in *Figure* 6.16 to ensure no further switching can be achieved.

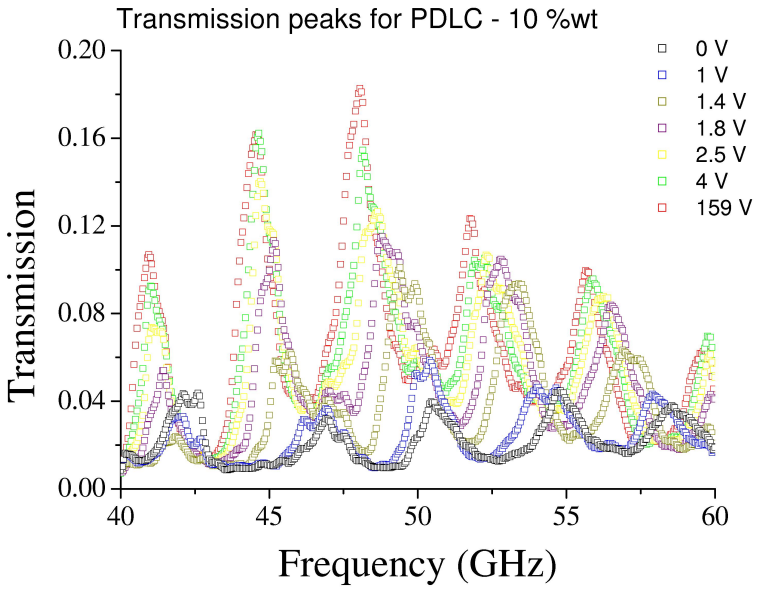

Figure 6.16: Transmission data taken from a PDLC-filled single slit with the PDLC having 10 %wt polymer. Applied voltage is AC at a frequency of 1 kHz.

The shift in resonant frequency due to the applied voltage can be translated into a shift in the refractive index of the PDLC filling the slit, as displayed in *Figure* 6.17. This indicates the index shift between the off- (0 V) and on- (high voltage) states, and is plotted for the observed shift in one of the transmission modes. The index shifts for pure LC, a PDLC with 10 %wt polymer, and a PDLC with 50 %wt polymer are displayed together.

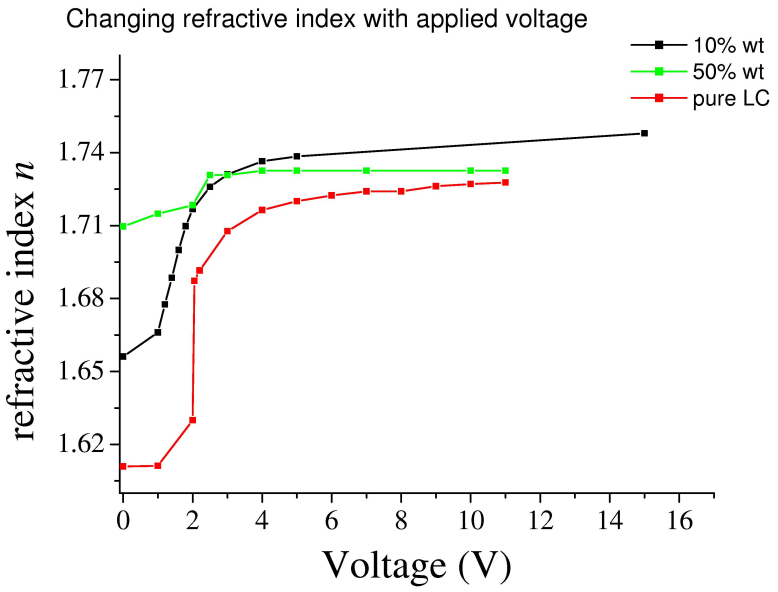

Figure 6.17: A comparison of the change in refractive index for one transmission mode with applied voltage for a pure LC, a PDLC with 10 %wt polymer and a PDLC with 50 %wt polymer.

As expected, the pure LC has the largest index shift, and the 10 %wt polymer PDLC also displayed a large shift. However the 50 %wt polymer PDLC has a greatly reduced index shift, indicating that the polymer is having a significant impact on the LC alignment. From *Figure* 6.17, the 50 %wt polymer does not have a low index in the off-state, implying that the LC molecules are not well aligned with the aligning layer. This is consistent with a high polymer content, and the LC being confined in droplets, as displayed in *Figure* 6.3. However in the 10 %wt polymer PDLC a lower index is obtained when in the off-state, indicating that some alignment of the LC molecules with the aligning layer is possible, and is more consistent with the LC being weakly contained within a polymer network.

Figure 6.18 displays the maximum index shift available between off- and on-states as a function of %wt polymer. Data is displayed for pure LC (0 %wt), 10 %wt and 50 %wt. Although three data points are not enough to establish a clear relationship between %wt and index shift, this graph clearly displays the improvement in index shift as the %wt of polymer is reduced. For the PDLC to be effective it is required to maintain stability, whilst having the maximum possible index shift available. If the %wt of polymer is reduced to less than 10 %wt, then the stability of the layer may be compromised. However, greater than 10 %wt polymer will inevitably lead to a reduction in the available shift in index.

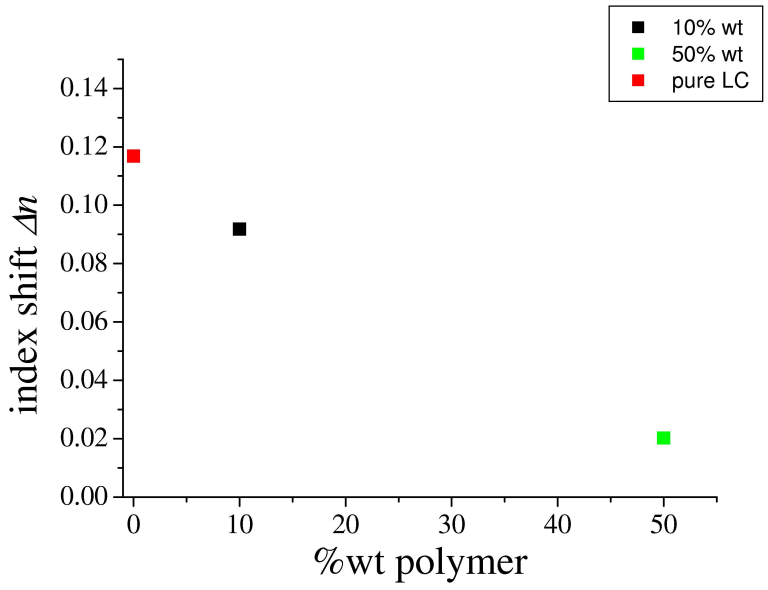

Figure 6.18: The maximum shift in refractive index for one transmission mode for a pure LC, a PDLC with 10 %wt polymer and a PDLC with 50 %wt polymer.

6.7 Summary

Results of resonant transmission of microwaves through a single, subwavelength slit have been presented, where the slit has been LC-filled, and then PDLC-filled. The transmission though the slit was found to be analogous to a Fabry-Perot type interferometer, and resonant transmission frequencies were shown to agree well with both a prediction from an FEM model, and frequencies determined from the Fabry-Perot equation, allowing the ordinary (off-state) and extraordinary (on-state) refractive indices to be found. Additionally, two PDLC mixtures of different %wt polymer were investigated by confining them in the same single slit geometry. Again, their ordinary and extraordinary indices were determined, and these were used to give an indication of the optimum %wt of polymer to be used for allowing the PDLC to have the maximum available index shift between the ordinary and extraordinary indices, whilst maintaining the stability of the overall layer.

Chapter 7

Microwave absorption by Penny Arrays

7.1 Introduction

Chapters 5 and *6* have focused on controlling the transmission of microwaves through subwavelength apertures. The following two experimental chapters will now focus on resonant absorption of incident microwaves. *Chapter* 2 introduced the absorption of microwaves at the interface between a metal and dielectric due to a corrugation in the metal layer. Shallow gratings allow incident radiation to resonantly couple to a SPP, with the SPP having a curved dispersion band. It is also possible to couple to flat-banded modes confined in the grooves of deep gratings, however these modes are strongly radiative and therefore rather broad and shallow. A combination of both shallow and deep corrugations of different pitches allows coupling to a non-dispersive zero-ordered mode that absorbs almost 100% of incident radiation at selected frequencies, and this was demonstrated theoretically by *Tan et al* (2000) [37] and experimentally by *Hibbins et al* (2002) [38] and *Lockyear et al* (2003) [39]. Another microwave absorbing structure that achieved resonant absorption by an entirely different mechanism was that investigated by *Hibbins et al* (2004) [40]. This consisted of a metal-clad dielectric of subwavelength thickness with metal removed from the core cladding to produce an array of subwavelength slits. Incident radiation with its electric vector polarised perpendicular to the slit direction was diffractively coupled into the core exciting a standing wave along the core length. Two remarkable aspects of this structure are that it resonantly absorbs radiation at a wavelength 100 times greater than the structure thickness and that half of the standing wave wavelength is compressed into a fraction of the expected distance. This chapter discusses the resonant absorption by structures based on a similar metal-dielectric-metal structure, however the samples discussed here display resonant absorption that, remarkably, is almost entirely independent of azimuthal angle, ϕ, polar angle, θ, and polarisation, unlike previous structures. The samples consist of an array of metallic "pennies" separated from a metal substrate by a dielectric layer. The first set of samples have aluminium pennies of approximately 1 mm height separated from an aluminium base plate by a dielectric layer, and will be referred to

as "thick" penny arrays. The second set of samples are formed from copper printed circuit boards (PCBs), and will be referred to as "thin" penny arrays.

7.2 The samples

The first set of samples are the "thick" penny arrays. Three samples were investigated, each of which consisted of a thick aluminium plate, 300 mm × 300 mm × 30 mm, which was covered with a 50 μm dielectric layer of Filmolux, on top of which an array of metallic pennies was assembled. The pennies were assembled by placing a wire mesh over the substrate, and each penny being spaced by the wire thickness. The wire mesh was then removed to leave an array of closely spaced pennies. Each penny had a diameter of ∼5.8 mm and 1 mm thickness. The first sample was a 6 mm pitch square array, the second was an 8 mm pitch square array, and the third was a hexagonal array with a pitch of 8.8 mm. In order to assemble the larger pitch penny arrays, an array of holes matching the penny size were drilled into a metal plate, this was then placed on top of the substrate and the pennies positioned in the holes, before the plate was removed to leave the array of pennies. The first thick penny array sample is shown in *Figure* 7.1.

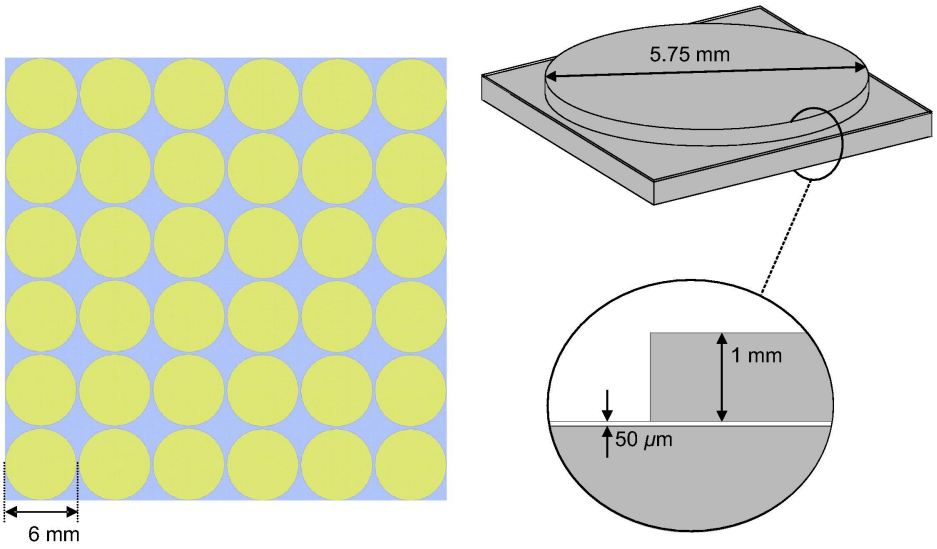

Figure 7.1: The thick penny array. (left) A top-down view of a section of the array. (right) A single penny and a side view of an aluminium penny separated from the thick substrate by a dielectric layer.

The fourth sample is the "thin" penny array. These are made using a standard "print and etch" technique and formed from PCBs, consisting of a polyester sheet of thickness 100 μm and bounded by copper layers of thickness 18 μm. The array is formed by etching into one face of the copper cladding, and an array of pitch 6.25 mm with penny radii of 2.98 mm is investigated. The thin penny array is displayed in *Figure* 7.2.

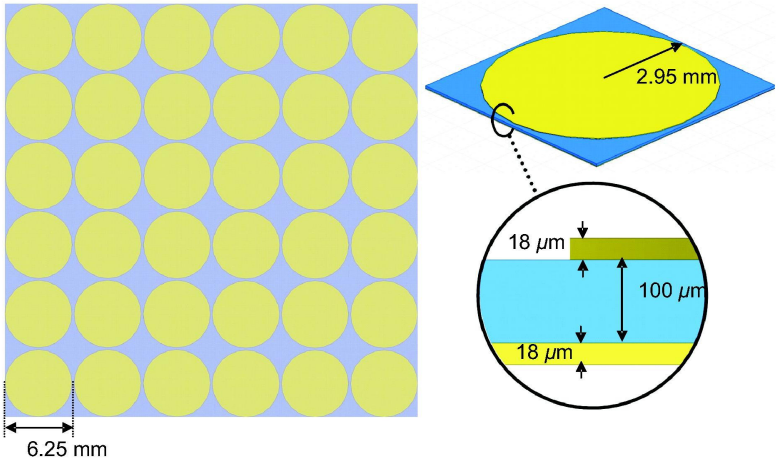

Figure 7.2: The thin penny array. (left) A top-down view of a section of the array. (right) A single penny and the copper-clad dielectric structure.

7.3 Reflection experiments

The experimental set-up is shown in *Figure* 7.3. The apparatus consists of a microwave source mounted within an impedance matching horn placed at the focal point of a 2 m focal length mirror. The mirror directs a well-collimated beam onto the sample, which is placed on a rotating turntable. The specular reflection from the sample is collected by an identical 2 m focal length mirror, and directed into a detector horn. The mirrors are spherical, not parabolic which would be the ideal for reducing aberrations. However, spherical mirrors are relatively easy to manufacture, and provide a good approximation to a parabolic mirror, particularly when the incident beam diameter is much less than the mirror's radius of curvature, as is the case here. Microwave absorbing material is used to reduce any stray reflections.

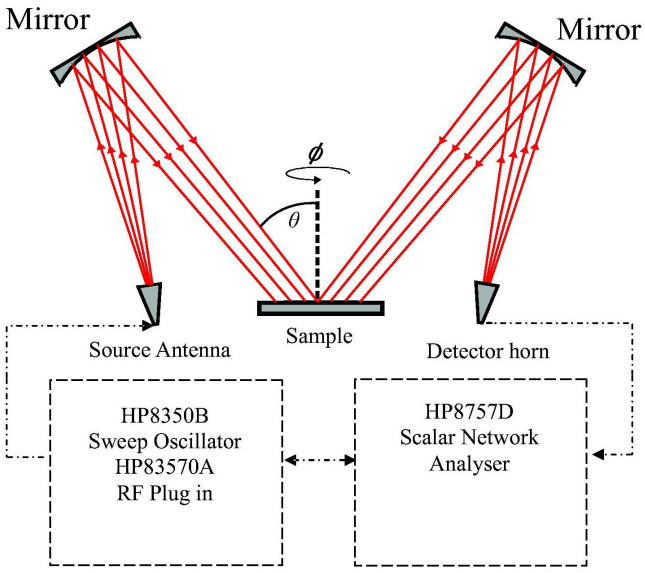

Figure 7.3: A schematic diagram of the experimental set-up used to investigate the sample's reflectivity.

The arrangement for recording specular reflectivity is shown in *Figure* 7.4. The mirrors are mounted in wooden supports that may be slid along runners to allow them to be set at any polar angle θ, and may have their height adjusted so as to maintain the 2 m distance to the source and detector horns. The horns themselves are also mounted on wooden sliders and can be moved relative to the mirrors as well as having their height and rotation changed. Wooden apparatus is used wherever possible in order to reduce any unwanted diffraction or scattering. The sample is mounted on a turntable that can be rotated to give any azimuthal angle ϕ. Both angles θ and ϕ may be set to an experimental precision of $\pm 1^{\circ}$.

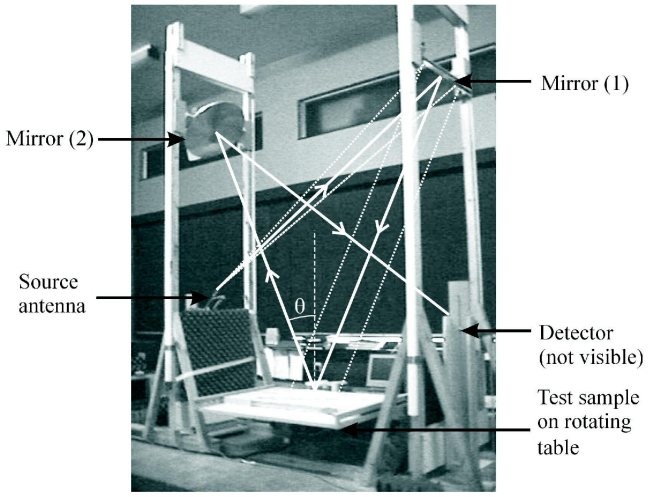

Figure 7.4: The apparatus used for reflectivity measurements.

A Hewlett Packard HP8350B sweep oscillator is used with a HP85370A RF plug-in (and other plug-ins) in order to generate a microwave signal of frequency 12 - 60 GHz (5 mm $\leq \lambda \leq$ 25 mm). Each plug-in has a matched high-gain microwave horn attached to it via a flexible waveguide, and directs the radiation onto the spherical mirror. At the source, the signal is split by a directional coupler into a source and reference signal which is fed back into a HP8757 scalar network analyser allowing the detected signal to be normalised. A detector horn matching the source horn collects the reflected signal, and is connected to the scalar network analyser and a PC in order to record data sets. The PC also controls the rotating turntable and records frequency dependent data. Each frequency range is split into 401 frequency steps, and can then be output as a .dat file to be read in any standard spreadsheet software. The .dat file contains information on frequency, azimuthal angle, ϕ, and intensity.

The source and detector horns can be set to pass either p- (transverse magnetic, TM) or s- (transverse electric, TE) polarisations, where the transverse vector direction is defined with respect to the plane of incidence. In general we measure reflectivities R_{pp}, R_{ss}, R_{ps} and R_{sp} where R_{ps} and R_{sp} are measures of polarisation conversion, and subscripts refer to incident and reflected polarisations respectively. All reflectivities from samples recorded in this chapter are normalised by comparison with signals from a flat metal plate of the same dimensions (placed on top of the sample) with the reflectivity from the flat plate being considered as unity.

Resonant modes from the structures under investigation may be observed as minima in the angle dependent reflectivity, with the resonant width being dependent on the loss channels available.

7.4 Modelling

In this section there will be a brief discussion of the models used to compare with data in the results section. A full description of the FEM modelling code, HFSS, can be found in *Chapter* 4. There are four samples, three of which are "thick" penny arrays, the other being the "thin" penny array. The models for all four samples reduce each array to a unit cell based on the dimensions described above, with the sample structure lying in the xy-plane. For the thick penny array samples, a 1 mm thick aluminium penny of radius ∼2.9 mm is separated from a 200 nm aluminium substrate (thick enough to be opaque to incident microwaves) by a 50 μm dielectric layer. The aluminium parameters are taken from the model library such that the aluminium has a conductivity, $\sigma = 3.8 \times 10^7 \mathrm{Sm}^{-1}$, and relative permeability $\mu = 1.000021$. A surface impedance approximation is used (discussed further in *Chapter* 4) due to the high conductivity, and therefore the relative permittivity is ignored. The dielectric layer is created as a new material in the library, and has an effective permittivity of $\varepsilon = 2.8 + 0.046i$. The x- and y-dimensions of the dielectric and substrate layers relate to the pitch of the sample in question. For the hexagonal array, the unit cell is lozenge-shaped in order to replicate the hexagonal symmetry of the array.

The thin penny array model consists of an 18 μm thick copper penny of radius ∼2.98 mm, separated from a 18 μm copper substrate by a 100 μm polyester layer. Materials are assigned from HFSS's material library, with the copper having a conductivity, $\sigma = 5.8 \times 10^7 \mathrm{Sm}^{-1}$, relative permeability, $\mu = 0.999991$, $\mu_i/\mu_r = 0$, and the polyester sheet having a relative permittivity $\varepsilon = 3.2$ and a dielectric loss tangent $\delta = 0.003$. Again, the x- and y-dimensions of the dielectric and substrate layers relate to the pitch of the sample.

In each of these models the structure layers are located at the base of a 10 mm airbox, and master-slave boundaries are assigned on the xy- and xz-plane faces. The top xy-plane face is assigned a radiation boundary for low polar angles, ($\theta \leq 15°$) and is assigned a PML for high polar angles ($\theta > 15°$), and an evaluation plane is located 1 mm below the top xy-plane face. For each model a mesh is generated by the adaptive pass method, with ∼20,000-40,000 tetrahedra generally deemed to give sufficient accuracy, depending on the model. Frequency sweeps are run over the relevant range over which features are observed in 0.5 GHz steps, and transmission, reflection and absorption predictions are then exported to compare with data. The field plots discussed in the following section are also generated from the models.

7.5 Results and discussion

This section contains a discussion of the reflectivity data obtained from the samples described above. *Figure* 7.5 displays reflectivity data from the 6 mm pitch thick penny array. Reflectivity data are shown for both p- (left) and s-polarisations (right) as a function of both azimuthal angle, ϕ, and frequency at a polar angle $\theta \approx 7°$. Absorption is shown on the z-axis with dark regions indicating high levels of absorption and lighter regions indicating reflection. Reflection is normalised to a scan with a metal plate placed over the sample and having the same dimensions as the sample, so that reflection from the sample is between 0 and 1.

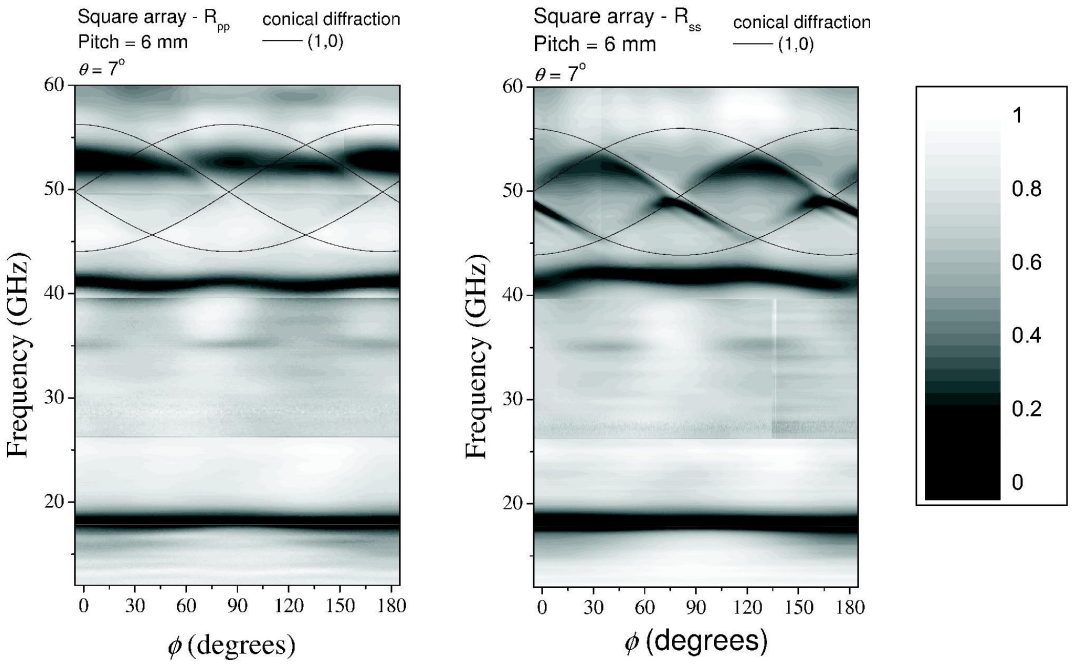

Figure 7.5: Reflectivity data as a function of both azimuthal angle, ϕ and frequency taken from a square array made up of thick pennies with a pitch of 6 mm. Data are taken at a polar angle of $\theta \approx 7°$, and conical diffraction lines are plotted as indicated. Data are shown for both p- (left) and s-polarisations (right).

Resonant absorption occurs from the sample for both polarisations, with clear reflectivity minima occurring at ∼18 GHz, and ∼41 GHz. The 18 GHz mode appears to be largely independent of azimuthal angle, whereas the 41 GHz mode displays a slight oscillation in frequency as the sample is rotated azimuthally. The reason for this will be discussed with reference to field plots later in this section. Also, there is a much weaker mode appearing at ∼35 GHz. This mode is azimuthal angle dependent, and peaks at angles of $\phi = 0°$, 90°, 180° in the p-polarised reflectivity data, and $\phi = 45°$, 135° in the s-polarised reflectivity data. Again, the reason for this will be discussed with reference to field plots later in this section. The pitch of this sample is 6 mm, so each of these modes occur in the zero-order region of the array. At higher frequencies the sample becomes diffractive; conical diffraction lines are plotted in *Figure* 7.5. Further reflectivity minima occur in this region, but the analysis here will be restricted to zero-order absorption.

Figures 7.6-7.8 display reflectivity data from the same sample at higher polar angles of $\theta = 12°$, 18° and 29° respectively. Data are displayed in the same way for both p- (left) and s-polarisations (right) as a function of both azimuthal angle, ϕ, and frequency, and conical diffraction lines are plotted on each figure as indicated in the legend. The increase in polar angle results in the frequency at which the sample becomes diffractive being reduced, resulting in the ∼41 GHz mode being lost to diffraction at each of these subsequent polar angles. The

~35 GHz mode remains, but is changed, becoming more absorbing and slightly reduced in frequency as the polar angle is increased. The mode occurring at ~18 GHz also remains, and does not appear to change in frequency as the polar angle is increased. As these modes appear consistently in the data they will be termed Mode 1 (18 GHz), Mode 2 (35 GHz), and although at this stage it has only appeared once, Mode 3 (41 GHz). Later in this section it will be shown that one or more of these modes appear in each of the samples investigated, and the absorption mechanism will be explained with reference to field plots provided from HFSS.

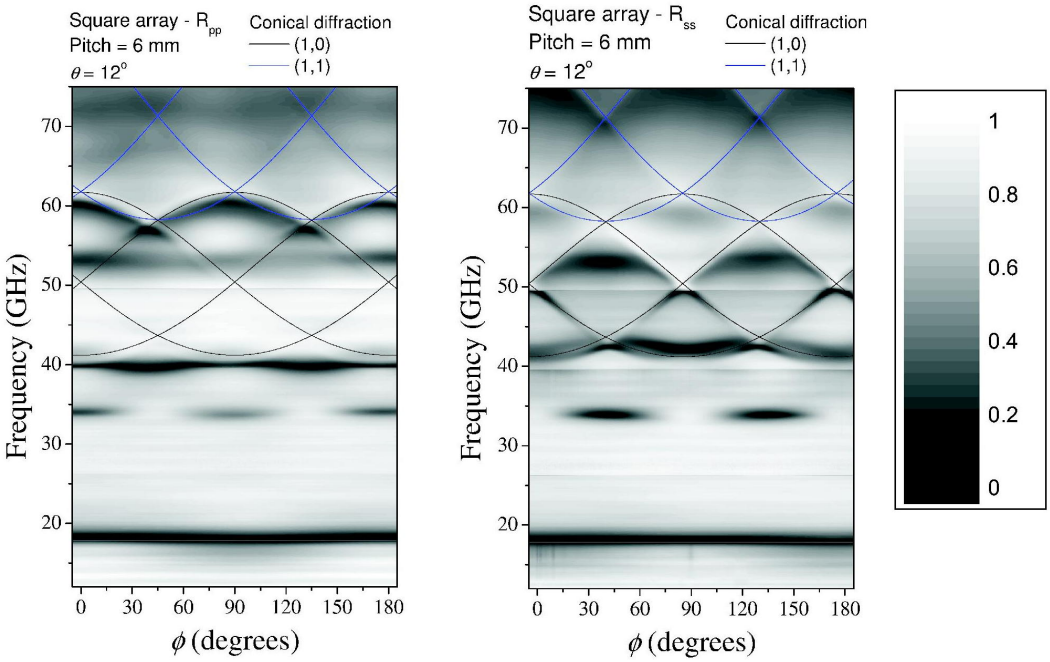

Figure 7.6: Reflectivity data as a function of both azimuthal angle, ϕ and frequency taken from a square array made up of thick pennies with a pitch of 6 mm. Data are taken at a polar angle of $\theta \approx 12°$, and conical diffraction lines are plotted as indicated. Data are shown for both p- (left) and s-polarisations (right).

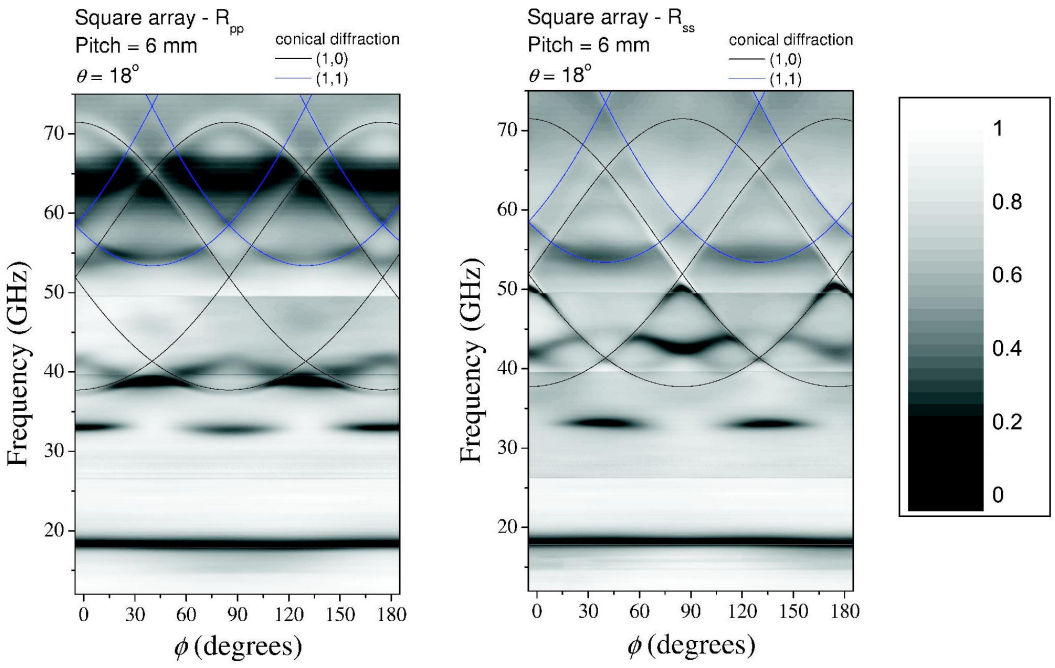

Figure 7.7: Reflectivity data as a function of both azimuthal angle, ϕ and frequency taken from a square array made up of thick pennies with a pitch of 6 mm. Data are taken at a polar angle of $\theta \approx 18°$, and conical diffraction lines are plotted as indicated. Data are shown for both p- (left) and s-polarisations (right).

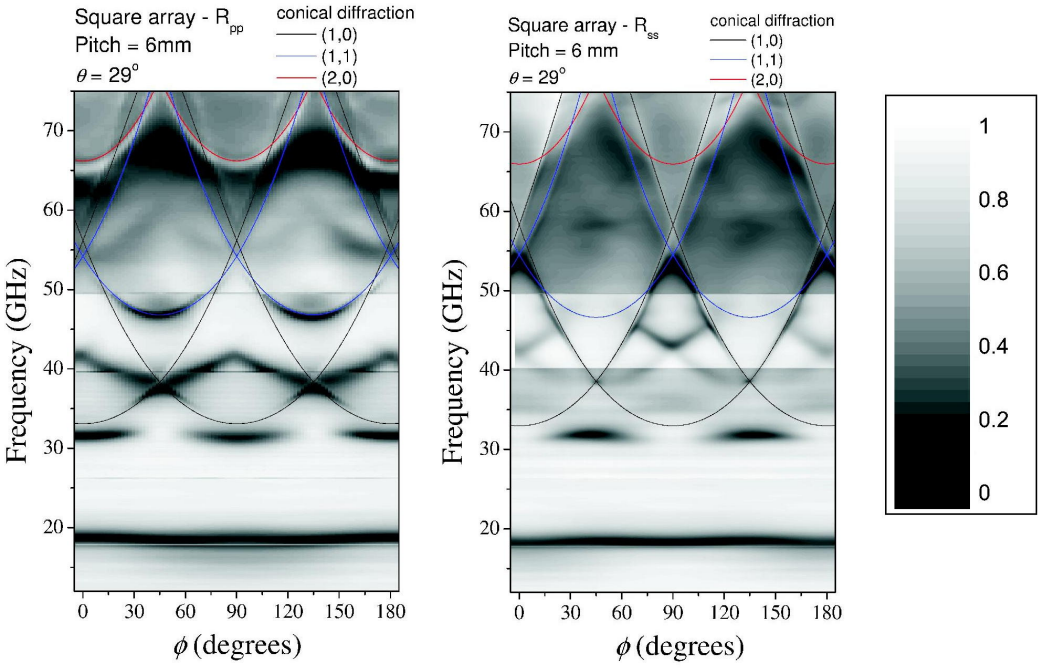

Figure 7.8: Reflectivity data as a function of both azimuthal angle, ϕ and frequency taken from a square array made up of thick pennies with a pitch of 6 mm. Data are taken at a polar angle of $\theta \approx 29°$, and conical diffraction lines are plotted as indicated. Data are shown for both p- (left) and s-polarisations (right).

The following two figures, *Figure* 7.9 and *Figure* 7.10 show reflectivity data from the 8 mm pitch thick penny array at polar angles of $\theta = 6°$ and $29°$ respectively. Data is displayed in the same way as for the previous samples, with p- (left) and s-polarisations (right) as a function of both azimuthal angle, ϕ, and frequency, and absorption on the z-axis. For this pitch, resonant absorption occurs at $\sim$20 GHz, and it will be shown later that this mode is the same as Mode 1 observed at 18 GHz in the 6 mm pitch array. Higher order modes may also occur, but are lost to diffraction as the increased pitch leads to diffraction occurring at a lower frequency.

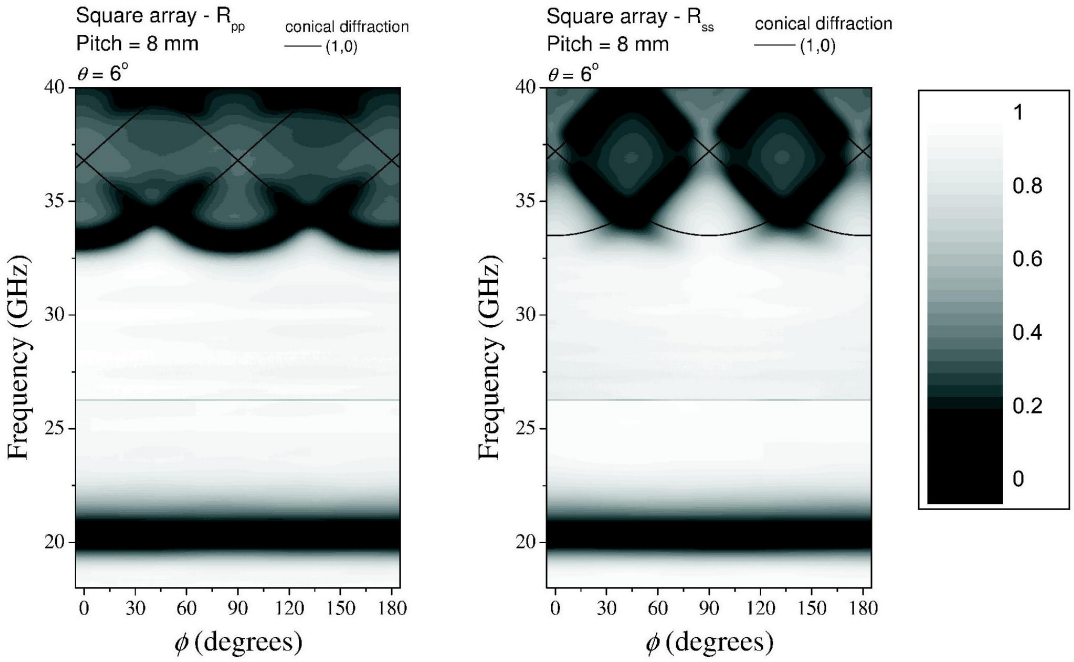

Figure 7.9: Reflectivity data as a function of both azimuthal angle, ϕ and frequency taken from a square array made up of thick pennies with a pitch of 8 mm. Data are taken at a polar angle of $\theta \approx 6^\circ$, and conical diffraction lines are plotted as indicated. Data are shown for both p- (left) and s-polarisations (right).

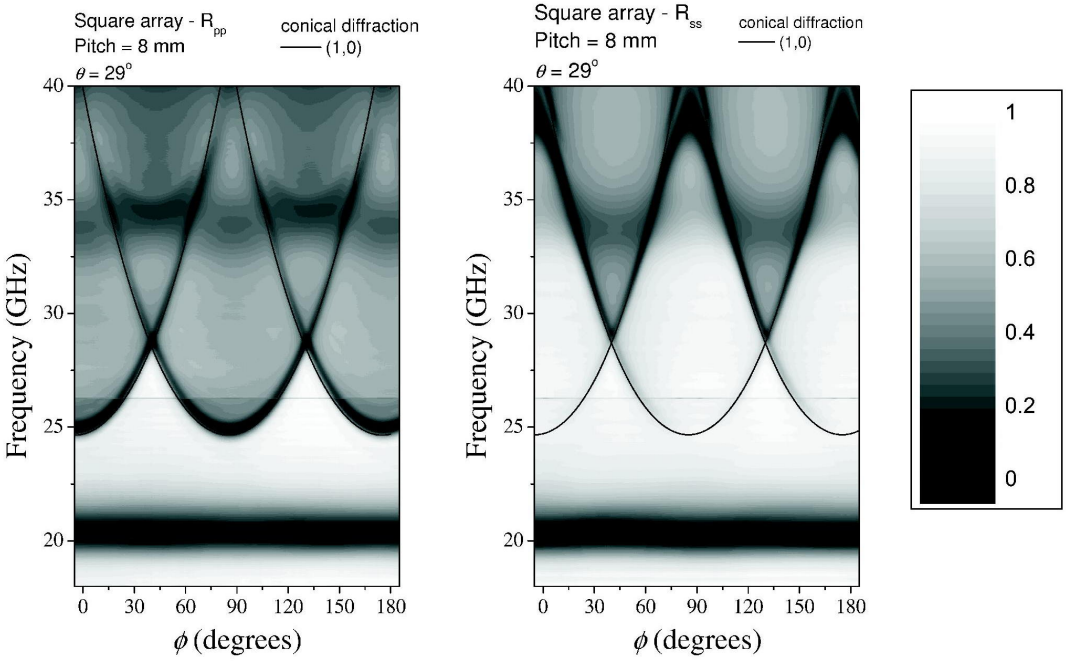

Figure 7.10: Reflectivity data as a function of both azimuthal angle, ϕ and frequency taken from a square array made up of thick pennies with a pitch of 8 mm. Data are taken at a polar angle of $\theta \approx 29°$, and conical diffraction lines are plotted as indicated. Data are shown for both p- (left) and s-polarisations (right).

The following two figures, *Figure* 7.11 and *Figure* 7.12 show reflectivity data from the hexagonal array made up of thick pennies with a pitch of 8.8 mm and at polar angles of $\theta = 7°$ and 31° respectively. Data is displayed in the same way as for the previous samples, with p- (left) and s-polarisations (right) as a function of both azimuthal angle, ϕ, and frequency, and absorption on the z-axis. Again, Mode 1 is observed, this time at a frequency of ∼20 GHz.

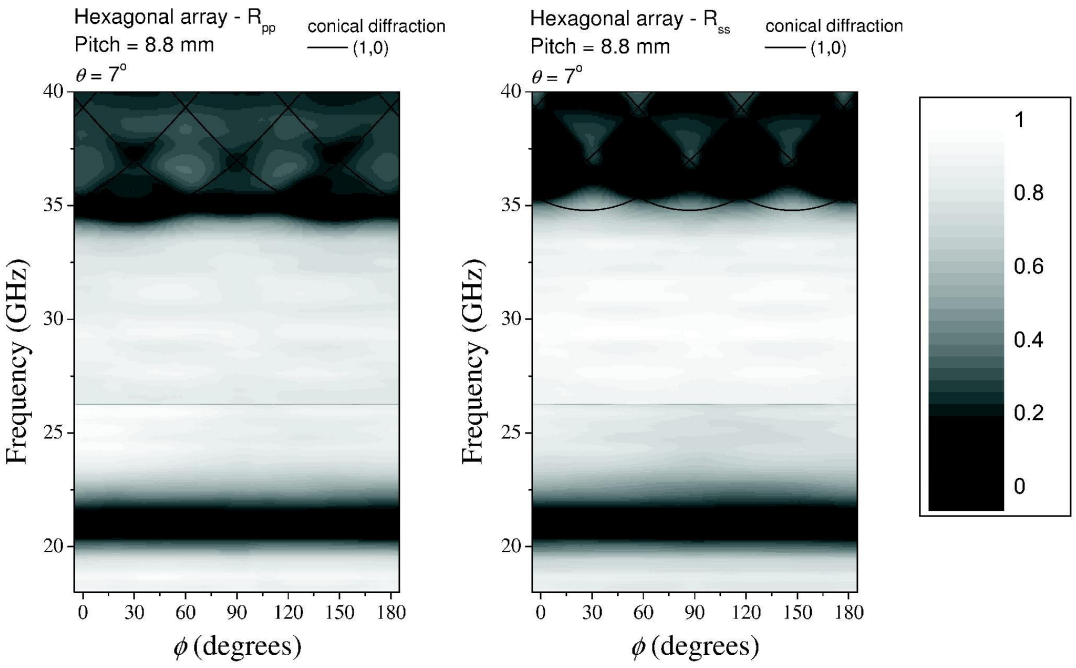

Figure 7.11: Reflectivity data as a function of both azimuthal angle, ϕ and frequency taken from a hexagonal array made up of thick pennies with a pitch of 8.8 mm. Data are taken at a polar angle of $\theta \approx 7°$, and conical diffraction lines are plotted as indicated. Data are shown for both p- (left) and s-polarisations (right).

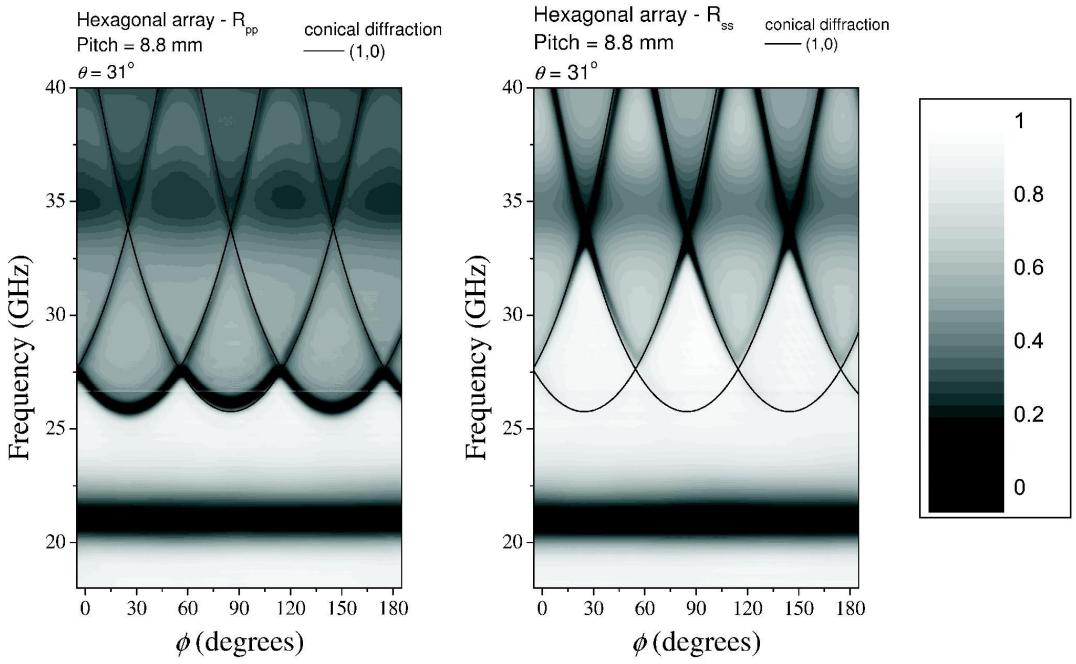

Figure 7.12: Reflectivity data as a function of both azimuthal angle, ϕ and frequency taken from a hexagonal array made up of thick pennies with a pitch of 8.8 mm. Data are taken at a polar angle of $\theta \approx 31°$, and conical diffraction lines are plotted as indicated. Data are shown for both p- (left) and s-polarisations (right).

The following four figures, *Figures* 7.13-7.16 show reflectivity data from the square array made up of thin pennies with a pitch of 6.25 mm and at polar angles of $\theta = 15°, 26°, 46°$and$64°$ respectively. Data is displayed in the same way as for the previous samples, with p- (left) and s-polarisations (right) as a function of both azimuthal angle, ϕ, and frequency, and absorption on the z-axis. *Figure* 7.13 shows three modes appearing in the p-polarised data, occurring at ∼16 GHz, ∼26 GHz and ∼34 GHz. Again, these modes will termed Mode 1, Mode 2 and Mode 3, and are the same as those occurring in the 6 mm pitch, thick penny array. Although it seems that Mode 3 does not appear in the s-polarised reflectivity data in the following figures, it will be shown later that it does exist at certain azimuthal angles, although it is very weakly absorbing. Again, as the polar angle is increased, the higher order modes are lost to diffraction.

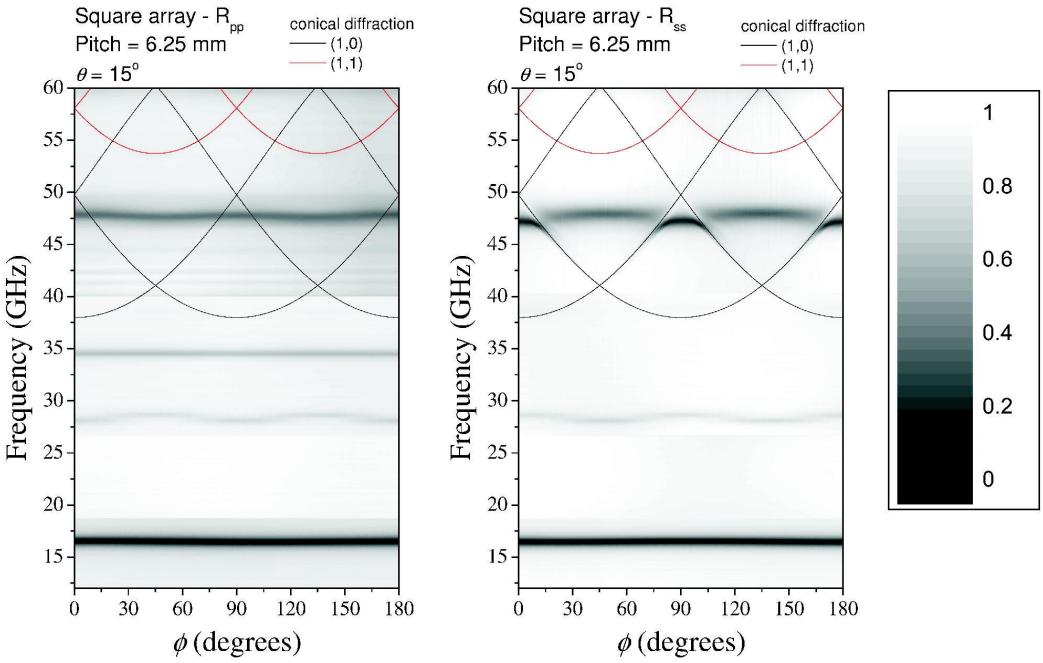

Figure 7.13: Reflectivity data as a function of both azimuthal angle, ϕ and frequency taken from a square array made up of thin pennies with a pitch of 6.25 mm. Data are taken at a polar angle of $\theta \approx 15°$, and conical diffraction lines are plotted as indicated. Data are shown for both p- (left) and s-polarisations (right).

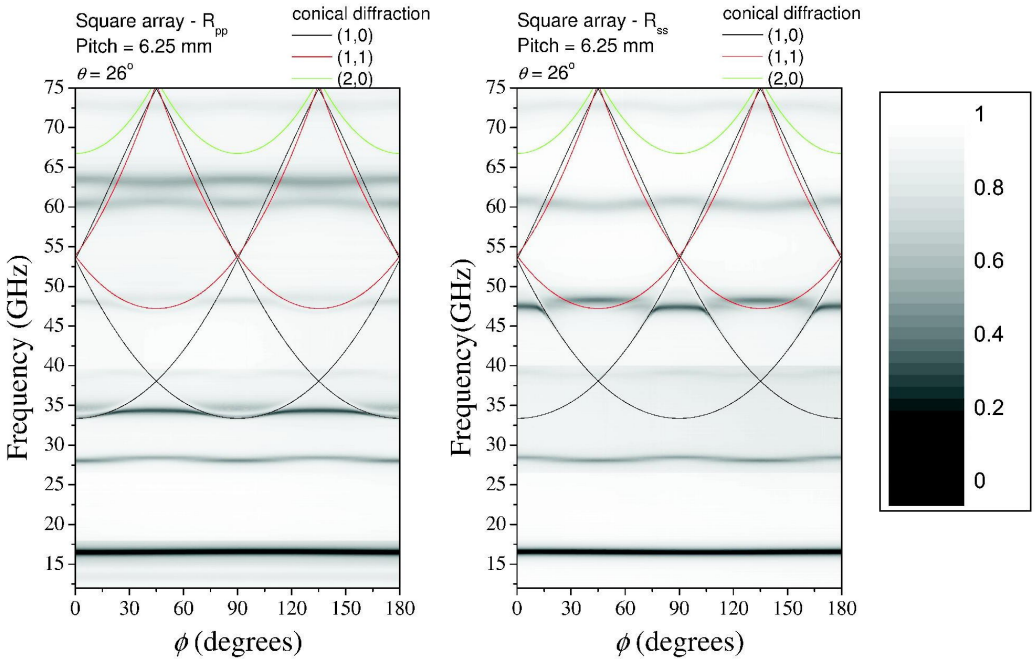

Figure 7.14: Reflectivity data as a function of both azimuthal angle, ϕ and frequency taken from a square array made up of thin pennies with a pitch of 6.25 mm. Data are taken at a polar angle of $\theta \approx 26°$, and conical diffraction lines are plotted as indicated. Data are shown for both p- (left) and s-polarisations (right).

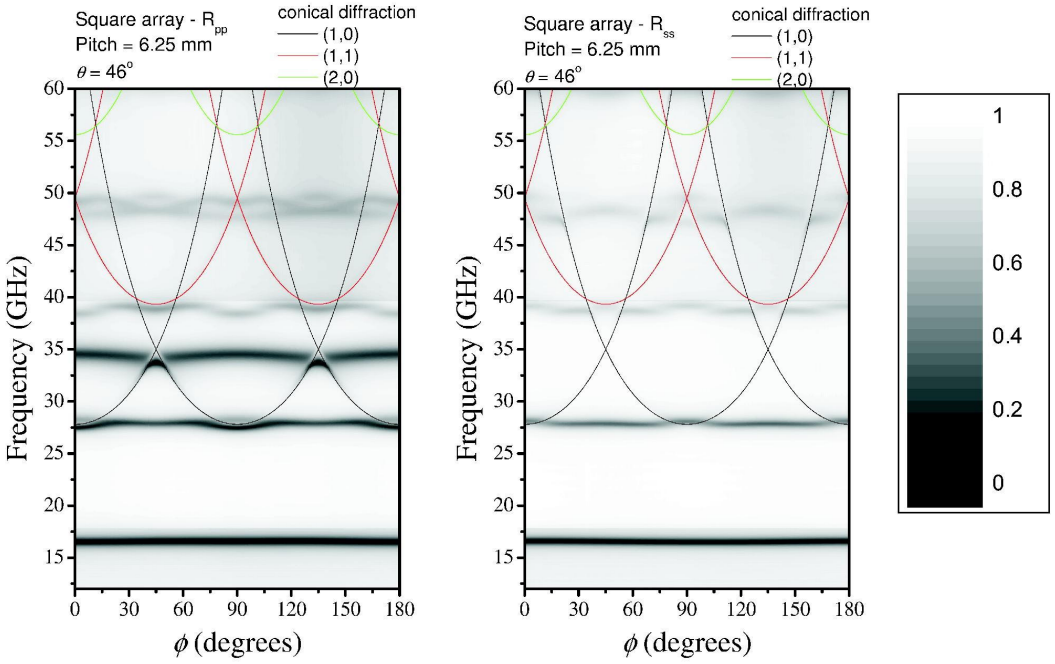

Figure 7.15: Reflectivity data as a function of both azimuthal angle, ϕ and frequency taken from a square array made up of thin pennies with a pitch of 6.25 mm. Data are taken at a polar angle of $\theta \approx 46°$, and conical diffraction lines are plotted as indicated. Data are shown for both p- (left) and s-polarisations (right).

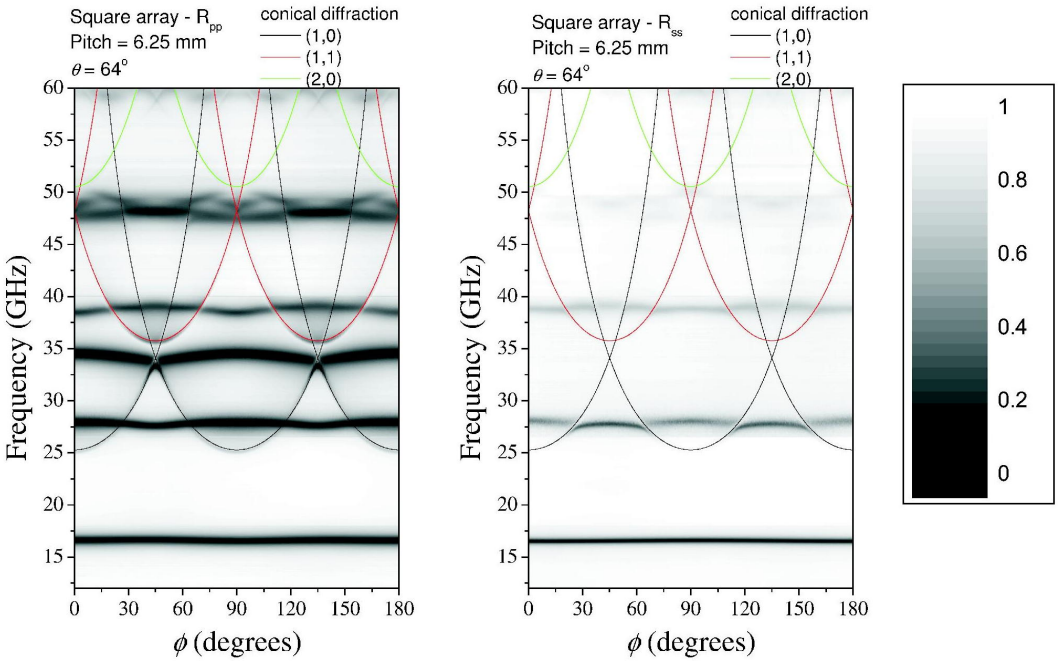

Figure 7.16: Reflectivity data as a function of both azimuthal angle, ϕ and frequency taken from a square array made up of thin pennies with a pitch of 6.25 mm. Data are taken at a polar angle of $\theta \approx 64°$, and conical diffraction lines are plotted as indicated. Data are shown for both p- (left) and s-polarisations (right).

Figures 7.17-7.22 show line plots taken from *Figures* 7.5-7.16 at selected azimuthal angles. The frequency at which each sample becomes diffractive is indicated by the dotted line in each plot.

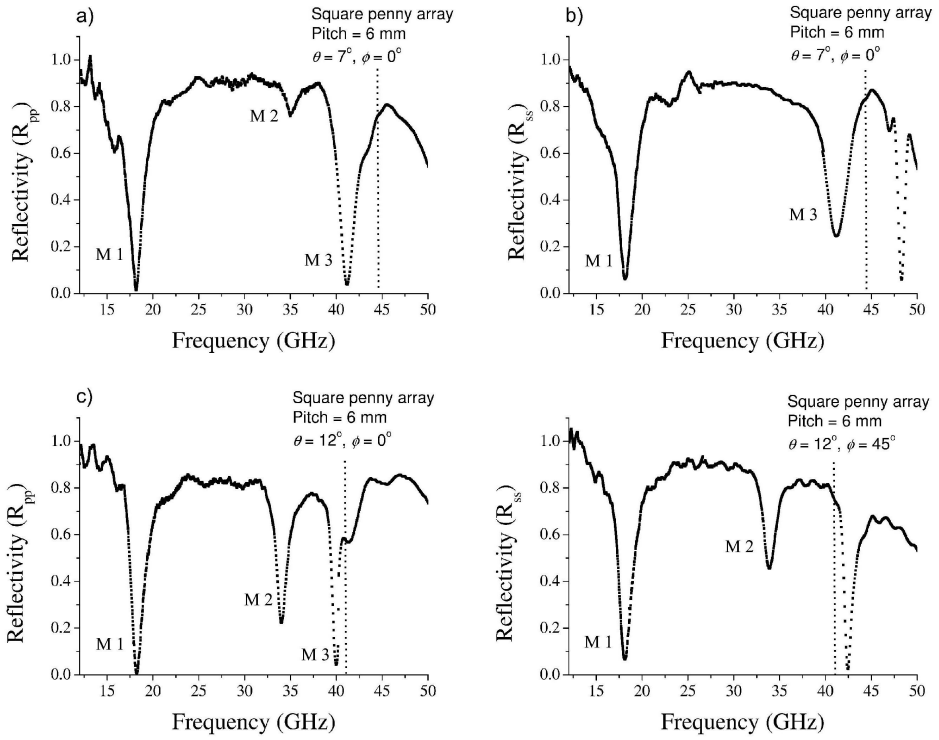

Figure 7.17: Line plots taken from *Figures* 7.5 and 7.6 at selected azimuthal angles, ϕ for the 6 mm pitch, thick penny array. 7.17a) and 7.17c) show R_{pp} for polar angles $\theta \approx 7°$, 12°respectively, and 7.17b) and 7.17d) show R_{ss} for the same polar angles. The dotted line indicates the frequency at which the sample becomes diffractive.

Figure 7.17 shows line plots taken from the 6 mm pitch, thick penny array at polar angles of $\theta \approx 7°$, 12° for both p- and s-polarisations. In the p-polarised data taken at $\theta \approx 7°$ (top left), Modes 1, 2 and 3 are all visible, with absorption due to Modes 1 and 3 reaching almost 100%. Absorption due to Mode 2 is much less. In the s-polarised data taken at the same angle (top right) Modes 1 and 3 occur again, but Mode 2 is not present, as the azimuthal angle is zero, and *Figure* 7.5 showed that Mode 2 does not occur at this angle and polarisation. The p-polarised data taken at $\theta \approx 12°$ (bottom left) again shows Modes 1, 2 and 3, and at this angle absorption due to Mode 2 is much greater, approaching 80%. Mode 3 occurs just below the frequency at which the sample becomes diffractive. The s-polarised data taken at $\theta \approx 12°$(bottom right) is shown for an azimuthal angle of $\phi = 45$, at which angle Mode 2 does occur, and is seen to have an absorption of more than 50%.

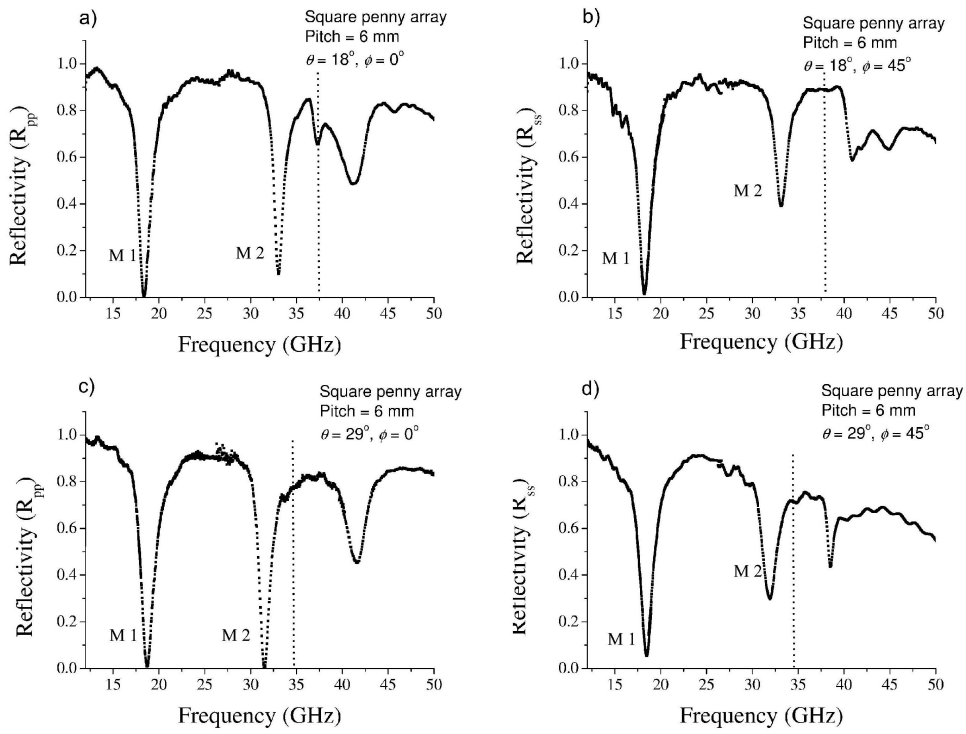

Figure 7.18: Line plots taken from *Figures* 7.7 and 7.8 at selected azimuthal angles, ϕ for the 6 mm pitch, thick penny array. 7.18a) and 7.18c) show R_{pp} for polar angles $\theta \approx 18°$, 29°respectively, and 7.18b) and 7.18d) show R_{ss} for the same polar angles. The dotted line indicates the frequency at which the sample becomes diffractive.

Figure 7.18 displays line plots taken from the 6 mm pitch, thick penny array at polar angles of $\theta \approx 18°$, 29° for both p- and s-polarisations. In this figure, both s-polarisation plots are made at an azimuthal angle of $\phi = 45$, and therefore in each of the four plots the first two reflectivity minima are absorption due to Modes 1 and 2. Any subsequent reflectivity minima are due to diffraction.

Figures 7.19 and 7.20 display line plots taken from the 8 mm pitch, thick penny array, and the 8.8 mm pitch hexagonal array made up of thick pennies. In each case both p- and s-polarisations are displayed for two polar angles. As these arrays have a larger pitch, the frequency at which diffraction occurs is lowered, and therefore only Mode 1 is observed in each plot, occurring at a frequency of ∼20 GHz.

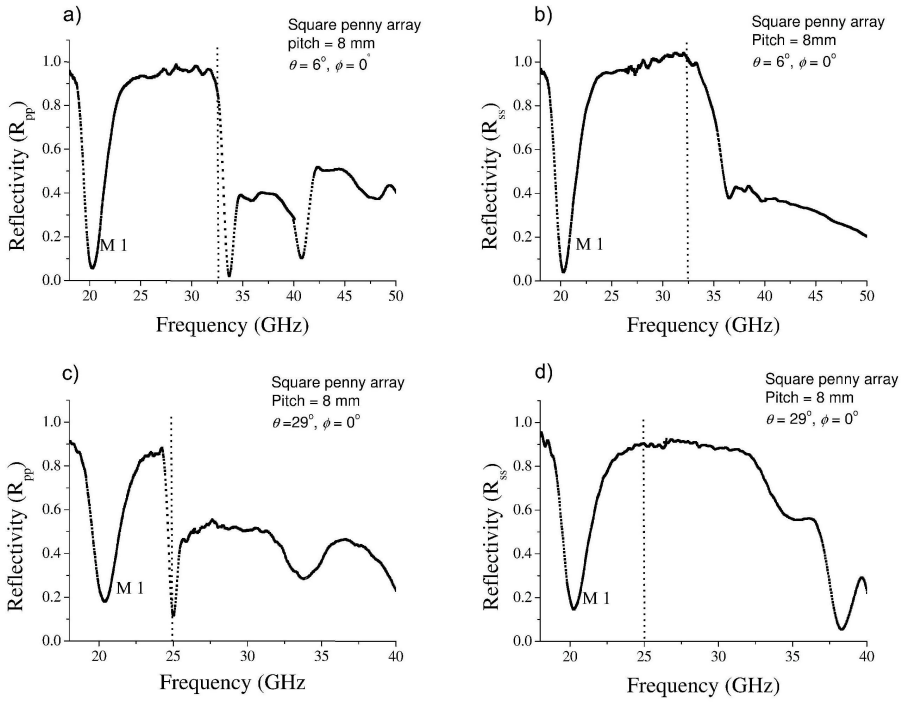

Figure 7.19: Line plots taken from *Figures* 7.9 and 7.10 at selected azimuthal angles, ϕ for the 8 mm pitch, thick penny array. 7.19a) and 7.19c) show R_{pp} for polar angles $\theta \approx 6°$, 29°respectively, and 7.19b) and 7.19d) show R_{ss} for the same polar angles. The dotted line indicates the frequency at which the sample becomes diffractive.

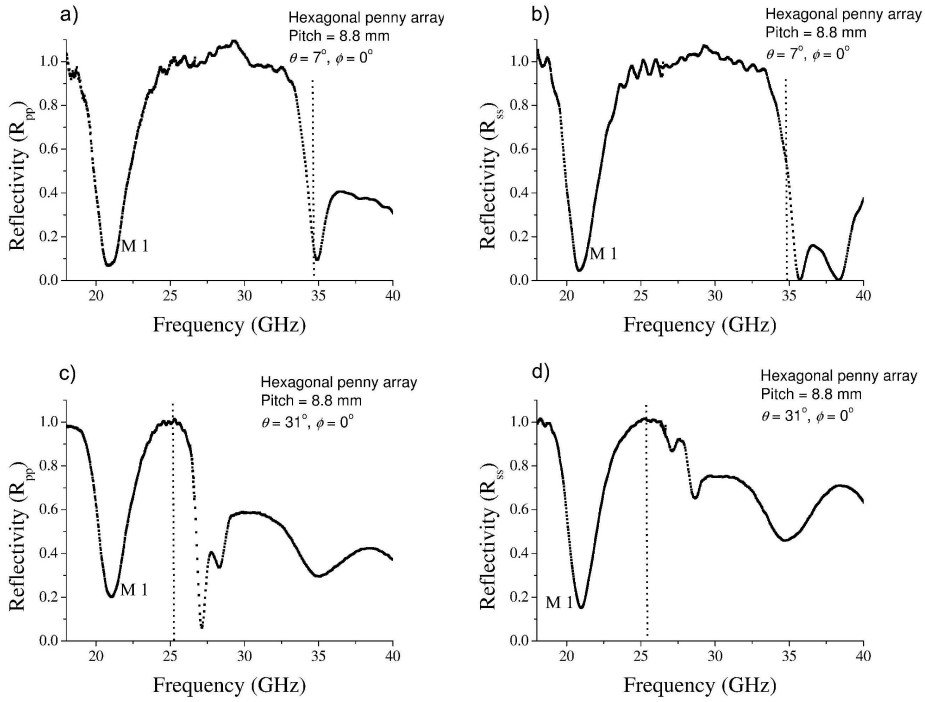

Figure 7.20: Line plots taken from *Figures* 7.11 and 7.12 at selected azimuthal angles, ϕ for the 8.8 mm pitch, hexagonal, thick penny array. 7.20a) and 7.20c) show R_{pp} for polar angles $\theta \approx 7°$, 31°respectively, and 7.20b) and 7.20d) show R_{ss} for the same polar angles. The dotted line indicates the frequency at which the sample becomes diffractive.

The following two line plots are taken from the thin penny array that has a pitch of 6.25 mm. *Figure* 7.21 displays data taken for both polarisations at two polar angles, $\theta \approx 15°$, 26°. In the p-polarised data taken at a polar angle of $\theta \approx 15°$(top left), the lowest three absorption minima are Modes 1, 2 and 3. The fourth absorption minimum is due to diffraction. In the s-polarised data taken at the same angle (top right), all three modes occur again, although the absorption due to Mode 3 is very small, only ∼2-3%. At a polar angle of $\theta \approx 26°$ Modes 1 and 2 appear in the data for both p- and s-polarisations (bottom left and right respectively), however Mode 3 is now lost to diffraction. *Figure* 7.22 shows data taken for both polarisations at polar angles of $\theta \approx 46°$, 64°. Mode 1 is present in all plots, however higher order modes all exist at at frequencies greater than the sample's diffraction limit.

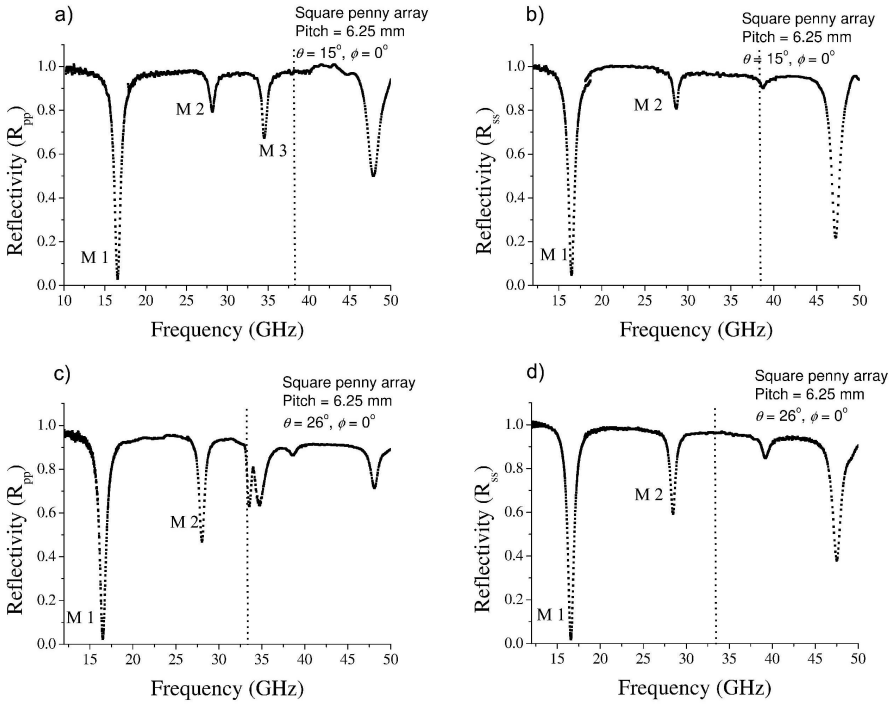

Figure 7.21: Line plots taken from *Figures* 7.13 and 7.14 at selected azimuthal angles, ϕ for the 6.25 mm pitch, thin penny array. 7.21a) and 7.21c) show R_{pp} for polar angles $\theta \approx 15°$, 26°respectively, and 7.21b) and 7.21d) show R_{ss} for the same polar angles. The dotted line indicates the frequency at which the sample becomes diffractive.

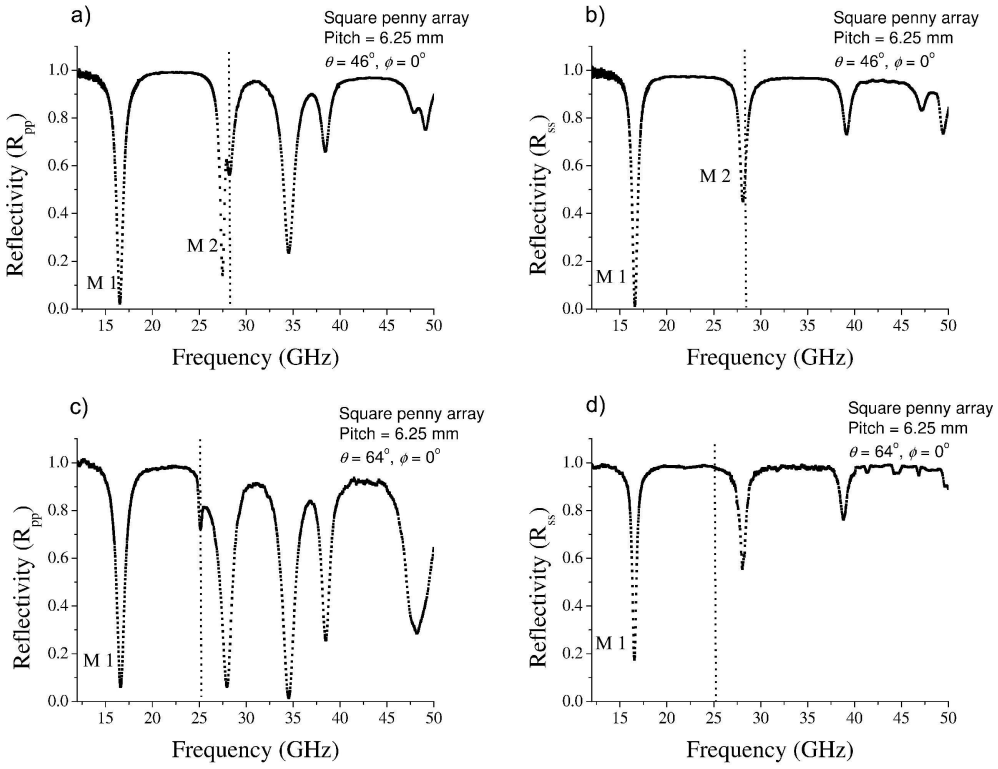

Figure 7.22: Line plots taken from *Figures* 7.15 and 7.16 at selected azimuthal angles, ϕ for the 6.25 mm pitch, thin penny array. 7.22a) and 7.22c) show R_{pp} for polar angles $\theta \approx 46°$, 64°respectively, and 7.22b) and 7.22d) show R_{ss} for the same polar angles. The dotted line indicates the frequency at which the sample becomes diffractive.

In order to understand the nature of these modes, predictions provided by an FEM model will now be compared with data. Then field plots provided by the model will give insight into the nature of the absorption resonances.

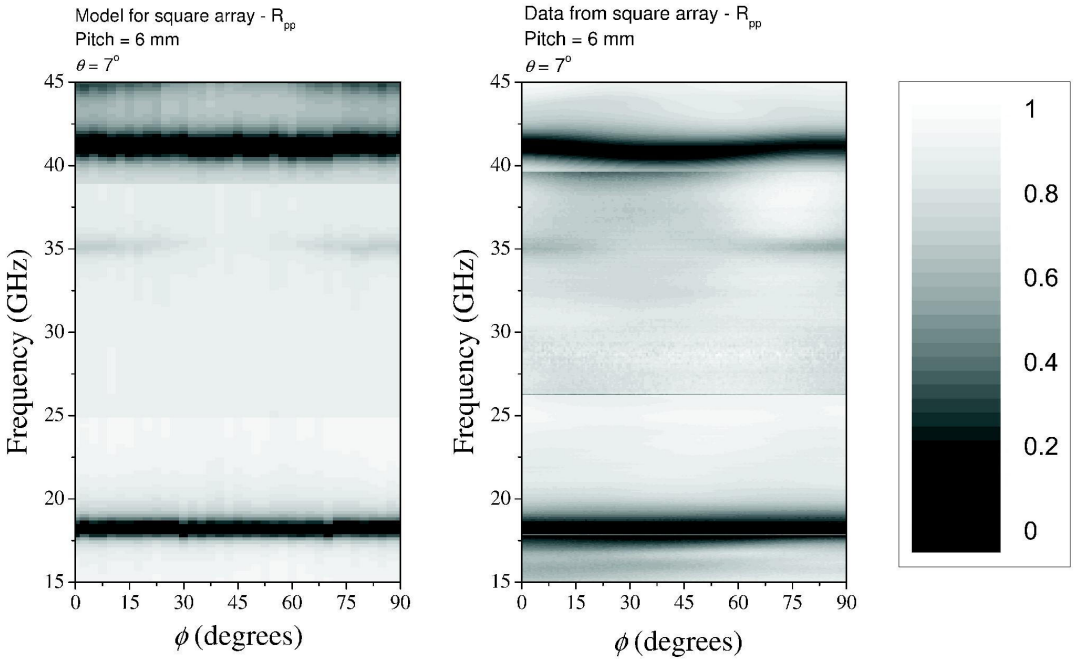

Figure 7.23: A comparison of the prediction provided by HFSS (left) with the data (right) obtained from the 6 mm pitch square array made up of thick pennies.

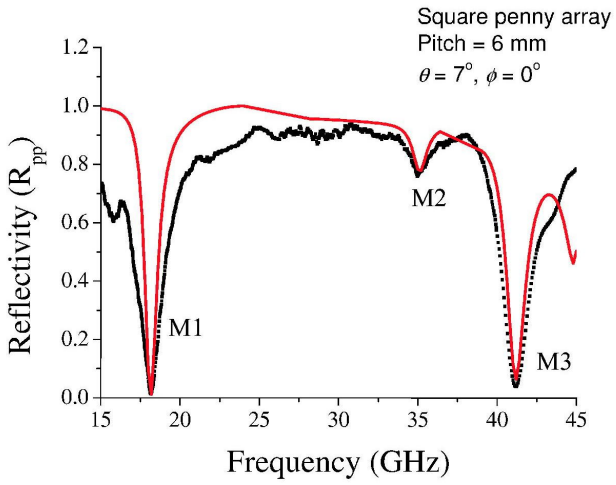

Figure 7.24: A comparison of the prediction provided by HFSS with the data obtained from the 6 mm pitch square array made up of thick pennies at an azimuthal angle $\phi = 0$.

Figures 7.23 and 7.24 display a comparison of data with theory provided by the FEM model for the 6 mm pitch square array made up of thick pennies. Good agreement is obtained, and the model can be used to generate field plots at frequencies corresponding to the resonant absorption features seen in both the data and the model.

Figure 7.25 displays the time-averaged electric (left) and magnetic (right) fields for Mode 1 on the thick penny array plotted across the xy-plane in the dielectric layer at a position 0.025 μm beneath the penny, plotted at a frequency of 18.2 GHz. Field enhancement is relative to the incident field and colour-coded as indicated by the key. At maximum, fields are enhanced by over 50 times; the incident field polarisation is indicated. Two peaks in electric field magnitude occur beneath the penny at the extrema of the penny dimensions in the x-direction, with a null occurring centrally through the penny parallel to the y-axis. It is worth noting that field enhancement is confined to the region directly beneath the penny, with no enhancement occurring outside of this region. The magnetic field magnitude has an oval shaped hotspot in the centre of the penny, with the long axis of the oval parallel to the y-axis.

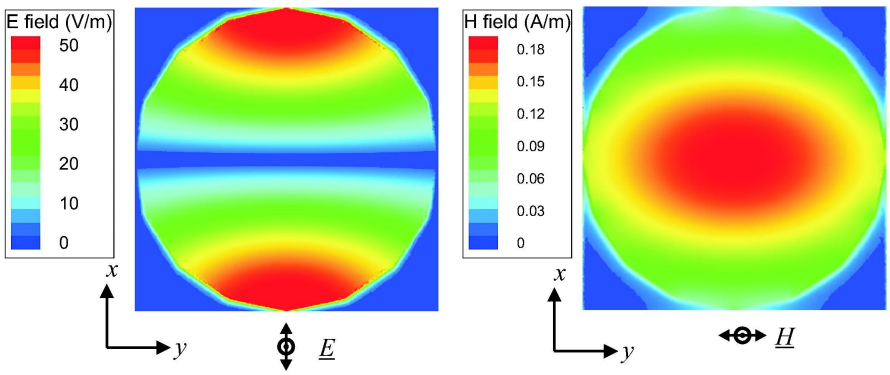

Figure 7.25: Field magnitudes taken from the FEM model for Mode 1 which appears at ~18 GHz (for $\theta = 7°$) in the 6 mm pitch, thick penny array. (left) Electric field magnitude, and (right) magnetic field magnitude. Fields are plotted across the xy-plane at a position 0.025 mm below the top metal layer. Incident polarisation direction is also indicated.

Figure 7.26 displays the electric field distribution for the TE_{11} mode in a circular waveguide as can be seen in *Chapter* 3. It is clear that the electric field distribution of the TE_{11} mode is very similar to that of the *magnetic* field distribution produced by the FEM model for Mode 1. The FEM model allows further comparisons to made between the Mode 1 resonance and the TE_{11} circular waveguide mode.

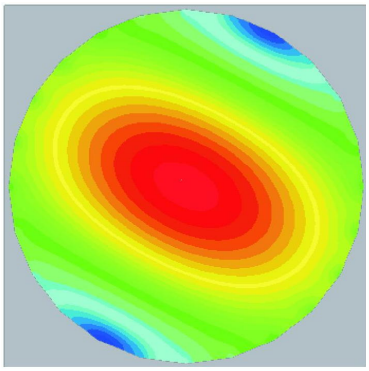

Figure 7.26: The electric field distribution for the TE_{11} mode in a circular waveguide.

Figure 7.27 displays the electric (left) and magnetic (right) field vectors for Mode 1 on the thick penny array plotted across the *xy*-plane at a phase corresponding to maximum enhancement, with incident polarisation direction also indicated. Field enhancement is colour-coded as indicated by the key, and arrows indicate the vector direction. *Figure* 7.28 shows the magnetic (left) and electric (right) field vectors for the TE_{11} mode in a circular waveguide. It is immediately clear that the electric vector field distribution from Mode 1 matches the *magnetic* vector field from the TE_{11} circular waveguide mode, whereas the magnetic vector field distribution from Mode 1 matches the *electric* vector field from the waveguide mode.

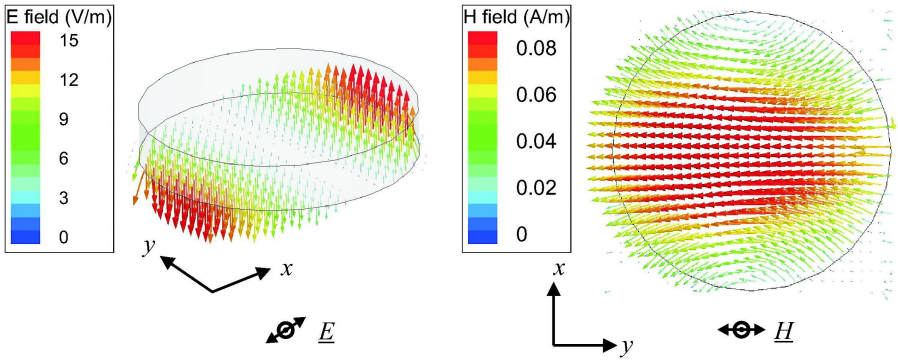

Figure 7.27: (left) Electric and (right) magnetic field vectors taken from the FEM model for Mode 1 in the 6 mm pitch, thick penny array. Fields are plotted across the *xy*-plane at a position 0.025 mm below the top metal layer at a phase corresponding to maximum enhancement. Incident polarisation direction is also indicated.

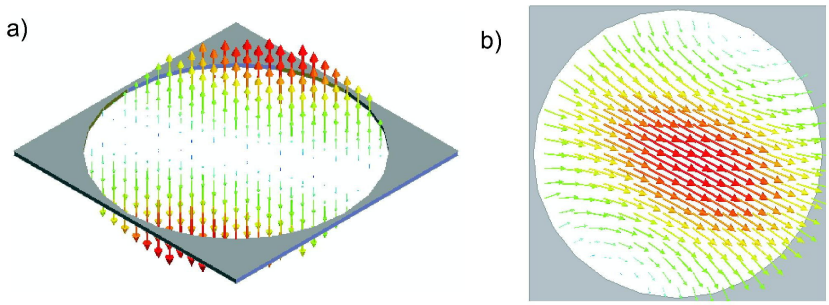

Figure 7.28: a) Magnetic and b) electric field vectors for the TE_{11} mode in a circular waveguide.

The similarity of, but "field-switched" nature of the field distributions between Mode 1 and the TE_{11} waveguide mode are less surprising when the boundaries of the two structures are considered. A vacuum-filled, metal-clad circular waveguide that is infinite in its extent is enclosed by an electric wall (as the metal is assumed to be perfectly conducting) such that tangential electric fields drop to zero at the waveguide walls. This approximates the "inverse" of the penny array structure, where the metal layers may be considered as analogous to the open ends of the waveguide, and these are the electric walls of the structure. This "reversal" of the boundary conditions between the two structures allows a mode to exist in the penny structure that has a field distribution similar to that of the TE_{11} waveguide mode, but with the electric and magnetic field distributions interchanged. *Chapter* 3 showed that it is possible to predict a cut-off frequency for the TE_{11} mode below which it cannot propagate, and we can use this equation to predict the lowest frequency at which this mode can exist.

The cut-off frequency for a circular waveguide is given by:

$$f_c = \frac{1.841c}{2\pi an}$$

where a is the radius of the waveguide and n is the refractive index of the core. A full derivation of this equation is in *Chapter* 3. Applying this equation to the penny structure yields a cut-off frequency of 18.1 GHz, closely matching the observed frequency of ~18 GHz. This it is confirms the identification of Mode 1 as being analogous to the TE_{11} mode in a circular waveguide. Continuing with circular waveguide theory, the next two lowest frequency modes to propagate are the TE_{21}, and the TE_{01}, and it may be reasonable to expect that Modes 2 and 3 observed in the penny arrays correspond to these waveguide modes.

Figure 7.29 displays the time-averaged electric (left) and magnetic (right) field magnitudes for Mode 2 on the thick penny array plotted across the xy-plane in the dielectric layer at a position 0.025 μm beneath the penny, plotted at a frequency of 35 GHz. Field enhancement is relative to the incident field and colour-coded as indicated by the key. At maximum, fields are enhanced by 15 times; the incident field polarisation is indicated. Four peaks in electric field are observed around the penny edge, at the penny maximum and minimum values of x and y. The magnetic field magnitude also has four peaks in intensity, located on the xy diagonals.

Figure 7.30 shows the electric field distribution for the TE_{21} mode in a circular waveguide, and indeed, the distribution matches the magnetic field distribution for Mode 2.

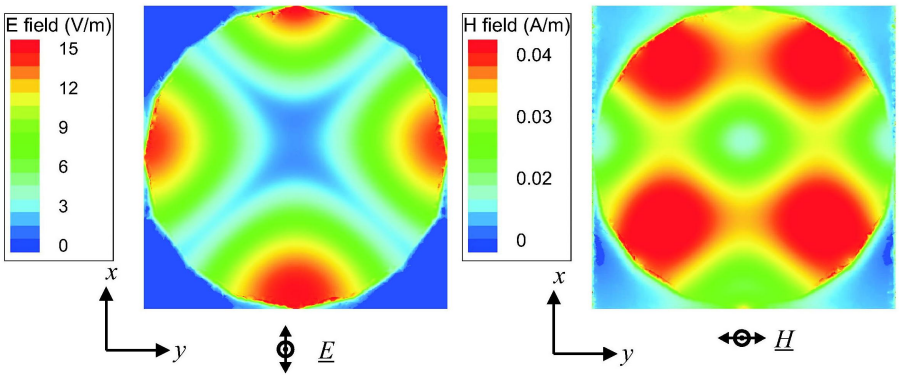

Figure 7.29: Field magnitudes taken from the FEM model for Mode 2 which appears at ~34 GHz (for $\theta = 7°$) in the 6 mm pitch, thick penny array. (left) Electric field magnitude, and (right) magnetic field magnitude. Fields are plotted across the xy-plane at a position 0.025 mm below the top metal layer. Incident polarisation direction is also indicated.

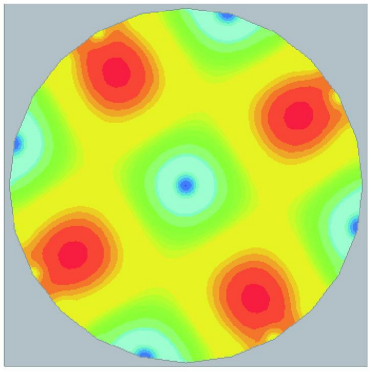

Figure 7.30: The electric field distribution for the TE_{21} mode in a circular waveguide.

Figure 7.31 displays the electric (left) and magnetic (right) field vectors for Mode 2 on the thick penny array plotted across the xy-plane at a phase corresponding to maximum enhancement, with incident polarisation direction also indicated. Field enhancement is colour-coded as indicated by the key, and arrows indicate the vector direction. *Figure* 7.32 shows the magnetic (left) and electric (right) field vectors for the TE_{11} mode in a circular waveguide. Once more, the field distributions for the electric and magnetic vectors of Mode 2 resemble very closely the field distributions of the magnetic and electric vectors of the TE_{21} waveguide mode.

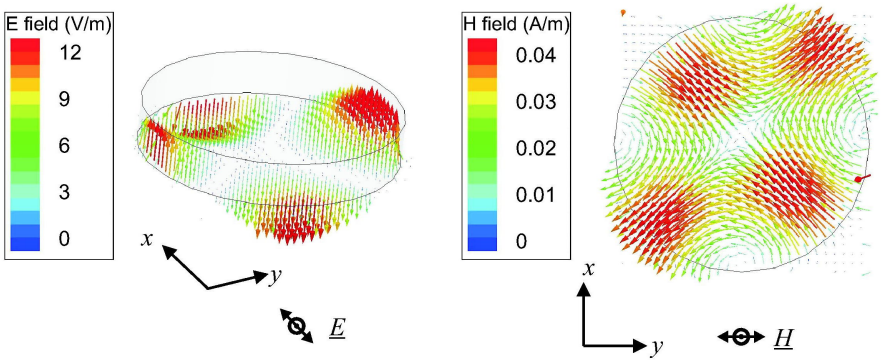

Figure 7.31: (left) Electric and (right) magnetic field vectors taken from the FEM model for Mode 2 in the 6 mm pitch, thick penny array. Fields are plotted across the xy-plane at a position 0.025 mm below the top metal layer at a phase corresponding to maximum enhancement. Incident polarisation direction is also indicated.

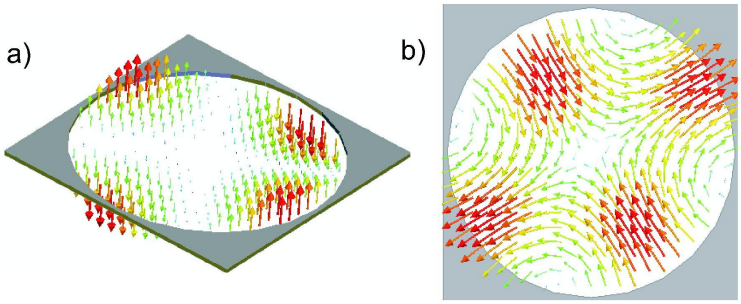

Figure 7.32: a) Magnetic and b) electric field vectors for the TE_{21} mode in a circular waveguide.

The similarity in the field distribution between the electric and magnetic fields of Mode 2 on the thick penny array, and the magnetic and electric fields of the TE_{21} mode in a circular waveguide are again due to the interchange of boundary condition between the two structures. Once more, we can calculate a cut-off frequency for Mode 2 based on the cut-off frequency of the TE_{21} waveguide mode.

$$f_c = \frac{3.054c}{2\pi an}$$

Applying this equation yields a cut-off frequency of 30.1 GHz. This is somewhat lower in frequency than the observed position of Mode 2, which is 35 GHz, however the calculation is derived from an infinite waveguide surrounded by a perfect conductor, and the penny array is only an approximation of such a system, with boundary conditions inverted.

Figure 7.33 shows the time-averaged electric (left) and magnetic (right) field magnitudes for Mode 3 on the thick penny array plotted across the xy-plane in the dielectric layer at a

position 0.025 μm beneath the penny, plotted at a frequency of 41.6 GHz. Field enhancement is relative to the incident field and colour-coded as indicated by the key. At maximum, fields are enhanced by 50 times and incident field polarisation is indicated. The field distribution for Mode 3 is quite different to that of Modes 1 and 2. The electric field magnitude distribution has a peak beneath the centre of the penny, surrounded by a field null, and then an increase in magnitude around the penny edge. The magnetic field distribution is the opposite, with a null in the centre of the penny, surrounded by a field maximum. If the magnetic field enhancement is compared to the electric field enhancement of the third propagating waveguide mode in a circular waveguide, the TE_{01} (shown in *Figure* 7.34), it appears almost identical, thereby confirming that Mode 3 is analogous to the TE_{01} waveguide mode.

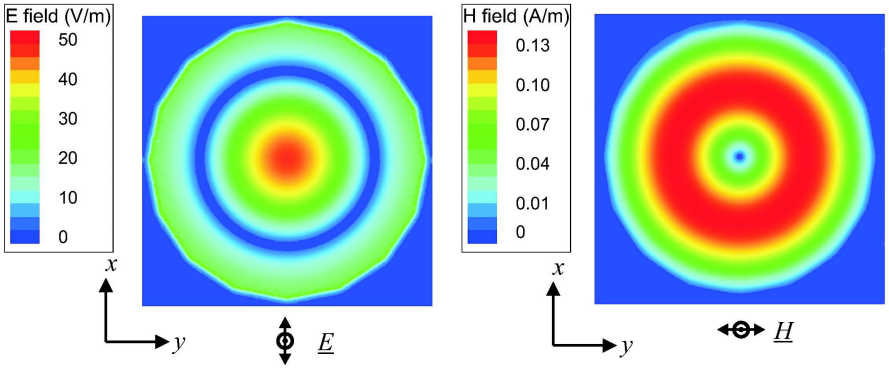

Figure 7.33: Field magnitudes taken from the FEM model for Mode 3 which appears at ~41.6 GHz (for $\theta = 6°$) in the 6 mm pitch thick penny array. (left) Electric field magnitude, and (right) magnetic field magnitude. Fields are plotted across the xy-plane at a position 0.025 mm below the top metal layer. Incident polarisation direction is also indicated.

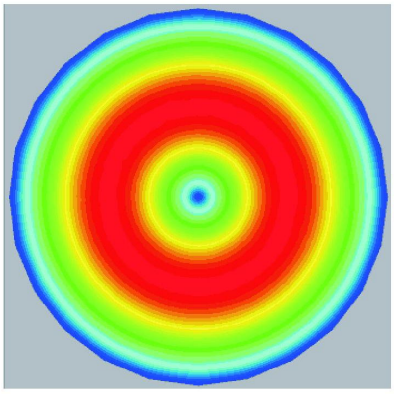

Figure 7.34: The electric field distribution for the TE_{01} mode in a circular waveguide.

Figure 7.35 displays the the electric (left) and magnetic (right) field vectors for Mode 3 on the thick penny array plotted across the xy-plane at a phase corresponding to maximum enhancement, with incident polarisation direction also indicated. Field enhancement is colour-coded as indicated by the key, and arrows indicate the vector direction. Once more, these vector distributions can be compared to those from the TE_{01} mode in a circular waveguide, shown in *Figure* 7.36.

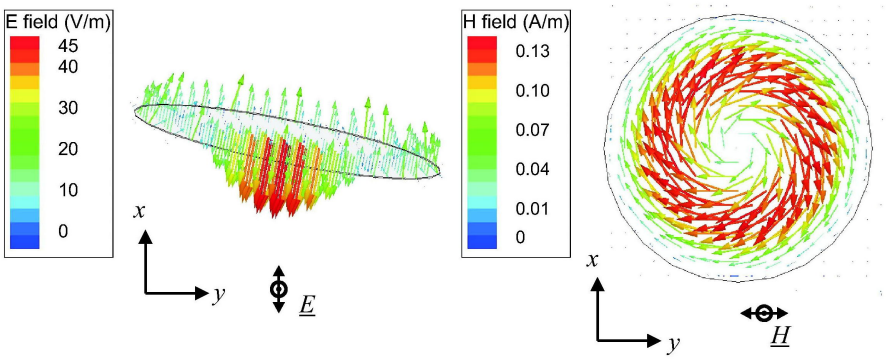

Figure 7.35: (left) Electric and (right) magnetic field vectors taken from the FEM model for Mode 3 in the 6 mm pitch, thick penny array. Fields are plotted across the xy-plane at a position 0.025 mm below the top metal layer at a phase corresponding to maximum enhancement. Incident polarisation direction is also indicated.

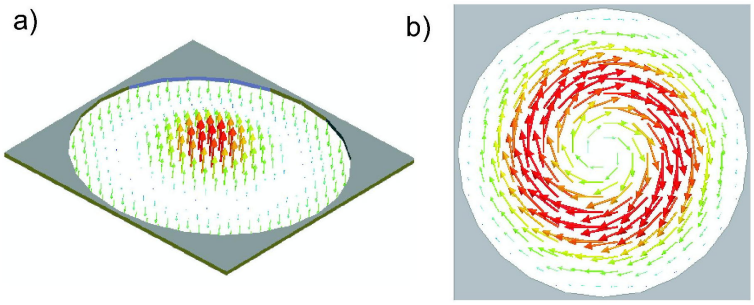

Figure 7.36: a) Magnetic and b) electric field vectors for the TE_{01} mode in a circular waveguide.

The electric and magnetic vector distributions for Mode 3 closely match the magnetic and electric vector distributions for the TE_{01} mode in a circular waveguide, and therefore we can calculate a cut-off frequency for this mode on the thick penny array, from the following equation.

$$f_c = \frac{3.832c}{2\pi an}$$

which yields a cut-off frequency of 37.7 GHz, again somewhat lower than the observed frequency of 41.6 GHz.

Both the 8 mm pitch square array and the 8.8 mm pitch hexagonal array made up of thick pennies display a mode at approximately 20 GHz. Field plots generated from models of these structures reveal the electric and magnetic field distributions to be virtually identical to those generated for Mode 1 in the 6 mm pitch penny array. Therefore the modes observed in both of these arrays is confirmed to be Mode 1.

Figures 7.37 and 7.38 displays the data taken from the thin penny array plotted with a prediction provided by the FEM model. Both figures give good comparison for Modes 1, 2 and 3, and field plots from HFSS will now be used to confirm that these are the same modes as observed in the previous sample, the thick penny array.

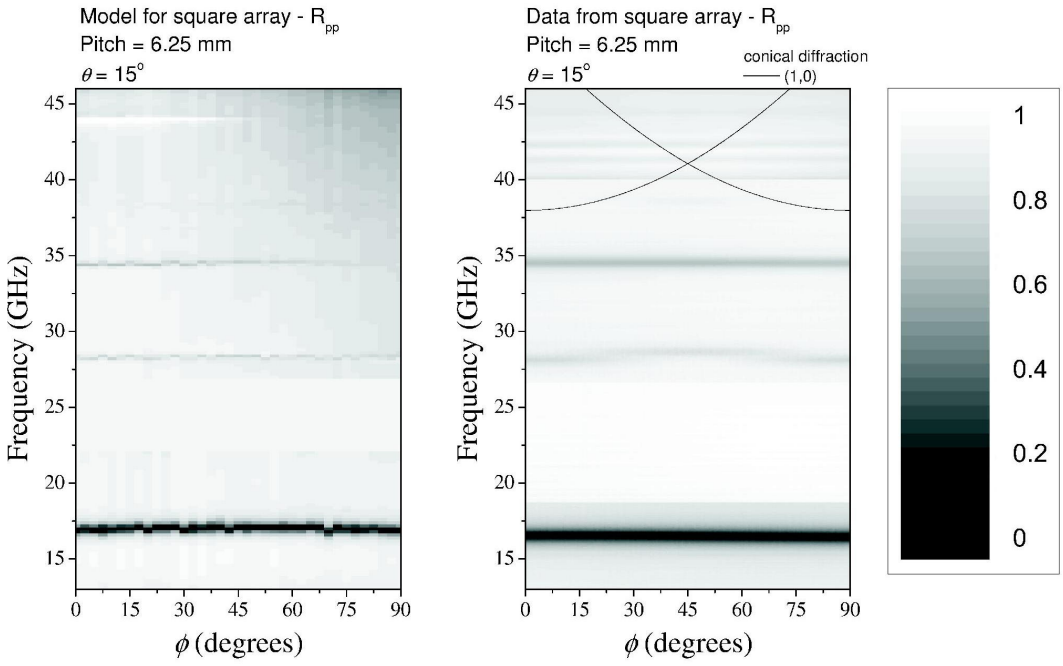

Figure 7.37: A comparison of the prediction provided by HFSS (left) with the data (right) obtained from the 6.25 mm pitch square array made up of thin pennies.

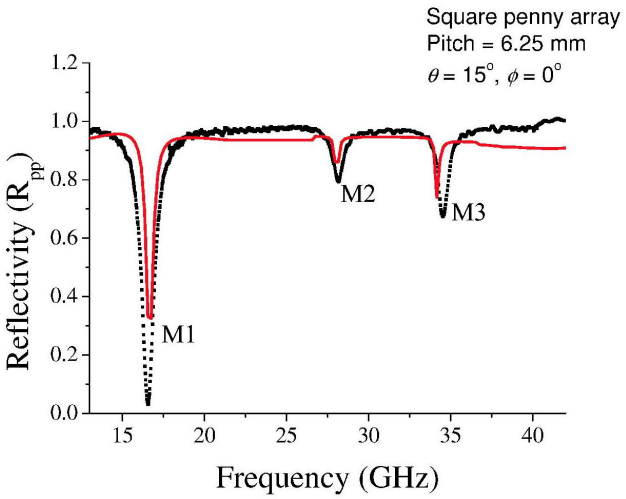

Figure 7.38: A comparison of the prediction provided by HFSS with the data obtained from the 6.25 mm pitch square array made up of thin pennies at an azimuthal angle $\phi = 0$.

Figure 7.39 shows the time-averaged electric (left) and magnetic (right) field magnitudes for Mode 1 on the thin penny array plotted across the xy-plane in the dielectric layer at a position 0.025 μm beneath the penny, plotted at a frequency of 16.5 GHz. Field enhancement is relative to the incident field and colour-coded as indicated by the key. At maximum, fields are enhanced by 50 times and incident field polarisation is indicated. The field distribution is very similar to that observed for the thick penny array, (shown in *Figure* 7.25) and as previously, these field distributions can be compared to those of the TE_{11} waveguide mode, (*Figure* 7.26) albeit with the electric and magnetic distributions interchanged.

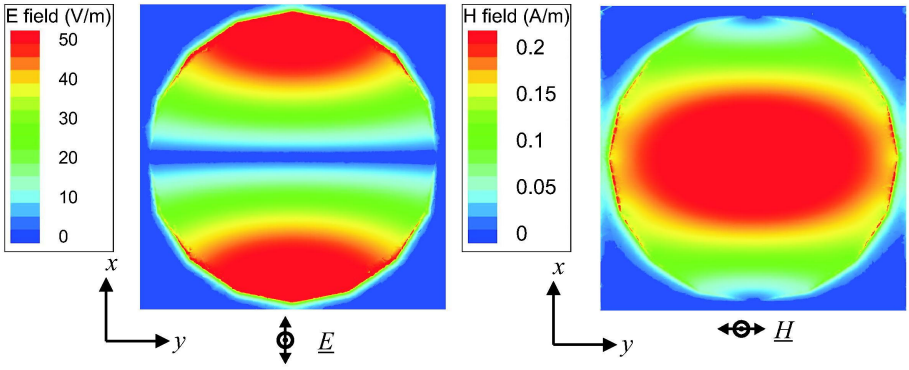

Figure 7.39: Field magnitudes taken from the FEM model for Mode 1 which appears at ~16.5 GHz (for $\theta = 6°$) in the 6.25 mm pitch thin penny array. (left) Electric field magnitude, and (right) magnetic field magnitude. Fields are plotted across the xy-plane at a position 0.017 mm below the top metal layer. Incident polarisation direction is also indicated.

Figure 7.40 displays the electric (left) and magnetic (right) field vectors for Mode 1 on the thin penny plotted across the xy-plane at a phase corresponding to maximum enhancement,

with incident polarisation direction also indicated. Field enhancement is colour-coded as indicated by the key, and arrows indicate the vector direction. The electric and magnetic vectors again correspond to the magnetic and electric vectors of the TE_{11} waveguide mode as seen in *Figure* 7.27. Once more a cut-off frequency for this mode can be calculated. It will be different to that of the thick penny array due to the different penny radius and core refractive index. It is calculated from the equation:

$$f_c = \frac{1.841c}{2\pi an}$$

and yields a cut-off frequency of 16.5 GHz, closely matching the observed frequency of ~16.5 GHz for Mode 1 on this structure.

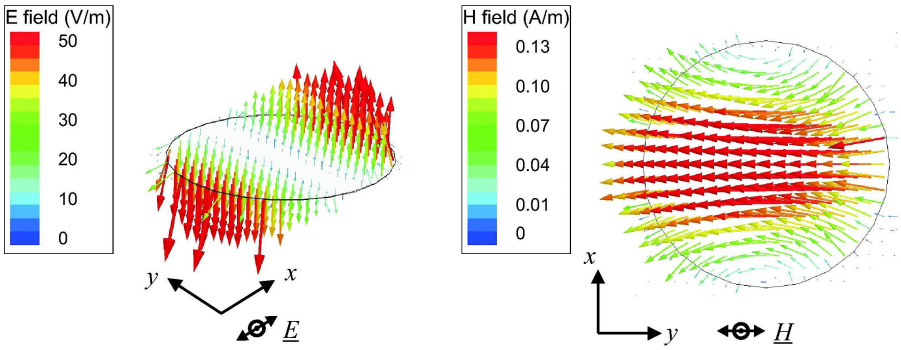

Figure 7.40: (left) Electric and (right) magnetic field vectors taken from the FEM model for Mode 1 in the 6.25 mm pitch, thin penny array. Fields are plotted across the *xy*-plane at a position 0.017 mm below the top metal layer at a phase corresponding to maximum enhancement. Incident polarisation direction is also indicated.

Figure 7.41 shows the time-averaged electric (left) and magnetic (right) field magnitudes for Mode 2 on the thin penny array plotted across the *xy*-plane in the dielectric layer at a position 0.025 μm beneath the penny, plotted at a frequency of 28 GHz. Field enhancement is relative to the incident field and colour-coded as indicated by the key. At maximum, fields are enhanced by 20 times and incident field polarisation is indicated. The field distributions match those observed for Mode 2 on the thick penny array, and therefore Mode 2 on the thin penny array is shown to be analogous Mode 2 on the thick penny array, and the TE_{21} waveguide mode also.

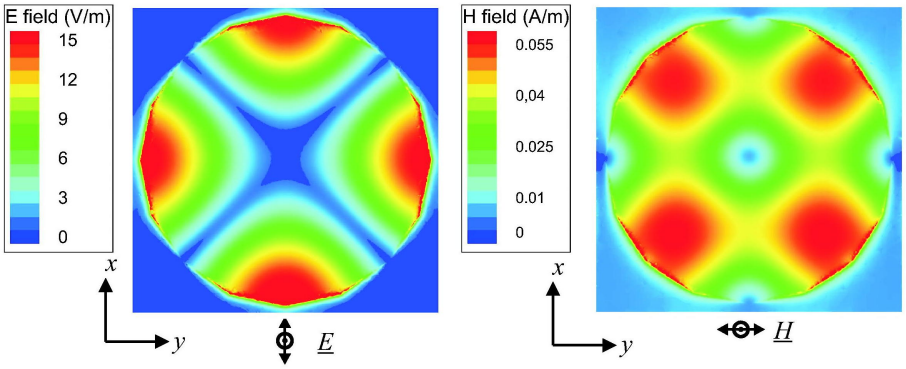

Figure 7.41: Field magnitudes taken from the FEM model for Mode 2 which appears at ∼28 GHz (for $\theta = 6°$) in the 6.25 mm pitch thin penny array. (left) Electric field magnitude, and (right) magnetic field magnitude. Fields are plotted across the xy-plane at a position 0.017 mm below the top metal layer. Incident polarisation direction is also indicated.

Figure 7.42 displays the electric (left) and magnetic (right) field vectors for Mode 2 on the thin penny array plotted across the xy-plane at a phase corresponding to maximum enhancement, with incident polarisation direction also indicated. Field enhancement is colour-coded as indicated by the key, and arrows indicate the vector direction. Both the magnetic field magnitude, and the electric vector and magnetic vector can be compared to those of the TE_{21} waveguide mode displayed in *Figures* 7.30 and 7.32, where the field distributions are matched for interchanged electric and magnetic distributions. The cut-off frequency for Mode 2 on the thin penny array is calculated from the following equation:

$$f_c = \frac{3.054c}{2\pi an}$$

and is found to be 27.3 GHz, closely matching the observed frequency of ∼28 GHz for Mode 2 on this structure.

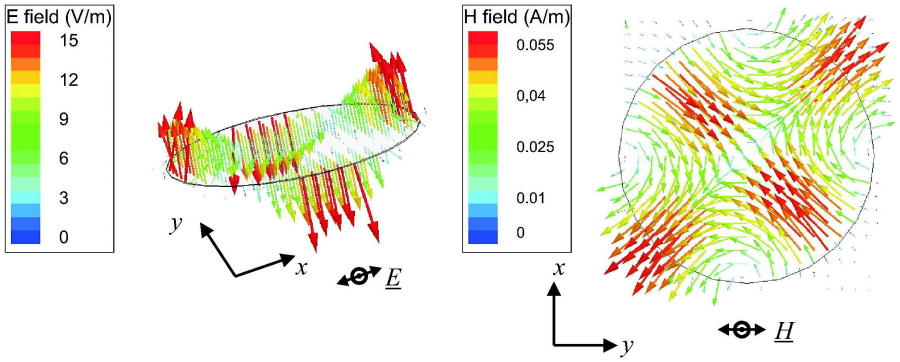

Figure 7.42: (left) Electric and (right) magnetic field vectors taken from the FEM model for Mode 2 in the 6.25 mm pitch, thin penny array. Fields are plotted across the xy-plane at a position 0.017 mm below the top metal layer at a phase corresponding to maximum enhancement. Incident polarisation direction is also indicated.

Figure 7.43 shows shows the time-averaged electric (left) and magnetic (right) field magnitudes for Mode 3 on the thin penny array plotted across the xy-plane in the dielectric layer at a position 0.017 μm beneath the penny, plotted at a frequency of 34.5 GHz. Field enhancement is relative to the incident field and colour-coded as indicated by the key. At maximum, fields are enhanced by 50 times and incident field polarisation is indicated.

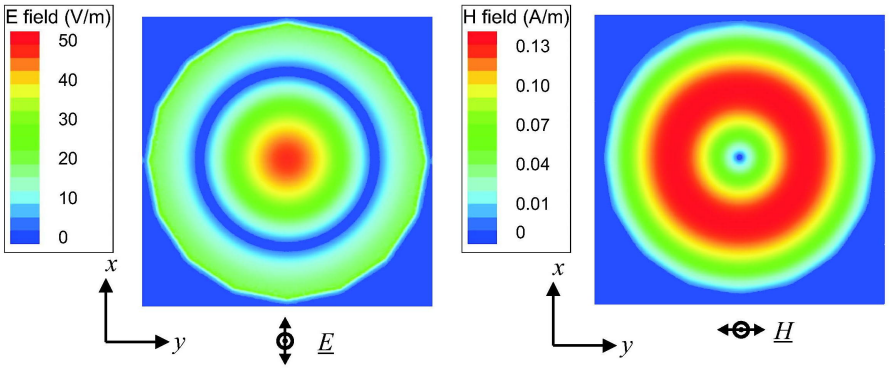

Figure 7.43: Field magnitudes taken from the FEM model for Mode 3 which appears at ~34 GHz (for $\theta = 6°$) in the 6.25 mm pitch thin penny array. (left) Electric field magnitude, and (right) magnetic field magnitude. Fields are plotted across the xy-plane at a position 0.017 mm below the top metal layer. Incident polarisation direction is also indicated.

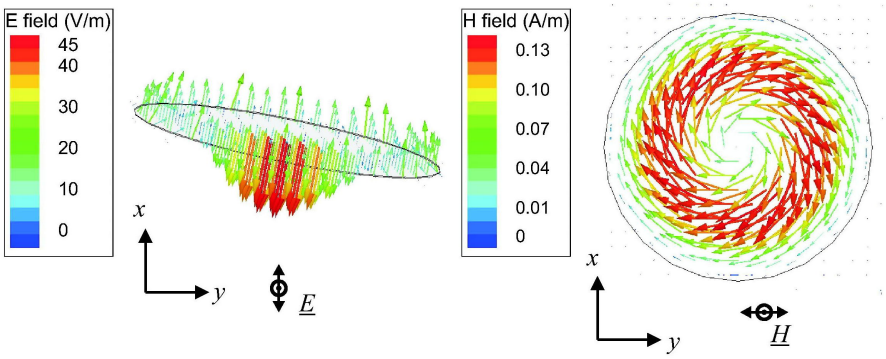

Figure 7.44: (left) Electric and (right) magnetic field vectors taken from the FEM model for Mode 3 in the 6.25 mm pitch, thin penny array. Fields are plotted across the xy-plane at a position 0.017 mm below the top metal layer at a phase corresponding to maximum enhancement. Incident polarisation direction is also indicated.

Figure 7.44 displays the the electric (left) and magnetic (right) field vectors for Mode 3 on the thin penny array plotted across the xy-plane at a phase corresponding to maximum enhancement, with incident polarisation direction also indicated. Field enhancement is colour-coded as indicated by the key, and arrows indicate the vector direction. Once more, these field magnitude and vector distributions can be compared to those from the TE_{01} mode in a circular waveguide, shown in *Figures* 7.34 and 7.36. The electric and magnetic vector distributions for Mode 3 closely match the magnetic and electric vector distributions for the TE_{01} mode in a circular waveguide, and therefore we can calculate a cut-off frequency for this mode on the thin penny array, from the following equation.

$$f_c = \frac{3.832c}{2\pi an}$$

which yields a cut-off frequency of 34.2 GHz, once more, close to the observed frequency of ~34 GHz for Mode 3 on this structure.

Each mode occurring in the non-diffractive region has now been identified with reference to waveguide modes, however, the frequency at which Modes 2 and 3 occur (and the level of absorption due to these modes) is clearly seen to be dependent on the azimuthal angle, ϕ. The above analysis is based on treating each a single penny as an analogy to a circular waveguide, however, the changing mode behaviour when scanning azimuthally clearly indicates that the resonant absorption of Modes 2 and 3 is dependent not only on the field distribution due to single pennies, but also due to the interaction of fields between pennies. The reason for the reduction in the absorption of Mode 2 in the square array made up of thick pennies may be understood by again examining the electric and magnetic vector profiles.

Recall *Figure* 7.6 (shown again in *Figure* 7.45). Here, in the p-polarised data, the level of resonant absorption due to Mode 2 is seen to oscillate over each 90° change in azimuthal angle.

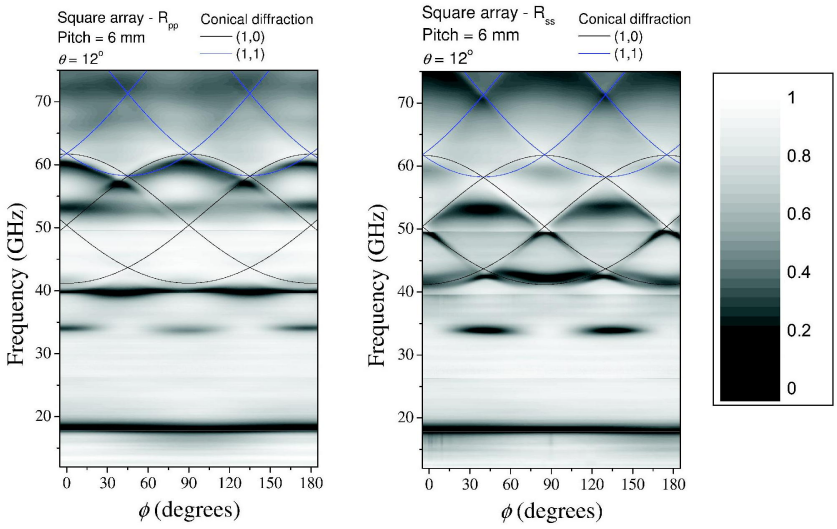

Figure 7.45: Reflectivity from the square array made up of thick pennies, with a 6 mm pitch.

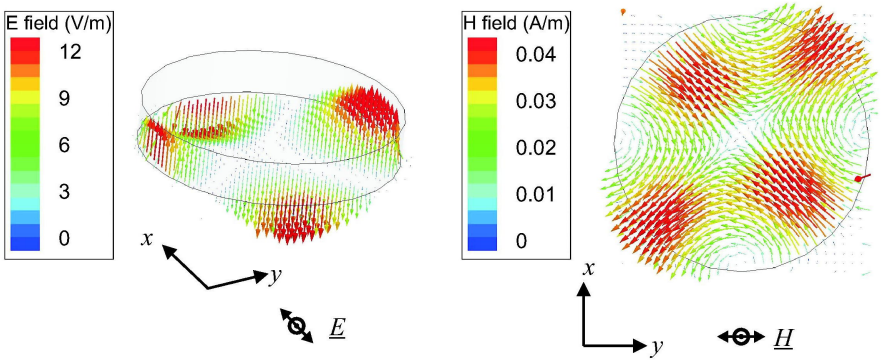

Figure 7.46: (left) Electric and (right) magnetic field vectors taken from the FEM model for Mode 2 in the 6 mm pitch, thick penny array.

Examining the field plots provided by HFSS allowed Mode 2 to be identified as an analogy to a waveguide mode, the TE_{01}. The electric (left) and magnetic (right) vectors are shown in *Figure* 7.46. The magnetic vector is directed outwards from the penny centre at 45° to the x-axis. If we consider the neighboring penny to having the same field profile, there is little interaction between the fields generated by each. However, if the penny undergoes a

45° rotation in azimuthal angle, then the magnetic vector direction from neighboring pennies will act in opposition parallel to the y-axis, resulting in a reduction in the field magnitude, and consequently a reduction in the absorption due to Mode 2. This is the reason for the oscillatory behaviour of Mode 2 with respect to azimuthal angle.

Finally, *Figures* 7.47 and 7.48 display the comparison of data with the prediction provided by HFSS, and in addition the cut-off frequencies provided by the comparison with waveguide theory.

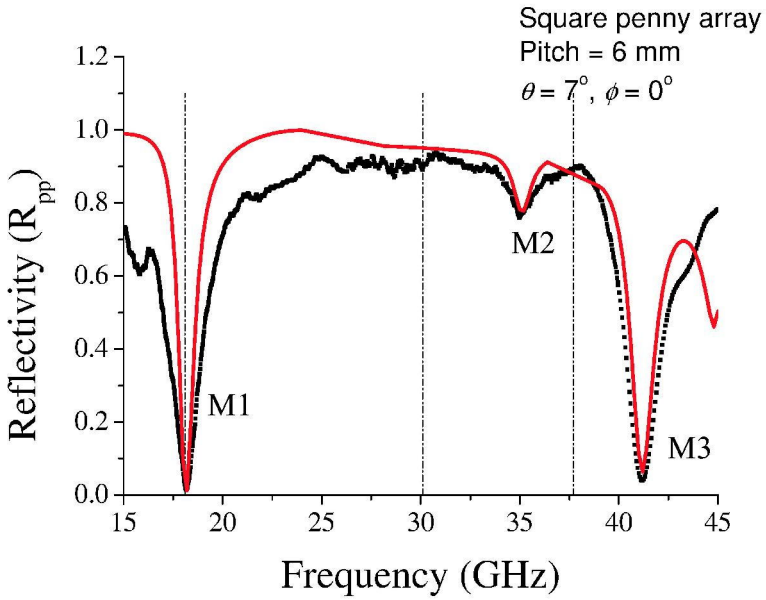

Figure 7.47: A comparison of the prediction provided by HFSS with the data obtained from the 6 mm pitch square array made up of thick pennies, along with the cut-off frequencies provided from the comparison with waveguide theory.

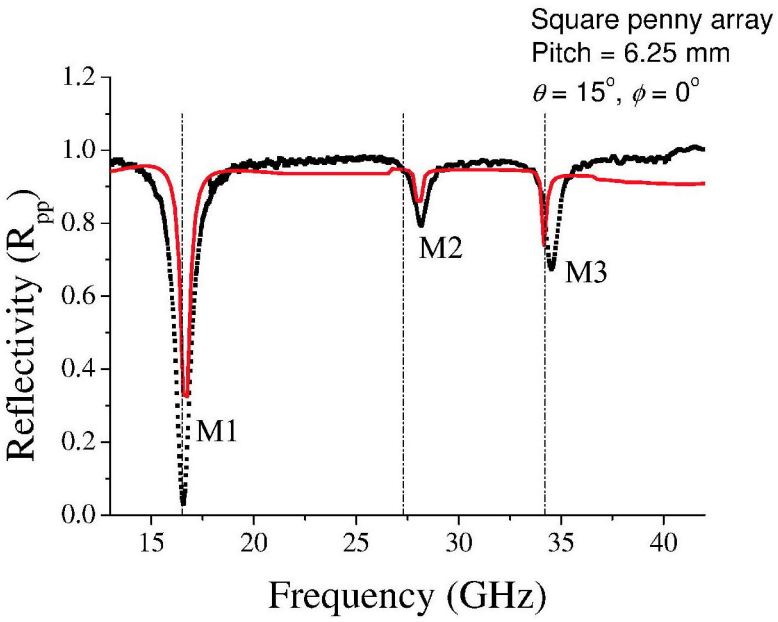

Figure 7.48: A comparison of the prediction provided by HFSS with the data obtained from the 6.25 mm pitch square array made up of thin pennies, along with the cut-off frequencies provided from the comparison with waveguide theory.

7.6 Summary

In summary, a completely original study of absorption of microwaves by penny arrays has been undertaken. The first sample type consisted of "thick" pennies in three different array arrangements, and the second consisted of a "thin" penny array, giving four samples in total. The reflection response of each sample has been determined for a range of polar angles, and scanned azimuthally. Several reflectivity minima were observed in the non-diffractive region of the samples, and a fundamental mode was found to be common to all samples. Remarkably, this mode was observed to absorb almost 100 %of incident radiation, and is completely independent of polar angle, azimuthal angle and polarisation. Higher order modes were detected on the two samples with the smallest pitch, and at the lowest polar angles. Of these, Mode 2 displayed angle and polarisation dependencies and achieved absorption of ∼20%, whereas Mode 3 was seen to absorb almost 100% of incident radiation on the thick penny array, and showed angle and polarisation independence. Each of these modes occurring in the non-diffractive region was found to be analogous to propagating modes in a circular waveguide, albeit with electric and magnetic components interchanged due to the boundary conditions of the waveguide structure and penny array structure being close approximations to the inverse of one another. This resulted in the three zero-order modes on the penny arrays, Modes 1, 2 and 3, being identified as analogous to the TE_{11}, TE_{21} and TE_{01} circular waveguide modes respectively. This analogy allowed a cut-off frequency for Modes 1, 2 and 3 to be calculated from waveguide theory, particular to the specific penny array structure, and a good approximation for the frequencies at which modes occur to be made.

Chapter 8

Liquid Crystal filled absorbing structures

8.1 Introduction

In previous chapters there has been discussion of structures that may resonantly absorb microwaves, and that consist of a metal-dielectric-metal arrangement where one metal layer has some subwavelength portion removed. For example, in *Chapter* 7 the structure investigated by *Hibbins et al* (2004) [40] was briefly discussed. This consisted of a metal-clad dielectric of subwavelength thickness with metal removed from the cladding to produce an array of subwavelength slits. Incident radiation with its electric vector polarised perpendicular to the slit direction was diffractively coupled into the core exciting a standing wave along the core length. The remarkable aspects of this structure are that it resonantly absorbs radiation at a wavelength 100 times greater than the structure thickness and that half of the standing wave wavelength is compressed into a fraction of the expected distance. *Chapter* 7 described structures based on a similar metal-dielectric-metal structure, with arrays of metallic "pennies" being separated from a continuous metal layer by a dielectric. In this chapter the reflectivity response of seven samples that are also based on the metal-dielectric-metal structure, with the dielectric layer consisting primarily of Liquid Crystal, will be investigated. Each sample consists of two glass sheets that are aluminised on one side. One sheet has some structure etched into the metal layer, and then the two sheets are assembled into an LC cell. With the metal layers acting as electrodes voltages may be applied and it is possible to cause the LC in the core to realign, causing a shift in a resonant absorption by the cell that is dependent on the core properties. The seven samples that are investigated are a slit array, a 2-D slit array (the same structure as sample A in *Chapter* 5), two square "penny" arrays, and three structures that are modified 2-D slit arrays (based on a similar structure to that of samples B, C and D in *Chapter* 5). In order for the metal layers to act as electrodes the metal must remain continuous, and therefore all the structures (except the slit array) have a connecting "wire" integral to the structure. The wire is not necessary for the slit array as a continuous metal border ensures electrical contact is maintained.

8.2 Background

8.2.1 Microwave absorption structures

The previous chapter discussed several samples that have been studied for the absorption of microwaves. Studies mentioned from the literature have consisted of samples that allow grating coupling to an SPP mode which propagates along the surface between a metal and a dielectric *(Hibbins et al* [38], *Lockyear et al* [39]), and a sample that is based on a metal-dielectric-metal structure, investigated by *Hibbins et al* [40] (2004). The penny arrays that formed the main experimental part of *Chapter* 7 were based on a similar metal-dielectric-metal structure, although the absorption mechanism was found to be entirely different to that of *Hibbins et al* [40] (2004). Samples discussed in this chapter bear some similarities to these metal-dielectric-metal structures, and therefore there will now be some further discussion of the sample investigated by *Hibbins et al* [40] (2004), and a summary of the conclusions regarding the penny arrays investigated in the previous chapter.

8.2.2 Metal-clad dielectric core structures

Hibbins et al [40] (2004) demonstrated a novel form of ultra-thin microwave absorber where the operating wavelength is much greater than the structure thickness. The work was inspired by the discovery that metals perforated with subwavelength apertures can transmit more radiation than impinges directly on the voids [29]. However, other studies had focused on single layer structures whereas *Hibbins et al* [40] proposed a 3-layer structure consisting of two metallic layers surrounding a dielectric core where the top metal layer had an array of subwavelength slits removed from it (shown in *Figure* 8.1).

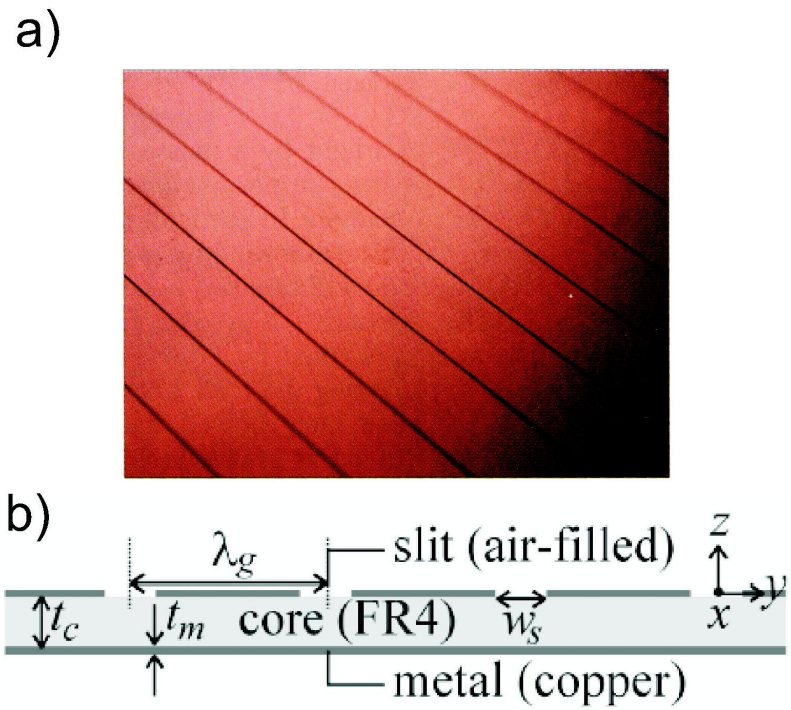

Figure 8.1: The structure studied by *Hibbins et al* [40]. a) A photograph of the sample. b) A schematic diagram of the sample, where t_c is core thickness, t_m is metal thickness, w_s is slit width and $\lambda_g$is the grating pitch.

When the structure is exposed to radiation polarised with a component of its electric vector orthogonal to the slit direction radiation couples through the gaps and excites a standing-wave within the metal-clad core. *Figure* 8.2 shows the frequency-dependent response of the structure for a polar angle θ= 11° with the sample orientated so that the slits are parallel to the plane of incidence and the incident electric vector is orthogonal the the slit direction (s polarised). There is a resonance located at ∼7 GHz due to absorption of energy by a resonant standing-wave within the core.

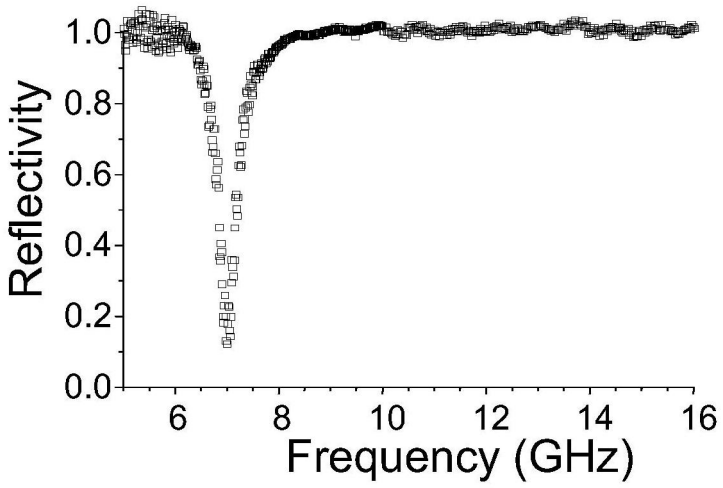

Figure 8.2: Data from the structure investigated by *Hibbins et al* [40]. The structure resonantly absorbs at a wavelength of ~ 43 mm whilst having a thickness of only 394 μm.

On examination of the fields, provided from an FEM model, a remarkable aspect of this structure was demonstrated. A region of zero field strength exists on the bottom layer of metal beneath the slits due to the incident electric field inducing charges of opposite sign on the metal on either side of the slit width, requiring the phase of the standing wave field within the core to be reversed across the slit width. Therefore whilst one half wavelength of the standing wave exists within the region of the core that is clad by metal on both sides, the other half exists in only the space underneath each slit. *Hibbins et al* [40] provide further inspection of this structure, demonstrating the modes available due to phase conditions, and also structures with perforations in both metal layers to allow transmission. The resonant frequency of these structures can be approximated by the Fabry-Perot equation, as the standing wave mode within the core is analogous to a Fabry-Perot mode. The equation is shown below:

$$f_n \approx \frac{Nc}{2nL}$$

Here f_n is the resonant frequency, N is the mode number, c is the speed of light, L is the length of metal between the slits and n is the refractive index of the core. As the resonant frequency is dependent on the core refractive index it is clear that a structure that has a variable core index would allow dynamic control of its resonant frequency. A device based on this structure with an LC core is therefore a desirable structure to produce.

8.2.3 Liquid Crystal devices

Chapter 3, *Section* 3.3 describes a series of devices utilising LCs designed to operate in the microwave regime. The primary focus of these structures has been in transmission, with relatively little work on structures for absorbing microwaves. This is primarily because of the

scales involved. The thickness over which LC may be well aligned in the homogeneous state by an aligning layer is ∼100 μm at best, placing a significant restriction on any device designed to absorb microwaves utilising LCs, as the thickness of the LC layer is then ∼1/100 of the operating wavelength. There have been several studies on microwave transmission structures that operate with such dimensions, but very few microwave absorption structures that do so. The work of *Hibbins et al* [40] (2004) demonstrates a possible structure for incorporating LCs in microwave absorption structures.

8.2.4 Penny arrays

Chapter 7 discusses the electromagnetic response of four penny arrays. These arrays are formed from two sample types, the first of which are the thick penny arrays, consisting of a number of metallic pennies arranged into an array, and separated from a continuous metal substrate by a dielectric layer. There were three of these thick penny arrays, the first of which was a 6 mm pitch square array, the second was an 8 mm pitch square array, and the third was a hexagonal array with a centre to centre spacing of 8.8 mm. The fourth sample was the thin penny array, formed from a printed circuit board, consisting of a copper-clad dielectric layer. A square array of pennies was etched into one of the copper layers, with a pitch of 6.25 mm. Each of these arrays displayed remarkable absorption of incident microwave radiation at frequencies determined by the structure dimensions. Each of the three lowest frequency modes on each array (termed Mode 1, 2 and 3, with Mode 1 being the lowest in frequency) were found to be due to the same absorption mechanism, and analysis of the fields provided by an FEM model revealed these modes to be analogous to waveguide modes, described in *Chapter* 3. *Figures* 8.3-8.5 display the magnetic field distributions taken from the FEM model for Modes 1-3 respectively, compared with the electric field distributions for the three lowest frequency modes in a circular waveguide.

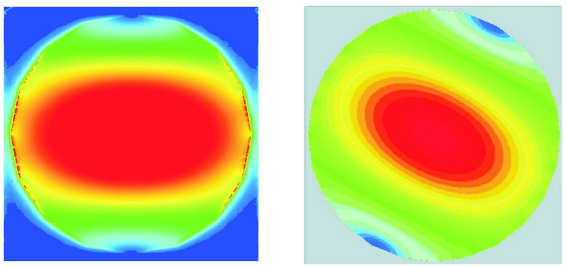

Figure 8.3: (left) The time-averaged magnetic field distribution for Mode 1 on the thin penny array. (right) The electric field distribution for the TE_{11} mode in a circular waveguide.

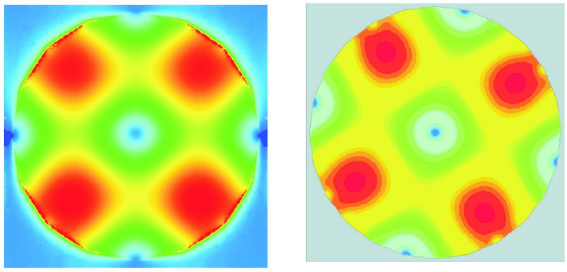

Figure 8.4: (left) The time-averaged magnetic field distribution for Mode 2 on the thin penny array. (right) The electric field distribution for the TE_{21} mode in a circular waveguide.

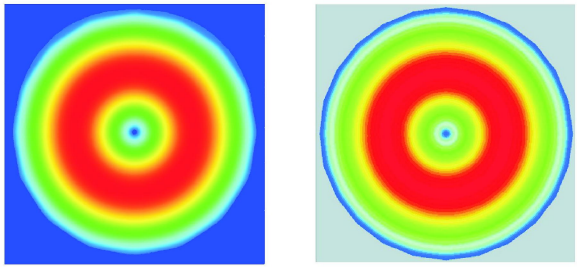

Figure 8.5: (left) The time-averaged magnetic field distribution for Mode 3 on the thin penny array. (right) The electric field distribution for the TE_{01} mode in a circular waveguide.

This analogy arises due to the fact that each penny array may be considered as a close approximation to an array of circular waveguide elements with their boundary conditions interchanged. A vacuum-filled, metal-clad circular waveguide that is infinite in its extent is enclosed by an electric wall (as the metal is assumed to be perfectly conducting) such that tangential electric fields drop to zero at the waveguide walls. This approximates the "reverse" of the penny array structure, where the metal layers may be considered as analogous to the open ends of the waveguide, and these are the electric walls of the structure. This "reversal" of the boundary conditions between the two structures allows a mode to exist in the penny structure that resembles a circular waveguide mode.

8.2.5 Zeroth-order Fabry-Perot mode structures

It was shown in *Chapter* 5 that it is possible to excite a zeroth-order Fabry-Perot type mode in a structured thin metal film. It may also be possible to use the same structure in the metal-dielectric-metal structure described above. If the structure described in *Chapter* 5 is etched onto the metalised side of a glass sheet, and is then assembled into an LC cell in the manner described briefly in *Section* 8.2.2, and in more detail below, then it may be possible to observe resonant absorption not only due to the 2-D slit array nature of the structure, but also due to the zeroth-order Fabry-Perot mode.

8.3 The samples

Each sample consists of two 300 mm × 300 mm × 1 mm glass sheets, each of which has ∼200 nm of aluminium evaporated onto one side. The sheets will be assembled into an LC cell for a reflectivity study, so the top sheet must have the required structure etched into it. This is achieved by applying a layer of photo resist to the metalised side of the glass sheet, and then exposing the photoresist to ultraviolet radiation through a mask displaying the surface structure. The sheet is then placed in a developer tank in order to remove the exposed photoresist, and finally in an aluminium etchant to remove the metal where the photoresist has been removed. The masks are made by drawing the structure in CorelDraw 12 of A1 size (821 mm × 594 mm). These are then printed and used to produce a mask that is reduced in size by a factor of 6 to ensure a high degree of accuracy. Once the structure has been etched into the metal, the plates must be assembled into an LC cell. The aluminium side of each plate was coated with a polyimide layer of ∼25 μm and then baked for 1 hour at 180° C in order to fix the polyimide. Each plate has a strip of ∼10 mm on one edge that is not coated with polyimide, so that the metal is still accessible to act as an electrode. Once the polyimide is set, it is unidirectionally rubbed using a rubbing cloth. The rubbing produces a series of microgrooves in the polyimide layer, which will cause the LC director to align with the rubbing direction. Once the aligning layers on both plates have been rubbed, they can be assembled into a cell. A thin strip of fast drying superglue is placed around the border of one plate, then glass microspheres of diameter 47 μm are scattered over the area of the plate. The second plate is then placed over the top of the first with a slight overlap so that a section (∼10 mm) of each plate protrudes from the other (the same section that was not coated with polyimide). This is in order for wires to be attached to each plate to apply the voltage required to change the LC alignment. Once the cell has been assembled, it must be filled with LC. In order to achieve the best LC alignment with the rubbed polyimide layer the cell is filled with the LC in its isotropic phase. The LC used in this case is Merck BL001 which enters its isotropic phase at 70° C, therefore the cell is placed on a "hot plate" to achieve the required temperature and the LC is syringed onto the protruding part of one of the plates. The LC enters its isotropic phase on coming into contact with the heated cell, and then fills the gap between the plates (maintained by the glass microspheres) by capillary action. The cell is then allowed to cool so that the LC enters its nematic phase and aligns with the aligning layer. Finally wires are attached to each plate (on the overlapping part that has no aligning layer) so that an external voltage may be applied. Each of the seven samples discussed in this chapter are constructed in the same way, and henceforth will be termed samples T, U, V, W, X, Y and Z. Now the dimensions of each structure will be discussed.

The first sample is the 1-D slit array, sample T. The pitch of the sample is 5.85 mm, with a slit width of 0.1 mm. The total size of the array is 200 mm × 180 mm, (the plate size being 300 mm × 300 mm) so that the array has a continuous metal border around it to maintain electrical contact. The second sample, a 2-D slit array, sample U, is a scaled down version of sample A in *Chapter* 5. The pitch of the sample is 5.75 mm, with a slit width of 0.2 mm. In

order for the metal to remain continuous so as to apply a voltage across the LC in the cell there is a connecting wire across each slit, as shown in *Figure* 8.6.

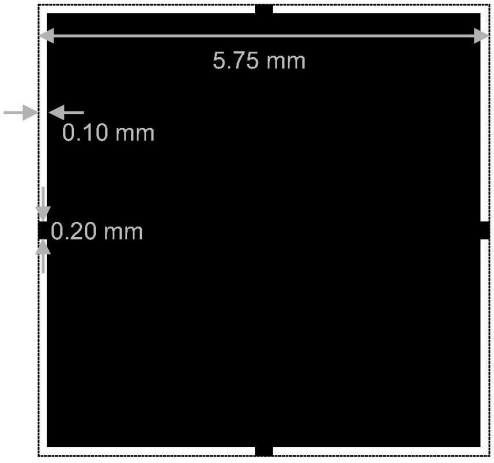

Figure 8.6: The unit cell of sample U.

The third and fourth samples, V and W, are "penny" arrays. In both cases the pennies are arranged into square arrays, but are different in pitch and connecting wire. For sample V the pennies have a diameter of 5.57 mm and the array has a pitch of 6.15 mm. The wire to maintain electrical contact is connected between nearest neighbour pennies, as shown in *Figure* 8.7, and has a thickness of 0.53 mm. Sample W has a pitch of 5.85 mm, with the pennies being 5.71 mm in diameter. For this sample the connecting wire is located between pennies that lie diagonally to one another, as shown in *Figure* 8.7, and has a thickness of 0.75 mm.

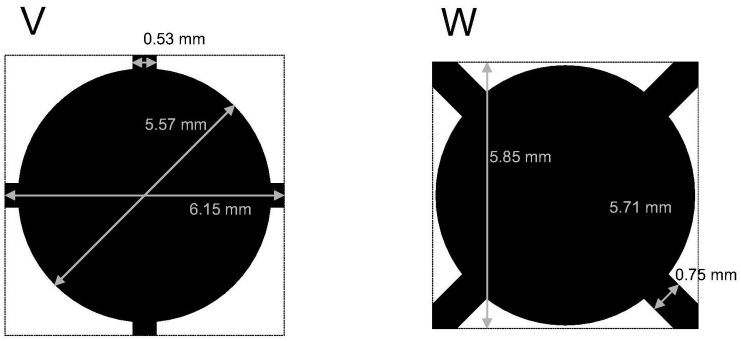

Figure 8.7: The unit cells of samples V and W.

The final three structures, X, Y and Z are scaled replicas of the structures B, C and D discussed in *Chapter* 5 and the unit cells of these structures are shown in *Figure* 8.8. The different sized cuts in samples Y and Z are drawn as single cuts to indicate scale, however the samples have cuts extending from each of the four slits.

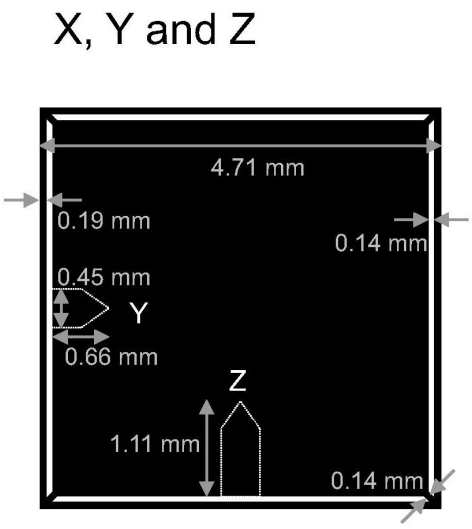

Figure 8.8: The unit cells of samples X, Y and Z. Sample X has no cuts, the size of the cuts for samples Y and Z are indicated, however in each of these samples the cuts extend from *each* of the four slits.

The unit cell of sample X consists of a square patch of metal with four slits located close to each edge of the patch, and is shown in *Figure* 8.8. The unit cell has dimensions 4.71 mm $\times$ 4.71 mm, with the slits located 0.19 mm from the edge of the unit cell. Each slit is terminated where the slits would otherwise cross by a connecting wire of thickness 0.14 mm at 45° to the slit direction. Structures Y and Z have the same unit cell but with an additional cut directed centrally from each slit and of differing lengths between the two structures, illustrated by the dashed lines in *Figure* 8.8. The cut for structure Y has a width of 0.45 mm and extends 0.34 mm towards the centre of the unit cell, tapering to a point over a further 0.32 mm. For structure Z, the cut again has the same cut width, but extends 0.79 mm towards the centre of the unit cell, again tapering to a point over a further 0.32 mm.

8.4 Reflection experiments

In order to carry out reflectivity experiments on the samples described above a set-up similar to that described in *Chapter* 7 is used, and therefore will only be discussed briefly here. The experimental set-up is shown in *Figure* 8.9, with the apparatus consists of a microwave source mounted within an impedance matching horn placed at the focal point of a 2 m focal length mirror. Samples are placed on a rotating turntable, and specular reflection from the sample

is collected by an identical 2 m focal length mirror, and directed into a detector horn. Due to the small sample size an aperture covered with microwave absorbing material is placed over the source mirror to reduce the beam footprint, and additionally the sample is surrounded with absorber to reduce stray reflections.

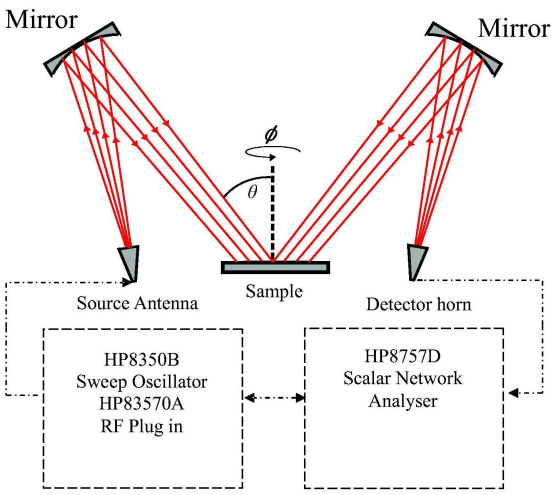

Figure 8.9: A schematic diagram of the experimental set-up used to investigate the sample's reflectivity.

The source and detector horns can be set to pass either p- (transverse magnetic, TM) or s- (transverse electric, TE) polarisations, where the transverse vector direction is defined with respect to the plane of incidence. In general we measure reflectivities R_{pp}, R_{ss}, $R_{ps}$and R_{sp} where $R_{ps}$and R_{sp} are measures of polarisation conversion, and subscripts refer to incident and reflected polarisations respectively. All reflectivities from samples recorded in this chapter are normalised by comparison with signals from a flat metal plate of the same dimensions (conveniently the reverse side of each cell has a continuous metal layer) with the reflectivity from the flat plate being considered as unity.

Resonant modes from the structures under investigation may be observed as minima in the angle dependent reflectivity, with the resonant width being dependent on the loss channels available. As there are several different structures under investigation, observed resonances may be different in nature and each will be discussed individually. However, all the samples discussed in this chapter are essentially large LC cells. The LC offers a degree of tuneability of the resonant frequency of each structure, assuming that the resonance is in some way dependent on the properties of the core of the LC cell. Each cell has wires attached to it so that a voltage may be applied from an external source. The voltage applied here is an A.C. source of 15 V at a frequency of 1 kHz. With no voltage applied the LC molecules remain homogeneously aligned due to the polyimide aligning layer, when the voltage is switched on

the LC molecules realign homeotropically with the field (see *Chapter* 3). The realignment in the LC layer causes the sensed dielectric properties of the core to change, resulting in a shift in resonant frequency.

8.5 Modelling

Chapter 4 discussed the FEM model, HFSS in depth, however here a brief consideration of the models used for fitting to the data in this chapter will be considered. Each structure is reduced to a unit cell based on the dimensions described above with the metal and dielectric layers lying in the xy-plane. Models consist of two aluminium layers of 200 nm thickness separated by an LC layer of 50 μm. The top metal layer has sections removed from it so as to resemble the structures described above. The material parameters are taken from the model library such that the aluminium has a conductivity, $\sigma = 3.8 \times 10^7 \mathrm{Sm}^{-1}$, and relative permeability $\mu = 1.000021$. A surface impedance approximation is used (discussed further in *Chapter* 4) as the conductivity is so high, and therefore the relative permittivity is ignored. The LC layer is simply a dielectric material modified to fit the permittivities of Merck BL001 as found in *Chapter* 6. Two separate models are run for each structure to replicate the LC in its homogeneous (no voltage applied) and homeotropic states (15 V applied) . For the homogeneous state the LC is treated as having a permittivity of $\varepsilon = 2.70 + 0.2i$, whereas for the homeotropic state the LC has an effective permittivity of $\varepsilon = 2.98 + 0.2i$. This is because the microwave electric field inside the structure is essentially normal to the metal plates, and thus parallel to the homeotropically aligned director. The metal and dielectric layers are located at the base of a 10 mm vacuum-filled airbox. A plane wave is injected into the model and has its polarisation, azimuthal angle ϕ and polar angle θ defined. For higher polar angles $\theta \leq 15°$ (where θ is defined as being relative to the surface normal) a PML layer was added on the top xy-plane face to avoid any secondary sources arising from scattered radiation. Master-slave boundaries are assigned on the xz- and yz-plane faces. The model space has a mesh injected into it consisting of approximately 40,000 tetrahedra. Once the mesh has been inserted, a frequency sweep is run from 18 GHz to 50 GHz in 0.5 GHz steps. Transmission, reflection and absorption predictions can then be exported to provide the expected electromagnetic response of each structure.

8.6 Results and discussion

In order to investigate the absorption properties of the structures described above, the reflectivity of each structure will now be examined. All data displayed in greyscales in the following section is taken with each sample in the off-state. *Figure* 8.10 shows reflectivity data from sample T, the slit array with a pitch of 5.85 mm. Reflectivity is displayed as a function of both frequency and azimuthal angle ϕ, for both p- and s-polarisation and for two fixed polar angles, $\theta = 10°, 35°$. *Figure* 8.10a) and 8.10b) show p- and s-polarisation respectively for $\theta = 10°$, and *Figure* 8.10c) and 8.10d) show p- and s-polarisation respectively for $\theta = 35°$.

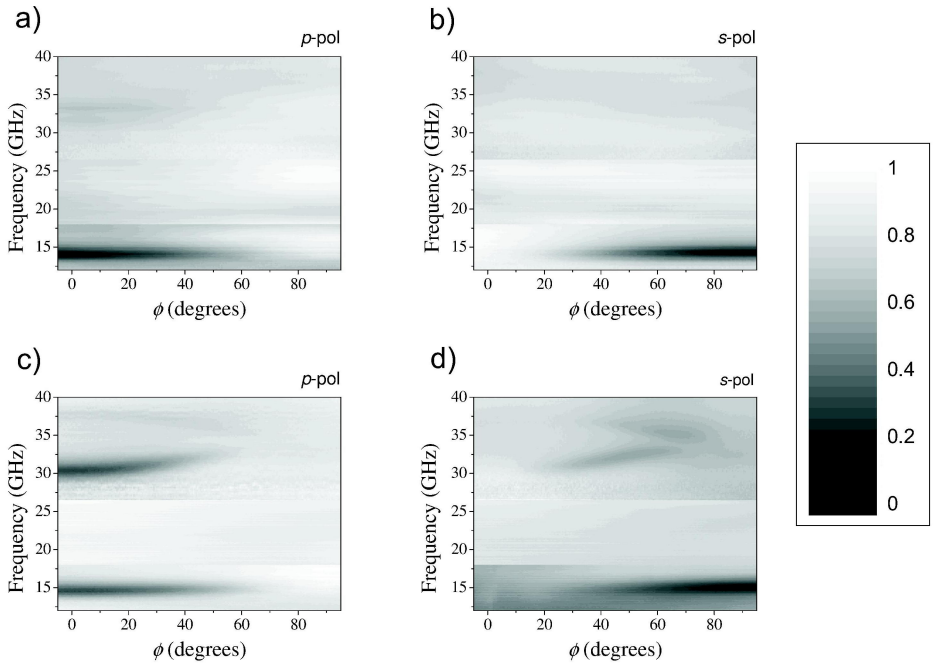

Figure 8.10: Reflectivity data from the slit array, sample T, as a function of frequency and azimuthal angle ϕ. Data are shown for both p- and s-polarisations at two polar angles, θ = 10°, 35°. a) p-polarised, θ = 10°. b) s-polarised, θ = 10°. c) p-polarised, θ = 35°. d) s-polarised, θ = 35°.

Reflectivity is shown on the z-axis with dark regions indicating a high level of absorption and light regions indicating reflection. The reflectivity is normalised to a continuous metal layer of the same dimensions as that of the sample. The sample is arranged so that at an azimuthal angle of ϕ= 0° for p-polarised incident radiation the slit direction is orthogonal to the electric vector direction. It is clear that for a polar angle of θ = 10° the most efficient resonant absorption occurs at ϕ= 0°for p-polarised incident radiation, with the efficiency reducing as the azimuthal angle is increased, with absorption falling to zero at $\phi \geq$50°. When the incident polarisation is set to s-polarised, no resonant absorption occurs at ϕ= 0° as expected, as there is no longer a component of the electric vector orthogonal to the slit direction at this orientation. Instead, absorption begins to occur at $\phi \approx 25°$, peaking at ϕ= 90°. Resonances in both polarisations occur at the same frequency, approximately 14 GHz. The pitch of the sample is 5.85 mm, so the absorption occurs in the zero-ordered region. No scattering due to diffraction is observed at this polar angle. Later in this chapter field plots provided by the FEM model will give insight into the absorption mechanism. At the higher polar angle of θ = 35°the fundamental resonance remains largely unchanged, as shown in *Figures* 8.10c) and 8.10d), however additional resonances occur in both p- and s-polarisations at higher frequencies, approximately 30 GHz.

Figure 8.11 shows the reflectivity from sample U, the 2-D slit array that has a pitch of 5.75 mm. Again, reflectivity is displayed as a function of both frequency and azimuthal angle ϕ, for both p- and s-polarisation and for two fixed polar angles, $\theta = 10°, 35°$. *Figures* 8.10a) and 8.10b) show p- and s-polarisation respectively for $\theta = 10°$, and *Figures* 8.10c) and 8.10d) show p- and s-polarisation respectively for $\theta = 35°$.

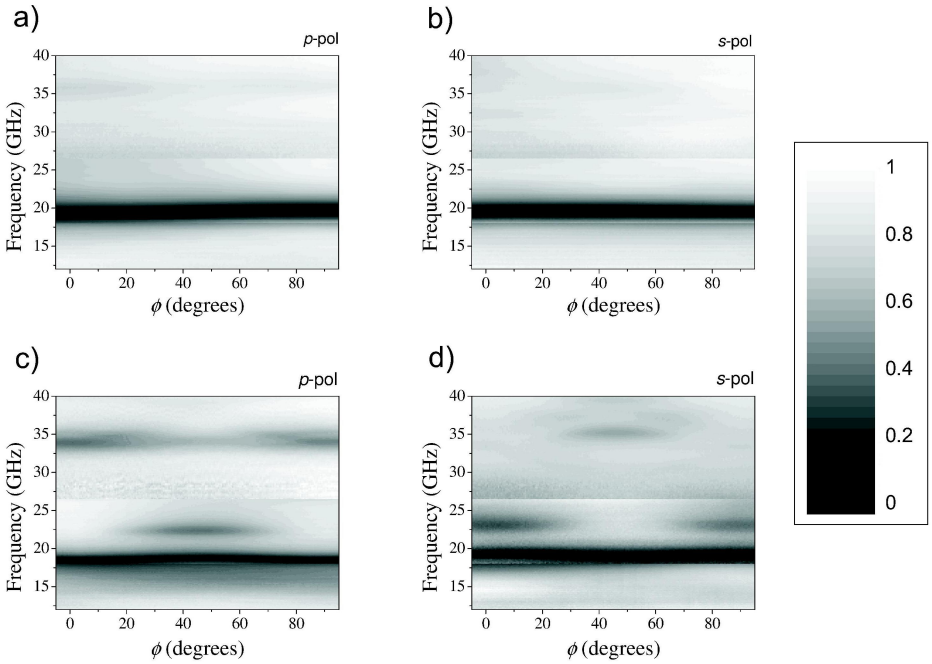

Figure 8.11: Reflectivity data from the 2-D slit array, sample U, as a function of frequency and azimuthal angle ϕ. Data are shown for both p- and s-polarisations at two polar angles, $\theta = 10°, 35°$. a) p-polarised, $\theta = 10°$. b) s-polarised, $\theta = 10°$. c) p-polarised, $\theta = 35°$. d) s-polarised, $\theta = 35°$.

Reflectivity is shown on the z-axis with dark regions indicating high levels of absorption and light regions indicating high reflectivity. The reflectivity is normalised to a continuous metal layer of the same dimensions as that of the sample. In the previous sample a fundamental resonance was observed at approximately 14 GHz, only occurring at certain azimuthal angles for each polarisation due to the requirement of having a component of the electric vector orthogonal to the slit direction. As this sample is a 2-D slit array, there is always a component of the electric vector orthogonal to the slit direction, therefore the fundamental resonance remains largely independent of azimuthal angle for both polarisations, and *Figure* 8.11a) is virtually indistinguishable from *Figure* 8.11b), and *Figures* 8.11c) 8.11d) also display a largely angle independent fundamental resonance. The resonance occurs at a frequency of approximately 19 GHz, and the pitch of the sample is 5.75 mm, so as in the first sample the fundamental resonance is not related solely to the pitch of the sample.

Reflectivity data from sample V, the square penny array with a pitch of 6.15 mm linked between nearest neighbours, is shown in *Figure* 8.12. *Figures* 8.12a) and 8.12b) show p- and s-polarisation respectively for $\theta = 10°$, and *Figures* 8.12c) and 8.12d) show p- and s-polarisation respectively for $\theta = 35°$.

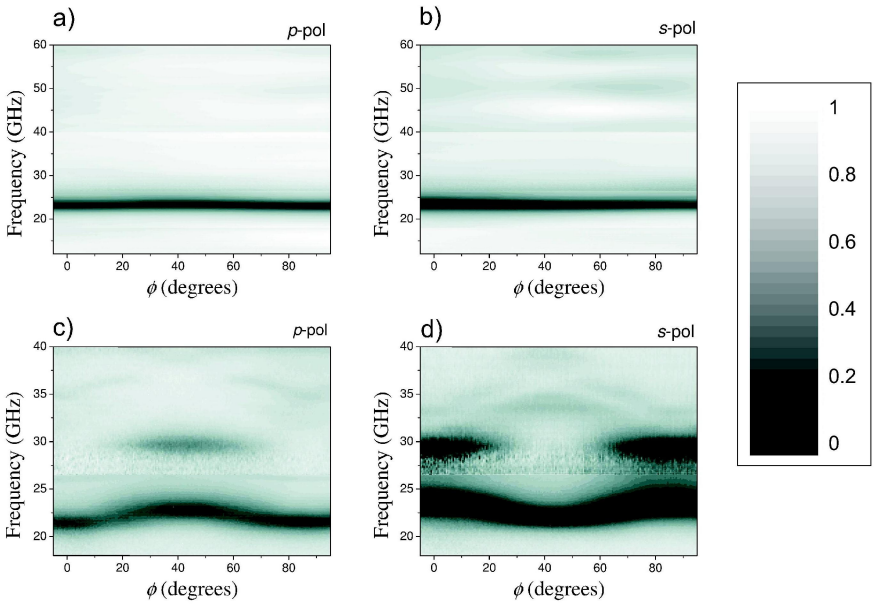

Figure 8.12: Reflectivity data from the square-linked penny array, sample V, as a function of frequency and azimuthal angle ϕ. Data are shown for both p- and s-polarisations at two polar angles, $\theta = 10°, 35°$. a) p-polarised, $\theta = 10°$. b) s-polarised, $\theta = 10°$. c) p-polarised, $\theta = 35°$. d) s-polarised, $\theta = 35°$.

The previous two structures are similar in nature, and it is reasonable to assume the fundamental resonance shown on those structures was due to the same phenomenon. Sample V is somewhat different, and has no subwavelength slits, however *Figures* 8.12a) and 8.12b) clearly show a resonance occurring at approximately 23 GHz. This is in the zero-order regime, so again, this resonance cannot be attributed to diffraction. *Figures* 8.12c) and 8.12d) show absorption at a higher polar angle of $\theta = 35°$, displaying a somewhat different response. The fundamental resonance still occurs, but appears to go through a large perturbation at certain azimuthal angles. Additionally, higher order modes occur that are not observed at a polar angle of $\theta = 10°$. Field plots provided from the FEM model will be used to give insight into these modes, and the perturbation that occurs to the fundamental resonance.

Figure 8.13 displays the reflectivity from the sample W, the second penny array which has pennies linked diagonally, and a smaller pitch of 5.85 mm. *Figures* 8.13a) and 8.13b) show p- and s-polarisation respectively for $\theta = 10°$, and *Figures* 8.13c) and 8.13d) show p- and s-polarisation respectively for $\theta = 35°$.

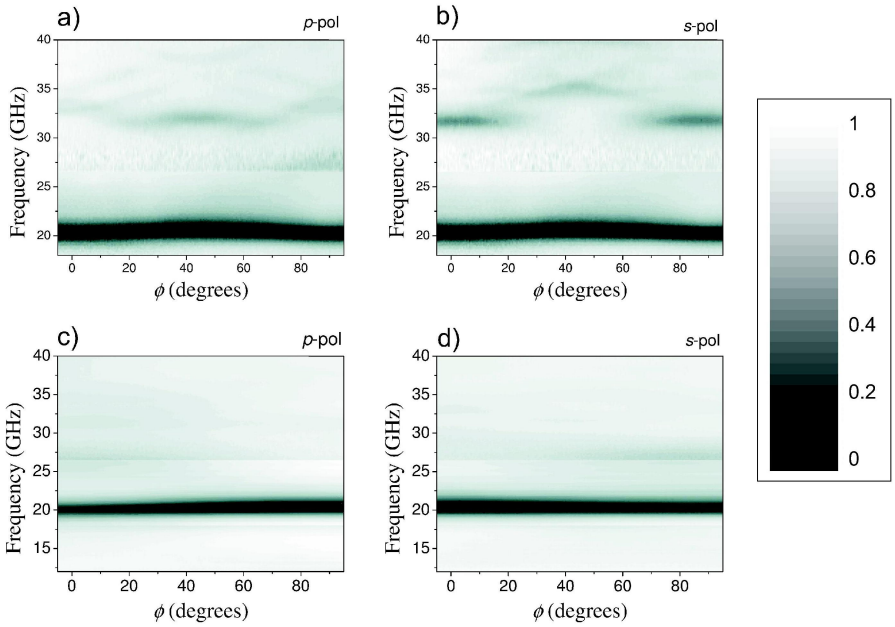

Figure 8.13: Reflectivity data from the diagonally-linked penny array, sample W, as a function of frequency and azimuthal angle ϕ. Data are shown for both p- and s-polarisations at two polar angles, $\theta = 10°, 35°$. a) p-polarised, $\theta = 10°$. b) s-polarised, $\theta = 10°$. c) p-polarised, $\theta = 35°$. d) s-polarised, $\theta = 35°$.

Each figure shows resonant absorption at a frequency of approximately 20 GHz, all four plots appearing largely the same. Recall that the reflectivity data from the previous sample, another square penny array, displayed some higher frequency modes, and a perturbation to the fundamental resonance at a polar angle of $\theta = 35°$ for certain azimuthal angles. This indicates that the location of the electrical contacts, either between nearest neighbours or between diagonal pennies, has a bearing on how the resonant frequency varies at high polar angles. This will be discussed further when analysing the field plots provided from HFSS.

Reflectivity data from sample X is displayed in *Figure* 8.14. This sample is a replica of sample B discussed in *Chapter* 5, and consists of a dual-pitch 2-D slit array. In *Chapter* 5 it was shown that in transmission a zeroth-order Fabry-Perot mode could exist on this type of structure when perpendicular "cuts" into the sample area were added. The two following samples have these cuts made to investigate the possibility of reducing the frequency of resonant absorption of this structure by simply adding and extending the cuts. The unit cell of this sample consists of a square patch of metal with four slits located close to each edge of the patch, and has a pitch of 4.71 mm, with the slits located 0.19 mm from the edge of the unit cell. Each slit is terminated in the where the slits would otherwise cross by a connecting wire of thickness 0.14 mm at 45° to the slit direction. *Figures* 8.14a) and 8.14b) show p- and s-polarisation respectively for $\theta = 10°$, and *Figures* 8.14c) and 8.14d) show p- and s-polarisation respectively for $\theta = 45°$.

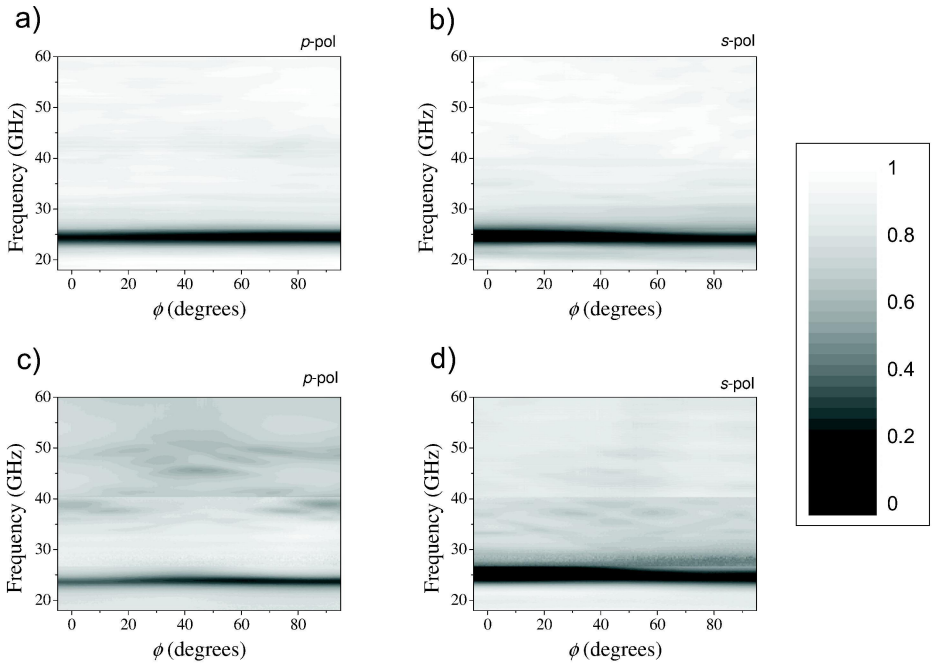

Figure 8.14: Reflectivity data from the second 2-D slit array, sample X, as a function of frequency and azimuthal angle ϕ. Data are shown for both p- and s-polarisations at two polar angles, $\theta = 10°, 45°$. a) p-polarised, $\theta = 10°$. b) s-polarised, $\theta = 10°$. c) p-polarised, $\theta = 45°$. d) s-polarised, $\theta = 45°$.

Each plot shows a resonance at approximately 24.5 GHz, and are otherwise relatively unremarkable. The resonance appears to be largely independent of polarisation, azimuthal angle and polar angle. Further discussion of the nature of this mode will appear later with reference to field plots.

Figure 8.15 displays the transmission from sample Y, which has a scaled version of the structure of sample C from *Chapter* 5 etched into its top plate. Reflectivity is displayed in the same way as previous samples, with *Figures* 8.15a) and 8.15b) showing p- and s-polarisation respectively for $\theta = 10°$, and *Figures* 8.15c) and 8.15d) showing p- and s-polarisation respectively for $\theta = 45°$ with absorption plotted on the z-axis. Similarly to sample X, the fundamental resonance appears to be largely independent of polarisation, and polar angle, however, there is a clear dependence on azimuthal angle, with greater absorption occurring at $\phi = 90°$ in the p-polarisation reflection data, and at $\phi = 0°$ in the s-polarisation reflection data. In addition, there is a slight shift in frequency of the resonance as compared with the reflection response of the previous sample, with the resonant frequency now occurring at approximately 24 GHz. This will be discussed later in the chapter with reference to field plots.

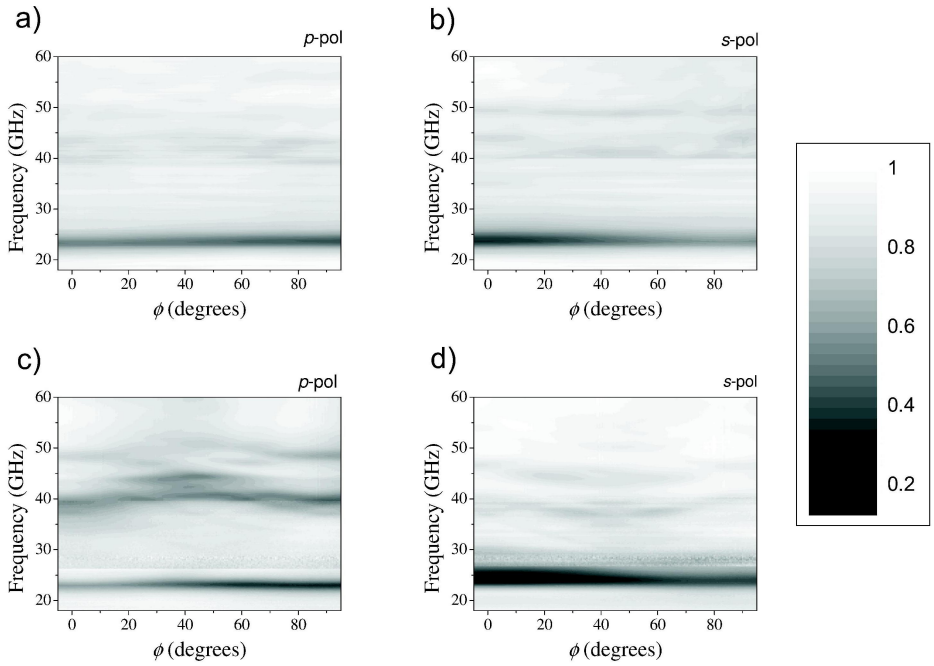

Figure 8.15: Reflectivity data from the 2-D slit array modified by the addition of small cuts, sample Y, as a function of frequency and azimuthal angle ϕ. Data are shown for both p- and s-polarisations at two polar angles, $\theta = 10°$, $45°$. a) p-polarised, $\theta = 10°$. b) s-polarised, $\theta = 10°$. c) p-polarised, $\theta = 45°$. d) s-polarised, $\theta = 45°$.

Reflectivity data for sample Z is shown in *Figure* 8.16. The structure etched into the top plate of sample Z is a scaled version of the structure of sample D from *Chapter* 5, however this sample proved the most difficult to obtain good reflectivity data from due to the efficiency of absorption being further reduced from that of the previous two samples. Therefore the data shown in *Figure* 8.16 is over a reduced frequency range from previous samples. However *Figures* 8.16a) and 8.16b) showing p- and s-polarisation respectively for $\theta = 10°$, and *Figures* 8.16c) and 8.16d) showing p- and s-polarisation respectively for $\theta = 45°$ with reflectivity plotted on the z-axis. Although the absorption resonance is much less efficient than in the previous two samples, it appears to have been further shifted in frequency, occurring at approximately 21 GHz, and the azimuthal-angle dependence of the resonance observed in the previous sample is indicated clearly here also. It therefore seems that for samples X, Y and Z the addition and increase in size of cuts causes a reduction in frequency of the resonant mode, but also introduces a reduction in coupling efficiency, and an azimuthal angle dependence to the absorption mode. These features will be discussed later in the chapter with reference to field plots provided by an FEM model.

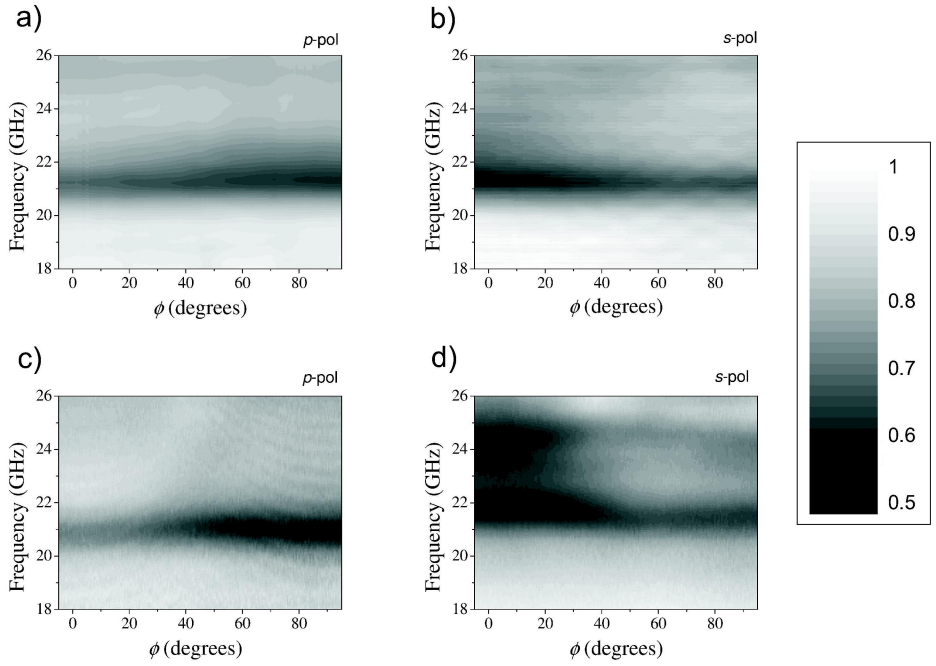

Figure 8.16: Reflectivity data from the 2-D slit array modified by the addition of small cuts, sample Z, as a function of frequency and azimuthal angle ϕ. Data are shown for both p- and s-polarisations at two polar angles, $\theta = 10°, 45°$. a) p-polarised, $\theta = 10°$. b) s-polarised, $\theta = 10°$. c) p-polarised, $\theta = 45°$.

In the following section HFSS modelling will be used to provide fits to line plots of the above data for all samples at selected azimuthal angles. In all cases, good fits to the mode position in frequency is achieved, however, the breadth and depth of each mode is less well fitted. This is due to in part to the construction of the samples. Each sample consists of glass sheets with a thin layer (∼200 nm) of aluminium evaporated onto them. However, the thickness of the aluminium layer on the glass sheets varies greatly (∼100 nm - 250 nm) due to the difficulty of evaporating aluminium over such a large area (300 mm × 300 mm) using the equipment available. Resonant mode depth and breadths are strongly dependent on the aluminium thickness, and coupling this to the fact that the sample size is small compared to the incident beamspot, it is not possible to exactly replicate the samples using HFSS, (which assumes the sample is perfect and infinite). Additionally, the absorption of the LC will affect the resonant mode depth and breath, and therefore good fits to mode breadth and depth are extremely difficult, if not impossible, to achieve. Nonetheless, mode positions in frequency are well fitted, and so field plots from HFSS can provide insight into the absorption mechanism of each of the samples.

Figure 8.17 displays selected line plots from taken from *Figure* 8.10 at certain azimuthal angles as stated on each plot. *Figures* 8.17a and 8.17b display data taken at a polar angle of θ=10°, with p- and s-polarised incident radiation taken at azimuthal angles of ϕ= 0°, 90°

respectively, and *Figures* 8.17c and 8.17d display data taken at a polar angle of θ=35°, with p- and s-polarised incident radiation taken at azimuthal angles of ϕ= 0°, 90° respectively. Also shown is the response of the sample when a voltage of 15 V is applied across the LC layer. The LC is initially homogeneously aligned due to the aligning layer, but on application of a voltage across the cell the LC molecules realign homeotropically with the applied field. This has the effect of increasing the sensed refractive index of the core of the structure, and so any resonant modes of the structure that are dependent on the core refractive index will be shifted in frequency. A higher index core will lead to a lower resonant frequency, and vice versa. When the LC is realigned homeotropically, the core index increases, so the resonant frequency should reduce. It is clear from *Figure* 8.17 that this is indeed the case for the observed reflectivity minima.

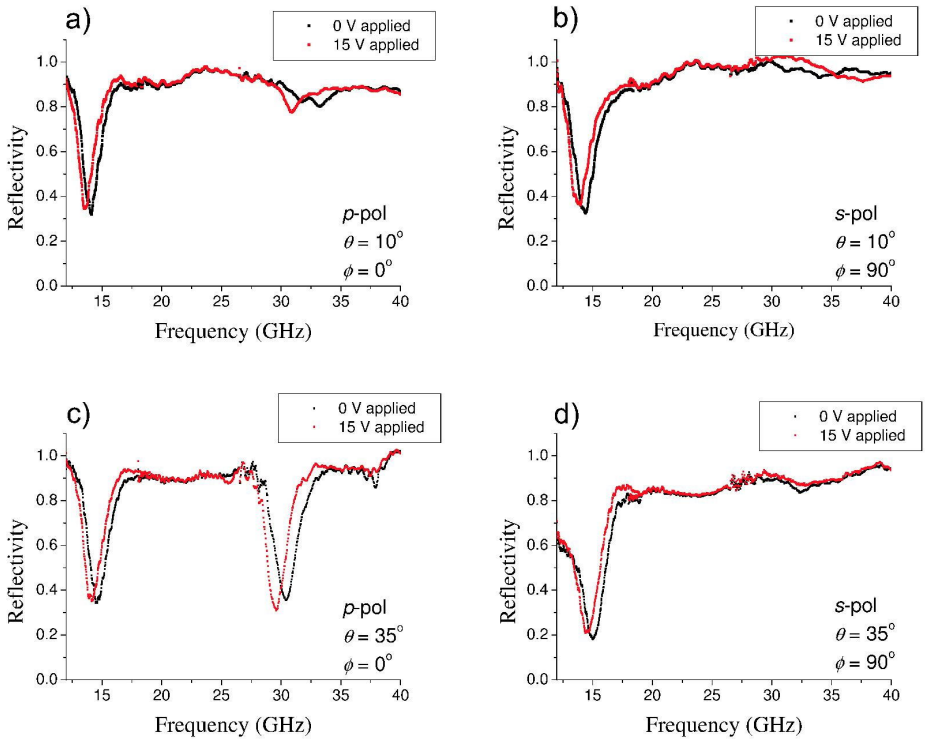

Figure 8.17: Reflectivity from sample T, the slit array, at selected azimuthal angles. Black squares indicate the cell is in the off-state with no voltage applied. Red squares indicate 15 V is applied across the cell. 8.17a) p-polarised, θ= 10°, ϕ= 0°. b) s-polarised, θ= 10°, ϕ= 90°. c) p-polarised, θ= 35°, ϕ= 0°. d) s-polarised, θ= 35°, ϕ= 90°.

Figure 8.18 shows a comparison between data taken at a polar angle of θ=10° for p-polarised incident radiation at an azimuthal angle of ϕ= 0° for both 0 V and 15 V applied, compared with theory provided by two FEM models, and good agreement in terms of mode position and breadth is observed.

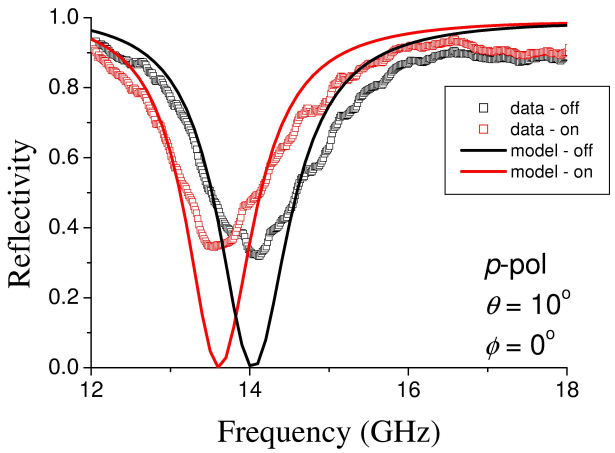

Figure 8.18: Reflectivity data for sample T, the slit array, plotted together with predictions provided by an FEM model. Data is shown for a polar angle of θ= 10°and azimuthal angle of ϕ= 0°, and incident radiation is p-polarised. Open squares indicate data, solid lines represent the model prediction.

The two models replicate the sample dimensions and are identical in all details except the permittivity of the LC core. For homogeneous alignment the permittivity of the LC core is $\varepsilon = 2.70{+}0.2i$, and for homeotropic alignment the permittivity of the LC core is $\varepsilon = 2.98{+}0.2i$. It is clear that the change in resonant frequency in the data can be wholly accounted for by this change in index, as the frequency shift in the model closely resembles that observed in the data. The mode positions and breadths are good fits, however the depth of resonance seen in the data is significantly less than that predicted by the FEM model. This is due to the model treating the structure as perfect and infinite in the sample plane, whereas the data is taken from a sample that is limited in size due to construction constraints, and suffers from a degree of variability. Interestingly, the model predicts reflectivity drops to zero, implying that on resonance all the incident radiation is completely absorbed by the structure. This is remarkable, and suggests the possibility that the resonant behaviour allows fields to penetrate deeper into the metal layer, where they are absorbed. Field plots provided by the FEM can now be examined in order to gain an insight into the absorption mechanism. *Figure* 8.19 displays the time-averaged magnitude of E-field magnitude in the low-index (0 V) model at a frequency of 14 GHz.

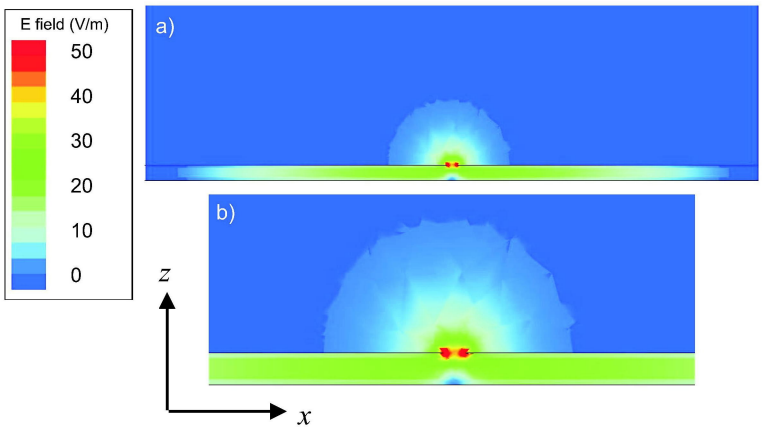

Figure 8.19: The electric field magnitude provided by the FEM model at a frequency of 14 GHz, polar angle of θ= 35°, azimuthal angle of ϕ = 0° with p-polarised incident radiation . Field enhancement is colour-coded and the key displays the level of enhancement to the incident field.

Figure 8.19a shows the unit cell of the sample with the slit centrally located, *Figure* 8.19b is a close-up view of the same plot. Field enhancement is colour-coded and the scale is also shown. The greatest field enhancement is located on the metal on opposite sides of the slit, with a region of zero field strength located directly below the slit. This is due to the incident field inducing charges of opposite sign on either side of the slit, causing the electric vector in the vertical direction to be completely reversed across the width of the slit. This is the same phenomenon as observed by *Hibbins et al* [40] (2004), however here it occurs in a structure with an LC core, allowing a degree of dynamic control over the resonant frequency.

Figure 8.20 shows the electric vector in the structure. It is clear that the E vector is reversed across the slit width, and as such the standing wave within the core has one half-wavelength fitted within the metal-clad region, with the other half-wavelength being compressed into the area beneath the slit.

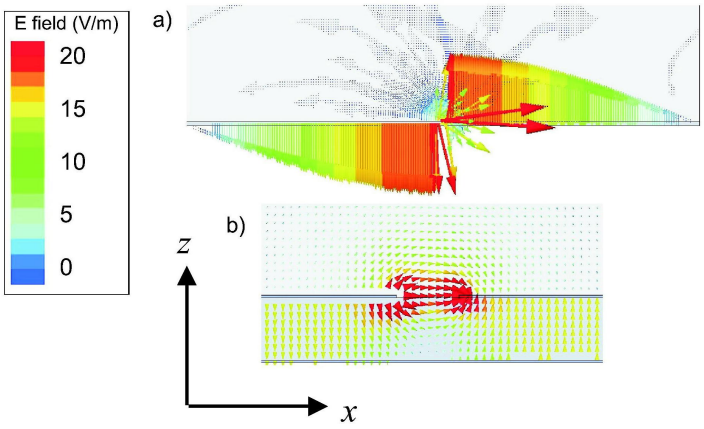

Figure 8.20: The electric field vector provided by the FEM model at a frequency of 14 GHz, polar angle of θ= 35°, azimuthal angle of ϕ = 0° and p-polarised incident radiation. Field enhancement is colour-coded and the key displays the level of enhancement of the incident field. 8.20a) displays the unit cell of the structure, with arrows indicating electric vector direction. 8.20b) is a close-up view of the region around the slit. Arrow tails are removed for clarity.

Therefore the resonant frequency of this structure can be approximated by the following equation:

$$f_n \approx \frac{Nc}{2nL}$$

Where f_n is the resonant frequency, N is the mode number, c is the speed of light, n is the refractive index of the core and L is the pitch of the structure. This equation predicts a resonant frequency for the structure of ~15.5 GHz. This expression takes no account of the slit width or core thickness, nor the effect of the aligning layer, but it nevertheless allows a rough approximation of the mode position to be made.

Figure 8.17c shows a secondary mode occurring at a frequency of approximately 30 GHz when the incident radiation is p-polarised for a polar angle of θ= 35° and an azimuthal angle of ϕ = 0°. HFSS can again provide an insight into the nature of this mode. *Figure* 8.21 displays the time-averaged electric field magnitude for a unit cell from a model replicating the polarisation and angles for which the secondary mode was observed. Field enhancement is colour coded, and at maximum the enhancement is 30 times that of the incident field, and is located on the metal at the slit opening. Regions of zero field are observed (as in the previous structure) directly underneath the slit, and also at points in the metal-clad region that are equidistant from the slit and the edge of the unit cell. The region of high field around the slit is concentrated in one direction in the plane of incidence due to the high incident polar angle (θ= 35°). The field distribution within the slit implies that this mode is of the same nature

as the fundamental mode, but of a higher order with the standing wave having three nodes along the slit length.

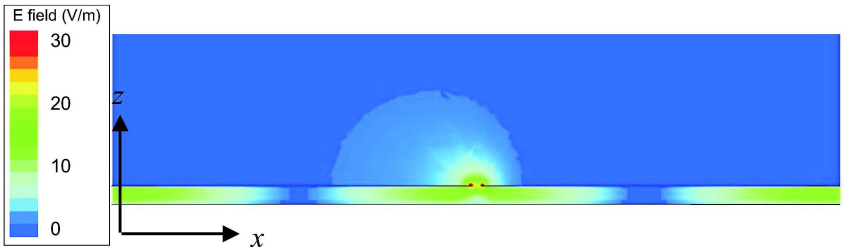

Figure 8.21: The electric field magnitude for the second mode occurring in structure T at approximately 30 GHz. Radiation is incident at a polar angle θ= 35°, azimuthal angle of ϕ = 0° and p-polarised incident radiation. Field enhancement is colour-coded at at maximum is 30 times that of the incident field.

Figure 8.22 shows the electric vector for the secondary mode in sample T. *Figure* 8.22a displays the unit cell of the structure, and *Figure* 8.22b shows a close-up view of the slit region. (Arrow tails are removed for clarity). Field enhancement is colour-coded and displayed in the key. The direction of the electric vector is shown to reverse a total of three times along the unit cell length, once directly under the slit, and once either side of the slit in the metal-clad region. This confirms that it is indeed a higher order mode of the same nature as the fundamental mode. The Fabry-Perot equation predicts a resonant frequency of ∼31 GHz, which again is a reasonable approximation.

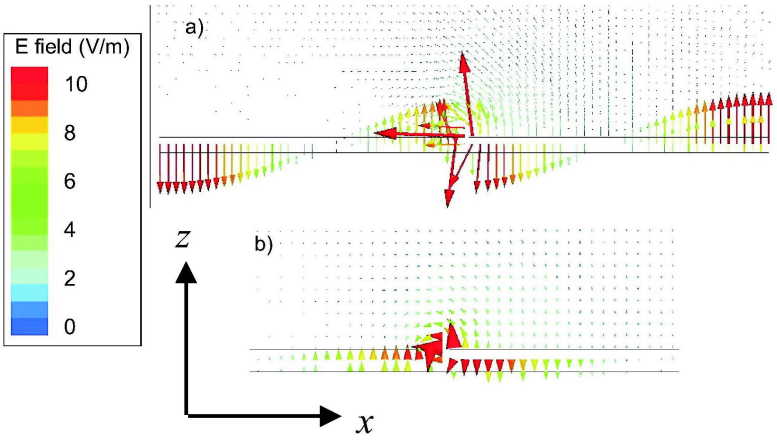

Figure 8.22: The electric field vector provided by the FEM model at a frequency of 30 GHz, polar angle of θ= 35°, azimuthal angle of ϕ = 0° and p-polarised incident radiation. Field enhancement is colour-coded and the key displays the level of enhancement of the incident field. a) displays the unit cell of the structure, with arrows indicating electric vector direction. b) is a close-up view of the region around the slit. Arrow tails are removed for clarity.

Figure 8.23 shows frequency-dependent reflectivity data from sample U, the 2-D slit array. Data is plotted at selected azimuthal angles taken from *Figure* 8.11. Data taken from the cell in the off-state with 0 V applied is shown as black squares, and data taken from the cell with 15 V applied across the cell is indicated by red squares. The fundamental mode is shown in all four plots, occurring at approximately 19 GHz in the off-state, and 18.5 GHz in the on-state. A secondary mode occurs in *Figure* 8.23d at approximately 23 GHz (off-state) for incident radiation which is s-polarised at an incident polar angle of θ= 35°, and an azimuthal angle of ϕ= 0°. Also, there is a tertiary mode at approximately 34 GHz (off-state) occurring at the same incident angles when radiation is p-polarised. Field plots from the FEM model will provide insight into the nature of these modes.

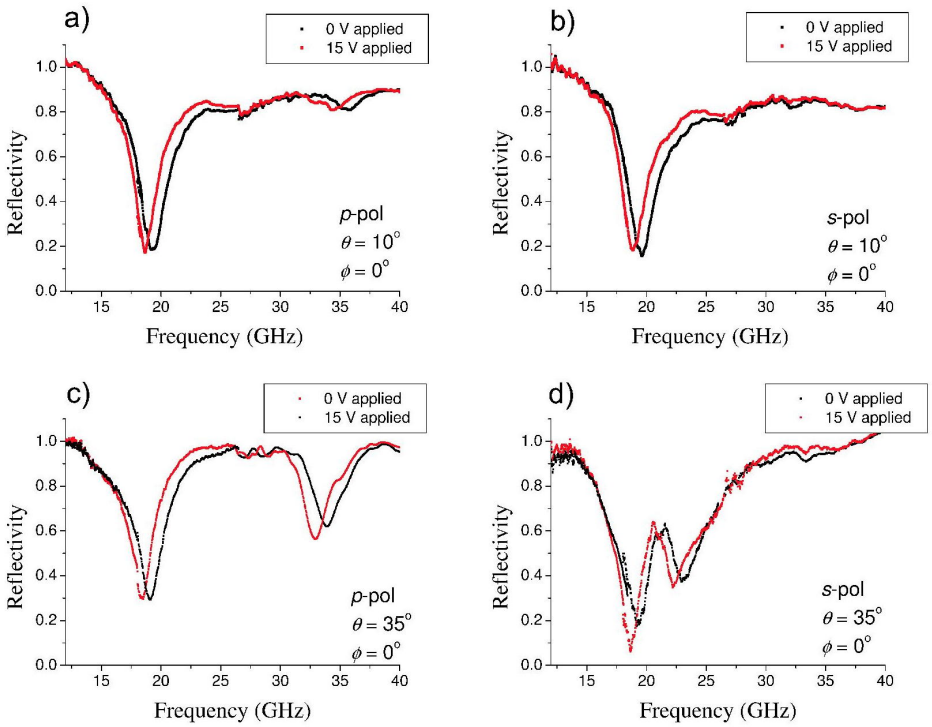

Figure 8.23: Reflectivity from sample U, the 2-D slit array, at selected azimuthal angles. Black squares indicate the cell is in the off-state with no voltage applied. Red squares are data for 15 V applied across the cell. 8.23a) p-polarised, θ= 10°, ϕ= 0°. b) s-polarised, θ= 10°, ϕ= 0°. c) p-polarised, θ= 35°, ϕ= 0°. d) s-polarised, θ= 35°, ϕ= 0°.

Figure 8.24 shows a comparison between data taken with p-polarised incident radiation at a polar angle of θ= 10° and an azimuthal angle of ϕ= 0° against the prediction from an FEM model replicating the same incident radiation polarisation and angles. Data are shown for both the off-state (0 V applied) and the on-state (15 V applied) and is plotted against

two models that replicate sample dimensions and are identical in all respects except for the permittivity of the dielectric core. The off-state model replicates the LC in its homogeneous state, having a permittivity of $\varepsilon = 2.70 + 0.2i$, and the on-state model has a dielectric core representing the LC in its homeotropic state, using a permittivity of $\varepsilon = 2.98 + 0.2i$.

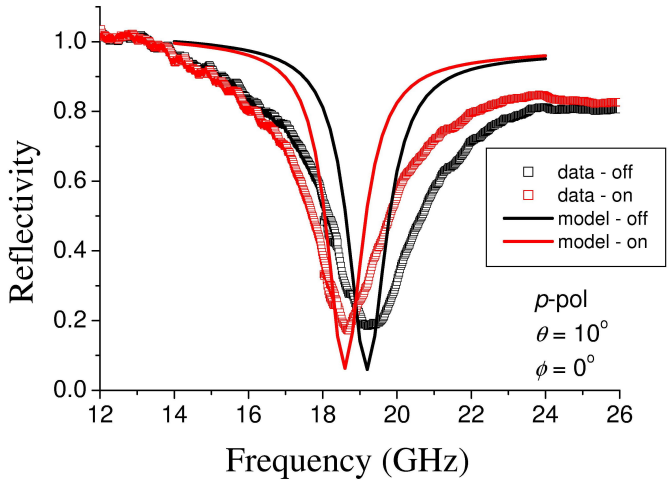

Figure 8.24: Reflectivity data for sample U, the 2-D slit array, plotted with prediction provided by an FEM model. Data is shown for a polar angle of θ= 10°and azimuthal angle of ϕ= 0°, and incident radiation is p-polarised. Open squares are data, solid lines represent the model prediction.

Good agreement in resonant frequency is observed, however there is some difference in the mode depth and breadth for both off- and on-states. This is in part due to the relatively small sample size compared with incident wavelength, which results in a loss of depth of resonance, and also sample variability, resulting in a broadening of the mode. In contrast the model is infinite in the surface plane and has no variability. Again it is clear that the shift in resonant frequency can be wholly accounted for by the change in refractive index of the LC, as this is the only change in the two models, and closely accounts for the observed shift. Field plots provided by the FEM will now be explored to examine the nature of the resonant mode.

Figure 8.25 displays the time-averaged electric field magnitude (8.25a) and the time averaged magnetic field magnitude (8.25b) taken from the FEM model for the off-state at a frequency off 19.2 GHz. Fields are plotted across the xy-plane at a position 0.025 mm below the top metal layer. Field enhancement is shown relative to the incident field, and at maximum is enhanced by 15 times. *Figure* 8.25a shows that in the case of the electric field magnitude, field enhancement is greatest closest to the slits that lie parallel to the polarisation direction, with a null through the centre of the metal region. The reverse is true for the magnetic field, with a field maximum occurring in the centre of the metal region, as shown in *Figure* 8.25b. However, for both electric and magnetic field distributions the electrical contact across slits

appears to cause a perturbation to the field, with a reduction in E-field appearing in the locality of the contact, and a H-field maximum occurring across the contact.

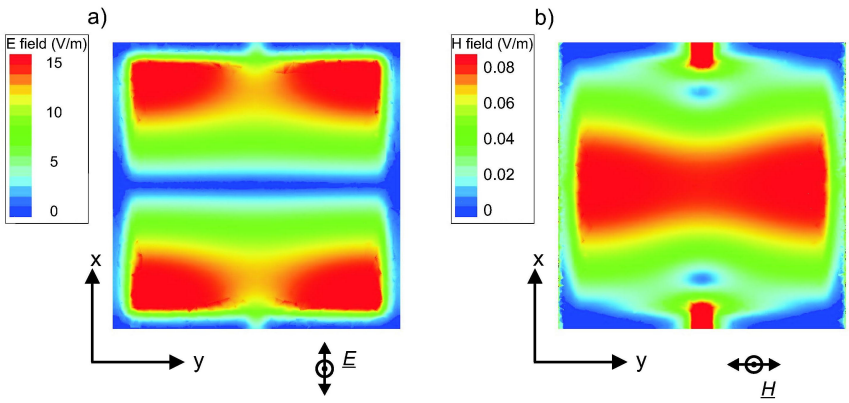

Figure 8.25: Field magnitudes taken from the FEM model for sample U. 8.25a) Electric field magnitude, and 8.25b) magnetic field magnitude. Fields are plotted across the xy-plane at a position 0.025 mm below the top metal layer. Incident polarisation direction is also indicated.

The field profiles observed for the electric and magnetic field magnitudes bear some resemblance to those fields presented in *Chapter* 3 in the discussion of waveguides. The TE_{01} mode in a rectangular waveguide has an electric field magnitude as shown in *Figure* 8.26, and bears a striking resemblance to that of the magnetic field magnitude shown in *Figure* 8.25b, with the difference being the effect of the electrical contacts. These field magnitude distributions and their relation to modes in a rectangular (or square) waveguide are much like those already discussed in *Chapter* 7 when considering arrays of metallic pennies separated from a continuous metal substrate by a dielectric layer. This sample is similar to the penny arrays in that it consists of a metallic array separated from a continuous metal substrate by a dielectric (LC) layer. In the previous chapter, and above in *Section* 8.2.4 the analogy is explained by considering the waveguide and array structures being close to having a direct reversal of electric and magnetic boundary conditions, thereby interchanging the electric and magnetic field distributions that arise on the two structures. The samples discussed here will be considered in the same way.

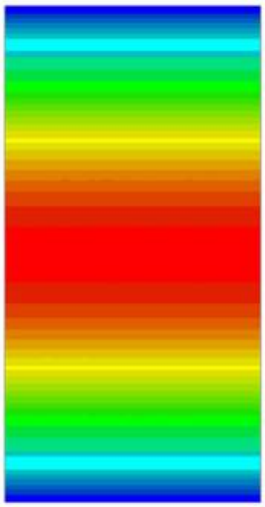

Figure 8.26: The electric field distribution for the TE_{01} mode in a rectangular waveguide.

The resemblance in fields can be further illustrated by plotting the electric and magnetic field vectors, as shown in *Figure* 8.27. Again, fields are plotted across the xy-plane at a position 0.025 mm below the top metal layer. 8.27a and 8.27b shows the electric and magnetic field vectors respectively, both plotted at a phase corresponding to maximum field enhancement. These vector plots allow insight into the field magnitude distribution around the region of the electrical contacts, around which the resemblance to the corresponding waveguide mode is somewhat interrupted. The electrical contacts interfere with the waveguide analogy as each array element can no longer be considered as independent, therefore the magnetic vector must reverse across the contacts, with a magnitude equal to that across the square patch, as illustrated in *Figure* 8.27.

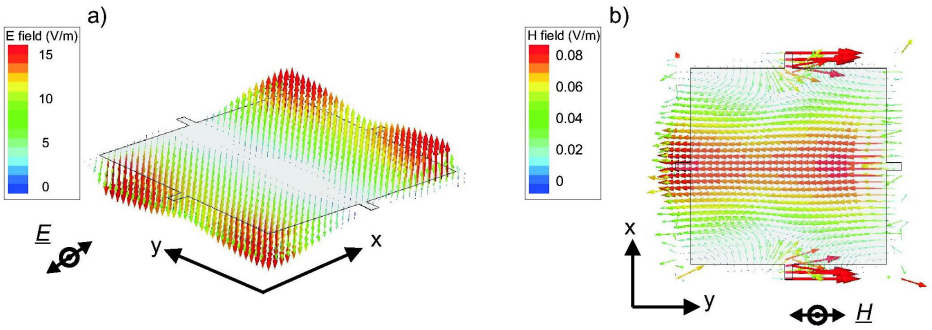

Figure 8.27: a) Electric and b) magnetic field vectors from the FEM model for sample U. Fields are plotted across the the xy-plane at a position 0.025 mm below the top metal layer at a phase corresponding to maximum enhancement. Incident polarisation direction is also indicated.

The electric and magnetic vectors shown in *Figure* 8.27a and 8.27b are very similar to those in *Figure* 8.28a and 8.28b, which show the magnetic and electric field vectors for the TE_{01} mode in a rectangular waveguide, with the difference being that the behaviour of the fields are interchanged, i.e. the electric fields from sample U resemble the magnetic fields in the TE_{01} mode.

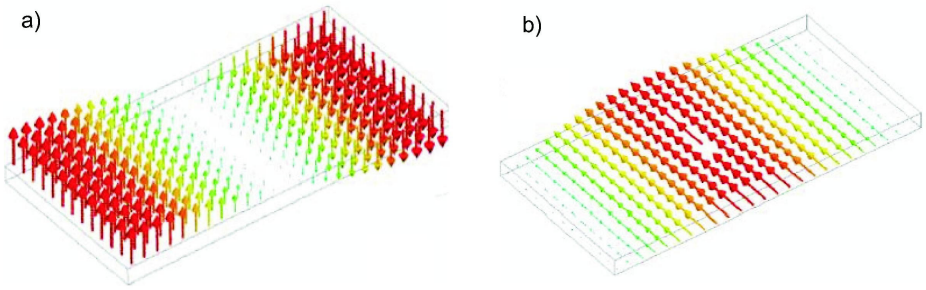

Figure 8.28: a) Magnetic and b) electric field vectors for the TE_{01} mode in a rectangular waveguide.

From *Chapter* 3 it is possible to calculate a cut-off frequency for the TE_{01} mode in a rectangular waveguide, which should also give a good approximation of the minimum frequency at which resonant absorption occurs on the structure discussed above.

The cut-off frequency for a TE_{01} mode in a rectangular waveguide is as follows:

$$f_c = \frac{c}{2\pi n}\sqrt{\left(\frac{M\pi}{a}\right)^2 + \left(\frac{N\pi}{b}\right)^2}$$

Here n is the refractive index of the core, M and N are the quantisation numbers along sides of length a and b. For a detailed description and derivation of this formula see *Chapter* 2. For the case of a square waveguide where a and b are equivalent the cut-off frequency reduces to:

$$f_c = \frac{c}{2an}$$

From this equation we can estimate the cut-off frequency of this mode, below which it cannot exist. For structure T in the off-state, the effective cut-off frequency is ~16.8 GHz, reducing further to ~15.8 GHz in the on-state. The resonant frequencies of the off- and on-states recorded in the data are ~19.3 GHz and ~18.6 GHz respectively. The cut-off frequencies are calculated for a thin slice from an infinite waveguide, with perfect H boundaries. In sample T the thickness off the structure, the effect of the aligning layer, and the effect of the electric contacts cause a perturbation to the mode, causing a rise in frequency. However, the waveguide approximation can still give a good guide as to the resonant frequency of this structure

in ideal conditions.

Figure 8.29 displays frequency dependent reflectivity data from sample V, the penny array with electrical contacts linking nearest neighbours. Data is displayed at selected azimuthal angles taken from *Figure* 8.12, and is shown for both 0 V applied across the cell (off-state, black squares) and 15 V applied across the cell (on-state, red squares). A mode appears at approximately 23 GHz (off-state) in all four plots and is considered the fundamental mode of this structure. A secondary mode appears for both p- and s-polarisations taken at a polar angle of $\theta = 35°$. Field plots provided by the FEM model will reveal the nature of these resonant modes.

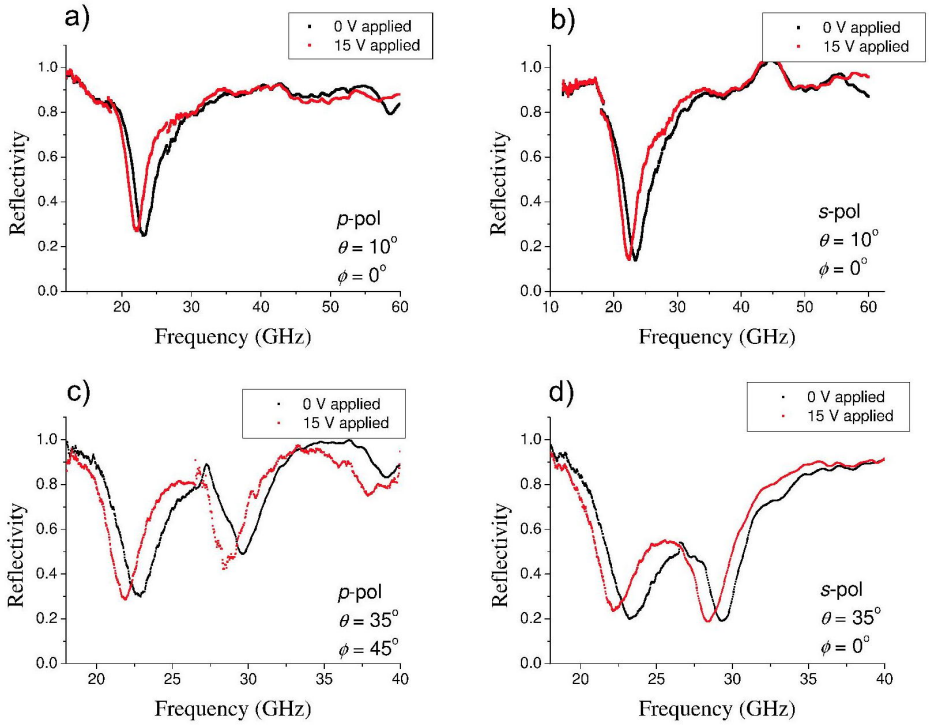

Figure 8.29: Reflectivity from sample V, the first penny array, at selected azimuthal angles. Black squares are for the cell in the off-state with no voltage applied, red squares are when 15 V is applied across the cell. 8.29a) p-polarised, θ= 10°, ϕ= 0°. b) s-polarised, θ= 10°, ϕ= 0°. c) p-polarised, θ= 35°, ϕ= 45°. d) s-polarised, θ= 35°, ϕ= 0°.

Figure 8.35 displays frequency dependent reflectivity data from sample W, the second penny array in which pennies have electrical contacts that link diagonally. Data is shown as black squares (off-state, 0 V applied) and red squares (on-state, 15 V applied) for selected azimuthal angles taken from *Figure* 8.13. The fundamental mode appears at approximately 20 GHz (off-state) in all four plots, which are for polar angles of θ= 10°, 35° and for both p- and s-polarisations. A secondary mode appears at approximately 32 GHz (off-state) for the

higher polar angle of θ= 35°. Field plots provided from an FEM model will reveal the nature of these modes.

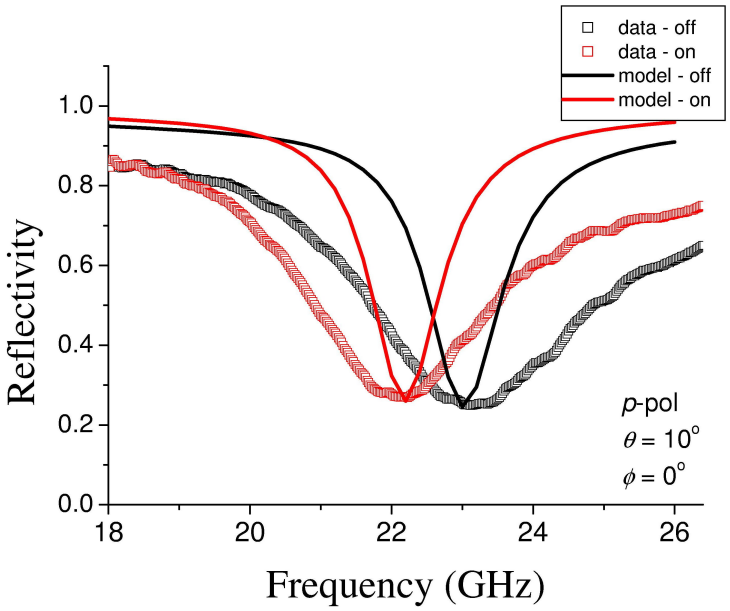

Figure 8.30: Reflectivity data for sample V, the first penny array, together with predictions provided by an FEM model. Data is shown for a polar angle of θ= 10°and azimuthal angle of ϕ= 0°, with p-polarised incident radiation. Open squares indicate data, solid lines represent the model predictions.

Figure 8.30 is a comparison between the reflectivity data obtained from the first penny array, sample V, and predictions from the FEM model for the same structure. Open squares indicate the data for both on- and off-states, whilst the solid line represents the model. The model replicates the experimental set-up which is taken at a polar angle of θ= 10° and an azimuthal angle of ϕ= 0°, with p-polarised incident radiation. Good agreement is obtained for resonant frequency in both on- and off-states, however there is disagreement in mode breadth. This is in part due to the model being perfect and infinite in the surface plane, whereas the sample is small (only a few wavelengths across) and suffers some variability over the array. The LC absorption will also affect the resonant width, and therefore it is impossible to determine the relative contributions to width of each effect. The only difference between the on- and off-state models is the permittivity of the dielectric core, which is $\varepsilon = 2.70 + 0.2i$ for the off-state and $\varepsilon = 2.98 + 0.2i$ for the on-state. This confirms that the shift in the resonant absorption is wholly due to the realignment of the liquid crystal under application of voltage. Further to this, as the values of permittivity used in the models assume that the LC is either wholly homogeneously aligned or wholly homeotropically aligned, it suggests that good alignment is indeed achieved in both on- and off-states. Further examination of the fields provided by the FEM model will give an insight to the nature of this mode.

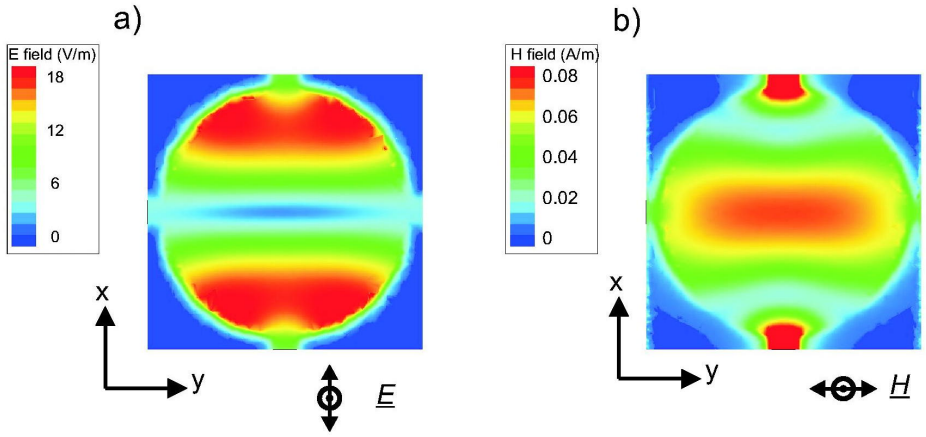

Figure 8.31: Field magnitudes taken from the FEM model for sample V. 8.31a) Electric field magnitude, and 8.31b) magnetic field magnitude. Fields are plotted across the xy-plane at a position 0.025 mm below the top metal layer. Incident polarisation direction is also indicated.

Figure 8.31a) and 8.31b) displays the time-averaged magnitude of electric and magnetic fields respectively. Field magnitude is colour-coded and indicated in the key, with electric fields being enhanced 15 times from that of the incident field at maximum. Fields are plotted over the xy-plane at a position 0.025 mm beneath the top metal layer, and incident polarisation direction is indicated. Similarly to the 2-D slit array, electric field maxima are observed on those edges of the penny that lie perpendicular to the incident field polarisation, with a null through the centre of the penny, and again, perpendicular to the incident field. The reverse is true for the magnetic field where there is a field maximum in the centre of the penny, and a reduction in H-field magnitude towards the penny edges. Further field maxima occur over the electrical contacts that coincide with the electric field maxima. Once more, the field magnitude plots can be compared to field magnitudes taken from *Chapter* 2. Below is the electric field magnitude distribution for the TE_{11} mode in a circular waveguide.

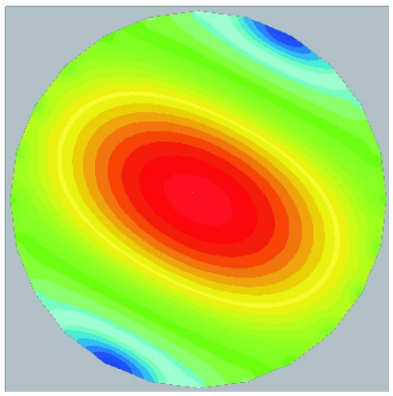

Figure 8.32: The electric field distribution for the TE_{11} mode in a circular waveguide.

It can be seen in *Figure* 8.32 that the electric field distribution for the TE_{11} mode in a circular waveguide is very similar to that of the magnetic field distribution shown in *Figure* 8.31 for structure V, with the exception of the effect of the electrical contacts. Examination of the behaviour of the electric and magnetic field vectors can give further insight into the nature of this mode.

Figure 8.33a) and 8.33b) shows the electric and magnetic vectors respectively for the first penny array, sample V. Fields are plotted across the xy-plane at a position 0.025 mm beneath the top metal layer, and incident polarisation direction is indicated. Field magnitude is colour-coded and indicated in the key, with electric fields being enhanced 15 times over that of the incident field at maximum. As with the previous sample, the electrical contacts cause a perturbation to the field distribution. For the electric fields to be matched across the boundary there must be a field null in order for the electric vector to reverse direction. Away from the contacts the field reduces to zero as the metal is non-continuous, however in the locality of the contacts the field direction must still be reversed, which causes a field reduction around the contacts. The H-field vector distribution is also significantly perturbed by the electrical contacts. As in the previous sample, at this phase the H-field is in the -y-direction, and is matched in magnitude and opposite in direction to the magnetic vector across the contacts, so there is no net flow across the unit cell and the boundary conditions are satisfied. With the exception of the effect of the electrical contacts it can be seen that the vector field distributions closely match those vector fields from the TE_{01} mode in a circular waveguide, albeit with the electric and magnetic fields reversed.

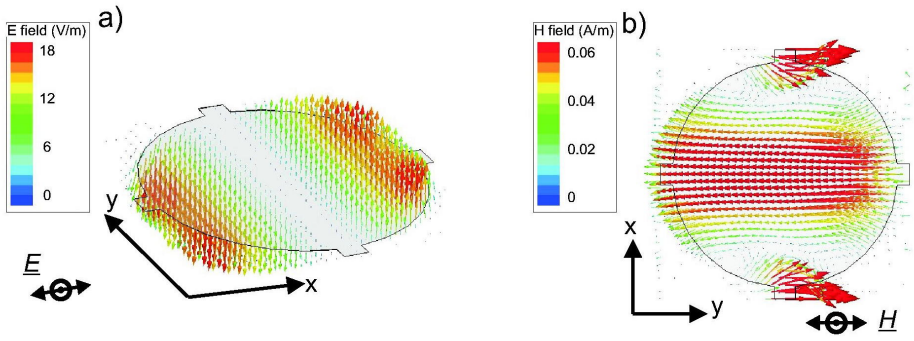

Figure 8.33: a) Electric and b) magnetic field vectors from the FEM model for sample V. Fields are plotted across the the xy-plane at a position 0.025 mm below the top metal layer at a phase corresponding to maximum enhancement. Incident polarisation direction is also indicated.

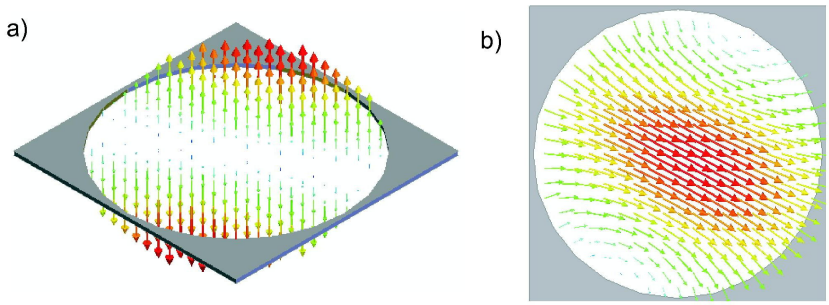

Figure 8.34: a) Magnetic and b) electric field vectors for the TE_{11} mode in a circular waveguide.

Figure 8.34a and 8.34b shows the magnetic and electric vector field distributions respectively for the TE_{11} mode in a circular waveguide. It is clear that the vector field distributions match those observed from the model for sample V, with the magnetic and electric field distributions reversed. As was the case with the 2-D slit array, sample U, this is due to the reversal of boundary conditions between the waveguide and the sample. A vacuum-filled, metal-clad waveguide that is considered to be infinite in the z-direction is enclosed by an electric wall, as the metal is assumed to be perfectly conducting tangential E-field drops to zero at the wall. The reverse is true of sample V, where the two metal layers may be considered in the analogy as the open ends of the waveguide, and are the electric walls of the structure. The interchange of boundary conditions between the waveguide and the sample allow a resonant mode to exist that is similar in nature to the TE_{11} in a circular waveguide, but with electric and magnetic field distributions interchanged. In a similar way to sample T, we can predict a cut-off frequency for this mode, below which the mode cannot propagate. The cut-off frequency for a circular waveguide is given by:

$$f_c = \frac{1.841c}{2\pi an}$$

Where a is the radius of the waveguide and n is the refractive index of the core. A full derivation of this equation can be found in *Chapter* 2. Applying this equation to structure V yields a cut-off frequency of ∼19.2 GHz for the off-state, and ∼18.2 GHz for the on-state, as compared with ∼23 GHz in the off-state and ∼22 GHz in the on-state for the data. Again, the cut-off frequency represents an idealised limit, and therefore it is not surprising that the resonances of structure V are higher in frequency. However, the cut-off frequency is a reasonable first approximation for the resonance of this structure.

Figure 8.35 displays reflectivity data for the second penny array, sample W. This sample differs from the previous sample as the electrical contacts are between diagonal nearest neighbours, and the pitch of the array is smaller at 5.85 mm. Data is plotted for both p- and s-polarisations and at two polar angles, θ= 10°, 35° and shown at selected azimuthal angles taken from *Figure* 8.13 and is shown for both off- (0 V applied, black squares) and on-states

(15 V applied, red squares). A mode is observed at approximately 21 GHz (off-state) in all four plots (higher polar angle plots are plotted over a different frequency range) and this mode is assumed to be the fundamental mode of the system. The higher polar angle plots (θ= 35°) also display a secondary mode at approximately 32 GHz (off-state).

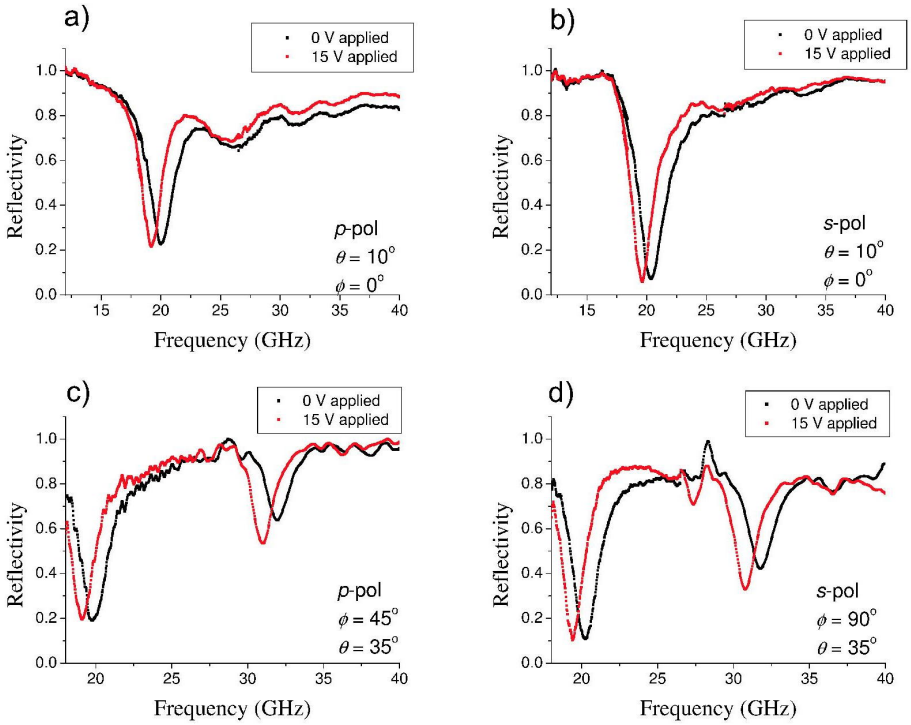

Figure 8.35: Reflectivity from sample W, the second penny array, at selected azimuthal angles. Black squares are for the cell is in the off-state with no voltage applied, red squares are for 15 V applied across the cell. 8.35a) p-polarised, θ= 10°, ϕ= 0°. b) s-polarised, θ= 10°, ϕ= 0°. c) p-polarised, θ= 35°, ϕ= 45°. d) s-polarised, θ= 35°, ϕ= 90°.

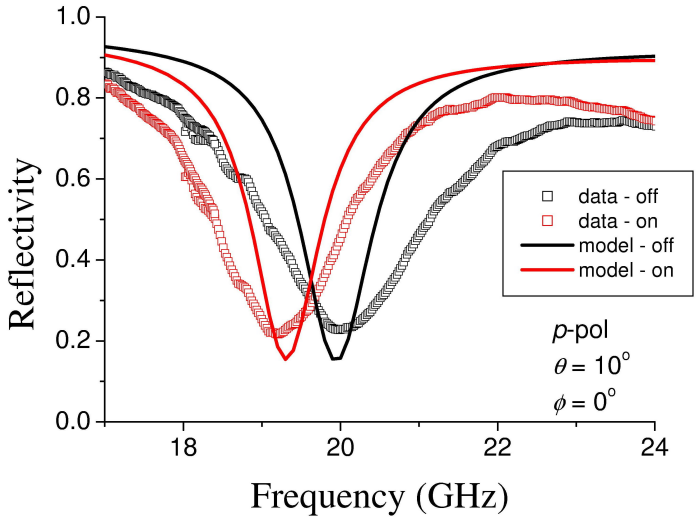

Figure 8.36: Reflectivity data for sample W, the second penny array, together with predictions provided by an FEM model. Data is shown for a polar angle of θ= 10° and azimuthal angle of ϕ= 0°, with p-polarised incident radiation. Open squares indicate data, solid lines represent the model predictions.

Figure 8.36 shows reflectivity data taken from the second penny array, sample W, plotted against predictions from the FEM model. Data is shown for a polar angle of θ= 10°and azimuthal angle of ϕ= 0°and incident radiation is p-polarised. Data is shown as black (off-state) and red (on-state) open squares, and the model prediction as a solid line with the same colour coding. Again, good agreement is obtained between model and data for the resonant frequency of the mode, with some disagreement in breadth and depth, with the reasons for any discrepancies being the same as in the previous sample, discussed above. Again, the shift in LC permittivity is confirmed as causing the shift in resonant frequency.

Figure 8.37 shows (a) the time-averaged electric field magnitude and (b) the time-averaged magnetic field magnitude plotted across the xy-plane at a position 0.025 mm beneath the top metal layer. Fields are plotted for the model replicating the off-state at a frequency of 20 GHz. Field magnitude is colour-coded and is illustrated by the key. The polarisation of the incident field is also indicated.

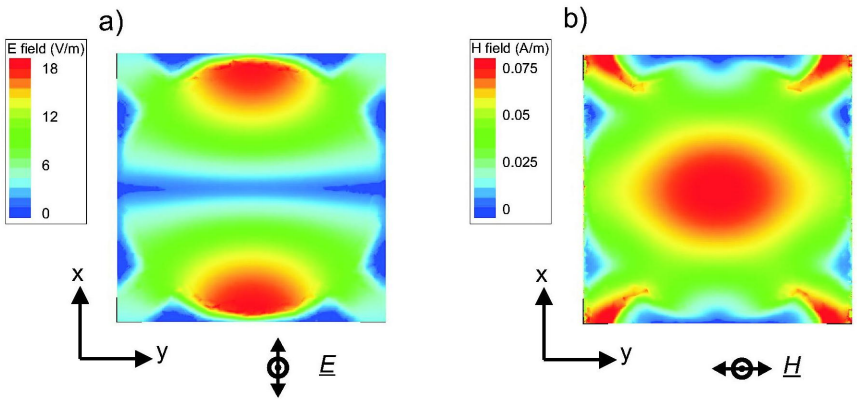

Figure 8.37: Field magnitudes taken from the FEM model for sample W. 8.37a) Electric field magnitude, and 8.37b) magnetic field magnitude. Fields are plotted across the xy-plane at a position 0.025 mm below the top metal layer. Incident polarisation direction is also indicated.

Electric field maxima occur towards the edge of the penny perpendicular to the polarisation direction, with a field null across the centre of the penny. For the previous sample where pennies were square-linked to nearest neighbours there was a perturbation to the field in the locality of the links, however for this sample the field maxima are located away from the metallic link, therefore the link does not have the same effect. This also means that the H-field maxima over the electrical contacts observed in the previous sample are reduced in magnitude, as the contacts do not coincide with the electric field maxima. Once more, the magnetic field distribution is very similar to the distribution of the electric field for the TE_{11} mode in a circular waveguide (*Figure* 8.38).

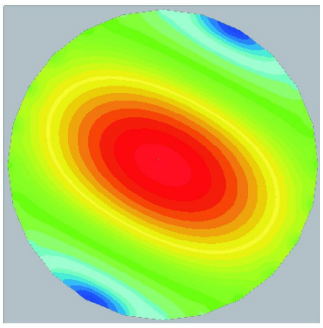

Figure 8.38: The electric field distribution for the TE_{11} mode in a circular waveguide.

Figure 8.39 shows the (a) electric vector and (b) magnetic vector field distributions plotted across the xy-plane at a position 0.025 mm beneath the top metal layer and at a phase corresponding to maximum enhancement. The field distributions are very similar to that of the previous sample, with the only exception being the effect of the electrical contacts. As

previously, if these field distributions are compared with that of the TE_{11} mode in a circular waveguide they will appear the same, with the role of electric and magnetic vectors reversed.

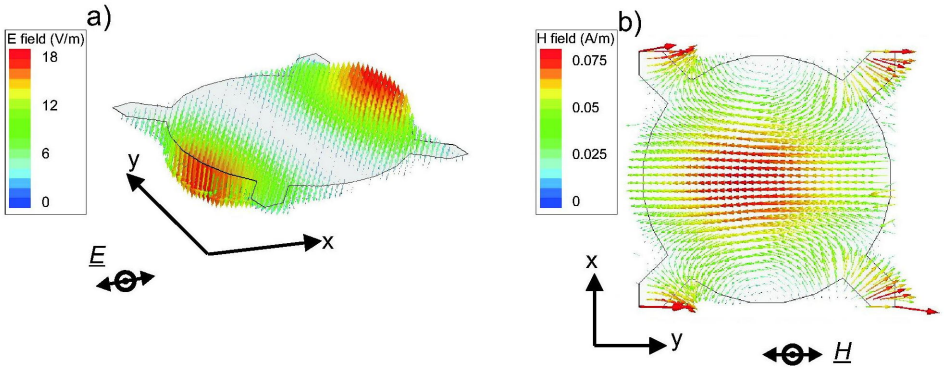

Figure 8.39: a) Electric and b) magnetic field vectors from the FEM model for sample W. Fields are plotted across the the *xy*-plane at a position 0.025 mm below the top metal layer at a phase corresponding to maximum enhancement. Incident polarisation direction is also indicated.

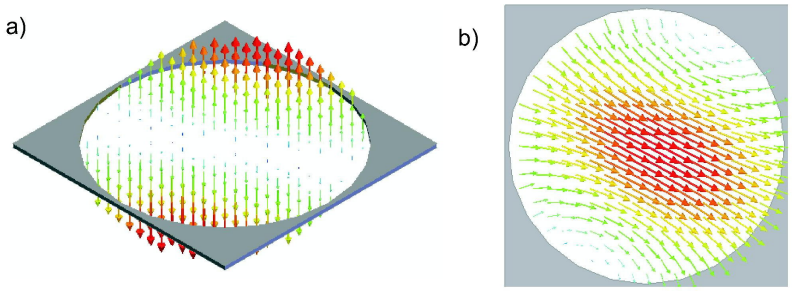

Figure 8.40: a) Magnetic and b) electric field vectors for the TE_{01} mode in a circular waveguide.

Figure 8.40 shows the (a) magnetic and (b) electric vector distributions for the TE_{01} mode in a circular waveguide. The vector plots in *Figure* 8.39 confirm that the mode observed in sample W may is analogous to a TE_{01} mode. In the same way as sample V, we can predict a cut-off frequency for this mode, below which the mode cannot propagate. The cut-off frequency for a circular waveguide is given by:

$$f_c = \frac{1.841c}{2\pi an}$$

Here a is the radius of the waveguide and n is the refractive index of the core. A full derivation of this equation is in *Chapter* 2. Applying this equation to structure W yields a cut-off frequency of ~18.3 GHz for the off-state, and ~17.4 GHz for the on-state as compared

with ∼20.1 GHz for the off-state and ∼19.2 GHz for the on-state from the reflectivity data. It may again be noted that the cut-off frequencies are predictions from an idealised system, and due to the effects of a finite thickness, the aligning layer, and the electrical contacts it is unsurprising that the resonant frequency of structure W is somewhat higher than cut-off.

The final three samples, X, Y and Z will be discussed together, as the structure of samples Y and Z are modified from that of X, and this modification results in a change in the resonant response of each sample. Sample X consists of a square metal patch perforated by four metal "slits" close to the edge of the patch, and is displayed in *Figure* 8.8 above. Samples Y and Z are modified from X by the addition of four "cuts" originating from the centre of each slit and directed towards the centre of the patch. It is important to note the lack of 90° degree symmetry in the azimuthal response of structures Y and Z as seen in *Figures* 8.15 and 8.16, however, this will be discussed once the absorption mechanism has ascertained. As with previous samples considered in this chapter, each sample X, Y and Z resonantly absorbs microwave radiation, and the frequency of this resonant behaviour may be shifted by applying a voltage across the dielectric core in order to realign the LC therein. The introduction of "cuts" to samples Y and Z also results in a shift in frequency of the resonant absorption, and therefore each sample will be considered only in the off-state in order to avoid any confusion over the frequency-shift mechanism. *Figure* 8.41 displays a comparison of data from samples X, Y and Z in the off-state with predictions provided from and FEM model.

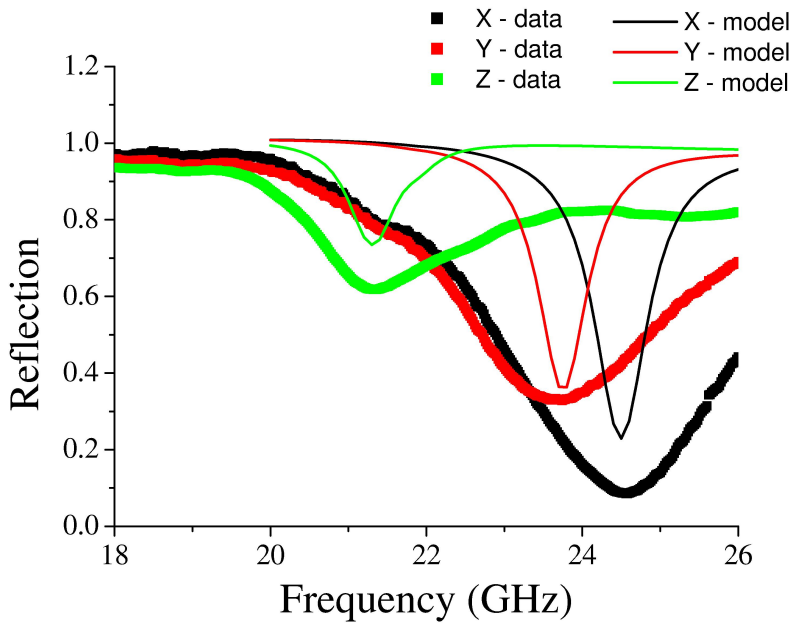

Figure 8.41: Reflectivity data from samples X, Y and Z compared with predictions provided by an FEM model.

The predictions provided by the FEM give good agreement with mode position, however there is a discrepancy in both depth and breadth. This is due to a combination of factors. The resonant breadth is sensitive to the thickness of the metal layers, however, the metal layer is achieved by evaporating aluminium onto a glass sheet, and therefore the thickness varies somewhat across each sample. In addition to this, the etched structure also suffers from a degree of variability, and is small as compared with the incident radiation beamspot, whereas the model is perfect and infinite in the surface plane. The imaginary part of the permittivity of the LC in the core also affects the breadth of the mode, and therefore it is not possible to separate out the relative contributions to width of each effect. However, the frequency position of each mode is good, so the field plots generated by HFSS can give insight into the absorption mechanism of the structure.

Figure 8.42 displays (a) the time-averaged electric field magnitude and (b) the time-averaged magnetic field magnitude for sample X plotted across the xy-plane at a position 0.025 mm beneath the top metal layer. Fields are plotted for the model replicating the off-state at a frequency of 24.5 GHz. Field magnitude is colour-coded and is illustrated by the key. The polarisation of the incident field is also indicated.

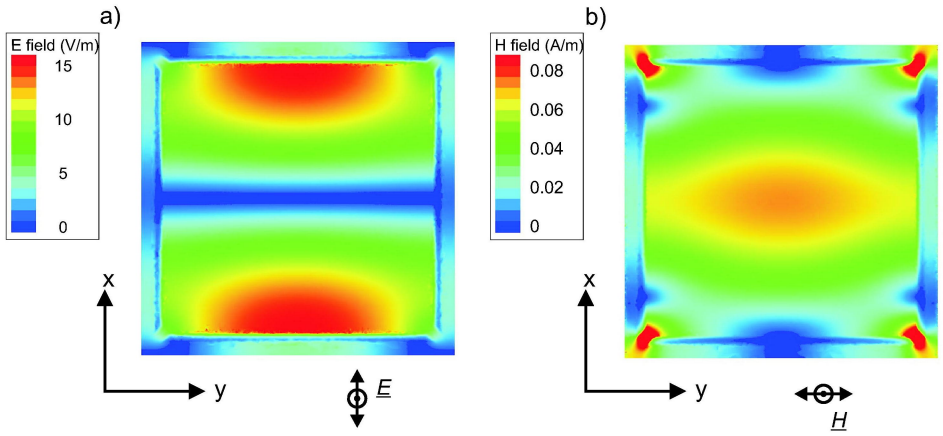

Figure 8.42: Field magnitudes taken from the FEM model for sample X. 8.42a) Electric field magnitude, and 8.42b) magnetic field magnitude. Fields are plotted across the xy-plane at a position 0.025 mm below the top metal layer. Incident polarisation direction is also indicated.

The electric and magnetic field distributions observed for this structure resemble those of sample U, which in turn were shown to be analogous to a TE_{01} mode in a rectangular waveguide. The structure of this sample differs from that of sample U, as here the slits are not at the edge of the unit cell, but surrounded by a continuous metal border. Nonetheless, the field distribution still resembles that of the TE_{01} mode in a rectangular waveguide, and therefore we can say the absorption mechanism is the same as that observed in previous samples. The electric field distribution for the TE_{01} mode in a rectangular waveguide is shown in *Figure* 8.43, and resembles the magnetic field distribution shown above in *Figure* 8.42. As in previous

cases, this sample is analogous to a metal-clad waveguide, but with the electric and magnetic boundaries interchanged, resulting in fields that resemble that of the waveguide mode, but with the magnetic and electric field distributions interchanged. Again, the electrical contacts perturb the field distributions as they create a continuous metal layer, and the array elements are no longer isolated.

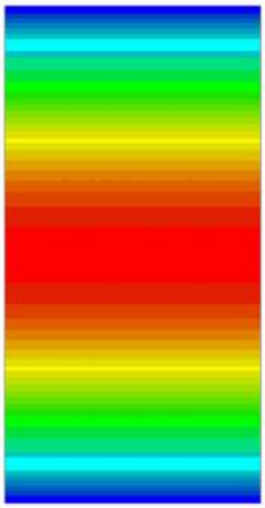

Figure 8.43: The electric field distribution for the TE_{01} mode in a rectangular waveguide.

As in previous samples we can see that the electric vector distribution of sample X (*Figure* 8.44) resembles the magnetic vector distribution of the TE_{01} mode in a rectangular waveguide (*Figure* 8.45), whereas the magnetic vector distribution of sample X (*Figure* 8.44) resembles the electric vector distribution of the TE_{01} mode in a rectangular waveguide (*Figure* 8.45).

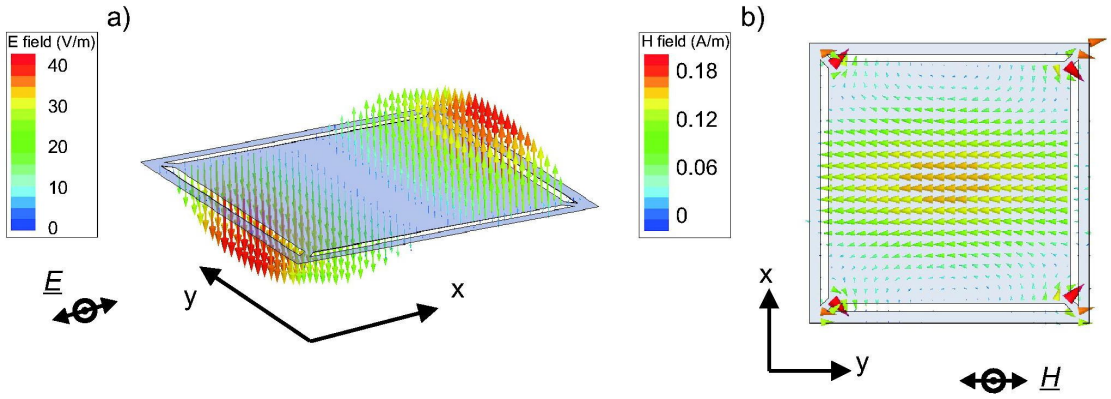

Figure 8.44: a) Electric and b) magnetic field vectors from the FEM model for sample X. Fields are plotted across the the *xy*-plane at a position 0.025 mm below the top metal layer at a phase corresponding to maximum enhancement. Incident polarisation direction is also indicated.

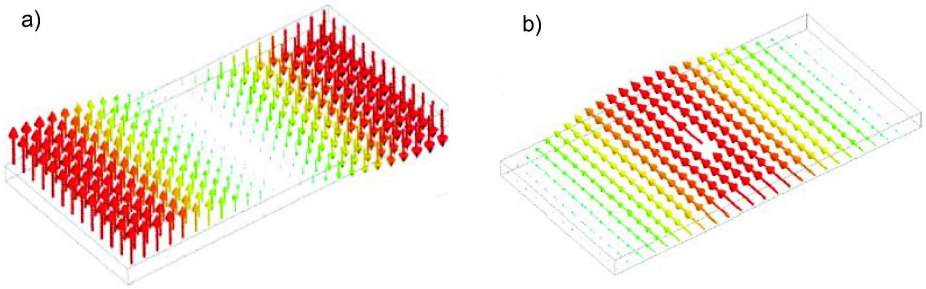

Figure 8.45: a) Magnetic and b) electric field vectors for the TE_{01} mode in a rectangular waveguide.

We have seen that the waveguide mode analogy holds for sample X, however, the introduction of cuts in samples Y and Z cause a reduction in the resonant frequency response of those samples. Examination of field plots for these samples can reveal the cause of this reduction in frequency.

Figure 8.46 displays (a) the time-averaged electric field magnitude and (b) the time-averaged magnetic field magnitude for sample Y plotted across the xy-plane at a position 0.025 mm beneath the top metal layer. Fields are plotted for the model replicating the off-state at a frequency of 23.8 GHz. Field magnitude is colour-coded and is illustrated by the key. The polarisation of the incident field is also indicated.

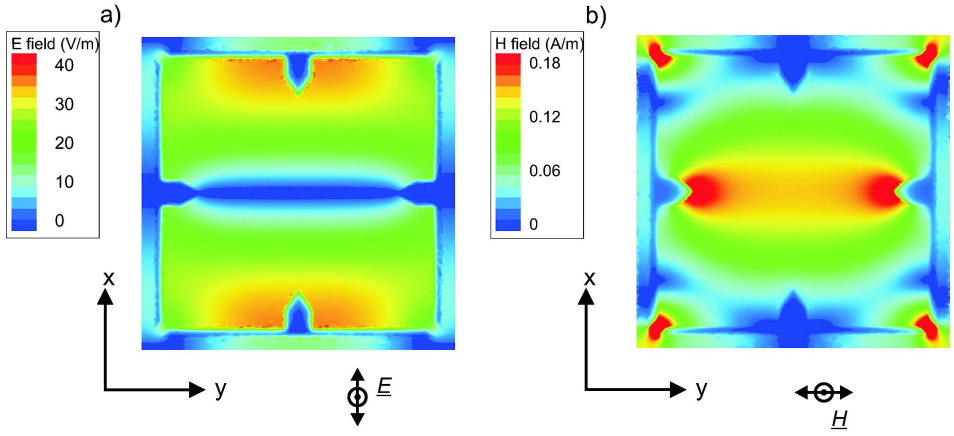

Figure 8.46: Field magnitudes taken from the FEM model for sample Y. 8.46a) Electric field magnitude, and 8.46b) magnetic field magnitude. Fields are plotted across the xy-plane at a position 0.025 mm below the top metal layer. Incident polarisation direction is also indicated.

The field distributions for sample Y displayed in *Figure* 8.46 display features similar to those seen in sample X, however there are some differences. *Figure* 8.46a) shows that the cuts that lie parallel to the y-axis seem to aid the existence of a field null through the centre of the unit cell, and those cuts that lie parallel to the x-axis seem to cause a reduction in the electric field magnitude. These affects may serve to reduce the enhancement to the incident field, and therefore reduce the coupling efficiency, as seen in *Figure* 8.41. *Figure* 8.46b) shows that the magnetic field peak is no longer located in the centre of the unit cell, but has split, and is now concentrated around the two cuts that lie parallel to the y-axis. A similar distribution to this was seen in *Chapter* 5 when discussing transmission through a scaled-up version of this structure. To understand what is happening on this structure we will now examine the electric and magnetic vector distributions of sample Y, and the field distributions on sample Z as they may give a clearer indication of the affect of the cuts on the resonant response of the structure.

Figure 8.47 displays the electric and magnetic field vectors from the FEM model for sample Y plotted across the the xy-plane at a position 0.025 mm below the top metal layer at a phase corresponding to maximum enhancement.

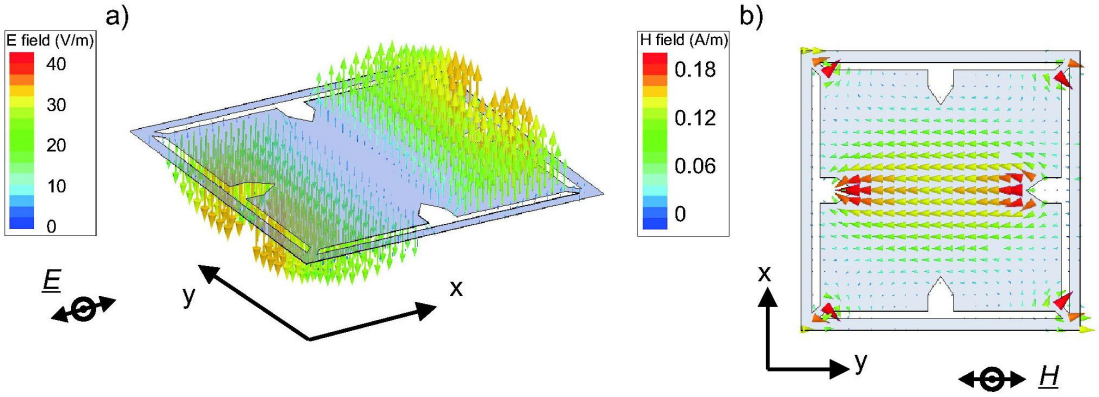

Figure 8.47: a) Electric and b) magnetic field vectors from the FEM model for sample Y. Fields are plotted across the the xy-plane at a position 0.025 mm below the top metal layer at a phase corresponding to maximum enhancement. Incident polarisation direction is also indicated.

Figure 8.48 displays (a) the time-averaged electric field magnitude and (b) the time-averaged magnetic field magnitude for sample Z plotted across the xy-plane at a position 0.025 mm beneath the top metal layer. Fields are plotted for the model replicating the off-state at a frequency of 21.3 GHz. Field magnitude is colour-coded and is illustrated by the key. The polarisation of the incident field is also indicated.

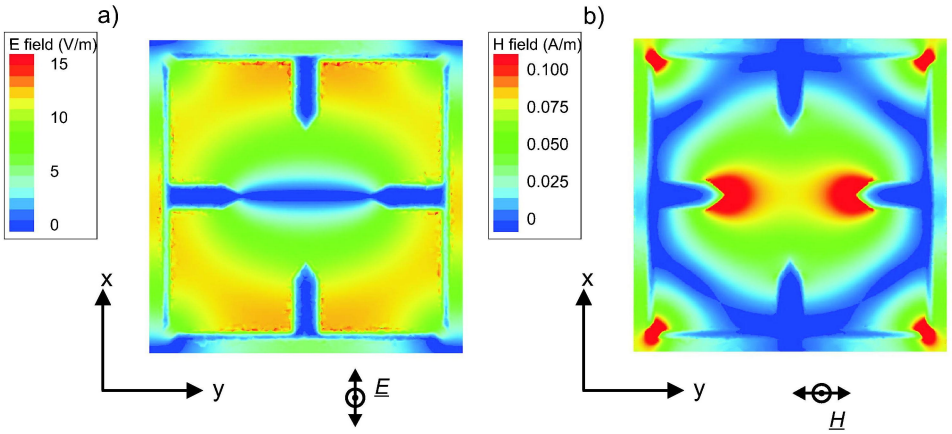

Figure 8.48: Field magnitudes taken from the FEM model for sample Z. 8.48a) Electric field magnitude, and 8.48b) magnetic field magnitude. Fields are plotted across the xy-plane at a position 0.025 mm below the top metal layer. Incident polarisation direction is also indicated.

Figure 8.47 displays the electric and magnetic field vectors from the FEM model for sample Y plotted across the the xy-plane at a position 0.025 mm below the top metal layer at a phase corresponding to maximum enhancement.

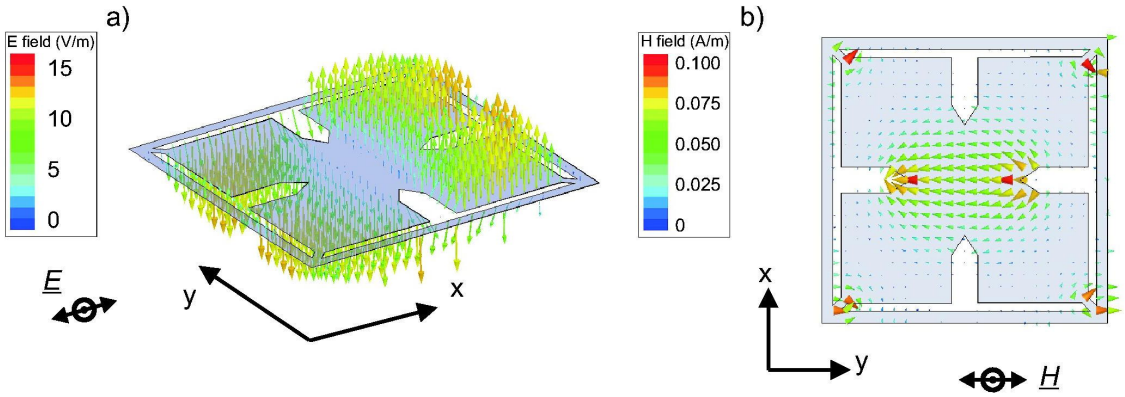

Figure 8.49: a) Electric and b) magnetic field vectors from the FEM model for sample Z. Fields are plotted across the the xy-plane at a position 0.025 mm below the top metal layer at a phase corresponding to maximum enhancement. Incident polarisation direction is also indicated.

It is clear that the field distributions seen in *Figure* 8.48 are somewhat different from that observed in *Figure* 8.42, and that the cuts have had a significant effect on the electric and magnetic fields. The electric field distribution (*Figure* 8.48a) does not closely resemble the magnetic field of the TE_{01} mode in a rectangular waveguide. The magnetic field has two clear

strong peaks around the cuts parallel to the y-axis, again, not resembling the electric field distribution in the TE_{01} mode in a rectangular waveguide. In *Chapter* 5 it was seen that the transmission through a "slit and cut" structure was due to the role of surface currents on the metal layer. Examination of the surface currents on this structure may give insight to the changing resonant behaviour, and therefore explain the reduction in the resonant frequency of absorption for samples Y and Z.

Figure 8.50 displays the surface current vector on the top metal layer of sample Z at a phase corresponding to maximum enhancement. It is clear that the surface currents are enhanced around those cuts that lie parallel to the y-axis in the same way as observed in the transmission structure discussed in *Chapter* 5. In the transmission sample, these currents lead to the cuts behaving as inductive element, and induced magnetic field loops in the yz-plane. This, in combination with a capacitance element across the slits lying parallel to the polarisation direction lead to the excitation of a zeroth-order Fabry-Perot mode.

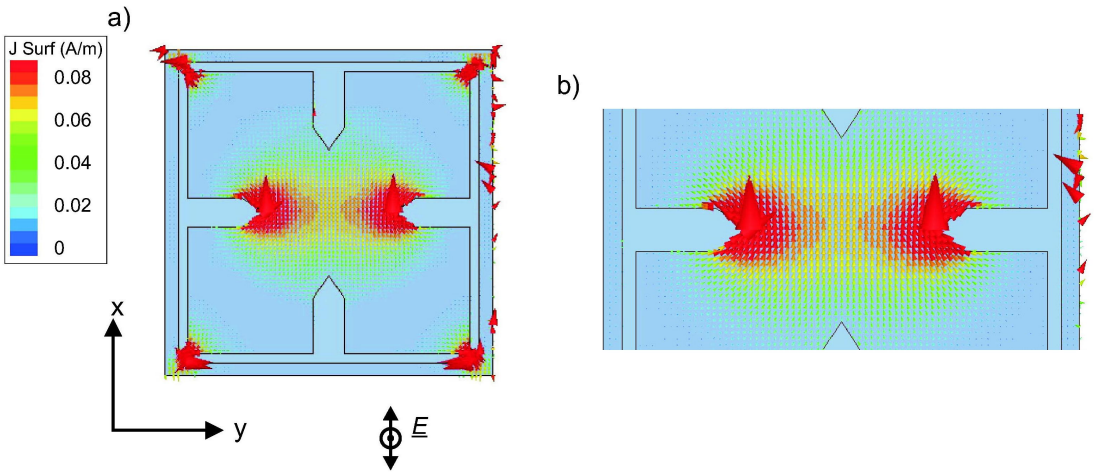

Figure 8.50: a) FEM field profile for surface currents on the metal layer of sample Z, plotted at a phase corresponding to maximum enhancement. 8.50b) a close up of the high surface currents around the cuts.

Therefore it should be possible to see the magnetic field loops in the yz-plane that are induced by the cuts. *Figure* 8.51 displays the magnetic vector across the yz-plane through the centre of the unit cell for sample Z, plotted at a phase corresponding to maximum enhancement. Indeed, the magnetic field loop is evident, confirming that the cuts are behaving as an inductive element, as in the zeroth-order Fabry-Perot mode discussed in *Chapter* 5.

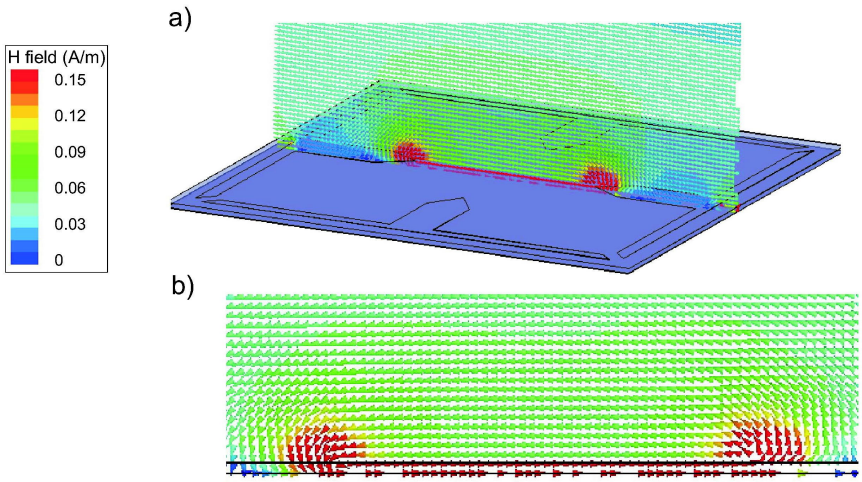

Figure 8.51: a) The magnetic vector across the yz-plane through the centre of the unit cell for sample Z, plotted at a phase corresponding to maximum enhancement.

However, it is not possible to now denote the resonance observed on sample Z as a zeroth-order Fabry-Perot mode, as there are significant differences to the mode observed on the transmission structure discussed in *Chapter* 5. In that case, there was clear evidence of a capacitive contribution from the slits lying parallel to the polarisation direction of the incident radiation, and greatly enhanced electric field magnitudes located around those same slits. From *Figure* 8.49, there is little evidence for a strong capacitive element, as there are already strong electric vector fields in the z-direction, however, *Figure* 8.48 does indicate some field enhancement in those slits that lie parallel to the incident polarisation direction. Therefore it is possible to attribute the response of samples Y and Z to a combination of absorption mechanisms. Previously, in *Chapter* 5, the introduction of cuts was seen to increase the inductive and capacitive elements of the structure, and drive the resonant frequency down. The transmission mode did not exist without the presence of the cuts. For samples Y and Z the situation is quite different. An absorption mode already exists on the structure, attributed to the analogy with a rectangular waveguide mode. The introduction of cuts to this structure allowed an alternative method of resonant absorption to occur, resulting in a combination of two absorption mechanisms. As the cuts were introduced and increased in size, the resonant frequency of the structure is reduced due to the behaviour of the surface currents, however there is also a reduction in coupling efficiency as the competing coupling mechanisms require different field distributions in order to resonantly absorb incident radiation.

Finally, *Figures* 8.15 and 8.16 display a clear change in coupling efficiency with azimuthal angle for samples Y and Z. The reasons for this can be attributed to two related affects when each structure is in the off-state and on-state. As already stated above, the cuts introduced into samples Y and Z allow a new method of coupling radiation to the structure due to the role of surface currents. In all previous samples discussed in this chapter, electric fields within the dielectric LC core have been primarily in the z-direction. However, for samples Y and Z

the surface current behaviour leads to an increased component of the electric vector in the xy-plane due to the existence of a capacitive element to the structure. When the sample is in the off-state, the LC is homogeneously aligned with the LC molecules lying parallel to the x-axis, and the sensed permittivity in the x-direction is different to that in the y-direction. Therefore as the sample is rotated azimuthally the relative contributions to the behaviour of the electric and magnetic field distributions by the two coupling mechanisms will be changed, resulting in a change in coupling efficiency of incident radiation to the sample. *Figure* 8.52 displays a comparison between p-polarised data taken from sample Z in the off-state at azimuthal angles of $\phi = 0°$, $90°$, with an FEM model of sample Z in the off-state (with the homogeneous LC birefringence included) at azimuthal angles of $\phi = 0°$, $90°$. It is clear that by considering the birefringence of the LC in the homogeneous state, the change in coupling efficiency may be accounted for.

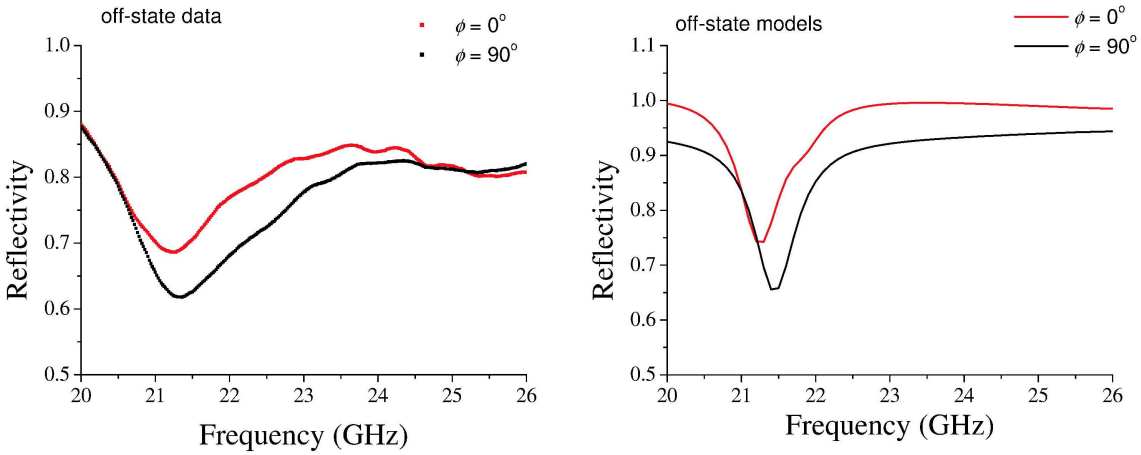

Figure 8.52: (left) p-polarised data from sample Z in the off-state at azimuthal angles of $\phi = 0°$, $90°$. (right) An FEM model of sample Z in the off-state with the LC birefringence included at azimuthal angles of $\phi = 0°$, $90°$.

However, when the sample is in the on-state, the LC becomes homeotropically aligned, and the above argument no longer applies, yet in the data there is still a change in coupling efficiency as the sample is rotated azimuthally. This may be accounted for by considering the area underneath the cuts. In this region, there is a relatively large area of LC that has no metal above it, and therefore will not be completely realigned by the applied field. *Figure* 8.53 displays a comparison of p-polarised data from sample Z in the on-state at azimuthal angles of $\phi = 0°$, $90°$ with a model of sample Z in the on-state at azimuthal angles of $\phi = 0°$, $90°$ that has a region of LC underneath the cuts that remains homogeneously aligned. It is not possible to perfectly replicate the data, as there will be some alignment of LC underneath the cuts, but it is clear that this can account for the change in coupling efficiency.

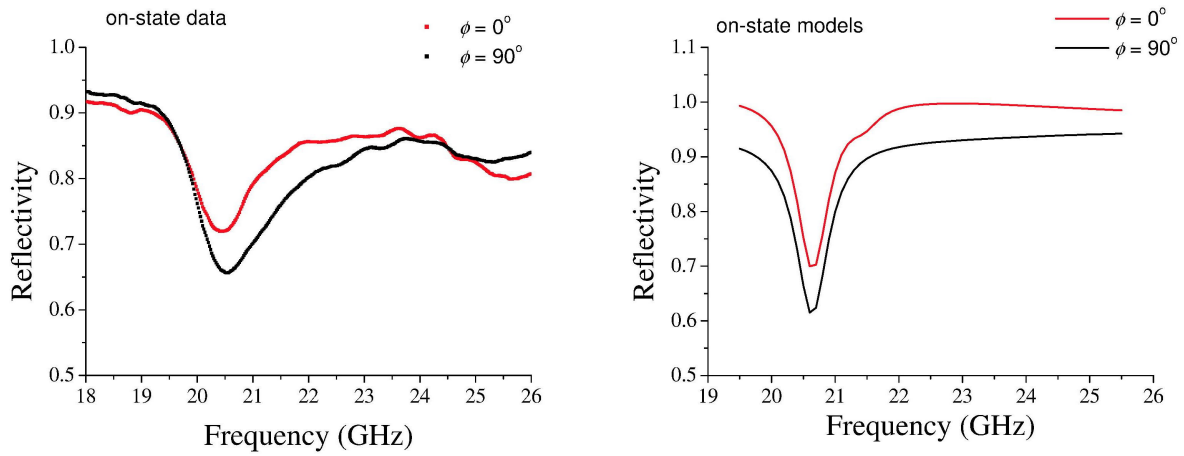

Figure 8.53: (left) p-polarised data from sample Z in the on-state at azimuthal angles of $\phi = 0°$, $90°$. (right) An FEM model of sample Z in the on-state at azimuthal angles of $\phi = 0°$, $90°$.

8.7 Summary

In summary, the microwave absorption response of seven samples has been presented, each of which consists of a novel metal-dielectric-metal structure where the dielectric layer is made up of homogeneously aligned LC. On application of a voltage it is possible to realign the LC and cause a shift in the resonant absorption of each sample. The samples that have been studied and described are a 1-D slit array, a 2-D slit array, two penny arrays, and three "slit and cut" arrays. The 1-D slit array was shown to resonantly couple radiation into the dielectric core and excite a standing wave, that remarkably compresses one half wavelength of the incident radiation into the area beneath the slits. The 2-D slit array and the two penny arrays were shown to resonantly absorb radiation, and by an analogy with waveguide modes in both rectangular and circular waveguides, it was shown it is possible to calculate a cut-off frequency for the frequency at which these structures absorb microwaves. The last three samples consisted of an arrangement of a 2-D slit array, modified by the addition of "cuts" in two of the samples. These samples displayed a reduction in their resonant frequency response, due in part to the behaviour of surface currents on the top metal surface. Each of these structures is the first of its kind, having tuneability introduced by the LC core, and all but two of the samples display resonant absorption by previously unreported mechanisms.

Chapter 9

Conclusions

9.1 Summary of Thesis

The work presented in this thesis has shown that the electromagnetic response of metallic structures in both absorption and transmission may be dramatically altered by the introduction of subwavelength structure, in a manner that has not been previously reported in the literature. The frequency at which subwavelength structures in metal transmit radiation has been shown to to be controlled by the dimensions of the structure, and separately, by the introduction of LCs. In reflection, remarkable absorption of radiation in the zero-order region is again shown to be due to subwavelength structure. Introduction of LCs into some of these absorbing structures has allowed a degree of control over the frequency at which the resonant absorption occurs.

In *Chapter* 5 the microwave transmission response of four samples, consisting of arrays of a "slit and cut" structure in a thin aluminium layer is discussed. Two of the four samples consist of 2-D arrays of slits modified by the addition of electrical contacts across each slit. The third and fourth samples are further modified by the addition of "cuts" (of differing depth) perpendicular to the slits. Samples were formed from a thin aluminium layer ($\sim$40 nm) backed by a dielectric layer ($\sim$100 μm), and arrays were cut into the metal film via a wet-etch technique. Over the frequency band explored, 18 to 60 GHz, two transmission modes were shown to propagate through this structure. One of these transmission modes was shown to be a coupled surface wave, occurring in all samples. Incident photons couple through slits that lie orthogonal to the polarisation direction, exciting a surface wave. This surface wave is then coupled to a similar wave on the back surface of the structure, which then re-radiates into free space. The second transmission mode was shown to occur due to an entirely different mechanism, and occurred only on those samples that have perpendicular cuts. The cuts allowed the accessing of a previously unreported "zeroth-order Fabry-Perot" mode on such a thin layer, which occurs due to the role of surface currents on the metal layer. The frequency at which the zeroth-order Fabry-Perot mode occurs was shown to be due to the dimensions of the cuts, which in turn dictates the surface current behaviour, with the mode being excited

via slits that lie parallel to the polarisation direction. Although transmission mediated by this mode occurs at a frequency higher than that at which the sample becomes diffractive, it may be possible to design a structure for which the zeroth-order Fabry-Perot mode occurs at a frequency below the diffraction limit, therefore realising a new mechanism for achieving zero-order resonant transmission.

In *Chapter* 6 the transmission of Liquid Crystal confined within a single, subwavelength slit in otherwise opaque metal was investigated. Transmission was found to be mediated by Fabry-Perot like resonances, and by comparison with field plots provided by the FEM model, and a simple calculation, the ordinary and extraordinary indices of the LC were found. Also, a PDLC was created from mixing LC with a UV curing glue in different ratios, and an indication of the relationship between available index shift and % wt polymer was found. This was achieved by determining the ordinary and extraordinary indices of the PDLC. The PDLC mixture provides the possibility of introducing tuneability into structures in which the dielectric layer has a degree of rigidity. This will allow for the fabrication of light-weight, flexible, voltage-tuneable coatings.

In *Chapter* 7 an investigation into the absorption response of four arrays of metallic pennies separated from a metal substrate by a dielectric layer was undertaken. The four samples were split into two types, the first three of these consisted of a thick aluminium plate, 300 mm $\times$ 300 mm $\times$ 30 mm, which was covered with a 50 μm dielectric layer of Filmolux, on top of which an array of metallic pennies was assembled. Each penny had a radius of $\sim$2.875 mm and a thickness of $\sim$1 mm. Three arrays of this type were investigated, two of which were square arrays, having pitches of 6 mm and 8 mm, and the third of which was a hexagonal array, having a pitch of 8.8 mm. The second type of sample was formed from a printed circuit board (PCB), which consisted of a polyester sheet of thickness 100 μm bounded by copper layers of thickness 16 μm. An array sample was formed by etching into one face of the copper cladding an array of pitch 6.25 mm with penny radii of 2.95 mm. The reflection response of these structures revealed several modes occurring in the zero-order region, and by examining the electric and magnetic field plots provided by the FEM model at the resonant frequencies these modes were found to be analogous to waveguide modes, in particular the first three modes to propagate in a circular waveguide, the TE_{11}, TE_{21} and the TE_{01} . However, the electric field distributions within in the penny arrays were seen to match the *magnetic* field distributions found in the waveguide modes, whilst the magnetic field distributions within in the penny arrays were seen to match the *electric* field distributions found in the waveguide modes. This was attributed to the boundary conditions of the two structures being approximately the inverse of one another, with the waveguide being surrounded by an electric wall and open-ended, and the penny arrays having open sides, with an electric wall on either end of the dielectric layer. This lead to the possibility of estimating a cut-off frequency for each mode occurring in the penny arrays by using simple waveguide theory. This in turn leads to it being possible to predict what modes may exist on other arrays of this type by simply

knowing the array properties, and the appropriate waveguide theory. Absorption of microwave radiation via the penny structures, and the accompanying waveguide theory analogy has not been reported in the literature, however, as **publication on this work has been restricted by our sponsors due to its sensitive nature and potential patent applications**.

In *Chapter* 8 the microwave absorption response of seven samples was investigated, each of which consists of a metal-dielectric-metal structure where some subwavelength structure is etched into the top metal layer, and the dielectric layer is made up of LC. In each case, it is this etched structure that allows resonant absorption of microwaves into the dielectric core, whereupon the absorption frequency can be changed by realignment of the LC material within the core. The sample investigated is a 1-D slit array, and absorption is shown to be via coupling into a standing wave within the core of the structure, in the manner reported by *Hibbins et al* (2002) [40]. The second sample is a 2-D slit array, and absorption can be again shown to be due to the excitation of standing waves within the LC core. Alternatively, it can be shown that the *electric* field distribution on the square metal "patch" surrounded by the slits closely resembles the *magnetic* field distribution of the TE_{11} mode in a square waveguide. Conversely the *magnetic* field distribution of the patch closely resembles the *electric* field distribution of the TE_{11} mode in a square waveguide. The cut-off frequency of the TE_{11} mode in a square waveguide can then be used to calculate the frequency at which the absorption occurs on the 2-D slit array. The third and fourth samples are penny arrays, similar to those discussed in the previous chapter (although in this case they have an LC-filled core). Again, the absorption is shown to be analogous to the TE_{11} mode in a circular waveguide, and the cut-off frequency can be used to calculate the frequency at which modes occur. This calculation includes the refractive index of the core material, and provides a good approximation to observed absorption frequencies for both homogeneous and homeotropic LC alignments within the core when the corresponding LC refractive indices are input. **Once more, publication on this work has been restricted by our sponsors due to its sensitive nature and potential patent applications.**

9.2 Future work

The microwave studies presented in this thesis were conducted as part of the work of the much larger Electromagnetic Materials group. This group has been at the forefront of optics research over the past 25 years, and has expertise in the visible, microwave and more recently, terahertz regimes, producing a large body of work including several publications in world leading journals. Some of the work presented in this thesis has sought to link previously separate areas of the group, by introducing Liquid Crystals into microwave structures. The results of this work have indicated a variety of potentially interesting future areas of work, some of which are listed below.

In *Chapter* 5 a zeroth-order Fabry-Perot type mode was observed on a thin metal film. The frequency at which this occurred was in the diffractive region of the structure. However,

Suckling et al (2004) [36] observed a zeroth-order Fabry-Perot type mode in a thick metal plate in the non-diffractive region. The frequency at which the mode occurs is dependent on the structure dimensions, and therefore changing the structure dimensions may allow the zeroth-order Fabry-Perot type mode on the thin film to be shifted into the non-diffractive region also. Further to this, it may also be possible to introduce tuneability to the excitation of this mode by introducing a second structured metal layer and a dielectric core. Indeed, there is an indication in *Chapter* 8 (when considering samples Y and Z) that an LC core does impact the response of the "slit and cut" type structures, but further work is required to understand the full nature of this behaviour.

In *Chapter* 8 one of the structures investigated is a metal-dielectric-metal structure that has an array of slits etched into the top surface, where the dielectric material was LC. Resonant absorption was demonstrated, and the frequency of absorption was dependent on the slit array structure and LC permittivity. The structure was similar to one described by *Hibbins et al* (2004) [40], in which a non-LC dielectric core had been used. However, *Hibbins et al* (2004) [40] also investigated the transmission of slit arrays constructed in a similar way to the absorbing structure. The transmission structures had an additional array of slits etched into the (previously continuous) metal substrate, allowing resonant transmission (shown in *Figure* 9.1). Therefore by replicating these transmission structures using the large LC cells described in *Chapter* 8 a tuneable microwave transmitting screen could be created. If a thinner substrate (than that of the 1mm glass substrates) then the transmission screens could be made at thicknesses of $\sim$50 μm, much less than the operating wavelength. Such structures would have potentially very high commercial value.

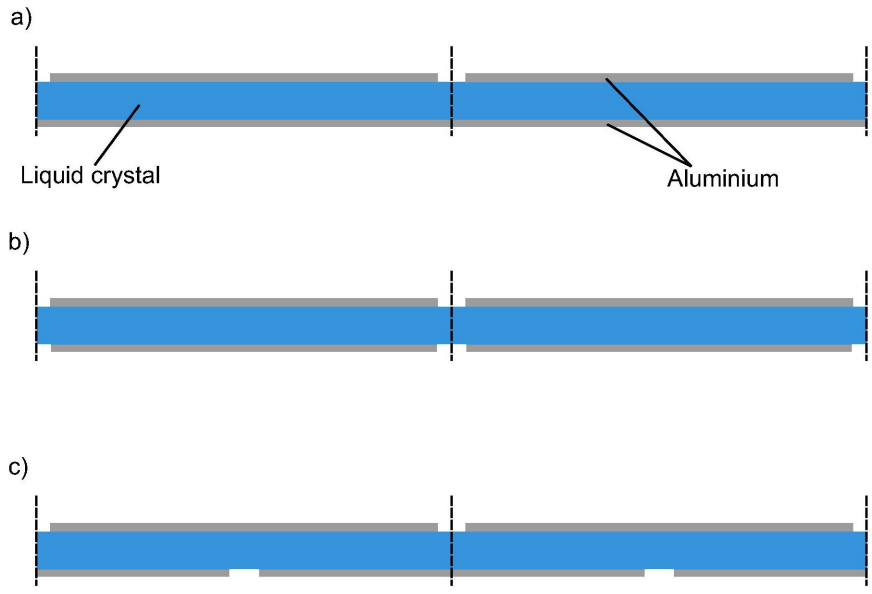

Figure 9.1: a) A structure investigated in *Chapter* 8. b) and c) possible configurations for selective transmission structures where radiation is incident on each structure from above. Dotted lines indicate the unit cell of each structure.

However, in order to maximise the applications of such a microwave filter, some issues

must be considered.

- Ideally, the operation of such a filter would be independent of angle and polarisation, therefore a 1-D slit array (as discussed by *Hibbins et al* (2004) [40]) is not sufficient. A 2-D array as discussed in *Chapter* 8 would be more suitable.

- In order to reduce thickness, a thinner substrate (from which the metal is etched) is required. This introduces the possibility of a flexible substrate, however if this is the case, the LC thickness must be maintained. A PDLC might be useful in order to maintain the core dielectric layer thickness and integrity.

- In addition to selective, tuneable microwave filters, tuneable microwave absorbers may also be achieveable by modifying the penny array structures (from *Chapter* 8) to a thin, flexible type structure. The realisation of such a structure would be extremely attractive in a commercial sense.

Chapter 7 discusses the absorption response of penny arrays, and finds that resonant absorption is virtually independent of both angle and incident polarisation. Such structures may be modified to work as microwave filters, perhaps allowing no transmission at a frequency determined by structure dimensions, whilst allowing all other frequency radiation to pass unimpeded. This may be achieved by having two arrays of pennies, separated by a dielectric layer. At the resonant frequency, incident radiation may be absorbed by the structure, whilst at other frequencies it may pass straight through the structure. Alternatively, it may be possible to increase the breadth of frequency over which the penny array absorbs radiation by having a stack of alternate metal and dielectric layers. Some work on this area has already been conducted within the group and results are promising.

Chapters 6 and 8 illustrate that it is possible to shift the frequency at which both resonant transmission and absorption occur by introducing LCs. However, the LCs used in the experimental work of this thesis are designed to operate at optical frequencies. It would be of great value to work with a chemistry group in order to develop LCs optimised for operation at microwave frequencies. Alternatively, it may be that there are other types of tuneable material already in existence that would fulfill the required role suitably. Additionally, the permeabilities of LCs are not commonly considered when dealing with optical LCs, but may be significant in some of the samples discussed in this thesis and other microwave structures. When considering the applications of thin, tuneable filters and absorbers mentioned above, the speed of switching and loss within the LC material becomes of significance. This is an area into which there has been significant study of the optical properties of LCs, and optimisation of such parameters, but virtually no work at microwave frequencies. The work of this thesis has demonstrated that LCs can have significant applications in structures designed for the control of microwave frequency radiation in both transmission and absorption, and the scope for potential ideas and applications is huge. Of course the LCs are not the only tuneable dielectrics which may be incorporated, and the investigation of the relative value of

alternatives would be valuable. Finally the good lessons learned here may be fruitfully applied to the Terahertz domain where there is presently much more recent activity.

9.3 List of publications and presentations

Enhanced microwave transmission through a patterned metal film
R. J. Kelly, M. J. Lcokyear, J. R. Suckling, C. R. Lawrence and J. R. Sambles
Applied Physics Letters, **90**, 22506, (2007)

Microwaves: Thin metal slits and liquid crystals
J. R. Sambles, A. P. Hibbins, R. J. Kelly, J. R. Suckling and F. Yang
Proc. SPIE Int. Soc. Opt. Eng. 5618, 1 (2004)

Micro-disc arrays as thin highly absorbing frequency selective metamaterial surfaces at microwave frequencies
M. J. Lockyear, R. J. Kelly, A. P. Hibbins and J. R. Sambles
Submission pending due to sponsor restrictions

Thin, tuneable microwave absorbers using liquid crystals and micro-disc arrays
R. J. Kelly, M. J. Lockyear, A. P. Hibbins and J. R. Sambles
In preparation

Determining liquid crystal permittivities at microwave frequencies
R. J. Kelly, C. R. Lawrence and J. R. Sambles
BLCS Conference, University of Exeter, UK (2005) *oral presentation*

Determining liquid crystal permittivities at microwave frequencies
R. J. Kelly, C. R. Lawrence and J. R. Sambles
ECLC Conference, Sesto, Italy (2005) *poster presentation*

Characterisation of liquid crystals at microwave frequencies
R. J. Kelly, C. R. Lawrence and J. R. Sambles
IoP Conference, Physics 2005, University of Warwick, UK (2005) *poster presentation*

Characterisation of liquid crystals and PDLCs at microwave frequencies
R. J. Kelly, C. R. Lawrence and J. R. Sambles
BLCS Conference, University of Exeter, UK (2006) *poster presentation*

Microwave transmission through subwavelength element arrays
R. J. Kelly, M. J. Lockyear, C. R. Lawrence and J. R. Sambles
NanoMeta Conference, Seefeld, Austria (2007) *poster presentation*

References

1. R. W. Wood, *Phil. Mag.* **4**, 396 (1902)
2. R.W. Wood, *Phil. Mag.* **23**, 310 (1912)
3. L. R. Ingersoll, *Astrophys. J.*, **51**, 129 (1920)
4. J. Strong, *Phys. Rev.*, **48**, 480 (1935)
5. U. Fano, *J. Opt. Soc. Am.*, **31**, 213 (1941)
6. R. A. Ferrel, *Phys. Rev.*, **111**, 1214 (1958)
7. W. Steinmann, *Phys. Rev. Lett.* **5**, 470 (1960)
8. R. H. Rithie and H.B. Eldridge, *Phys. Rev.*, **126**, 1935 (1962)
9. J. Zenneck, *Ann. Phys.*, **28**, 665 (1909)
10. A. Sommerfeld, *Ann. Phys.*, **28**, 665 (1909)
11. Y. Y. Teng and E. A. Stern, *Phys. Rev. Lett.*, **19**, 511 (1967)
12. R. H. Ritchie, E. T. Arakawa, J. J. Cowan and R. M. Hamm, *Phys. Rev. Lett.* **21**, 1530 (1968)
13. D. Beaglehole, *Phys. Rev. Lett.*, **22**, 708 (1969)
14. E. Kretschmann and H. Raether, *Z. Natur.*, **23a**, 2135 (1968)
15. A. Otto, *S. Physik*, **216**, 398 (1968)
16. G. Friedel, *Ann. Phys.*, **19**, (1922)
17. K. C. Lim, J. D. Margerum and A. M. Lackner, *Electron. Lett.*, **29**, 1065-1067 (1992)
18. K. C. Lim, J. D. Margerum and A. M. Lackner, L. J. Miller, E. Sherman and W. H. Smith, *Liq. Cryst.*, **14**, 327-337 (1993)
19. F. Guerin, J. M. Chappe, P. Joffre and D. Dolfi, *Jap. J. Appl. Phys. Pt. 1*, **36**, 4409-4413 (1997)
20. M. Tanaka, T. Nose, S. Sato, *Jap. J. Appl. Phys.*, **39**, 6393-6396 (2000)

21. H. Fujikake, T. Kuki, T. Nomoto, Y. Tsuchiya and Y. Utsumi, *J. Appl. Phys.*, **89**, 5295-5298 (2001)

22. M. Tanaka and S. Sato, *J. Appl. Phys.*, **40**, L1123-L1125 (2001)

23. F. Yang and J. R. Sambles, *Appl. Phys. Lett.*, **79**, 3717-3719 (2001)

24. M. Tanaka and S. Sato, *IEEE Microw. Wirel. Compon. Lett.*, **12**, 163-165 (2002)

25. F. Yang and J. R. Sambles, *Appl. Phys. Lett.*, **81**, 2047-2049 (2002)

26. T. Kuki, H. Fujikake and T. Nomoto, *IEEE Trans. Microw. Theo.*, **50**, 2604-2609 (2002)

27. F. Yang and J. R. Sambles, *Appl. Phys. Lett.*, **85**, 2041-2043 (2004)

28. J. A. Porto, F. J. Garcia-Vidal and J.B. Pendry, *Phys. Rev. Lett.*, **83**, 14 (1999)

29. T. W. Ebbesen, H. J. Lezec, H. F. Ghaemi, T. Thio and P. A. Wolff, *Nature*, **391**, 667 (1998)

30. U. Schröter and D. Heitmann, *Phys Rev B*, **58**, 23, (1998)

31. S. Astilean, Ph. Lalanne and M. Palamaru, *Opt. Comm.*, **92**, 265 (2000)

32. S. Collin, F. Pardo, R. Teissier and J-L. Pelouard, *J. Opt. A: Pure Appl. Opt.*, **4**, 154, (2002)

33. H. E. Went, A. P. Hibbins, J. R. Sambles, C. R. Lawrence and A. P. Crick, *Appl. Phys. Lett.*, **77**, 18 (2000)

34. A. P. Hibbins, J. R. Sambles, C. R. Lawrence and D. M. Robinson, *Appl. Phys. Lett.*. **79**, 17 (2001)

35. Y. Takakura, *Phys. Rev. Lett.*, **86**, 24, (2001)

36. J. R. Suckling, A. P. Hibbins, M. J. Lockyear, T. W. Priest and J. R. Sambles, *Phys. Rev. Lett.*, **92**, 14 (2004)

37. W. C. Tan, J. R. Sambles and T. W. Priest, *Phys. Rev. B.*, **61**, 19 (2000)

38. A. P. Hibbins and J. R. Sambles, *Appl. Phys. Lett.*, **80**, 13 (2002)

39. M. J. Lockyear, A. P. Hibbins and J. R. Sambles, *Appl. Phys. Lett.*, **83**, 4 (2003)

40. A. P. Hibbins, C. R. Lawrence, J. R. Brown and J. R. Sambles, *Phys. Rev. Lett.*, **92**, 14 (2004)

Bibliography

[1] R. W. Wood, *Phil. Mag.* **4**, 396 (1902)

[2] R.W. Wood, *Phil. Mag.* **23**, 310 (1912)

[3] L. R. Ingersoll, *Astrophys. J.*, **51**, 129 (1920)

[4] J. Strong, *Phys. Rev.*, **48**, 480 (1935)

[5] U. Fano, *J. Opt. Soc. Am.*, **31**, 213 (1941)

[6] R. A. Ferrel, *Phys. Rev.*, **111**, 1214 (1958)

[7] W. Steinmann, *Phys. Rev. Lett.* **5**, 470 (1960)

[8] R. H. Rithie and H.B. Eldridge, *Phys. Rev.*, **126**, 1935 (1962)

[9] J. Zenneck, *Ann. Phys.*, **28**, 665 (1909)

[10] A. Sommerfeld, *Ann. Phys.*, **28**, 665 (1909)

[11] Y. Y. Teng and E. A. Stern, *Phys. Rev. Lett.*, **19**, 511 (1967)

[12] R. H. Ritchie, E. T. Arakawa, J. J. Cowan and R. M. Hamm, *Phys. Rev. Lett.* **21**, 1530 (1968)

[13] D. Beaglehole, *Phys. Rev. Lett.*, **22**, 708 (1969)

[14] E. Kretschmann and H. Raether, *Z. Natur.*, **23a**, 2135 (1968)

[15] A. Otto, *S. Physik*, **216**, 398 (1968)

[16] G. Friedel, *Ann. Phys.*, **19**, (1922)

[17] K. C. Lim, J. D. Margerum and A. M. Lackner, *Electron. Lett.*, **29**, 1065-1067 (1992)

[18] K. C. Lim, J. D. Margerum and A. M. Lackner, L. J. Miller, E. Sherman and W. H. Smith, *Liq. Cryst.*, **14**, 327-337 (1993)

[19] F. Guerin, J. M. Chappe, P. Joffre and D. Dolfi, *Jap. J. Appl. Phys. Pt. 1*, **36**, 4409-4413 (1997)

[20] M. Tanaka, T. Nose, S. Sato, *Jap. J. Appl. Phys.*, **39**, 6393-6396 (2000)

[21] H. Fujikake, T. Kuki, T. Nomoto, Y. Tsuchiya and Y. Utsumi, *J. Appl. Phys.*, **89**, 5295-5298 (2001)

[22] M. Tanaka and S. Sato, *J. Appl. Phys.*, **40**, L1123-L1125 (2001)

[23] F. Yang and J. R. Sambles, *Appl. Phys. Lett.*, **79**, 3717-3719 (2001)

[24] M. Tanaka and S. Sato, *IEEE Microw. Wirel. Compon. Lett.*, **12**, 163-165 (2002)

[25] F. Yang and J. R. Sambles, *Appl. Phys. Lett.*, **81**, 2047-2049 (2002)

[26] T. Kuki, H. Fujikake and T. Nomoto, *IEEE Trans. Microw. Theo.*, **50**, 2604-2609 (2002)

[27] F. Yang and J. R. Sambles, *Appl. Phys. Lett.*, **85**, 2041-2043 (2004)

[28] J. A. Porto, F. J. Garcia-Vidal and J.B. Pendry, *Phys. Rev. Lett.*, **83**, 14 (1999)

[29] T. W. Ebbesen, H. J. Lezec, H. F. Ghaemi, T. Thio and P. A. Wolff, *Nature*, **391**, 667 (1998)

[30] U. Schröter and D. Heitmann, *Phys Rev B*, **58**, 23, (1998)

[31] S. Astilean, Ph. Lalanne and M. Palamaru, *Opt. Comm.*, **92**, 265 (2000)

[32] S. Collin, F. Pardo, R. Teissier and J-L. Pelouard, *J. Opt. A: Pure Appl. Opt.*, **4**, 154, (2002)

[33] H. E. Went, A. P. Hibbins, J. R. Sambles, C. R. Lawrence and A. P. Crick, *Appl. Phys. Lett.*, **77**, 18 (2000)

[34] A. P. Hibbins, J. R. Sambles, C. R. Lawrence and D. M. Robinson, *Appl. Phys. Lett.*. **79**, 17 (2001)

[35] Y. Takakura, *Phys. Rev. Lett.*, **86**, 24, (2001)

[36] J. R. Suckling, A. P. Hibbins, M. J. Lockyear, T. W. Priest and J. R. Sambles, *Phys. Rev. Lett.*, **92**, 14 (2004)

[37] W. C. Tan, J. R. Sambles and T. W. Priest, *Phys. Rev. B.*, **61**, 19 (2000)

[38] A. P. Hibbins and J. R. Sambles, *Appl. Phys. Lett.*, **80**, 13 (2002)

[39] M. J. Lockyear, A. P. Hibbins and J. R. Sambles, *Appl. Phys. Lett.*, **83**, 4 (2003)

[40] A. P. Hibbins, C. R. Lawrence, J. R. Brown and J. R. Sambles, *Phys. Rev. Lett.*, **92**, 14 (2004)